Space Plane Trajectory Optimization

Investigation of a Launch Window Extension by Lateral Motion

Joël de Vries

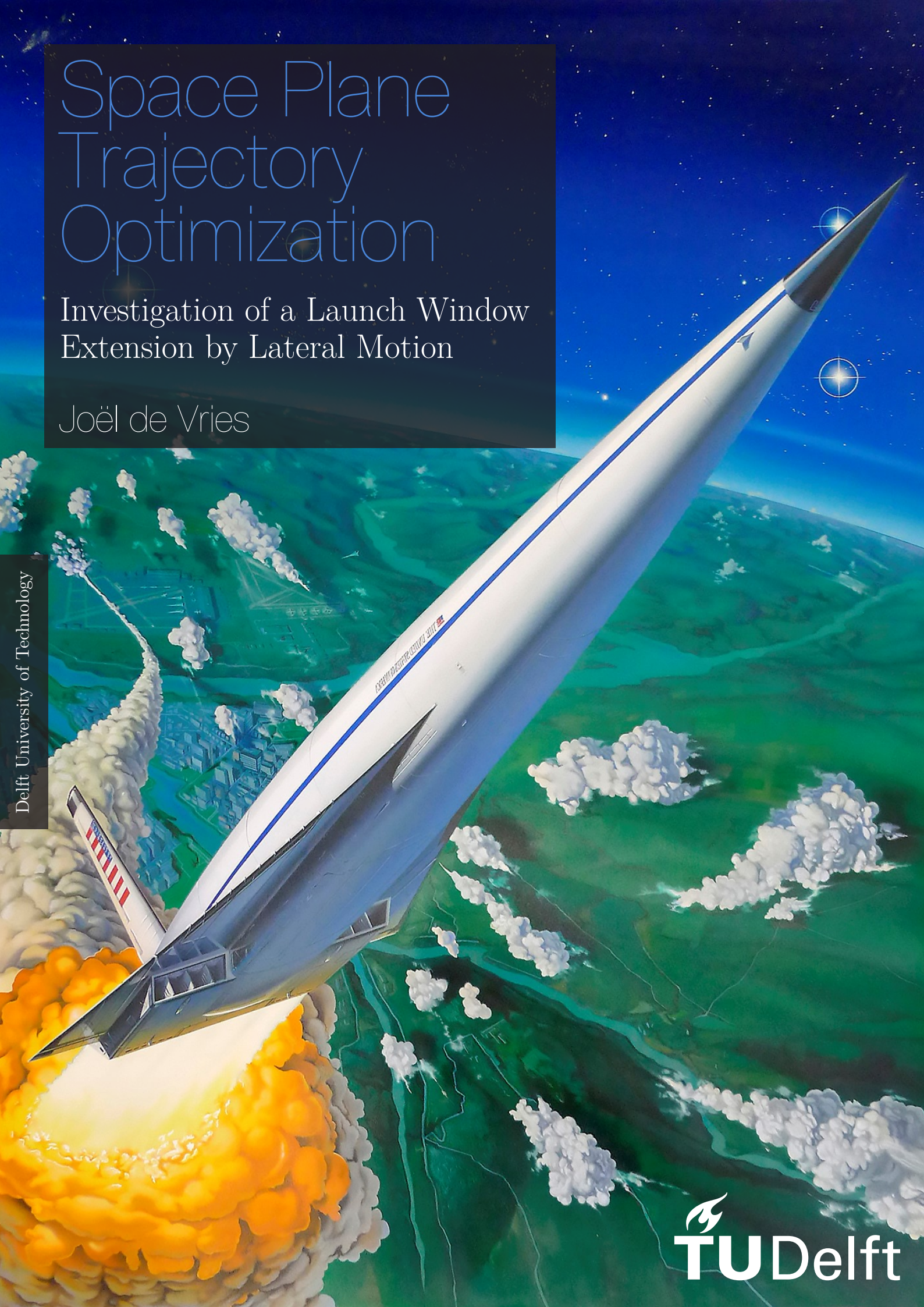

Delft University of Technology

TU Delft

Space Plane Trajectory Optimization

Investigation of a Launch Window Extension by Lateral Motion

by

Joël de Vries

to obtain the degree of Master of Science
at the Delft University of Technology,
to be defended publicly on Friday June 24, 2022 at 14:00.

Student number:	4222571	
Project Duration:	July 12, 2021 – June 24, 2022	
Thesis committee:	Prof. Dr. Ir. P.N.A.M. Visser	TU Delft, chairman
	Ir. M.C. Naeije	TU Delft, supervisor
	Ir. D. Dirkx	TU Delft
	Ir. E. van Kampen	TU Delft

Cover image: An artist concept of the National AeroSpace Plane (NASP) taking off.[1]

An electronic version of this thesis is available at `http://repository.tudelft.nl/`.

[1] Correll, J.T., 2022, 'The Spaceplane: 60 Years On.', *Air Force Magazine*, `https://www.airforcemag.com/article/the-spaceplane-60-years-on/`, accessed June 11, 2022.

TU Delft

Preface

I am proud to present the work that I have done for almost a year. Even though this report is a requirement to complete my Master of Science at the TU Delft, it has not felt like it. Throughout the year, I have discovered amazing theories and methods. I have been able to create a piece of software that is capable of simulating the ascent of a space plane. And I have struggled to find some pesky bugs in the process. Looking back on that now, I can say that I have learned and grown so much, while having an amazing time.

This report details the investigation of a space plane to ascent to orbit with an increased launch window. In order to investigate this I have challenged myself to do two things. First, I wanted to be able to define the space plane equations of motion in six degrees of freedom. And second, I wanted to build a robust guidance and control system that would be able to guide the space plane towards space. All of the knowledge that I gained to achieve these to goals is written down in this report. I hope that any reader, perhaps at the cusp of starting their own Master thesis, finds this information useful.

I also would like to thank a number of amazing people that have helped me throughout this study. First of, my supervisor Marc Naeije. Thank you for the many hours that you have spent listening to me, guiding me to achieve my goals, and the accompanying encouragements. The patience and understanding that you have given me, sometimes throughout difficult times, is very much appreciated. Secondly I would like to thank two professors that have been helping me. Dominic Dirkx, who helped me in the amazing and difficult realm of TUDAT. The amount of emails that you have responded to with issues that seemed impossible to solve is astounding. And Erik-Jan van Kampen who guided me with the guidance and control methods that I have applied to the space plane. Thirdly, I would like to thank my sister Inez for helping me proofread the report and my brother Melle for taking the time to listen. I would also like to thank my thesis support group. Weilun, Gemo and Emilie thank you for your support and the laughs that we had. I am very happy that we were able to have dinner and drinks together and that we were able to share our enthusiasm of anything related to space. Last but not least, I would like to thank my girlfriend Kim. The support that you give me to realize my dreams and goals means the world to me.

Joël de Vries,
Delft, June 2022

Abstract

Single-Stage-To-Orbit (SSTO) launch vehicles are capable of reaching orbit while being potentially fully reusable. A technology capable of enabling SSTO access to space are air-breathing engines, such as the Synthetic Air Breathing Rocket Engine (SABRE) and Rocket-Based Combined Cycle (RBCC) engines. These promise higher engine performance in terms of specific impulse at the cost of a lower thrust-over-weight (T/W) ratio. These engines necessitate the use of a Horizontal Take-off and Horizontal Landing (HTHL) launch vehicle with a lifting surface to compensate for the low thrust-over-weight (T/W) ratio. The inclusion of a lifting surface enables the launch vehicle to use banking maneuvers to manipulate the orbital Right Ascensions of the Ascending Node (RAAN) that the space plane achieves. This means that the space plane is capable of advancing or delaying its time of launch, while still achieving a similar orbital RAAN. This effectively increases the launch window even if a precise orbit insertion is necessary.

In this thesis, the fuel-optimal ascent trajectory for a space plane is investigated that would include an extended launch window. In order to simulate a banking maneuver the full six Degrees of Freedom (DoF) Equations of Motion (EoM) have been defined for a theoretical space plane called the National Aero-Space Plane (NASP), which is developed to enable hypersonic and SSTO space plane research. In order to guide and control the space plane, a robust Guidance and Control (G&C) system is designed that is capable of using the nonlinear EoM. The algorithms used are the Non-linear Dynamic Inversion (NDI) and Incremental Non-linear Dynamic Inversion (INDI) algorithms. The latter has the benefit of reducing its dependency on the dynamic models, which ensures that the space plane can be effectively controlled even if the vehicle model has uncertainties in it.

The optimization of the ascent trajectory of a space plane is an optimal control problem. In order to optimize the ascent, the control problem is converted into a NonLinear Programming (NLP) problem by defining for specific altitudes the flight path angle. The discrete number of flight path angles is used together with the Hermite spline interpolation method to define a continuous function of the flight path angle, which is dependent on the altitude. For the heading angle, a target orbital inclination together with a deviation is used to compute the heading angle. The deviation is used as an optimization parameter, which is dependent on the altitude. By using the deviation, it was possible to define the heading angle for the majority of the ascent with a minimal amount of optimization parameters.

The ascent trajectory is optimized with the global optimization algorithm Multi-Objective Evolutionary Algorithm with Decomposition (MOEA/D). Two objectives were defined that had to be optimized by the algorithm. These objectives are the final achieved orbit and the propellant used during the ascent. In addition, several constraints were implemented, such as the maximum allowable dynamic pressure and heat flux. These parameters are automatically controlled by the G&C system, which ensures that the constraints are never violated.

The ascent has been optimized for a number of different launch times ranging from an advanced launch of two hours to a delayed launch of two hours. The ascent trajectory has been optimized that included a deviation in the inclination in order to achieve the same RAAN irregardless of the launch time. It was found that, at the cost of propellant, it is possible to have a launch time delayed are advanced by as much as two hours. This means that the space plane can manipulate the RAAN by $\pm$ 30 degrees. The extra cost in terms of propellant is related to an increase in drag losses. The banking maneuvers that are done to manipulate the RAAN require a higher angle of attack to maintain the required flight path angle, which in turn increases the drag force. The increased propellant cost consequently means that the amount of payload to be inserted is reduced. For a nominal launch, it was found that approximately 5106 kg of payload could be brought into orbit. For a one hour advanced launch, the maximum payload would be reduced to 3554 kg. A one hour delayed launch would result in a maximum payload of 3426 kg. For a two hour advanced launch it was found that 1514 kg is available as payload. For a two hour delayed launch it was found that the definition of the heading angle was a limiting factor, which meant that the optimized ascent trajectory with banking maneuver was sub-optimal. This resulted in a maximum available payload of 772 kg.

Keywords: *Space Plane, Multi-Objective Optimization, Ascent Trajectory, Launch Window Extension*

Contents

List of Figures

List of Tables

List of Abbreviations

Abbreviation	Description
APAS	Aerodynamic Preliminary Analysis System
ATS	Access To Space
CFD	Computational Fluid Dynamics
CoG	Center of Gravity
CoT	Center of Thrust
DATCOM	Digital Datcom
DC-X	Delta Clipper Experimental
DC-XA	Delta Clipper Advanced
DE	Differential Evolution
DEAN	Dual-Expander Aerospike Nozzle
DoF	Degrees of Freedom
E/D	Expansion Deflection
EoM	Equations of Motion
ESA	European Space Agency
FESTIP	Future European Space Transportation Initiation Programme
GA	Genetic Algorithm
GTO	Geostationary Transfer Orbit
G&C	Guidance and Control
HTHL	Horizontal Take-off and Horizontal Landing
INDI	Incremental Non-linear Dynamic Inversion
ISS	International Space Station
JAXA	Japan Aerospace Exploration Agency
LACE	Liquid Air Cycle Engine
LEO	Low Earth Orbit
LTE	Local Truncation Error
MAC	Mean Aerodynamic Chord
MECO	Main Engine Cut-Off
MHACO	Multi-Objective Hypervolume-based Ant Colony Optimizer
MOEA/D	Multi-Objective Evolutionary Algorithm with Decomposition
MRP	Moment Reference Point
MTOW	Maximum TakeOff Weight
NASA	National Aeronautics and Space Administration
NASP	National Aero-Space Plane
NDI	Non-linear Dynamic Inversion
NLP	NonLinear Programming
NOAA	National Oceanic and Atmospheric Administration
NSGA2	Non-dominated Sorting Genetic Algorithm
NSPSO	Non-dominated Sorting Particle Swarm Optimizer
OEW	Operating Empty Weight
PaGMO	Parallel Global Multiobjective framework for Optimization
PANAIR	Panel Aerodynamics

Abbreviation	Description
PDAS	Public Domain Aeronautical Software
PLS	Personnel Launch System
PSO	Particle Swarm Optimizer
RAAN	Right Ascensions of the Ascending Node
RBCC	Rocket-Based Combined Cycle
RCS	Reaction Control System
REL	Rocket Engine Limited
RK4	Runge-Kutta 4
RLV	Reusable Launch Vehicle
RMS	Root Mean Square
SA	Simulated Annealing
SABRE	Synthetic Air Breathing Rocket Engine
SSTO	Single-Stage-To-Orbit
TBCC	Turbo-Based Combined Cycle
TSTO	Two-Stage-To-Orbit
TUDAT	TU Delft Astrodynamics Toolbox
TVC	Thrust Vector Control
US76	United States standard atmosphere 1976
VTHL	Vertical Take-off Horizontal Landing
VTVL	Vertical Take-off and Vertical Landing

List of Symbols

Roman Symbol	Unit	Description
a	[km]	Semi-major axis
A_e	[m^2]	Exhaust area
b	[km]	Semi-minor axis
b_{ref}	[m]	Wingspan
C_D	[-]	Total drag force coefficient
C_L	[-]	Total lift force coefficient
C_l	[-]	Total rolling moment coefficient
C_m	[-]	Total pitching moment coefficient
C_n	[-]	Total yawing moment coefficient
c_{ref}	[m]	Mean Aerodynamic Chord (MAC)
C_S	[-]	Total side force coefficient
D	[N]	Drag force
e	[-]	Eccentricity
g	[m/s^2]	Gravitational acceleration
G	[$m^3/kg\ s^2$]	Universal gravity constant
g_0	[m/s^2]	Standard gravity of the Earth
i	[rad]	Inclination
I	[kgm^2]	Moment of Inertia
I_{sp}	[s]	Specific impulse
L	[N]	Lift force
$\mathcal{L}$	[Nm]	Aerodynamic rolling moment
m	[kg]	Mass
$\dot{m}$	[kg/s]	Mass flow rate
M	[-]	Mach number
M	[rad]	Mean Anomaly
M	[kg/kmole]	Molecular mass
$\mathcal{M}$	[Nm]	Aerodynamic pitching moment
M_c	[Nm]	Actuator induced moment
$\dot{m}_f$	[kg/s]	Fuel mass flow rate
M_f	[kg]	Final launcher mass
M_v	[Nm]	Vehicle induced moment
M_x	[Nm]	Moment about the x_B-axis
M_y	[Nm]	Moment about the y_B-axis
M_z	[Nm]	Moment about the z_B-axis
M_0	[kg]	Initial launcher mass
n	[rad/s]	Mean angular velocity
N	[m^{-3}]	Total number density
$\mathcal{N}$	[Nm]	Aerodynamic yawing moment
N_A	[$kmol^{-1}$]	Avogadro's constant
p	[Pa]	Pressure
p	[rad/s]	Roll rate
p_a	[Pa]	Ambient pressure

Roman Symbol	Unit	Description
p_e	[Pa]	Exhaust pressure
q	[Rad/s]	Pitch rate
$q_{c,\text{lam}}$	[W/cm^2]	Maximum heat flux for laminar flow
$q_{c,\text{turb}}$	[W/cm^2]	Maximum heat flux for turbulent flow
r	[Rad/s]	Yaw rate
R	[km]	Distance
R^*	[J/kmole K]	Universal gas constant
R_e	[km]	Earth radius
S_{ref}	[m^2]	Vehicle reference area
T	[N]	Thrust force
T/W	[-]	Thrust-to-weight ratio
v_e	[m/s]	Exhaust velocity
v_{eq}	[m/s]	Effective exhaust velocity
V	[m/s]	Velocity

Greek Symbol	Unit	Description
α	[rad]	Angle of attack
β	[rad]	Angle of sideslip
γ	[rad]	Flight-path angle
δ	[rad]	Latitude
δ_{dc}	[rad]	Canard deflection angle
$\delta_{\text{de,l}}$	[rad]	Left elevon deflection angle
$\delta_{\text{de,r}}$	[rad]	Right elevon deflection angle
δ_{dr}	[rad]	Rudder deflection angle
ΔV	[km/s]	Change in velocity
ϵ_t	[rad]	Elevation thrust off-set angle
ζ	[rad]	Heading error
θ	[rad]	Pitch angle
μ	[s]	Gravitational parameter of a central body
ρ	[kg/m^3]	Density
σ	[rad]	Bank angle
τ	[rad]	Longitude
τ	[s]	Time of pericenter passage
ϕ	[rad]	Roll angle
ϕ	[-]	Fuel equivalence ratio
χ	[rad]	Heading angle
ψ	[rad]	Yaw angle
ψ_T	[rad]	Azimuth thrust off-set angle
ω	[rad/s]	Angular velocity
ω	[rad]	Argument of pericenter
Ω	[rad]	Right ascension of the ascending node

1 Introduction

Throughout the last decades, attempts have been made to develop Single-Stage-To-Orbit (SSTO) launch vehicles that would be reusable. Initially, even the space shuttle was meant to be a reusable launch vehicle. Unfortunately, these attempts have been halted due to low technological readiness and high development costs. At the end of the previous century, the X-33 came close but failed due to difficulties with the construction of the composite hydrogen fuel tanks (Coppinger, 2005). Currently, reusable booster stages are being developed, which means that launch vehicles become at least semi-reusable. The main issue with developing a fully reusable SSTO launch vehicle is the relatively low performance that a conventional rocket engine yields, and the high structural weight. To mitigate the first issue, altitude compensating nozzles have been developed, which increases the performance of the engine. However, these do not yield the performance to achieve actual SSTO access to space. Instead, completely new engines are being developed, which incorporate air-breathing modes to lower the amount of liquid oxygen that needs to be carried by the launch vehicle. This effectively increases the engine performance. The downside of using an air-breathing mode is that the thrust-over-weight ratio (T/W) is lower compared to conventional rocket engines. This necessitates the use of a horizontally launched launch vehicle with a lifting surface. These so-called space planes will horizontally launch and land.

The inclusion of a lifting surface enables new maneuvers, not available to conventional rockets. A space plane can more easily maneuver in lateral direction, which enables manipulation of the inclination and Right Ascensions of the Ascending Node (RAAN) during the ascent trajectory (Zhou, Wang, and Cui, 2020). The manipulation of the RAAN means that a space plane can potentially increase the launch window, even if the mission requires a very precise orbit insertion such as a rendezvous with the International Space Station (ISS). Due to the novelty, not much research has been done on the lateral motion of space planes.

The focus of this MSc thesis is to identify the fuel-optimal trajectory for a space plane that would have a delayed or advanced launch. The goal of the ascent is to achieve a similar orbit in terms of semi-major axis, eccentricity, inclination and RAAN irregardless of the launch time, while minimizing the required propellant to reach that orbit. By minimizing the amount of propellant used, the amount of payload that can be brought into orbit can be maximized. The following research question has been formulated to guide the identification of the fuel-optimal trajectory.

Research Question: *What is the fuel-optimal ascent trajectory for a Horizontal Take-off and Horizontal Landing (HTHL) space plane, which includes a change in the Right Ascensions of the Ascending Node (RAAN) to extend the launch window?*

The change in the RAAN is accomplished by initiating a banking maneuver during the ascent, which will change the heading angle of the space plane. In order to quantify the cost of such a maneuver, the ascent trajectory with a change in RAAN is compared to a nominal ascent trajectory. The nominal ascent trajectory will launch at such a time that a change in RAAN is not necessary. The propellant cost of the nominal ascent trajectory will be compared to the propellant cost of the ascent trajectory that manipulates the RAAN. Additionally, a simple maneuver to change the RAAN in-orbit is computed, which can be used to quantify the efficiency of the change in RAAN by the space plane. The following Sub-Questions (SQ) have been formulated to support the answer to the research question and to enable comparison between the nominal, and advanced

or delayed launch.

SQ1 *What is the fuel-optimal ascent trajectory for a Horizontal Take-off and Horizontal Landing (HTHL) launch vehicle without considering a launch window?*

SQ2 *How does the required propellant during the ascent trajectory vary due to the inclusion of an extended launch window?*

SQ3 *How does the required propellant for a change in the Right Ascensions of the Ascending Node (RAAN) by a space plane compare to the same change in the right ascension of the ascending node by a traditional secondary stage?*

In order to answer the research question, a number of objectives are identified. First of all, the inclusion of a banking maneuver requires the inclusion of the full six Degrees of Freedom (DoF) translational and rotational Equations of Motion (EoM). In practice, the angle of sideslip can be assumed small, which reduces the EoM by eliminating the side force generated by the space plane. In this study it is chosen to not use this assumption and incorporate the side force. Second of all, a Guidance and Control (G&C) system needs to be designed that guides the space plane and controls its orientation. In previous studies, a linearized G&C system is used, which introduces eigenmotions. In order to eliminate the eigenmotions, it is chosen to design a robust nonlinear G&C system. The use of this robust system, will support the optimization process and the sensitivity analysis that will be performed on the obtained results. Third of all, this study will incorporate a vehicle model that has been used in previous studies. The vehicle model used is the National Aero-Space Plane (NASP), also named the winged cone configuration. This vehicle has been used by Mooij (1998) to find a fuel-optimal trajectory. That trajectory is launched along the equator and does not change the heading angle. In conjunction with the vehicle model, constraints such as the maximum dynamic pressure, heat flux and maximum axial acceleration are adopted from this study. This enables extensive verification of the integrated vehicle model and the obtained results. The objectives for the study can be summarized by a number of Additional Goals (AG):

AG1 Include the full six Degrees of Freedom (DoF) translational and rotational Equations of Motion (EoM).

AG2 Include a G&C system that can deal with the nonlinear translational and rotational Equations of Motion (EoM).

AG3 Include a vehicle model that has been used before to optimize the longitudinal ascent, which includes constraints.

This thesis is structured to first give background information on the development of SSTO space planes in Chapter 2. Additionally, this chapter will discuss engine developments that enable SSTO access to space and an overview of previous ascent trajectory optimization studies for space planes. In Chapter 3 the theoretical information that is needed to define the EoM of a space plane and the required transformation matrices are presented. Chapter 4 discusses the environmental models and vehicle model used to simulate the ascent trajectory. This includes the forces acting on the space plane.

Chapter 5 gives an overview of the optimization theory of an optimal control problem. This includes the method to transcribe the problem to a NonLinear Programming (NLP) problem and a general overview of global optimization theory. Additionally, this chapter discusses the problem definition and a number of issues that came up during this study. The preliminary results obtained from the initial problem definition necessitated a number of changes, which have been described in detail. This is done to give the reader insight into the choices made to define the NLP problem.

Based on the definitive problem definition, a G&C system is designed for the space plane. This system is presented in Chapter 6, which includes a brief introduction to the theory of Non-linear Dynamic Inversion (NDI) and Incremental Non-linear Dynamic Inversion (INDI) control algorithms. In Chapter 7 the numerical methods used to simulate the ascent trajectory of the NASP is discussed. Primarily, the interpolation methods to determine the vehicle data for given variables and the reference trajectory is discussed. In conjunction, the simulation architecture is presented, which includes the integration of the vehicle model and G&C system in the TU Delft Astrodynamics Toolbox (TUDAT) package.

The results of the optimization of the ascent trajectory is presented in Chapter 8. In this chapter, results are presented and discussed that directly can be used to answer the aforementioned research question and sub-questions. Chapter 9 discusses the verification and sensitivity analysis of the obtained results. Finally, in

Chapter 10 the conclusions that can be drawn from the obtained results are discussed. The conclusions drawn are based on the research question and sub-questions that have been formulated in this chapter. Furthermore, a number of recommendations for future research are given based on the results of this thesis.

2

Single-Stage-To-Orbit & Space Plane Launch Vehicles

A Single-Stage-To-Orbit (SSTO) launch vehicle is capable of transporting cargo or personnel from the surface of a planetary body to space. It does so without expending parts of the rocket. Traditional rockets expend parts of the rocket, which until recently would not be reused. An SSTO launch vehicle can potentially be reused and have a low turn-around time since no major parts have to be reconstructed. Alternatively, a space plane, which uses an initial stage, can be used to achieve a similar goal. The initial stage can be retrieved after launch and reused, while the space plane itself can land after it has performed a mission in space. In this chapter, a brief overview will be given of historical and current SSTO and space plane launch vehicles. This will be followed by a discussion about technologies that will enable SSTO access to space. Finally, the chapter will conclude by presenting previous ascent trajectory optimization studies and unique investigations that can still be done.

2.1. Historical SSTO & Space Plane Launch Vehicles

At the end of the 1960s the National Aeronautics and Space Administration (NASA) started development of the space shuttle. The space shuttle was meant to be a low-cost, reusable transportation launch vehicle (Launius, 1994). However, due to high technical requirements, the space shuttle was never developed as a fully reusable launch vehicle (Launius, 2013). Instead, it would expend solid rocket boosters and an external tank during the launch of the shuttle, while landing as a space plane. During the 1990s, studies were conducted to assess the options that were available to replace the Space Shuttle. The recommendation, that followed from the NASA Access To Space (ATS) study, was to develop a new fully reusable system as a replacement for the Space Shuttle (Freeman et al., 1995). Based on those recommendations, the Reusable Launch Vehicle (RLV) program was created, which would focus on assessing vehicle concept, maturing required technologies, and identifying approaches to demonstrate these technologies. Within the program, a number of concepts were proposed, which can be seen in Figure 2.1. Two of these concepts are Vertical Take-off Horizontal Landing (VTHL) launch vehicles, of which one is a lifting body and the other is a winged body. The other concept is a SSTO Vertical Take-off and Vertical Landing (VTVL) launch vehicle.

The lifting body VTHL concept is the X-33 launch vehicle. It was developed as a sub-orbital demonstrator for advanced technologies, which would increase the safety and reliability of launch vehicles as well as reduce the payload cost[1]. Furthermore, the X-33 would enable the development of the VentureStar reusable launch vehicle, which was proposed by Lockheed Martin. In 2001 NASA stopped funding the program since there were difficulties with the composite hydrogen tanks. According to Coppinger (2005), the hydrogen tanks failed due to microcracking in the tank wall. The use of composite hydrogen tanks, aerospike engines, and several other technological advances were necessary in order to reduce the dry weight of the launch vehicle. The reduction in dry weight would ensure that it would meet the SSTO performance requirements (Freeman et al., 1995).

The VTVL launch vehicle is the Delta Clipper Experimental (DC-X) developed by McDonnel Douglas. It

[1]NASA, X-33 Advanced Technology Demonstrator, accessed on 27 Feb 2021, `https://www.nasa.gov/centers/marshall/news/background/facts/x33.html`.

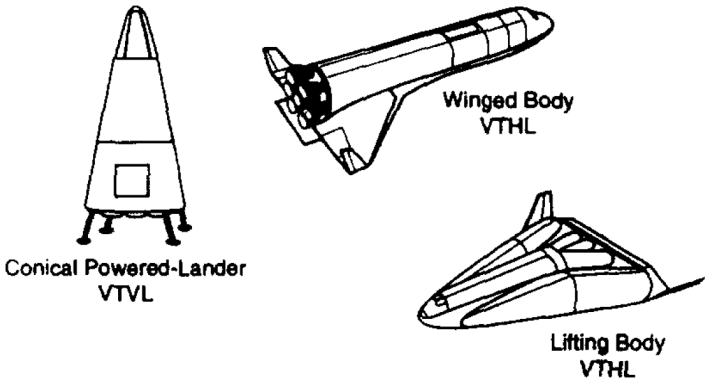

Figure 2.1: Concepts of the Reusable Launch Vehicle program (Freeman et al., 1995).

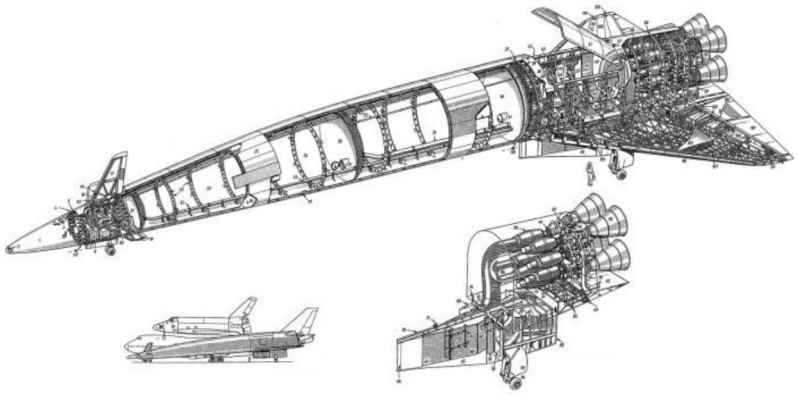

Figure 2.2: Cutaway drawing of the HOTOL space plane[a].

[a] `http://www.aerospaceweb.org/question/spacecraft/q0202.shtml`, accessed on 28 Apr 2021.

was a scale model of an SSTO launch vehicle[2]. In 1995 the DC-X design was procured by NASA and modified to the Delta Clipper Advanced (DC-XA). The technological advances made with the DC-X and DC-XA would help the development of the X-33 (National Research Council, 1995). After the DC-XA suffered severe damage during landing, the program was terminated due to a lack of funding.

Besides the American effort, the British government in combination with British Aerospace and Rolls-Royce have worked on an SSTO RLV, which was also a space plane, see Figure 2.2. During the 1980s the British Aerospace HOTOL, a Horizontal Take-off and Horizontal Landing (HTHL) launch vehicle was developed. It would utilize atmospheric oxygen for part of the launch trajectory, reducing the amount of liquid oxygen needed during launch (Brown, 1986). In 1989 the development of the HOTOL was terminated after the British government and Rolls Royce withdrew their support, after which Rocket Engine Limited was formed to continue the development of an HTHL SSTO launch vehicle (Hempsell, 2013).

The European Space Agency (ESA) has also been working on a space plane called the Hopper, an orbital space plane conceived during the Future European Space Transportation Initiation Programme (FESTIP) (Dujarric, 1999). It was intended as an unmanned RLV that would be able to deliver satellite payloads into orbit[3]. Several test flights have been performed with a prototype of the Hopper.

[2] NASA, 2012, The Delta Clipper Experimental: Flight Testing Archive, accessed on 01 Mar 2021, `https://www.hq.nasa.gov/pao/History/x-33/dc-xa.htm`.

[3] BBC News, Launching the Next Generation of Rockets, accessed on 20 Apr 2021, `http://news.bbc.co.uk/2/hi/science/nature/3699848.stm`.

Figure 2.3: Impression of the SpaceLiner as a rocket-propelled intercontinental passenger transport vehicle (Sippel, Trivailo, et al., 2016).

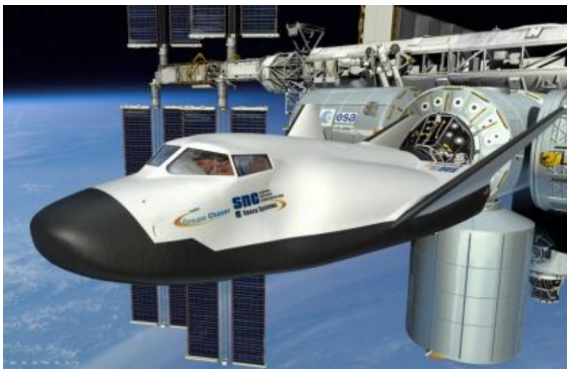

Figure 2.4: Rendering of the Dream Chaser docked to the International Space Station (ISS) (Krevor et al., 2011).

2.2. Current SSTO & Space Plane Launch Vehicles

Currently, a number of SSTO launch vehicles and space planes are being developed. One of these is the SpaceLiner, a reusable Two-Stage-To-Orbit (TSTO) space plane, a passenger transportation concept based on rocket propulsion developed by the German Aerospace Center (Sippel, Trivailo, et al., 2016). The design consists of a fully reusable booster stage and a passenger stage, see Figure 2.3. It is capable of ultra long-haul distances. Several configurations have been developed which could accommodate approximately between fifty and one hundred passengers. Furthermore, the SpaceLiner is seen as a technical basis for a TSTO fully reusable launch vehicle. It can deliver payloads of approximately 26150 kg to Low Earth Orbit (LEO). Furthermore, it is possible to outfit an upper stage, which could transfer from LEO to Geostationary Transfer Orbit (GTO). Estimation is that approximately 8250 kg of payload could be transferred to GTO. Similar to the passenger space plane, the booster will feature wings. It is intended that the booster stage separates at Mach number 12.5. According to Sippel, Trivailo, et al., 2016, such a velocity is too high for a powered fly-back. It is therefore chosen to use an in-air-capturing method (Sippel, Klevanski, and Kauffmann, 2001).

Another space plane currently under development is the Dream Chaser developed by Sierra Nevada Corporation, see Figure 2.4. It is a TSTO VTHL space plane that uses an expendable Atlas V rocket booster as a first stage (Krevor et al., 2011). The space plane itself is a direct continuation of the HL-20, a NASA concept. The HL-20 was designed as a lifting-body Personnel Launch System (PLS), with operational efficiency, reliability and safety in mind (Stone and Piland, 1991). The primary mission of the Dream Chaser is to enable crewed transport to the ISS and back to Earth. It can support a crew of up to seven people for 3.5 days in orbit and

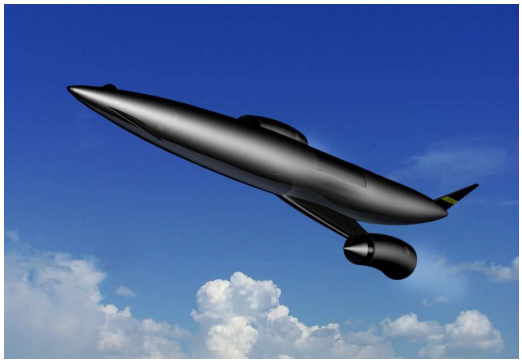

Figure 2.5: Impression of Skylon in flight (Hempsell and Longstaff, 2009).

has a maximum deceleration of 1.5 g during re-entry. The secondary mission is to transport pressurized cargo to and from the ISS.

On a smaller scale, a suborbital space plane HTHL is developed by Dawn Aerospace, a start-up located in the Netherlands and New Zealand. The Dawn Mk-II Aurora is capable of reaching an altitude of approximately 110 km and can deliver $3U$ payloads of up to 4 kg. It furthermore has a take-off weight of 280 kg. The Mk-II is built to demonstrate Dawn's core technologies[4]. Based on these technologies an Mk-III is in development which will be able to deliver 50 to 100 kg satellites to orbit, by utilizing an expendable secondary stage. The method of delivery and the comparison to the Mk-II capabilities can be seen in Figure 2.6. Dawn Aerospace markets its space plane as a launch vehicle with a turn-around time of less than a day, meaning that access to space is possible multiple times per day.

The last SSTO space plane to mention is being developed by Rocket Engine Limited. It is a space plane called the Skylon and is intended as a hybrid air-breathing HTHL launch vehicle utilising the Synthetic Air Breathing Rocket Engine (SABRE). The idea behind SABRE is to utilize the oxygen in the air until an altitude of approximately 25 km is reached and the space plane is accelerated to over Mach 5 (Hempsell, 2013). The development of Skylon and its SABRE engine is a direct result of the study done for the British Aerospace HOTOL. The Skylon will feature two SABRE engines attached to the wings, see Figure 2.5. It will both take-off and land horizontally, enabled by the high specific impulse that the hybrid engines yield during air-breathing mode (Varvill and Bond, 2003). The space plane is capable to deliver 15 tonnes of payload into a 300 km low earth orbit with a take-off mass of 325 tonnes (Hempsell, 2013).

2.3. SSTO Enabling Technologies

In order for a launch vehicle to reach a Low Earth Orbit (LEO) approximately 9 km/s of ΔV is needed, which includes gravity and aerodynamic losses (Varvill and Bond, 2003). The current and historical launch vehicles, previously discussed, use innovative methods to enable SSTO launch vehicles to reach LEO. Before these technologies are discussed, a brief introduction should be given in the formulation of the rocket equation.

2.3.1. The Rocket Equation

In order to understand what might enable an SSTO launch vehicle to reach LEO, first the equation that governs the motion of a rocket needs to be defined. The Tsiolkovsky equation *i.e.* , the rocket equation, which describes the available ΔV of a launch system, is given by:

$$\Delta V = v_{eq} \ln \frac{M_0}{M_f} \tag{2.1}$$

It relates the ΔV that can be obtained by a launch vehicle to the effective exhaust velocity v_{eq} and the propellant mass fraction, M_0/M_f. The mass fraction relates the initial launcher mass to the final launcher mass, *i.e.*, the mass at the moment of engine cut-off. Traditional launch vehicles cannot obtain the required ΔV with a single stage due to low specific impulse I_{sp} of the engines used, which is related to the effective exhaust velocity v_{eq} by:

$$v_{eq} = I_{sp} g_0 \tag{2.2}$$

[4]Dawn Aerospace, Introducing the Dawn Mk-II Aurora, accessed on 20 Apr 2021, `https://www.dawnaerospace.com/dawn-mkii-aurora`.

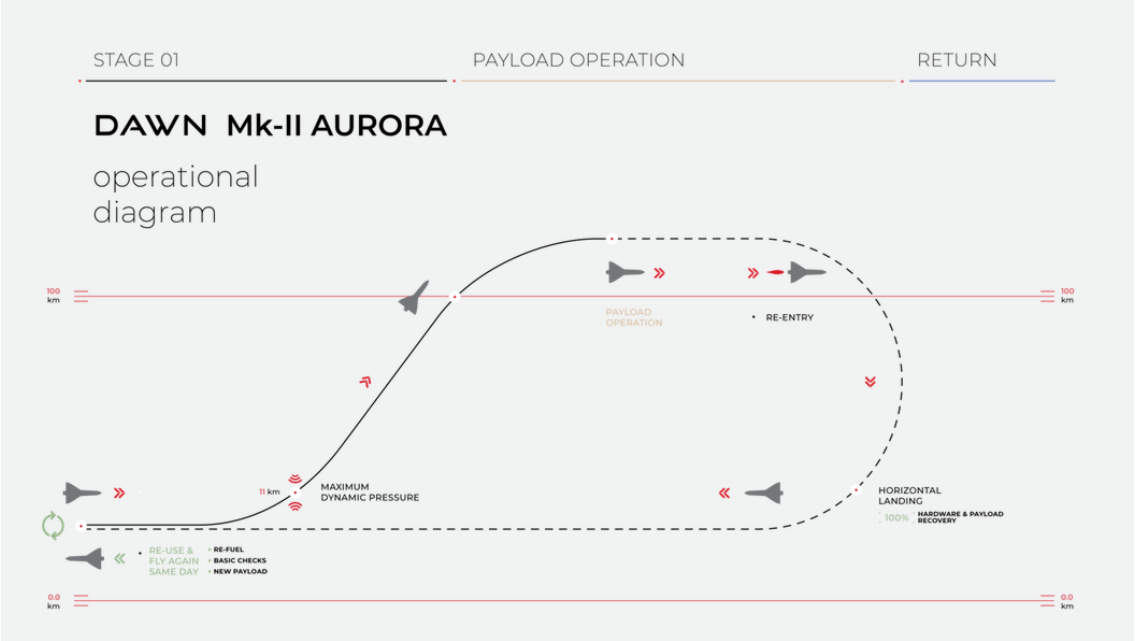

(a) Mk-II

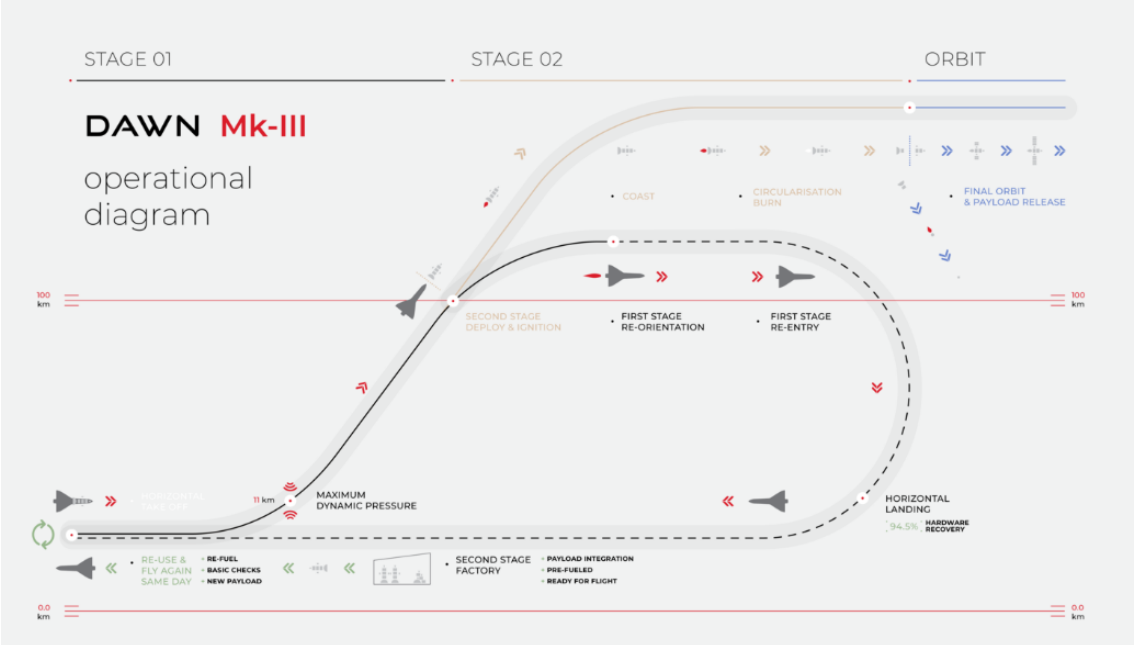

(b) Mk-III

Figure 2.6: Launch envelope for the Dawn Aerospace launch vehicles[b].

[b] `https://www.dawnaerospace.com/dawn-mkii-aurora`, accessed on 20 Apr 2021.

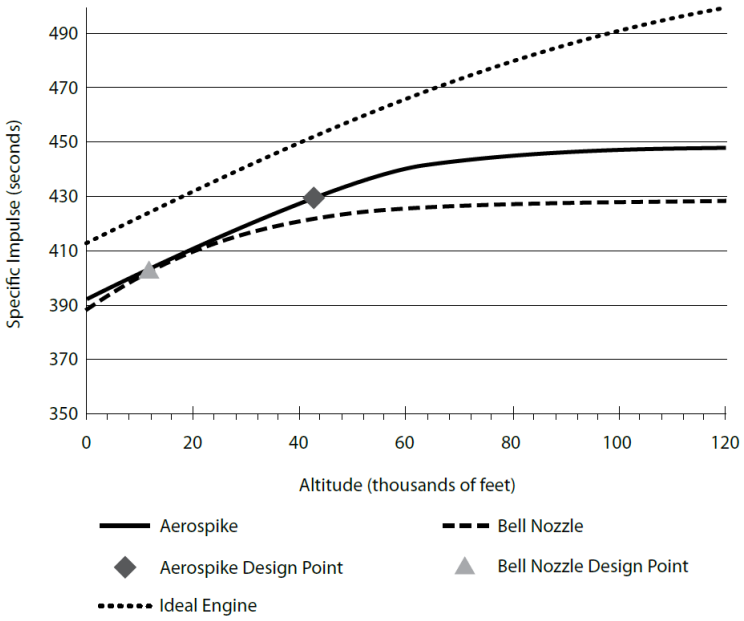

Figure 2.7: Specific impulse variation with altitude for the aerospike and bell nozzle (Hartsfield et al., 2011).

where $g_0 = 9.80665$ m/s^2 is the standard gravity of the Earth. For instance, the most efficient pure rocket engine, utilizing liquid hydrogen and oxygen has a specific impulse of approximately 450 s (Varvill and Bond, 2003).

2.3.2. Altitude Compensating Nozzle

In order to increase the specific impulse of a launch vehicle, the effective exhaust velocity, which relates to the atmospheric pressure and the exhaust pressure, can compensate for the change in atmospheric pressure. The equation for the effective exhaust velocity is given by:

$$v_{eq} = v_e + \frac{A_e(p_e - p_a)}{\dot{m}} \tag{2.3}$$

where v_{eq} is the effective exhaust velocity, v_e is the exhaust velocity, A_e is the exhaust area, p_e is the exhaust pressure, p_a is the atmospheric pressure, and $\dot{m}$ is the mass flow (Huang and Huzel, 1971). In order to ensure optimal thrust, it is necessary that there is no over or under expansion, meaning that the exhaust pressure and the atmospheric pressure are equal to each other. However, bell-nozzle rocket engines are designed for one specific altitude, taking into account that the exhaust pressure should not become too low. If the exhaust pressure would become too low, the exhaust flow would separate and form shock waves (Hartsfield et al., 2011). Typically, the bell nozzle is designed to have an exit pressure that is not lower than approximately 60 % of the atmospheric pressure. This means that the performance of the launch vehicle is only optimal for a brief moment, as can be seen in Figure 2.7. Engine nozzles exist which increase the efficiency, the most notable altitude compensating nozzle is the aerospike engine. This engine was developed for the X-33 lifting body launch vehicle, discussed in Section 2.1.

A modern version of the aerospike engine is the Dual-Expander Aerospike Nozzle (DEAN), which utilizes separate expander cycles for the oxidizer and fuel (Hartsfield et al., 2011). Furthermore, this engine uses an aerospike nozzle (radial inflow plug) in contrast to the bell nozzle, as can be seen in Figure 2.8. The aerospike nozzle does not suffer from an increased ambient pressure. In contrast, it reduces the expansion ratio in such a way that the exhaust pressure matches the ambient pressure. This means that the aerospike nozzle compensates for the change in pressure up to its design altitude (Hartsfield et al., 2011). Above the design altitude, the engine functions as a conventional bell nozzle, effectively increasing the thrust due to an excess in exhaust pressure. The improved performance of the DEAN compared to a conventional bell-nozzle engine can be seen in Figure 2.7.

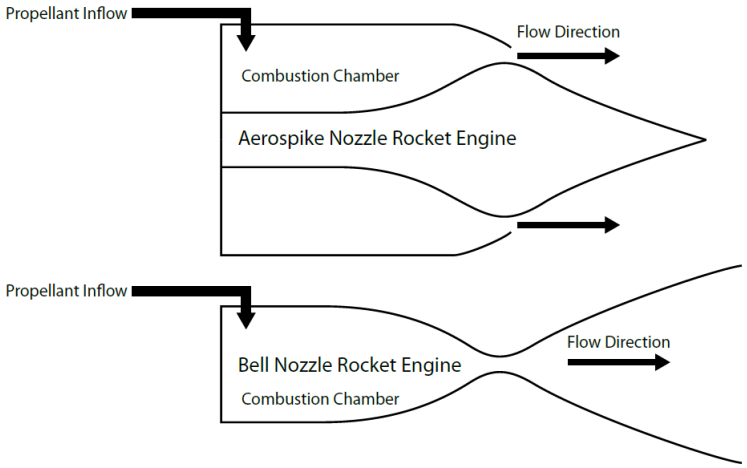

Figure 2.8: Geometry of a rocket engine using an aerospike or bell nozzle (Hartsfield et al., 2011).

2.3.3. Alternative Rocket Engines

Another method in which the specific impulse could be increased is by using engines that use oxygen contained in the atmosphere. This eliminates the use of liquid oxygen during parts of the ascent, significantly increasing the specific impulse. This increase in specific impulse can be explained by:

$$I_{sp} = \frac{T}{\dot{m}_f g_0} \tag{2.4}$$

where T is the engine thrust, and $\dot{m}_f$ is the mass flow rate of the fuel expelled by the engine (Sutton and Biblarz, 2016). Since oxygen is used from the atmosphere, the mass flow rate only includes fuel and is, therefore, lower compared to a conventional rocket engine. Because of the decreased mass fuel flow, the specific impulse of the engine is higher. The drawback of these engine types is the relatively low thrust-to-weight ratio (T/W). Whereas a typical rocket engine has a T/W of approximately $60-80$, air-breathing engines have a T/W which ranges approximately between $1-14$ (Webber, Bond, and Hempsell, 2006). Therefore, it is necessary for a launch vehicle that utilizes an air-breathing engine to generate lift during the ascent trajectory (Varvill and Bond, 2003). This means that a vertical take-off launch vehicle cannot employ air-breathing engines, since the initial T/W would be too low. Instead, a launch vehicle should take off horizontally if it uses air-breathing engines.

Ramjet and Scramjet Engines

One of the air-breathing engines is the ramjet, an engine capable of creating thrust in supersonic conditions and up to approximately Mach 6. The supersonic airflow is used in combination with the geometry of the inlet of the ramjet to create shock waves that increase the pressure and temperature. Within the inlet, a series of oblique shock waves are created, which end in a normal shock. Figure 2.9 shows a schematic of a ramjet, including the shock waves that are created. The fact that the shock waves end with a normal shock guarantees that the velocity of the airflow is decreased to subsonic levels, after which fuel is injected within the subsonic combustor (Veeran, Pesyridis, and Ganippa, 2018). The use of shock waves eliminates the need for a compressor, typically used in a jet engine (Mateu, 2013). Above Mach 5 the ramjet loses efficiency due to dissociation of the flow, reducing the effective heat addition (Varvill and Bond, 2003). Instead, a scramjet is used, where the flow is slowed from hypersonic speeds to supersonic speeds, ensuring that no dissociation of the flow occurs. This is done by ensuring that only oblique shock waves exist within the scramjet, see Figure 2.10. The main issue with the ramjet and scramjet is that they both have distinct Mach numbers at which the engines can operate. They also have, as mentioned previously, low T/W ratios. This can be seen in Table 2.1 and compared to the engine performance values for a conventional rocket engine. Furthermore, both engines are not able to function below a certain Mach number, meaning that these engines are unable to take-off by themselves. This necessitates the use of an engine that can accelerate a launch vehicle to supersonic speeds. A combined cycle propulsion method should be used. One such combined cycle method is the Rocket-Based Combined Cycle (RBCC) engine. The initial acceleration of the RBCC engine is provided by a pure rocket engine. This engine mode accelerates a launch vehicle to supersonic speeds after which the ramjet and

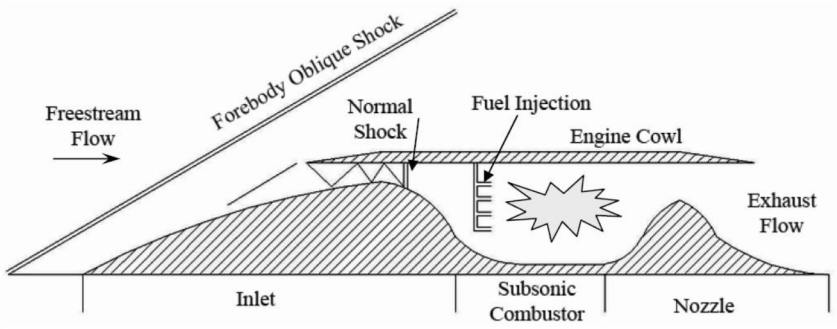

Figure 2.9: Schematic of the working principle of a ramjet (Mateu, 2013).

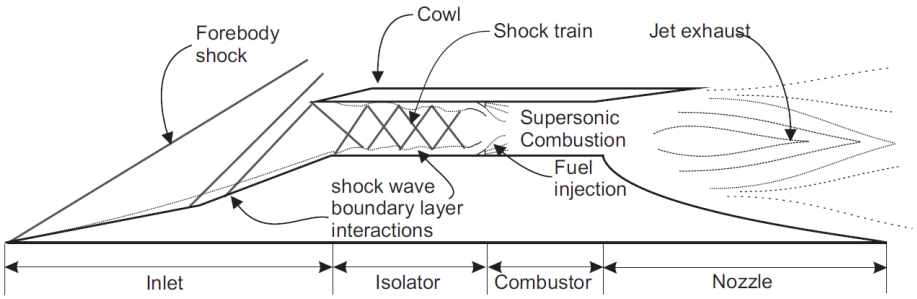

Figure 2.10: Schematic of the working principle of a scramjet engine (Idris et al., 2014).

subsequently the scramjet takes over. Since the ramjet and scramjet both use oxygen from the atmosphere, a fourth mode is necessary to provide thrust during high altitude and vacuum conditions (Olds and Bradford, 2001). The Combined Propulsion Research Group of Japan Aerospace Exploration Agency (JAXA) have been working on a scramjet and combined-cycle engine (Hiraiwa et al., 2008). A rocket-ramjet combined cycle engine model was build and tested under static sea-level conditions (Tomioka et al., 2021).

It is also possible to combine the pure rocket, ramjet and scramjet engine modes together with a turbojet engine mode. This is called a Turbo-Based Combined Cycle (TBCC). The turbojet engine is used to accelerate to supersonic conditions followed by the ramjet and scramjet engine modes, and as a fourth mode, the pure rocket engine is used during the high altitude and vacuum part of the ascent trajectory. The turbojet engine has a superior specific impulse compared to the ejectorjet mode, as can be seen in Table 2.1.

Table 2.1: Engine performance for several air-breathing engines and for a conventional rocket engine (Webber, Bond, and Hempsell, 2006).

Engine	Mach range [-]	Specific Impulse [s]	T/W ratio [-]
Rocket (vac)	$0-27$	$450-475$	$60-80$
Ramjet	$1-6$	$1500-3000$	$1-3.5$
Scramjet	$4-15$	$1000-3000$	$0.5-2$
Turbojet	$0-2.5$	$2000-6000$	$1-4$
LACE	$0-6$	$600-1000$	$6-14$
SABRE	$0-5.5$	$1500-3200$	$6-14$

Liquid Air Cycle Engines

Another air-breathing engine is the Liquid Air Cycle Engine (LACE). The engine uses the liquid hydrogen onboard to liquefy the airflow that is captured in the engine. This is made possible because of the low temperature and high specific heat of liquid hydrogen (Varvill and Bond, 2003). Due to the way that the incoming air is used in the engine, the air-breathing and rocket propulsion systems can be combined with only a single nozzle (Webber, Bond, and Hempsell, 2006). In Figure 2.11 an arrangement can be seen, where the

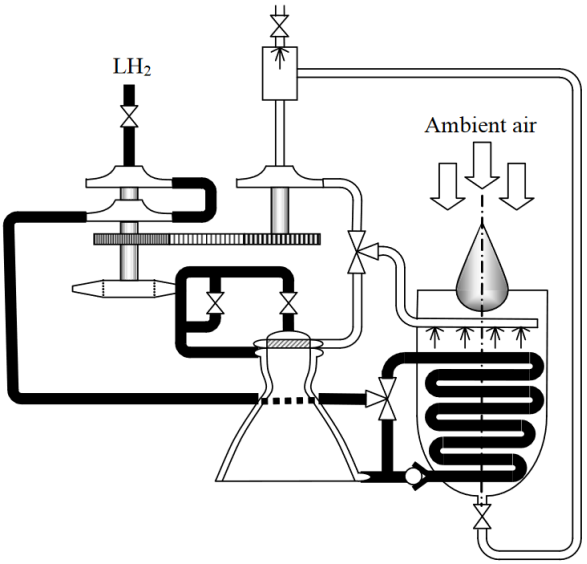

Figure 2.11: Arrangement of a Liquid Air Cycle Engine using ambient air and liquid hydrogen (Segal, 2005).

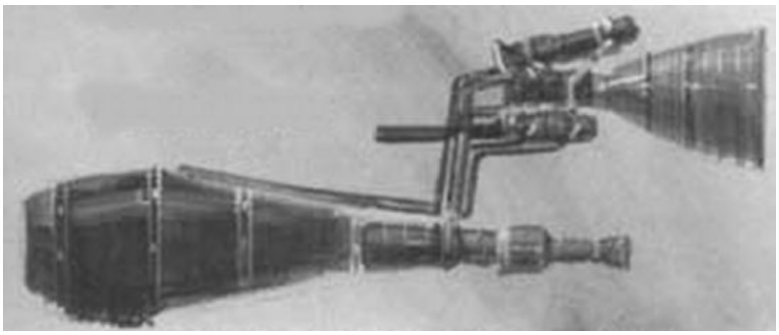

Figure 2.12: RB545 air-breating rocket engine concept[a].

[a] `http://www.aerospaceweb.org/question/spacecraft/q0202.shtml`, accessed on 28 Apr 2021.

airflow is captured and liquefied. Another benefit of LACE is the higher T/W ratio compared to that of a ramjet or scramjet, see Table 2.1. Also, the engine is capable of functioning from a stand-still. A downside of LACE is a high fuel consumption compared to the ramjet or scramjet. The high fuel consumption is the result of the required cooling of the oxygen in the air, where the mass flow of the liquid hydrogen is dictated by the required capacity rate. According to Webber, Bond, and Hempsell, 2006, "The liquid hydrogen fuel must have sufficient thermal capacity to absorb the enthalpy equal to the latent heat of condensation of air at its saturated conditions" (p. 8260). Due to this higher fuel consumption, the specific impulse of the engine is approximately $600 - 1000$ s. Another difficulty of the LACE is the condensation of the other substances in the air such as water vapor, carbon dioxide and argon, which clog the condenser (Varvill and Bond, 2003).

Based on the LACE concept, the RB545 engine was designed for the British Aerospace HOTOL project, see Figure 2.12. The design improved in such a way that the major downside of the LACE concepts was eliminated. The cooling process was terminated close to the vapor boundary of approximately 80 K, creating a more efficient division between the cooling of the incoming airflow and the work requirements of the engine. This meant that the amount of liquid hydrogen required to cool the incoming airflow was reduced, creating a more efficient fuel/air ratio (Varvill and Bond, 2003). However, due to metal temperature limitations in the pre-cooler caused by hydrogen embrittlement, the improved fuel/air ratio was negated at higher Mach numbers. With the termination of the development of the HOTOL, the RB545 development was stopped.

With the formation of Rocket Engine Limited (REL), after the development stop of the HOTOL, the concept of the RB545 was improved upon. The newly developed engine is called the SABRE, see Figure 2.13.

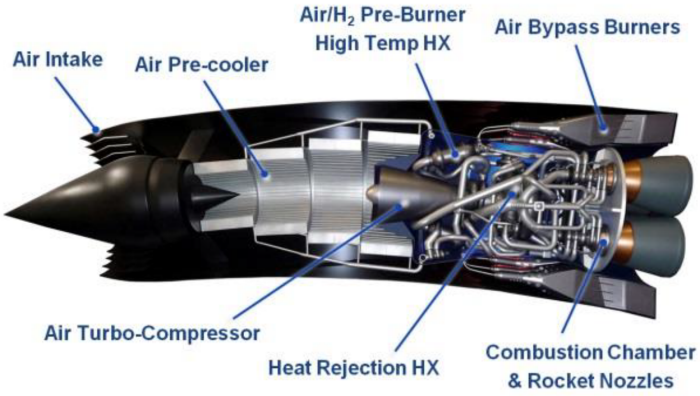

Figure 2.13: Cutaway of the SABRE engine (Hempsell, 2013).

The engine incorporates a Brayton cycle helium loop between the incoming airflow and the hydrogen stream (Varvill and Bond, 2003). In air-breathing mode, the atmospheric air is cooled with a pre-cooler heat exchanger, which is part of the closed cycle helium loop. After the air is cooled to 140 K, it is compressed to approximately 145 bar and 700 K. From there, the compressed air is used in a preburner together with the liquid hydrogen. The hot exhaust flow then heats the helium with a heat exchanger (HX3) to a constant value, such that the turbomachinery can operate with constant conditions (Webber, Bond, and Hempsell, 2006). Before the helium is used again to cool the incoming airflow, it is cooled down by using the hydrogen heat exchanger (HX4). By using helium instead of the liquid hydrogen, hydrogen embrittlement is avoided in the pre-cooler tubes (Webber, Bond, and Hempsell, 2006). Furthermore, the fuel/air ratio (12.5) is improved compared to both the LACE and RB545, since helium is the working fluid (Varvill and Bond, 2003). Due to the improved fuel efficiency, the specific impulse of the SABRE is improved, see Table 2.1. Above Mach 5 and an altitude of 25 km, the air-breathing mode is disabled (Hempsell, 2013). The intake is closed and the engine switched to pure rocket engine mode, where the performance of the engine is similar to that of a conventional rocket engine (Varvill and Bond, 2003). The major new technology needed for the SABRE is the pre-cooler heat exchanger. The pre-cooler has been successfully tested, demonstrating sustained operation (Hempsell, 2013). Besides the heat exchanger, REL has been investigating an Expansion Deflection (E/D) nozzle to compensate for the changing pressure in the atmosphere during the ascent (Taylor et al., 2010).

2.4. Space Plane Ascent Trajectory

During the discussion about the enabling technologies it became apparent that air-breathing engines have a good specific impulse compared to a traditional rocket engine even when considering an altitude compensating nozzle. Using an air-breathing engine, however, requires the launch vehicle to launch horizontally due to the low thrust-to-weight ratio (T/W). A horizontally launched space plane has a different ascent trajectory compared to a vertically launched rocket.

Previous studies that optimized the ascent trajectory of a space plane have primarily been focusing on longitudinal flight only. By assuming a constant flight heading and latitude, the longitudinal and lateral motion could be decoupled, which would reduce the Equations of Motion (EoM) of the space plane to three Degrees of Freedom (DoF) (Mooij, 2019b). A study that incorporates this assumption is done by Pescetelli et al. (2012). It studies the fuel-optimal ascent trajectory for an air-breathing engine, similar to the SABRE. Furthermore, a multi-object optimization method was used to determine the fuel-optimal ascent trajectory. A study done by Mukundan et al. (2019) did incorporate six DoF, where only the longitudinal control parameters were used to optimize the ascent trajectory. Similarly, a study done by Maddock and Minisci (2016) focussed on longitudinal ascent trajectory for the CFASTT-1, while incorporating sixDoF. The CFASTT-1 is a conceptual test vehicle, which is similar to the Skylon in scale and function. In this study the control parameters, used for the optimization of the ascent trajectory, were the engine throttle and the angle of attack.

Another study was done by, Zhou, Wang, and Cui (2020), which studied six DoF motion to account for an extension of the launch window. By incorporating lateral motion, it was shown that a space plane with a lifting surface could manipulate the Right Ascensions of the Ascending Node (RAAN), successfully extending the launch window. This is an important finding, since launches that would have a specific target orbit can use

this adjustment to extend the launch window. For instance, rendezvous with an object in space will require an instantaneous launch window[5]. Typically, a launch is postponed due to bad weather or a technical malfunction. The postponement means that, depending on the target inclination, the next possible moment is at minimum 12 hours later.

2.5. Research Objective

With the development of air-breathing engines and the low T/W characteristics of these engines, it is expected that reusable HTHL space planes will be developed. A primary example is the Skylon, designed by REL due to the development of the SABRE. It has been discussed previously that a space plane with a lifting surface is capable of manipulating the RAAN during the ascent to extend the launch window. This extension could ensure that a launch is not postponed to another day due to bad weather or technical issues. In the research done by Zhou, Wang, and Cui (2020) the primary focus was to extend the launch window and to assess the range and altitude capabilities of a theoretical space plane.

The objective of this MSc study is to extend on the work done by Zhou, Wang, and Cui (2020), by studying the fuel-optimal ascent trajectory *i.e.*, identify the fuel needs of the space plane to incorporate an extended launch window. In order to study this, the National Aero-Space Plane (NASP) conceptual vehicle is used. The conceptual model will be introduced in Chapter 4, and is used in multiple occasions to study the longitudinal ascent trajectory (Powell et al., 1991; Shaughnessy, 1992; Mooij, 1998). This enables verification of the longitudinal ascent and the vehicle model, while the study by Zhou, Wang, and Cui (2020) serves to verify the lateral motion.

The results from this study will compare the ascent of a space plane for multiple launch times, including a control ascent, where the launch time is zero and the target RAAN is automatically reached. With these different launch times a comparison can be made to assess the propellant used during the ascent, which in turn will give insight in the available payload that can be brought into orbit. The difference in available payload can be compared to the required propellant for a satellite to do a simplified in-orbit maneuver to change the RAAN.

Additionally, a robust nonlinear control algorithm will be used to guide and control the space plane to the target orbit. This removes the necessity to linearize the EoM, eliminating eigenmotions that could occur, and gain scheduling. The robust algorithm will also enable sensitivity analysis of the vehicle model, since the algorithm is capable of controlling the space plane, even though the vehicle model is uncertain.

In general the research objective can be summarized by:

AG1 Include the full six Degrees of Freedom (DoF) translational and rotational Equations of Motion (EoM).

AG2 Include a Guidance and Control (G&C) system that can deal with the nonlinear translational and rotational Equations of Motion (EoM).

AG3 Include a vehicle model that has been used before to optimize the longitudinal ascent, which includes constraints.

[5]ESA, Getting ready for launch, accessed on 19 Jun 2021, `https://www.esa.int/Science_Exploration/Space_Science/Getting_ready_for_launch`.

3

Flight Dynamics

In this chapter the dynamics and kinematics that apply to a space plane are discussed. Flight dynamics relates to the motion of a space plane in flight which is subject to forces and moments. These forces and moments can be due to the aerodynamic, gravitational and propulsive forces. The forces that a space plane in flight is subjected to results in rotational and translational motions (Mooij, 2019a). In Section 3.1 reference frames, state variables and transformation matrices will be discussed. In Section 3.2 the translational and rotational Equations of Motion (EoM) will be derived.

3.1. Reference Frames, State Variables and Transformations

A reference frame is used to define the motion of an object with respect to the origin of the reference frame. Vectors are used to define the motion of an object, which in a Cartesian coordinate system will yield a vector with three elements corresponding to the x, y and z position. Reference frames can be classified as either inertial or non-inertial. Originally, Newton's laws have been defined in an inertial frame and are not suitable for a rotating reference frame. For the ascent trajectory optimization of a space plane, which moves from the surface of the Earth to an orbit around the Earth, a number of reference frames are useful. These reference frames will be discussed here.

Inertial Planetocentric Reference Frame

The origin of the inertial planetocentric reference frame coincides with the Center of Gravity (CoG) of the central body around which the space plane is moving. Due to the motion of the central body, the reference frame can be considered pseudo-inertial, where the rotation of the reference frame itself has only a marginal effect. This inertial reference frame uses index I. The OX_IY_I-plane coincides the the equatorial plane of the central body, with the Z_I-axis pointing north. Figure 3.1 shows the location and orientation of the reference frame. For a general body, the X_I-axis is defined by the prime meridian at zero time. For an inertial Earthcentric reference frame, the X_I-axis is pointing at a fixed point in inertial space at a specified time. One such reference frame is called J2000, with X_I-axis pointing towards the Vernal Equinox at 12h on the 1$^{\text{st}}$ of January 2000 (Mooij, 2019a).

Rotating Planetocentric Reference Frame

The rotating planetocentric reference frame uses index R, with many similarities to the inertial planetocentric reference frame. The main difference is the X_R-axis, which intersects with the equator at the prime meridian *i.e.*, zero longitude. The Y_R-axis completes the right-handed system and the Z_R-axis points north. Because of this definition, the rotation of the frame is defined by the rotation of the central body, denoted with ω_{cb} (Mooij, 2019a). The rotating planetocentric reference frame can be seen in Figure 3.1.

Vertical Reference Frame

For the vertical reference frame, index V, the Z_V-axis is pointing towards the CoG of the central body, which is also the direction of the radial component of the gravitational acceleration. The X_V-axis points towards the northern hemisphere, perpendicular to the Z_V-axis, and along a meridian plane. The remaining Y_V-axis completes the right-handed system by pointing in the eastward direction (Mooij, 2019a). The vertical

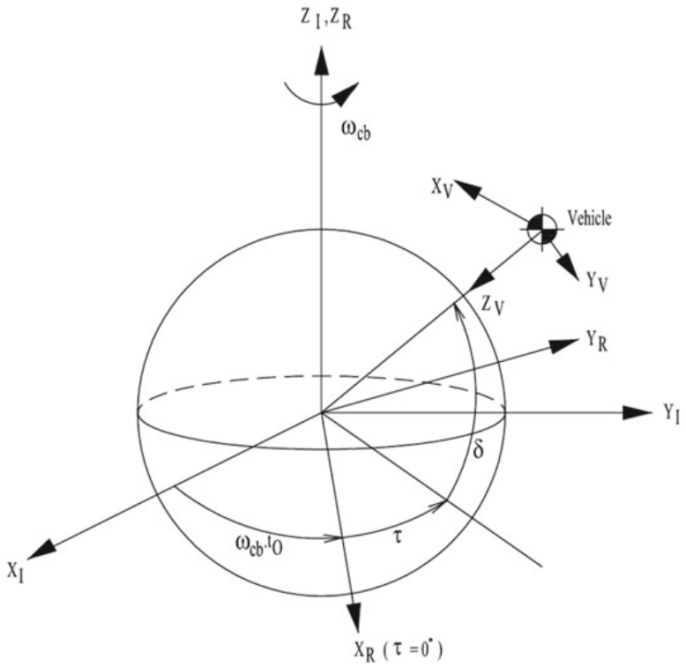

Figure 3.1: Schematic representation of the inertial and rotating planetocentric reference frames, together with the vertical frame (Dirkx and Mooij, 2017).

reference frame is also referred to as the North, East, Down (NED) reference frame. The V-frame can be seen in Figure 3.1.

Trajectory Reference Frame
The trajectory reference frame can be either groundspeed-based, index TG or airspeed-based, index TA. For the ground speed based reference frame, the X_{TG}-axis points in the direction of the velocity vector, which is relative to the R-frame. The Z_{TG} -axis lies in the vertical plane, pointing downwards and the Y_{TG}-axis completes the right-handed system. For the airspeed-based frame, the X_{TA}-axis is still positive along the velocity vector, which is now relative to the atmosphere. The Z_{TA}-axis still lies in the vertical plane, pointing downwards and the Y_{TA}-axis completes the right-handed system. Even though the definition of the Z_{TA}-axis and Y_{TA}-axis are similar for both groundspeed- and airspeed-based reference frame, the absolute orientation is affected by the different definitions of the X_{TG}- and X_{TA}-axis (Mooij, 2019a).

Aerodynamic Reference Frame
The aerodynamic reference frame is also defined for both the groundspeed and airspeed, index AG and AA, respectively. The X_{AG}- and X_{AA}-axis are both positive along the velocity vector, where the velocity is either relative to the R-frame or to the atmosphere, respectively. Furthermore, the X_{TG}- and X_{AG}-axis are collinear, and the X_{TA}- and X_{AA}-axis are collinear. The Z_{AG}- and Z_{AA}-axis both are collinear with the lift force, but opposite in direction. The Y_{AG}- and Y_{AA}-axis complete right-handed system. It should be noted that when the space plane is not banking, the TG- and AG-frame, and TA- and AA-frame coincide. Furthermore, when wind speeds are not considered, the AG- and AA frame coincide (Mooij, 2019a).

Body Reference Frame
The body reference frame is a fixed vehicle frame, which is denoted by index B. The X_B and Z_B lie in the plane of symmetry of the body. The X_B-axis is positive in the forward direction of the body, while the Z_B-axis is positive in the downward direction. The Y_B-axis completes the right-handed system (Mooij, 2019a).

Propulsion Reference Frame
The propulsion frame is an uncommon reference frame, with index P. Usually, the thrust force is defined in the body frame. However, the thrust force can be defined in its own reference frame, which is useful when dealing with a thrust vector which does not align with the B-frame. The X_P-axis is collinear with the thrust

Table 3.1: Illustration of the spherical components (Mooij, 2019a).

Spherical Components	Description	Value Range
R	Distance	$(0 \leq R < \infty)$
τ	Longitude	$(0 \text{ rad} \leq \tau \leq 2\pi \text{ rad})$
δ	Latitude	$(-\pi/2 \text{ rad} \leq \delta \leq \pi/2 \text{ rad})$
V_g	Groundspeed	$(0 \leq V_g < \infty)$
γ_g	Flight-path angle	$(-\pi/2 \text{ rad} \leq \gamma_g \leq \pi/2 \text{ rad})$
χ_g	Heading	$(-\pi \text{ rad} \leq \chi_g \leq \pi \text{ rad})$

vector, while the Y_P-axis completes the right-handed system and the Z_P-axis lies in the vertical plane with the positive direction pointing downward (Mooij, 2019a).

3.1.1. State Variables

State variables determine both the position and velocity, and the attitude and angular rates of a space plane. For the former, the Cartesian and Spherical components as well as the orbital elements will be discussed. For the latter, classical attitude angles, aerodynamic angles and quaternions will be discussed.

Position and Velocity

The most common method of describing the translational motion of a space plane is with Cartesian or Spherical components. Within TU Delft Astrodynamics Toolbox (TUDAT), Cartesian coordinates are used to propagate the space plane. However, Cartesian coordinates do not offer good insight in the current position or velocity of the space plane with respect to the central body. Conversely, Spherical coordinates are better at giving this insight. It is therefore beneficial to convert the Carthesian components to Spherical components. Furthermore, when optimizing the ascent trajectory of a space plane to reach a specific orbit around Earth, it can be particularly helpful to use the orbital elements to compare the target orbit with the final orbit achieved by the space plane.

The Cartesian coordinate system is used with respect to the I-frame. The position is given by components x, y, z, while the velocity is either given by $\dot{x}, \dot{y}, \dot{z}$ or V_x, V_y, V_z (Mooij, 2019a). The spherical coordinates are used to define the initial translational state of the space plane and to interpret the simulated ascent trajectory. Spherical components consist of six parameters. Table 3.1 shows the parameters, where R, τ and δ are used to determine the position. The distance is measured from the CoG of the central body to the CoG of the space plane. The longitude is positive due east, with the latitude being zero at the equator and positive in northward direction. V_g, γ_g and χ_g are used to determine the velocity. The groundspeed is defined with respect to the R-frame. The flight-path angle is measured between the local horizontal plane and the velocity vector, while the heading is measured between local north and the projection of the velocity vector on the local horizontal plane. The heading is 90 degrees ($\pi/2$) when the velocity vector projection is pointing parallel to the equator due east. Figure 3.2 shows the six spherical components with respect to the R-frame.

For the orbital elements, a distinction needs to be made between elliptical, parabolic and hyperbolic orbits. In the case of the space plane ascent trajectory to a Low Earth Orbit (LEO), both the parabolic and hyperbolic orbits can be neglected. For an elliptical orbit, the position and velocity of a space plane is, according to Mooij (2019a), defined by six parameters, see Table 3.2. The eccentricity and semi-major axis are properties of the ellipse, see Figure 3.3. The eccentricity is defined by the semi-major axis, a, and the semi-minor axis, b:

$$e = \sqrt{1 - \frac{b^2}{a^2}}. \tag{3.1}$$

The inclination, argument of pericenter and right ascension of the ascending node determine the orientation of the orbit with respect to the I-frame, see Figure 3.4. The mean anomaly is a parameter that describes the location of the space plane along the orbit. It is a product of the mean angular velocity and the time since the last pericentre passage (Mooij, 2019a). It is defined by:

$$M = n(t - \tau) = M_0 + n(t - t_0) \tag{3.2}$$

with

$$n = \sqrt{\frac{\mu^3}{a}}, \tag{3.3}$$

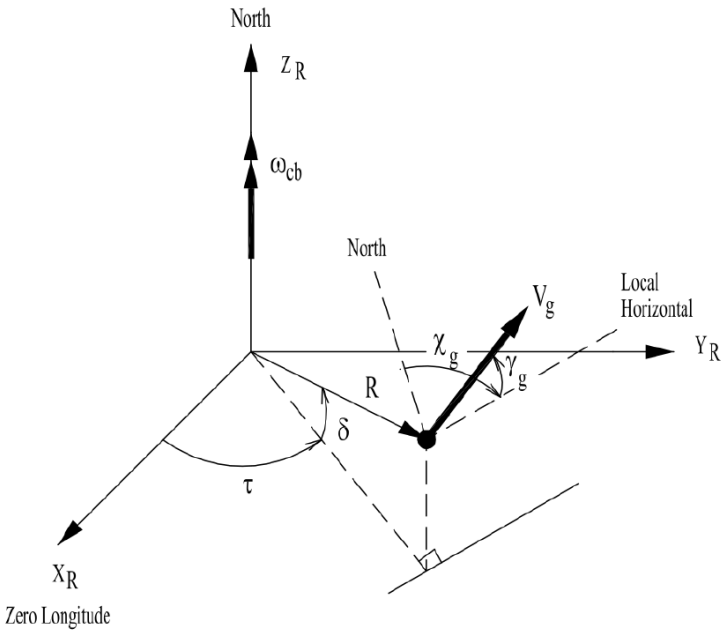

Figure 3.2: Definition of the spherical components w.r.t. the R-frame, where τ, δ, γ_g and χ_g are positive (Mooij, 2019a).

Table 3.2: Definition of the orbital elements (Mooij, 2019a).

Orbital Element	Description	Value Range
e	the eccentricity	$(0 \leq e < 1)$
a	the semi-major axis	$(a > R_e)$
i	the inclination	$(0 \text{ rad} \leq i \leq \pi)$
ω	the argument of pericenter	$(0 \text{ rad} \leq \omega < 2\pi \text{ rad})$
Ω	the right ascension of the ascending node	$(0 \text{ rad} \leq \Omega < 2\pi \text{ rad})$
M	mean anomaly	$(0 \text{ rad} \leq M < 2\pi \text{ rad})$

where μ is the gravitational parameter of the central body. Furthermore, τ is the time of pericentre passage, which can be replaced with the mean anomaly at epoch t_0, M_0:

$$M_0 = n(t_0 - \tau) \tag{3.4}$$

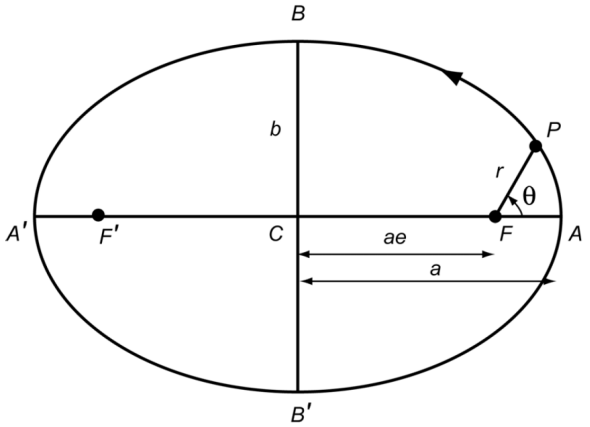

Figure 3.3: Geometry of an elliptical orbit (K. F. Wakker, 2015).

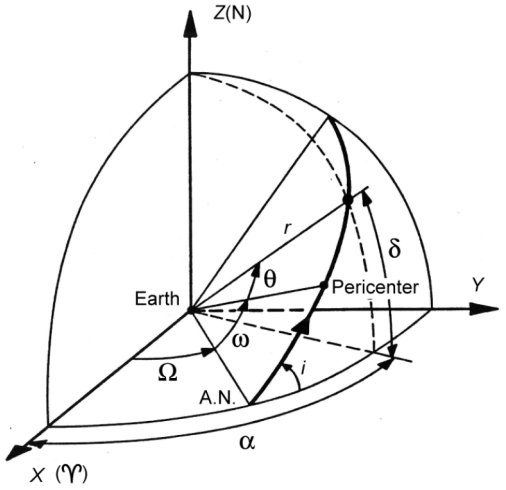

Figure 3.4: Definition of the orbital elements that determine the orientation of the orbit w.r.t. the I-frame (K. F. Wakker, 2015).

Attitude and Angular Rates

The orientation of a space plane within the B-frame with respect to another frame is also called the attitude of a space plane. The attitude can be expressed in a number of different ways, where the most commonly used ways for aerospace applications are classical attitude angles, aerodynamic angles and quaternions. The first two expressions both make use of angles which can be defined in both degrees and radians.

The classical attitude angles are the roll, ϕ, pitch, θ, and yaw angle ψ. According to Mooij (1994), these angles define the attitude of a space plane with respect to the I-frame. However, it is also possible to define the classical attitude angles with respect to the B-frame. In order to construct the transformation matrix, the correct sequence of basic transformation matrices needs to be used. For aerospace applications it is common to first rotate about the z-axis, followed by a rotation about the y- and x-axis, respectively. The resulting transformation matrix is called a type-1 matrix with sequence 3-2-1, where 3-2-1 is analogous to z-y-x. Additionally, the rotational velocity of the body in the B-frame with respect to the I-frame is described by rotation vector, $\boldsymbol{\omega}$, which consists of the roll rate, p, pitch rate, q, and yaw rate, r (Mooij, 2019a). The derivative of the rotation vector is described by Equation 3.33, which is used by the control module of the Guidance and Control (G&C) module to find appropriate deflection angles for the control surfaces of the space plane.

In a similar fashion, aerodynamic angles can be used, with angle of attack, α, angle of sideslip, β, and bank angle, σ. The aerodynamic angles relate the B-, A- and T-frame, see Figure 3.8. The aerodynamic angles are used to determine the force and moment coefficients of the space plane. Furthermore, the guidance module of the G&C system computes desired aerodynamic angles and relates these to the orientation of the space plane expressed in classical attitude angles, see Section 6.2.1.

Quaternions are an alternative to the Euler angles, which are hyper-complex numbers describing a 4-dimensional sphere (Mooij, 2019a). It consists of a real part and an imaginary parts, where the imaginary numbers adhere to:

$$i^2 = j^2 = k^2 = ijk = -1. \tag{3.5}$$

According to Wie (2008), the quaternions are determined by the Euler axis, $\mathbf{a}$, and the rotation angle about the Euler axis, Φ. The Euler axis has the specific property that the axis is stationary in both a body and an inertial reference frame. The quaternions are separated by a vector part, which is defined by:

$$\mathbf{q} = \begin{bmatrix} q_1 & q_2 & q_3 \end{bmatrix}^\top = \mathbf{a} \sin \frac{\Phi}{2}, \tag{3.6}$$

while the scalar part is only defined by the Euler rotation angle:

$$q_4 = \cos \frac{\Phi}{2}. \tag{3.7}$$

The quaternions are constrained by:

$$\mathbf{q}^\top \mathbf{q} + q_4^2 = q_1^2 + q_2^2 + q_3^2 + q_4^2 = 1. \tag{3.8}$$

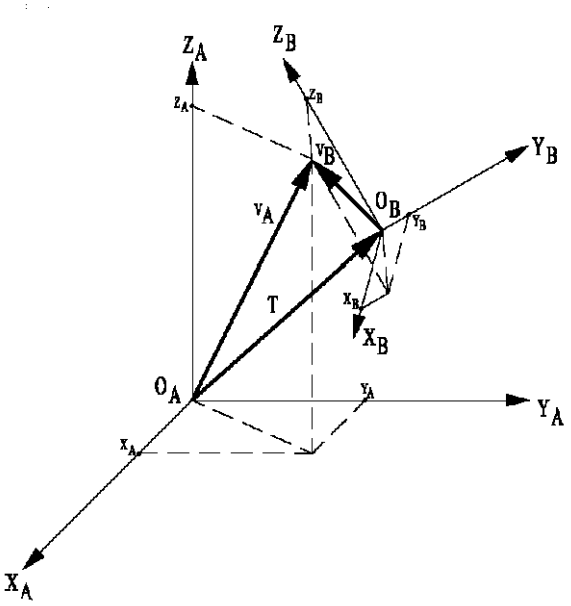

Figure 3.5: Vector transformation from frame A to frame B, using both translation and rotation (Mooij, 2019a).

The rotation described by the quaternions can be seen as a trajectory on a 4-dimensional unit sphere. The orientation is specified by the vector and scalar part of the quaternions, where the negative or positive quaternions yield the same orientation. In the negative case, the rotation is described with the negative Euler axis and angle. This results in a situation where, if the positive quaternions describe the shortest rotation on the 4-dimensional unit sphere, the negative quaternions describe the longest rotation. If the shortest rotation is needed, the scalar quaternion should be positive (Mooij, 2019a).

The benefit of using quaternions is to eliminate potential singularities that can occur when using classical Euler or aerodynamic angles. For instance, when using the classical Euler angles, a singularity occurs when the pitch angle, $\theta = \pm 90$ deg (J. Mulder et al., 2013). For this reason, TUDAT uses quaternions to propagate the orientation of the space plane.

3.1.2. Transformations

It is possible to express a vector, defined in a reference frame, in another reference frame by transforming the vector. This can be useful when dealing with forces or moments, which are expressed in the B- or A-frame. By transforming, these forces and moments can, for instance, be expressed in the I-frame. A vector transformation is possible by translation and rotation. The equation that corresponds to this transformation can be expressed in a general term by using a transformation from a generic reference frame, A, to generic reference frame B with:

$$\mathbf{v_B} = \mathbf{T} + \mathbf{C_{B,A}} \mathbf{v_A}, \tag{3.9}$$

where $\mathbf{T}$ corresponds with the translation vector from the origin in frame A, O_A, to the origin of frame B, O_B. $\mathbf{C_{B,A}}$ is the transformation matrix, which defines the rotation from frame A to B. Figure 3.5 shows the vector transformation from $\mathbf{v_A}$ to $\mathbf{v_B}$.

The transformation matrix is constructed with a number of unit axis-rotations. The matrix is constructed for each axis in a similar fashion. Figure 3.6 shows the rotation of reference frame A to reference frame B, which is rotated about the x-axis. From the figure it can be derived that:

$$x_B = x_A \tag{3.10a}$$

$$y_B = y_A \cos\alpha + z_A \sin\alpha \tag{3.10b}$$

$$z_B = -z_A \sin\alpha + z_A \cos\alpha \tag{3.10c}$$

From these equations the basic transformation matrix, about the x-axis as a function of angle α, can be

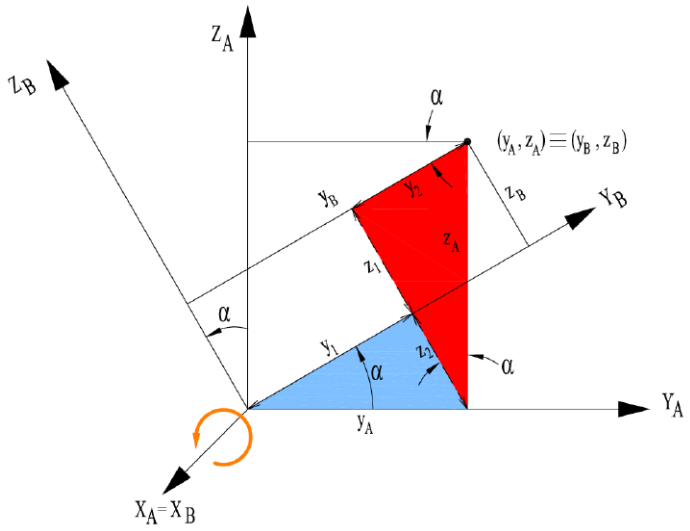

Figure 3.6: Rotation about the x axis from reference frame A to reference frame B (Mooij, 2019a).

constructed as:

$$\mathbf{C_x}(\alpha) = \begin{bmatrix} 1 & 0 & 0 \\ 0 & \cos\alpha & \sin\alpha \\ 0 & -\sin\alpha & \cos\alpha \end{bmatrix}. \tag{3.11}$$

In a similar fashion, the basic transformation matrices about the y- and z-axis can be found, where the transformation matrix is a function of angle α:

$$\mathbf{C_y}(\alpha) = \begin{bmatrix} \cos\alpha & 0 & -\sin\alpha \\ 0 & 1 & 0 \\ \sin\alpha & 0 & \cos\alpha \end{bmatrix}, \tag{3.12}$$

$$\mathbf{C_z}(\alpha) = \begin{bmatrix} \cos\alpha & \sin\alpha & 0 \\ -\sin\alpha & \cos\alpha & 0 \\ 0 & 0 & 1 \end{bmatrix}. \tag{3.13}$$

For a multiple axis rotation, a transformation matrix is constructed with the help of multiple basic transformation matrices. It is important to identify the order in which the rotations occurs. Based on this order, matrix multiplication is applied where the matrices are in reverse order. As an example, suppose the transformation of reference frame A to reference frame B is to be done first about the x-axis followed by the z-axis and y-axis, respectively. In this case, the transformation matrix is constructed with:

$$\mathbf{C_{B,A}} = \mathbf{C_Y}(\alpha_2)\mathbf{C_Z}(\alpha_3)\mathbf{C_X}(\alpha_1). \tag{3.14}$$

The transformation matrices about a single axis are orthogonal matrices. Furthermore, the product of any number of orthogonal matrices is also orthogonal. Orthogonal matrices have the property:

$$\mathbf{C}^T\mathbf{C} = \mathbf{C}\mathbf{C}^T = \mathbf{I} \;\rightarrow\; \mathbf{C}^T = \mathbf{C}^{-1}. \tag{3.15}$$

With this property, the computation for the inverse transformation matrix *i.e.*, the transformation matrix from reference frame B to reference frame A is simply done with the transpose of transformation matrix $\mathbf{C_{B,A}}$:

$$\mathbf{C_{A,B}} = \mathbf{C_{B,A}}^{-1} = \mathbf{C_{B,A}}^{T} \tag{3.16}$$

3.1.3. Commonly Used Transformation Matrices

Previously, a general description has been given how to construct the transformation matrix. There are numerous frame transformations that are used to either define the initial state, or throughout the propagation. In this section, the basic frame transformation will be discussed. Based on these basic transformations, a combined transformation matrix can be constructed.

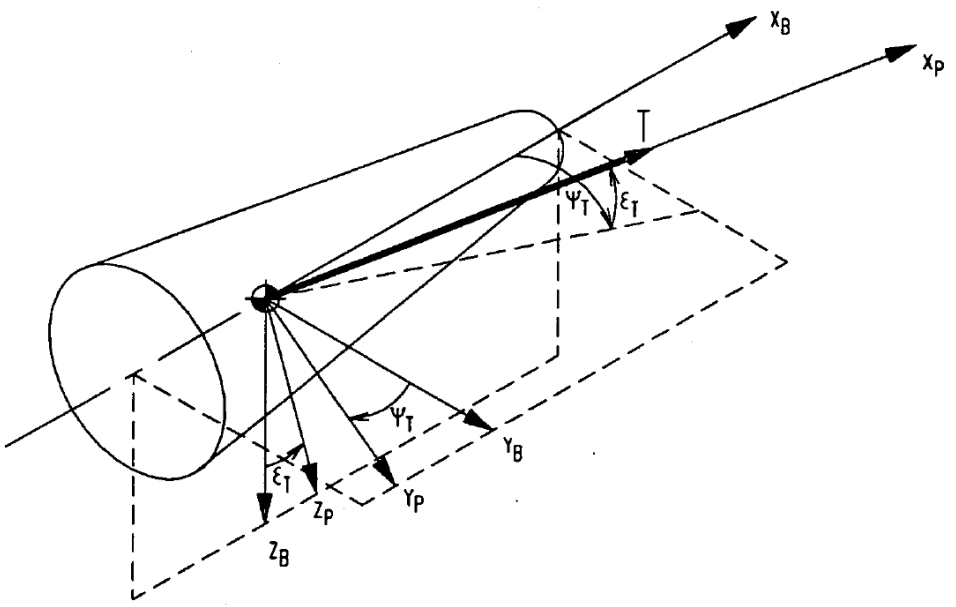

Figure 3.7: Relation between the body and propulsion reference frame (Mooij, 1994).

The first basic transformation matrix is for the transformation from the P-frame to the B-frame. The transformation is done with the elevation and azimuth thrust off-set angle, ϵ_T and ψ_T (Mooij, 2019a). Figure 3.7 depicts the situation. The transformation matrix is given by:

$$\mathbf{C_{B,P}} = \mathbf{C_Z}(-\psi_T)\mathbf{C_Y}(-\epsilon_T) = \begin{bmatrix} \cos\psi_T \cos\epsilon_T & -\sin\psi_T & \cos\psi_T \sin\epsilon_T \\ \sin\psi_T \cos\epsilon_T & \cos\psi_T & \sin\psi_T \sin\epsilon_T \\ -\sin\epsilon_T & 0 & \cos\epsilon_T \end{bmatrix}. \tag{3.17}$$

The second basic transformation matrix is the transformation from the B- to A-frame. In this transformation two angles are defined, which can also be seen in Figure 3.8. The two angles are the angle of attack, α, and angle of sideslip, β, which both can be either with respect to the airspeed or the groundspeed (Mooij, 2019a). The transformation matrix is a combination of Equations 3.12 and 3.13, resulting into:

$$\mathbf{C_{A,B}} = \mathbf{C_Z}(\beta)\mathbf{C_Y}(-\alpha) = \begin{bmatrix} \cos\alpha\cos\beta & \sin\beta & \sin\alpha\cos\beta \\ -\cos\alpha\sin\beta & \cos\beta & -\sin\alpha\sin\beta \\ -\sin\alpha & 0 & \cos\alpha \end{bmatrix}. \tag{3.18}$$

The third basic transformation matrix is the transformation from the AG- to TG-frame. The transformation is defined by the bank angle, σ_G. Only a single angle is needed to transform the transformation matrix between these two frames, which is simply given by:

$$\mathbf{C_{TG,AG}} = \mathbf{C_x}(\sigma_G) = \begin{bmatrix} 1 & 0 & 0 \\ 0 & \cos\sigma_G & \sin\sigma_G \\ 0 & -\sin\sigma_G & \cos\sigma_G \end{bmatrix}. \tag{3.19}$$

The fourth basic transformation matrix is for the transformation from the TG- to the V-frame. This frame transformation is defined by the flight path angle and the heading of the space plane (Mooij, 2019a). The transformation is defined by a rotation about the y-axis followed by a rotation about the z-axis. The total transformation matrix can be expressed by:

$$\mathbf{C_{V,TG}} = \mathbf{C_z}(-\chi_a)\mathbf{C_y}(-\gamma_a) = \begin{bmatrix} \cos\chi_G\cos\gamma_G & -\sin\chi_G & \cos\chi_G\sin\gamma_G \\ \sin\chi_G\cos\gamma_G & \cos\chi_G & \sin\chi_G\sin\gamma_G \\ -\sin\gamma_G & 0 & \cos\gamma_G \end{bmatrix}. \tag{3.20}$$

The fifth basic transformation matrix is the transformation between the V- and R-frame. The transformation matrix is defined by the longitude, τ, and latitude, δ, as can be seen in Figure 3.1. The transformation is

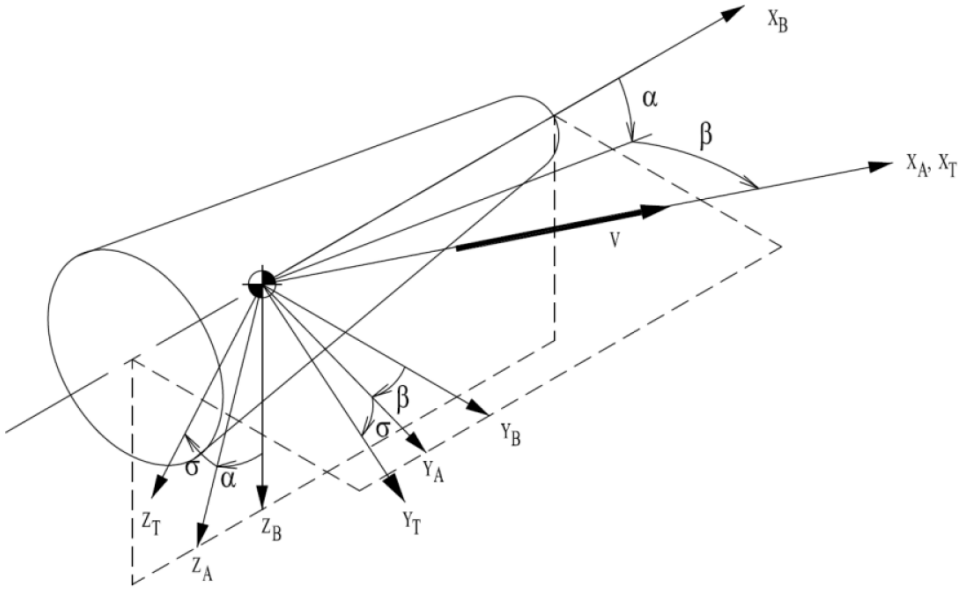

Figure 3.8: Relation between the aerodynamic, body and trajectory reference frame. The sideslip and bank angle are considered positive, while the angle of attack is considered negative (Mooij, 2019a).

defined by first a rotation about the y-axis followed by a rotation about the z-axis. The total transformation matrix is:

$$\mathbf{C_{R,V}} = \mathbf{C_z}(-\tau)\mathbf{C_y}(\frac{\pi}{2}+\delta) = \begin{bmatrix} -\cos\tau\sin\delta & -\sin\tau & -\cos\tau\cos\delta \\ -\sin\tau\sin\delta & \cos\tau & -\sin\tau\cos\delta \\ \cos\delta & 0 & sin\delta \end{bmatrix}. \tag{3.21}$$

The sixth and last basic transformation matrix is from the R-frame to the I-frame, denoted with $\mathbf{C_{I,R}}$. In this transformation, only a rotation about the z-axis is necessary (Figure 3.1), where the angle is defined by the rotational rate of the central body, ω_{cb}, and the time since the two frames have coincided. Per definition, the I- and R-frame coincide at $t_0 = 0$ (Mooij, 2019a). The transformation matrix becomes:

$$\mathbf{C_{I,R}} = \mathbf{C_Z}(-\omega_{cb}t) = \begin{bmatrix} \cos\omega_{cb}t & -\sin\omega_{cb}t & 0 \\ \sin\omega_{cb}t & \cos\omega_{cb}t & 0 \\ 0 & 0 & 1 \end{bmatrix}, \tag{3.22}$$

where the angle is negative, due to the right hand rule, for the situation that the transformation is from the R- to the I-frame.

Applications

The six basic transformation matrices are used to define the forces and moments acting on the space plane in the inertial reference frame. Typically, the aerodynamic forces are defined in the A-frame, the propulsive force is defined in the P-frame and the aerodynamic moments are defined in the B-frame. By adding any number of the basic transformations, a total transformation matrix can be constructed. For instance, a transformation from the B to the I-frame can be done by multiplying:

$$\mathbf{C_{I,B}} = \mathbf{C_{I,R}}\mathbf{C_{R,V}}\mathbf{C_{V,TG}}\mathbf{C_{TG,AG}}\mathbf{C_{A,B}}. \tag{3.23}$$

The transformation matrices are also used to transform the initial state, defined by spherical components to a Cartesian coordinate system. The position vector, which consists of the distance between the CoG of the space plane and the CoG of the central body is transformed with the use of the latitude and longitude. These angles are used to define the transformation matrix between the V- and R-frame. The velocity vector is transformed with the flight path and heading angle, which are used to construct the transformation matrix between the TA- and V-frame. With the position and velocity expressed in Cartesian coordinates, a transformation matrix

can be constructed to transform them to the I-frame. For the position, a transformation matrix from the rotating to the inertial reference frame, $\mathbf{C_{I,R}}$ is necessary. For the velocity, two transformation matrices are necessary to transform the velocity vector. Both the transformation matrix from the vertical to the rotating frame, $\mathbf{C_{R,V}}$, and the transformation matrix from the rotating to the inertial frame, $\mathbf{C_{I,R}}$, is necessary.

Another use of the transformation matrices, is to express the angular velocity in another frame. For the initial angular velocity of the body with respect to the inertial planetocentric reference frame, it is assumed that the space plane does not have an angular velocity with respect to the rotating planetocentric reference frame. This means that the angular velocity is only defined by the rotation of the Earth with respect to the inertial planetocentric reference frame. The angular velocity of the B-frame with respect to the I-frame can be written as:

$$\boldsymbol{\Omega}_{B,I} = \boldsymbol{\Omega}^I_{E,I} + \boldsymbol{\Omega}^E_{V,E} + \boldsymbol{\Omega}^V_{T,V} + \boldsymbol{\Omega}^T_{A,T} + \boldsymbol{\Omega}^A_{B,A} = \boldsymbol{\Omega}^I_{E,I}, \tag{3.24}$$

where the superscript indicates along which reference frame axes the angular velocity is defined. In order to define the rotation vector of the B-frame with respect to the I-frame, expressed in components along the body axes, the angular velocity $\boldsymbol{\Omega}_{EI}$ needs to be defined in the B-frame. This is done with:

$$\boldsymbol{\Omega}^B_{E,I} = \mathbf{C_{B,I}}\boldsymbol{\Omega}^I_{E,I}, \tag{3.25}$$

where the transformation matrix between the I- and the B-frame, $\mathbf{C_{B,I}}$, is defined with the basic transformations previously discussed.

In a similar fashion, the angular velocity along a single axis can be expressed along axes of another frame. This is particularly useful for the G&C system, where the reference trajectory produces desired aerodynamic angles. In order to compute the required change in deflection angles of the control surfaces, an expression needs to be found between the derivative of the aerodynamic angles and the roll, pitch and yaw rate. A derivation of the required transformation can be found in Section 6.2.2.

3.2. Equations of Motion

In this section the equations that govern the translational and rotational motion will be described. Generally one can speak of the translational motion of a vehicle as the motion of the CoG. Translation motion deals with the position and velocity state variables. It can be described in 3-dimensional space, also referred to as three Degrees of Freedom (DoF). The rotational motion is described by the motion around the CoG and deals with the attitude and the angular motion of the vehicle. The attitude and angular motion is described about three axes, corresponding to another three DoF (Mooij, 2019a). A typical simplification of the ascent trajectory is to reduce the amount of DoF to three, by only considering translational motion in a plane. This results in two DoF, while the third degree of freedom is defined by rotational motion about a single axis. As discussed in Chapter 5, the extension of a launch window requires longitudinal and lateral motion, which means that the reduction of DoF is not possible.

3.2.1. Translational Equations of Motion

The equations that govern the translational motion are based on Newtonian mechanics. These mechanics are based on the three laws of motion, derived by Newton, and Galileo's principle of relativity (Mooij, 2019a). For a launch vehicle, it should be assumed that the mass will vary over the duration of the ascent. Furthermore, it is assumed that the body is rigid.

Translational Motion with respect to an Inertial Frame

In order to derive the equations of motion of a space plane, first the general expression of the translational motion of it is described in an the inertial planetocentric reference frame. The space plane is subjected to a total sum of external forces, F^I_{ext}, the derivation of the forces acting on a space plane will be discussed in Section 4.2. The position of the CoG of the space plane with respect to the origin of the inertial frame is defined by position vector, $\mathbf{r}^I_{cm}$, and the velocity of the CoG with respect to the inertial frame is defined by a velocity vector, V_I. Additionally, the rotation of the space plane with respect to the I-frame, expressed in components along the body axes, is given by an angular velocity vector, $\boldsymbol{\Omega}^B_{BI}$. The translational motion of a vehicle in inertial space is shown in Figure 3.9. A general formulation of the motion of a space plane, which is subjected to an external force, is derived in the lecture notes of Mooij (2019a). The result is given by:

$$\mathbf{F}^I_{\text{ext}} = m\frac{d^2\mathbf{r}^I_{cm}}{dt^2} + 2\boldsymbol{\Omega}^B_{BI} \times \int_m \frac{\delta\tilde{r}}{\delta t}dm + \int_m \frac{\delta^2\tilde{r}}{\delta t^2}dm, \tag{3.26a}$$

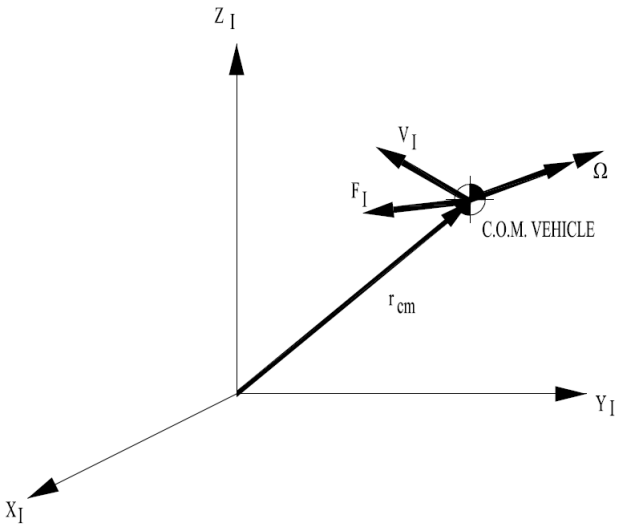

Figure 3.9: Motion of a vehicle with respect to the inertial space (Mooij, 2019a).

$$\mathbf{F}^I_{\text{ext}} = m\frac{d^2\mathbf{r}^I_{cm}}{dt^2} - \mathbf{F}^I_C - \mathbf{F}^I_{\text{rel}}, \tag{3.26b}$$

$$\tilde{\mathbf{F}}^I_{\text{ext}} = \mathbf{F}^I_{\text{ext}} + \mathbf{F}^I_C + \mathbf{F}^I_{\text{rel}} = m\frac{d^2\mathbf{r}^I_{cm}}{dt^2}, \tag{3.26c}$$

where $\tilde{r}$ is distance between the CoG of the vehicle and the location of a mass element. The first term on the right hand side of Equation 3.26a depicts the acceleration of the CoG of the vehicle with respect to the inertial frame, and the apparent forces, F^I_C and F^I_{rel}, are called the Coriolis and relative force, respectively. These forces exist due to a time variation in the mass distribution. For a non-elastic body these forces are only related to the propulsion system. The Coriolis force, which relates the mass flow with the angular rate of the space plane, can be neglected if the angular velocity is small. According to Mooij (1994), the Coriolis force can be neglected when compared to the relative force and due to low angular velocity of the space plane. The relative force, also known for a non-elastic body as the impulse thrust, is typically defined as the external propulsive force, $F_{P,I}$ (Mooij, 1994).

With these assumptions, the translational state derivative of the space plane can be defined in the inertial reference frame. In TUDAT, spherical components are not used to propagate the state of the space plane. Therefore, the Cartesian coordinates system is used to define the state derivative. The position and velocity, defined in the inertial frame, are given by:

$$\mathbf{r}^I_{cm} = \begin{bmatrix} x_I & y_I & z_I \end{bmatrix} \quad \text{and} \quad \mathbf{V}_I = \begin{bmatrix} \dot{x}_I & \dot{y}_I & \dot{z}_I \end{bmatrix}. \tag{3.27}$$

The state derivative *i.e.*, the change in position and velocity can be desribed by:

$$\dot{\mathbf{r}}^I_{cm} = \begin{bmatrix} \dot{x}_I & \dot{y}_I & \dot{z}_I \end{bmatrix} \quad \text{and} \quad \dot{\mathbf{V}}_I = \frac{1}{m}\left[\mathbf{F}_{A,I} + \mathbf{F}_{G,I} + \mathbf{F}_{P,I}\right]. \tag{3.28}$$

The acceleration of the space plane is influenced by the aerodynamic forces, $\mathbf{F}_{A,I}$, gravitational forces, $\mathbf{F}_{G,I}$, and propulsive forces, $\mathbf{F}_{P,I}$. These forces need to be defined in the I-frame, which is possible with the basic transformation matrices that have been described previously.

3.2.2. Rotational Equations of Motion

The equations that govern the rotational motion are based on the same principles discussed in Section 3.2.1.

Rotational Motion with respect to an Inertial Frame

For a vehicle moving in an inertial reference frame, a general expression can be given for the rotational motion, where $\boldsymbol{\omega}^B_{BI}$ defines the angular velocity and $\mathbf{r}_{cm}$ gives the distance between the vehicle CoG and the origin of the I-frame (Mooij, 1994). The general expression, which yields the total external moment, M^B_{cm}, is given by:

$$\mathbf{M}_{cm}^{B} = \int_m \tilde{\mathbf{r}} \times \left(\frac{\boldsymbol{\omega}_{BI}^{B}}{dt} \times \tilde{\mathbf{r}} \right) dm + \int_m \tilde{\mathbf{r}} \times [\boldsymbol{\omega}_{BI}^{B} \times (\boldsymbol{\omega}_{BI}^{B} \times \tilde{\mathbf{r}})] dm + 2 \int_m \tilde{\mathbf{r}} \times \left(\boldsymbol{\omega}_{BI}^{B} \times \frac{\delta \tilde{\mathbf{r}}}{\delta t} \right) dm + \int_m \tilde{\mathbf{r}} \times \frac{\delta^2 \tilde{\mathbf{r}}}{\delta t^2} dm, \quad (3.29a)$$

$$\mathbf{M}_{cm}^{B} = \int_m \tilde{\mathbf{r}} \times \left(\frac{\boldsymbol{\omega}_{BI}^{B}}{dt} \times \tilde{\mathbf{r}} \right) dm + \int_m \tilde{\mathbf{r}} \times [\boldsymbol{\omega}_{BI}^{B} \times (\boldsymbol{\omega}_{BI}^{B} \times \tilde{\mathbf{r}})] dm - \mathbf{M}_{C}^{B} - \mathbf{M}_{\text{rel}}^{B}, \quad (3.29b)$$

$$\tilde{\mathbf{M}}_{cm}^{B} = \mathbf{M}_{cm}^{B} + \mathbf{M}_{C}^{B} + \mathbf{M}_{\text{rel}}^{B} = \int_m \tilde{\mathbf{r}} \times \left(\frac{\boldsymbol{\omega}_{BI}^{B}}{dt} \times \tilde{\mathbf{r}} \right) dm + \int_m \tilde{\mathbf{r}} \times [\boldsymbol{\omega}_{BI}^{B} \times (\boldsymbol{\omega}_{BI}^{B} \times \tilde{\mathbf{r}})] dm, \quad (3.29c)$$

where the first and second term on the right hand side are the apparent moment due to the angular acceleration and velocity, respectively, with respect to the I-frame (Mooij, 2019a). Additionally, the principle of solidification (Cornelisse, Schöyer, and K. Wakker, 1979) is applied to reduce the rotational equations of motion to Equation 3.29c. In a study done by Mooij (1998), it was concluded that the Coriolis moment was small compared to other moments present. For this reason, the Coriolis moment is assumed to have negligible effect and, therefore, not modelled. The relative moment is defined as the misalignment of the thrust vector, due to the difference between the CoG and Center of Thrust (CoT). The relative moment is added as an external moment, expressed in the body frame by:

$$\mathbf{M}_{P,B} = \mathbf{F}_{P,B}(\mathbf{x}_{\text{CoG}} - \mathbf{x}_{\text{CoT}}) \quad (3.30)$$

With these assumptions, the rotational state derivative can be defined in the inertial reference frame. TUDAT uses quaternions to define and propagate the attitude of the space plane. The angular velocity is defined with the roll, pitch and yaw rate, which relates the rotation of the B-frame with respect to the I-frame. The attitude and angular velocity are defined by:

$$\mathbf{q}_{I,B} = \begin{bmatrix} q_1 & q_2 & q_3 & q_4 \end{bmatrix} \quad \text{and} \quad \boldsymbol{\omega}_{B,I}^{B} = \begin{bmatrix} p & q & r \end{bmatrix}. \quad (3.31)$$

The time derivative of the attitude and angular velocity are, according to Mooij (1994), given by:

$$\dot{\mathbf{q}}_{I,B} = \frac{1}{2} \begin{bmatrix} -q_4 & -q_3 & q_2 \\ q_3 & -q_4 & -q_1 \\ -q_2 & q_1 & -q_4 \\ q_1 & q_2 & q_3 \end{bmatrix} \begin{bmatrix} p \\ q \\ r \end{bmatrix} \quad \text{and} \quad \dot{\boldsymbol{\omega}}_{B,I}^{B} = \mathbf{I}^{-1}(\tilde{\mathbf{M}}_{cm}^{B} - \boldsymbol{\omega}_{B,I}^{B} \times \mathbf{I}\boldsymbol{\omega}_{B,I}^{B}), \quad (3.32)$$

where $\mathbf{I}$ is the inertia tensor of the space plane and $\tilde{\mathbf{M}}_{cm}$ is to total moment acting about the CoG of the space plane.

Definition of the Derivative of the Roll, Pitch and Yaw Rate

The derivative of the roll, pitch and yaw rate can be expressed analytically by assuming that the $X_B z_B$-plane is symmetric. In this case, the products of inertia $I_{xy} - I_{yz} = 0$ Mooij (2019a). In this case the derivatives are expressed by:

$$\dot{p} = \frac{I_{zz}}{I_{xx}I_{zz} - I_{xz}^2} M_x + \frac{I_{xz}}{I_{xx}I_{zz} - I_{xz}^2} M_z + \frac{(I_{xx} - I_{yy} + I_{zz})I_{xz}}{I_{xx}I_{zz} - I_{xz}^2} pq + \frac{(I_{yy} - I_{zz})I_{zz} - I_{xz}^2}{I_{xx}I_{zz} - I_{xz}^2} qr, \quad (3.33a)$$

$$\dot{q} = \frac{M_y}{I_{yy}} + \frac{I_{xz}}{I_{yy}}(r^2 - p^2) + \frac{I_{zz} - I_{xx}}{I_{yy}} pr, \quad (3.33b)$$

$$\dot{r} = \frac{I_{xz}}{I_{xx}I_{zz} - I_{xz}^2} M_x + \frac{I_{xx}}{I_{xx}I_{zz} - I_{xz}^2} M_z + \frac{(I_{xx} - I_{yy})I_{xx} + I_{xz}^2}{I_{xx}I_{zz} - I_{xz}^2} pq + \frac{(-I_{xx} + I_{yy} - I_{zz})I_{xz}}{I_{xx}I_{zz} - I_{xz}^2} qr. \quad (3.33c)$$

The conceptual vehicle chosen to simulate the ascent trajectory has two planes of symmetry, see Section 4.2. When two planes of symmetry exist, the expression can be simplified to:

$$\dot{p} = \frac{M_x}{I_{xx}} + \frac{I_{yy} - I_{zz}}{I_{xx}} qr, \quad (3.34a)$$

$$\dot{q} = \frac{M_y}{I_{yy}} + \frac{I_{zz} - I_{xx}}{I_{yy}} pr, \quad (3.34b)$$

$$\dot{r} = \frac{M_z}{I_{zz}} + \frac{I_{xx} - I_{yy}}{I_{zz}} pq. \quad (3.34c)$$

These equations are used in the G&C system to compute the derivative of the roll, pitch and yaw rate before a change in the deflection angle is applied. The application of these equations is further explained in Chapter 6.

4

Environment & Vehicle Models

In the previous chapter the Equations of Motion (EoM) for a space plane have been defined. The forces and moments, which have only been expressed in the most general form, are dependent on the choice of vehicle and are influenced by the environment. The environment model consists of the Earth and optional additional celestial bodies and the atmosphere of the Earth. The atmosphere influences the thrust, drag and lift forces, while the central body and other celestial bodies determine the gravitational acceleration acting on the space plane. The vehicle itself, as a model needs to represent the engine, the mass characteristics, and the shape of the vehicle. In Section 4.1 the environmental models that are used will be discussed. Section 4.2 will discuss the conceptual vehicle that has been chosen to optimize the ascent trajectory for.

4.1. Environmental Models

In this section, the environmental models that have been used for the simulation of the ascent trajectory are discussed. This includes the shape of the Earth, the gravitational model and the atmospheric model. Since the forces acting on the space plane due to atmospheric forces and the gravitational acceleration of the Earth are large, it is assumed that the gravitational acceleration of the Sun or Moon can be neglected.

4.1.1. Earth Shape Model

For the ascent trajectory of a space plane, which will ascent from the Earth and will target an orbit around the Earth, it is important to have an accurate model of the Earth. In most situations, the Earth is described by a sphere, with an average radius applicable at any latitude. For this thesis, it is chosen to use a spherical Earth model for two reasons. First of all, the optimal control problem is converted into a NonLinear Programming (NLP) problem with optimization parameters that are defined in terms of altitude instead of time. Since the target orbit is inclined, the altitude behaves predictably no matter at what latitude the space plane is located. Second of all, the space plane uses a target altitude instead of a target semi-major axis as an optimization objective, due to convergence issues that will be discussed in Chapter 5.

In practice the surface of the Earth is deformed due to numerous natural effects. A more suitable representation of the Earth is an ellipsoid, where the radius of the Earth at the poles is approximately 21 km shorter compared to the equatorial radius (Mooij, 2019a). The ellipticity, e, of an ellipsoid can be described by:

$$e = 1 - \frac{R_p}{R_e}, \tag{4.1}$$

where R_p is the mean polar radius and R_e is the mean equatorial radius. Figure 4.1 depicts an ellipsoidal body, with a vehicle at an altitude h above the surface of the body. In the figure, it can be seen that a distinction is made between the geographic latitude, δ^*, and the geocentric latitude, δ. Due to the small ellipticity of for instance the Earth, the geographic latitude can be approximated with the geocentric latitude (Mooij, 2019a). With this assumption, an approximation can be made of the radius of the Earth at a specific latitude, with:

$$R_s \approx R_e\left[1 - \frac{e}{2}(1 - \cos 2\delta)\right] = R_e(1 - e\sin^2\delta), \tag{4.2}$$

which allows for a more accurate representation of the space plane altitude. However, the altitude varies based on the latitude if an ellipsoidal model is used, which will increase the complexity of the ascent trajectory with

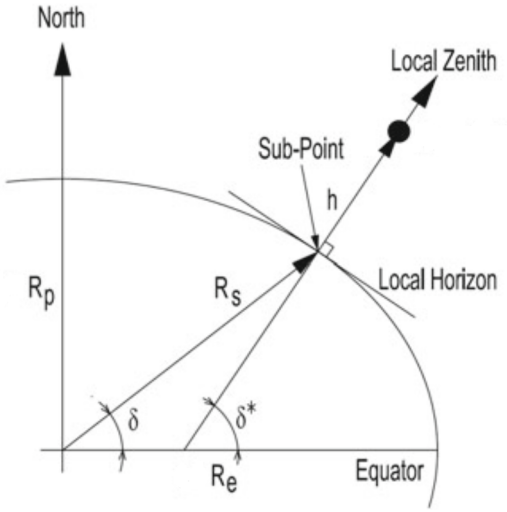

Figure 4.1: A vehicle above the ellipsoidal body (Mooij, 2019a).

annded launch window due to t extehe lateral motion of the space plane. A future study could study the influence of the spherical Earth on the found ascent trajectory.

4.1.2. Gravity Field Model

According to Newton, Bernard, and Whitman (1999), a point mass attracts every other point mass by a force, $\mathbf{F_G}$, acting along the line intersecting the two points. Mathematically, this force can be expressed by:

$$\mathbf{F_G} = \frac{GMm}{r^2}\hat{\mathbf{r}}, \tag{4.3}$$

where r is the distance between the two particles, M is the mass of the central body, m is the mass of a secondary body, G is the universal gravity constant and $\hat{\mathbf{r}}$ is the distance unit vector. When the secondary body has a mass much smaller compared to the central body, the equation becomes:

$$\mathbf{F_G} = \frac{\mu}{r^2}\hat{\mathbf{r}}, \tag{4.4}$$

where μ is the gravitational parameter specific to the central body. Even though the Earth is not a particle, the aforementioned equations still holds. According to Newton, Bernard, and Whitman (1999), if the central body has a spherically symmetric mass distribution, then the central body can be modelled as a point mass. However, bodies such as Earth have a non-symmetric mass distribution, which can be corrected with the use of spherical harmonics (Mooij, 2019a). The reason that the gravity has to be corrected is due to the ellipicity of the Earth. Furthermore, other mass deformations such as mountains and seas influence the gravity model. The correctional term, a function of the distance, r, the geocentric longitude, τ, and the geocentric latitude, δ, is included to express the gravitational potential, U, by:

$$U(r,\tau,\theta) = \frac{\mu}{r}\left\{1 + \sum_{n=2}^{n_{\max}}\left[\left(\frac{R_e}{r}\right)^n \sum_{m=0}^{n}(C_{mn}\cos m\tau + S_{nm}\sin m\tau)P_n^m(\sin\delta)\right]\right\}. \tag{4.5}$$

From the gravitational potential the gravitational acceleration vector $\mathbf{g}$ can be found, which can be applied to the equations of motion. The vector is given in spherical coordinates by:

$$\mathbf{g} = \begin{bmatrix} g_r & g_\tau & g_\delta \end{bmatrix}^\top = \begin{bmatrix} -\dfrac{\partial U}{\partial r} & -\dfrac{1}{r\cos\delta}\dfrac{\partial U}{\partial \tau} & -\dfrac{1}{r}\dfrac{\partial U}{\partial \delta} \end{bmatrix}^\top \tag{4.6}$$

The derivation of the partial derivatives is omitted from this report for the sake of brevity. However, these are available in the lecture notes by Mooij (2019a). Including a model that represents the ellipicity of the Earth and other mass deformations is computationally pricey. Using a lower fidelity model of the gravity field will improve the computational speed of the simulation, while reducing the accuracy of the model. The most

significant inclusion that could be made is the elliptical mass distribution of the Earth. This effect is included in the gravity model, while higher order gravitational models are not included to limit the computation time of a single simulation.

4.1.3. Atmosphere Model

The atmosphere of the Earth will influence the ascent trajectory of a space plane considerably. It induces forces and moments, which act on the space plane. Additionally, a space plane is a high speed vehicle, where the heat transfer between the super and hypersonic airflow to the space plane cannot be neglected. Furthermore, the atmosphere will influence the air-breathing engine performance. There are numerous atmospheric models that can be used for the optimization of an ascent trajectory. A number of models are presented, follow by a brief discussion of the most appropriate model.

Exponential Model

The most simple atmospheric model available in the TU Delft Astrodynamics Toolbox (TUDAT) library is the exponential atmospheric model, which is also used for analytical solution methods. This model assumes that the atmosphere is an ideal gas, where the particles in the atmosphere do not interact with each other. Based on this assumption, the ideal gas law can be used, given by:

$$p = \rho RT = \rho \frac{R^*}{M} T, \tag{4.7}$$

where p is the pressure, ρ is the density and T is the temperature of the atmosphere. The gas constant R, which is specified for air, can be computed with the universal gas constant, R^*, and the molecular mass of the atmosphere, M. The ideal gas law can be used in combination with the hydrostatic equation for the atmosphere (Equation 4.10) to express the density in terms of altitude, h. The resulting expression is given by:

$$\frac{\rho}{\rho_0} = \exp^{-\beta h} = \exp^{-\frac{h}{H_s}}, \tag{4.8}$$

where H_s is defined as the scale height, which is related to the gas constant, R, temperature, T, and the standard gravity of Earth, g_0, by:

$$H_s = \frac{1}{\beta} = \frac{RT}{g_0}. \tag{4.9}$$

It is important to realize that the exponential atmospheric model uses a constant temperature, while in reality the temperature is variable with altitude. Due to this assumption also the speed of sound is defined as constant (Mooij, 2019a).

$$dp = -\rho g \mathrm{d}h \tag{4.10}$$

United States Standard Atmosphere 1976

The United States standard atmosphere 1976 (US76) atmospheric model still uses the ideal gas law and the hydrostatic equation to find the density and pressure at a specific height. In addition, the temperature is defined in terms of geopotential altitude, z, with:

$$z = \int_0^h \frac{g}{g_0} \mathrm{d}h \approx \frac{R_0 h}{R_0 + h}, \tag{4.11}$$

where R_0 is the earth radius, where the gravitational acceleration is equal to the standard gravity. In Figure 4.2 the temperature variation of the US76 atmospheric model compared to the exponential model can be seen. A scale temperature, T_M, is used in combination with the molecular mass, M, to compute the temperature with:

$$T = T_M \frac{M}{M_0}. \tag{4.12}$$

The molecular mass is assumed to be constant up to 80 km altitude, denoted with M_0. Between 80 and 86 km altitude, the molecular mass is computed using a small correction. The scale temperature is computed depending on an altitude interval, where for each interval the initial scale temperature is given and will either

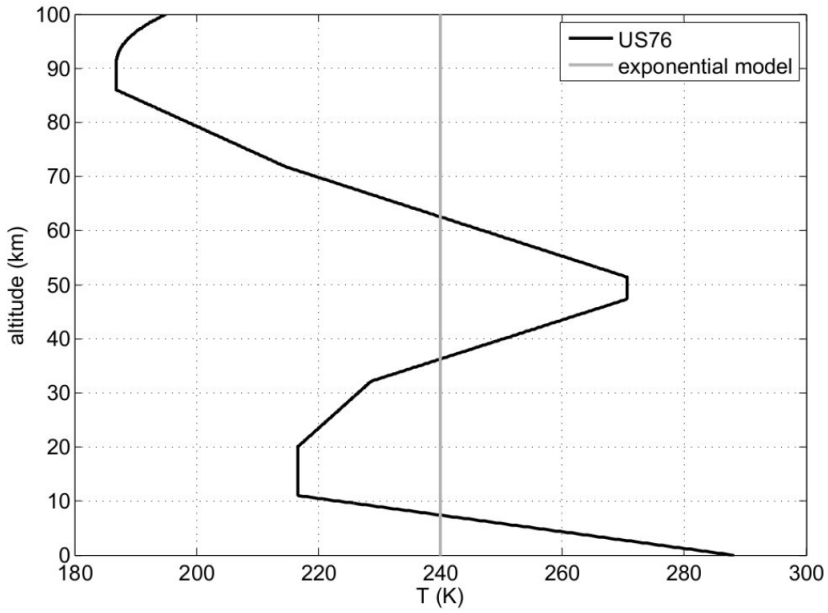

Figure 4.2: Temperature comparison of the exponential and US76 atmospheric model (Mooij, 2019a).

vary linearly as a function of altitude, z, or will remain constant. Up to an altitude of 86 km the pressure can be computed with:

$$p = \begin{cases} p_i \exp\left[\dfrac{-g_0 M_0 (z - z_i)}{R^* T_{M_i}}\right], & \text{for } L_{z_i} = 0 \\ p_i \left[\dfrac{T_{M_i}}{T_{M_i} + L_{z_i}(z - z_i)}\right]^{\frac{g_0 M_0}{R^* L_{z_i}}}, & \text{for } L_{z_i} \neq 0 \end{cases} \tag{4.13}$$

where the subscript i denotes the altitude interval and L_{z_i} denotes the rate of change of the scale temperature. Above 86 km and up to 120 km, the temperature is computed with a several methods, which can be found in the lecture notes by Mooij (2019a), and the pressure is computed with:

$$p = \frac{N R^* T}{N_A}, \tag{4.14}$$

which is a different expression of the ideal gas law. Here N_A is Avagadro's constant and N is the total number density, based on data provided by the National Oceanic and Atmospheric Administration (NOAA), computed with linear interpolation[1]. Finally, the density is computed with the original form of the ideal gas law, Equation 4.7 (Mooij, 2019a).

NRLMSISE-00

The NRLMSISE-00 model is a more accurate model compared to the previously discussed atmospheric models. It is especially suited for simulations where orbit decay information is important (Mooij, 2019a). In general, the model produces atmospheric parameters which are a function of altitude, longitude, latitude and time (Picone et al., 2002). In case of the space plane, this atmospheric model is not necessary for the optimization of the ascent trajectory, due to the high thrust forces compared to the aerodynamic forces. However, due to the relatively low target altitude of 120 km, this model will produce more accurate results when orbit decay is considered.

Selected Model

The three models discuss increase in accuracy. The exponential model assumes a constant temperature, which means that the Mach number is constant. The vehicle model, which will be discussed later, has many variables that depend on the Mach number. The exponential atmosphere model lacks the detail to accurately compute

[1]NOAA, National Geodetic Survey, accessed on 5 Jun 2021, `https://geodesy.noaa.gov/orbits/orbit_data.shtml`.

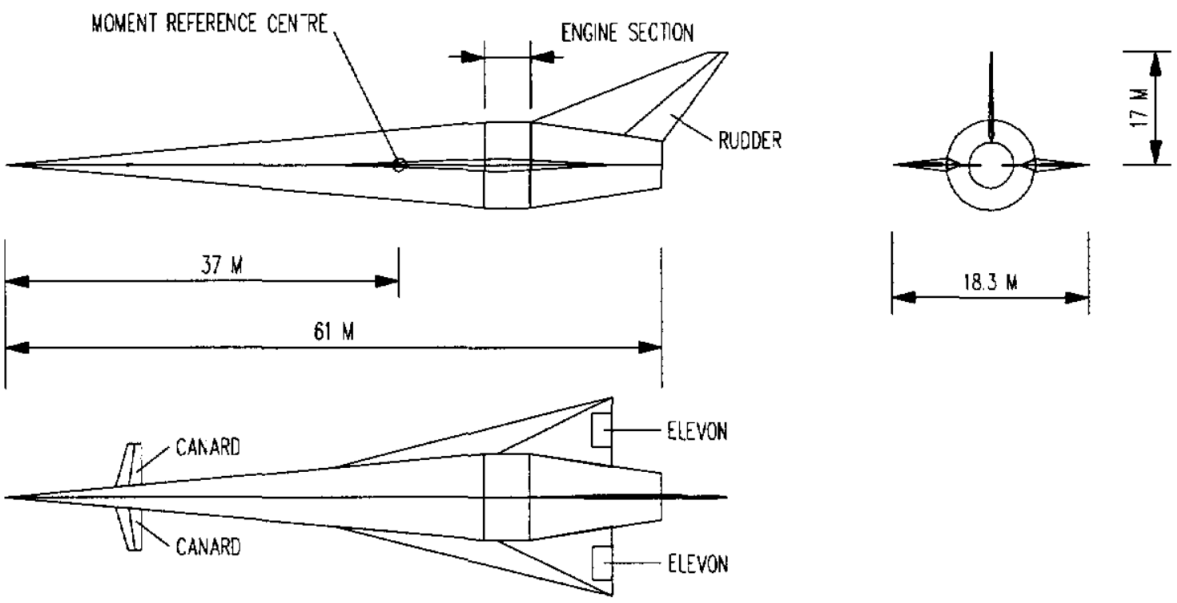

Figure 4.3: Top- side- and rear-view of the Winged-cone configuration (Mooij, 1998).

the Mach number. On the other hand, the NRLMSISE-00 model is high accuracy and computationally heavy. The simulation itself does not deal with orbital decay and, therefore, it is assumed that using NRLMSISE-00 does not influence the final results compared to the US76 atmosphere model. For these reasons, the US76 atmospheric model is chosen to represent the atmosphere.

4.2. Vehicle Model

Due to the limited research in lateral motion of a space plane, aerodynamic coefficients are difficult to come by. There have been a number of researchers that have been able to receive CAD data from Rocket Engine Limited (REL) to determine the aerodynamic coefficients. However, the aerodynamic coefficients, required for lateral motion, have never been published. On the other hand, another reference vehicle does include the coefficients necessary to model the lateral motion.

The vehicle in questions is the National Aero-Space Plane (NASP), which has a theoretical air-breathing engine. The NASP was a theoretical space plane designed to enable hypersonic and Single-Stage-To-Orbit (SSTO) space plane research (Shaughnessy et al., 1990). It has been used in studies by Mooij (1998) and Shaughnessy (1992). Furthermore, a modified version has been used in more recent studies by Zhou, Wang, and Cui (2020), Murillo and Lu (2010) and the thesis work done by Spillenaar Bilgen (2017). Due to the extensive research done with the NASP, it is chosen to use this reference vehicle for the thesis. The advantage of using this vehicle is the appropriate studies that have used a similar vehicle configuration, which will enable verification of the optimization results. In particular, the study done by Mooij (1998) can be used to determine the longitudinal ascent trajectory, while the study by Zhou, Wang, and Cui (2020) can be used to verify the inclusion of a change in the Right Ascensions of the Ascending Node (RAAN).

The winged-cone configuration can be seen in Figure 4.3 and the geometric characteristics can be seen in Table 4.1. The winged-cone configuration has a take-off mass of $136,079$ kg and a dry mass of $59,968$ kg. For the optimization of an ascent trajectory, it is assumed that any fuel not used during the ascent can be used for payload instead. Thus, the initial mass conditions for the ascent trajectory are always the same. Due to a change in mass during the ascent, the center of gravity and the moments of inertia will vary. The shift of the center of gravity, which is assumed to vary along the x_B-axis only, and the change in moment of inertia is recorded by Shaughnessy et al. (1990) and does not have to be computed during the simulation. Furthermore, it is assumed that the products of inertia are negligible *i.e.*, only I_{xx}, I_{yy} and I_{zz} are taken into account. The location of the center of gravity and the moment of inertia are used to determine the aerodynamic and thrust-induced moments of the winged-cone configuration.

Table 4.1: Geometric information about the winged-cone configuration (Mooij, 1994).

Body	*Value*
Fuselage length	61.0 m
Moment reference centre from nose	37.8 m
Vertical Tail	*Value*
Vertical tail area	60.0 m^2
Span	9.9 m
Wing	*Value*
Wing reference area	334.7 m^2
Aspect ratio	1.0
Span	18.3 m
Mean Aerodynamic Chord (MAC)	24.4 m
Rudder	*Value*
Rudder area	15.0 m^2
Span	7.0 m
Chord (relative to tail)	25 %
Canard	*Value*
Canard Area	14.3 m^2
Aspect ratio	5.48
Span	10.2 m

4.2.1. Aerodynamic Forces and Moments

The trajectory of a space plane has a large difference in velocity. Usually, this is measured in terms of Mach number, which is determined with:

$$M = \frac{V}{a}, \tag{4.15}$$

where a is the speed of sound, which is a function of the atmosphere around the vehicle. Typically, a space plane will accelerate from Mach zero to over Mach twenty. The large difference in Mach numbers means that the space plane will encounter sub-, trans-, supersonic and hypersonic flow.

General Expression

The aerodynamic forces acting on a space plane are typically expressed in terms of the AA-frame, where the general expression is given by:

$$\mathbf{F}_{A,AA} = \begin{bmatrix} -D \\ -S \\ -L \end{bmatrix} = \begin{bmatrix} -C_D \frac{1}{2}\rho V^2 S_{\text{ref}} \\ -C_S \frac{1}{2}\rho V^2 S_{\text{ref}} \\ -C_L \frac{1}{2}\rho V^2 S_{\text{ref}} \end{bmatrix}, \tag{4.16}$$

where C_D, C_L and C_S are the drag, lift and side force coefficients of the vehicle, and S_{ref} is the aerodynamic reference area. The forces are defined in the aerodynamic reference frame and need to be transformed into the inertial reference frame, to be used in the EoM. The other variables, ρ, V together form the dynamic pressure:

$$q_{\text{dyn}} = \frac{1}{2}\rho V^2. \tag{4.17}$$

Similar to the aerodynamic forces, also three moments can be defined. The moments are expressed about axes in the body reference frame, see Figure 4.4. The moments expressed in the B-frame can be used as is in the rotational equations to define the roll, pitch and yaw rate. The shape of the vehicle induces a moment, which is expressed as:

$$\mathbf{M}_{A_M,B} = \begin{bmatrix} \mathcal{L} \\ \mathcal{M} \\ \mathcal{N} \end{bmatrix} = \begin{bmatrix} C_l \frac{1}{2}\rho V^2 S_{\text{ref}} b_{\text{ref}} \\ C_m \frac{1}{2}\rho V^2 S_{\text{ref}} c_{\text{ref}} \\ C_n \frac{1}{2}\rho V^2 S_{\text{ref}} b_{\text{ref}} \end{bmatrix}, \tag{4.18}$$

where b_{ref} and c_{ref} are typically the wingspan and aerodynamic chord, respectively (Mooij, 1994). Besides the moments created by the vehicle, also a moment exists due to the misalignment of the Center of Gravity (CoG) and the aerodynamic reference point. The Moment Reference Point (MRP) is the point where the

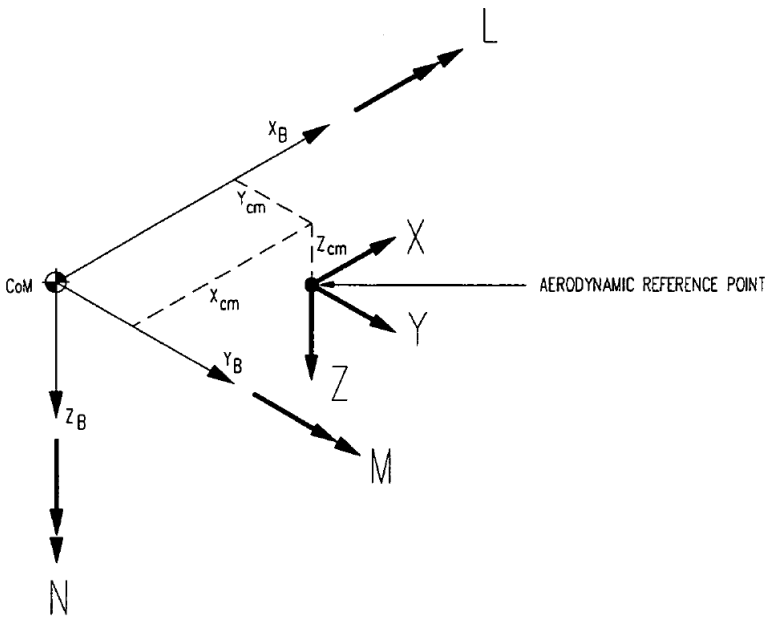

Figure 4.4: Illustration of the aerodynamic moments acting on a vehicle, where the aerodynamic reference point does not coincide with the center of mass (Mooij, 1994).

aerodynamic forces act. If there is misalignment, the moments induced due to the aerodynamic forces can be expressed with:

$$\mathbf{M}_{A_F,B} = \mathbf{r}_{cm} \times \mathbf{F}_{A,B}, \tag{4.19}$$

where $\mathbf{r}_{cm}$ is the distance between the CoG and the MRP. The aerodynamic forces, $\mathbf{F}_{A,B}$, need to be transformed from the AA-frame to the B-frame. The resulting total aerodynamic moment is given by:

$$\mathbf{M}_{A,B} = \mathbf{M}_{A_M,B} + \mathbf{M}_{A_F,B}. \tag{4.20}$$

For the NASP, only a misalignment exists on the x_B-axis, simplifying the aerodynamic forces induced moments. Due to this misalignment, the aerodynamic force induced moment exist only about the y_B-axis.

Decomposition of the Aerodynamic Coefficients

The coefficient used to compute the forces and moments in the previous subsection is the total coefficient for the entire body, which can be broken down into smaller parts. These parts are for instance the wing, body and control surfaces. The total coefficient is then computed by summing the constituents. The NASP has, as control surfaces, a canard, two elevons and a rudder. The elevons can be operated separately in order to induce a bank angle, and the canard is only operational in subsonic conditions (Shaughnessy et al., 1990) and subtracted when the Mach number exceeds 0.9. The aerodynamic coefficients of the different surfaces of the NASP depend on the Mach number, surface deflection and angle of attack. The sum of the aerodynamic coefficients can be computed with:

$$C_D = C_{D_a} + C_{D_{de,l}} + C_{D_{de,r}} + C_{D_{dr}} + C_{D_{dc}}, \tag{4.21a}$$

$$C_S = C_{S_\beta}\beta + C_{S_{de,l}} + C_{S_{de,r}} + C_{S_{dr}}, \tag{4.21b}$$

$$C_L = C_{L_a} + C_{L_{de,l}} + C_{L_{de,r}} + C_{L_{dc}}, \tag{4.21c}$$

$$C_l = C_{l_\beta}\beta + C_{l_{de,l}} + C_{l_{de,r}} + C_{l_{dr}} + C_{l_p}\left(\frac{pb_{\text{ref}}}{2V}\right) + C_{l_r}\left(\frac{rb_{\text{ref}}}{2V}\right), \tag{4.21d}$$

$$C_m = C_{m_a} + C_{m_{de,l}} + C_{m_{de,r}} + C_{m_{dr}} + C_{m_{dc}} + C_{m_q}\left(\frac{qc_{\text{ref}}}{2V}\right), \tag{4.21e}$$

$$C_n = C_{n_\beta}\beta + C_{n_{de,l}} + C_{n_{de,r}} + C_{n_{dr}} + C_{n_p}\left(\frac{pb_{\text{ref}}}{2V}\right) + C_{n_r}\left(\frac{rb_{\text{ref}}}{2V}\right). \tag{4.21f}$$

Table 4.2: Differentiation of the flow regimes in terms of Mach number.

Flow Regime	Mach Number (M_∞) [-]
Subsonic	$M_\infty < 0.8$
Transonic	$0.8 < M_\infty < 1.2$
Supersonic	$1.2 < M_\infty < 4.5$
Hypersonic	$4.5 < M_\infty$

The aerodynamic coefficients all depend on the angle of attack and Mach number. In the equations, each subscript denotes whether it contributes to one of the forces and moments, which have been specified before. The second part of the subscript determines where the contribution comes from. There is the normal vehicle contribution, subscript a, the left elevon, de, l, the right elevon, de, r, the canard, dc, and the rudder dr. These coefficients have been found by Aerodynamic Preliminary Analysis System (APAS) and indicate the increment coefficients with respect to the angle of attack and Mach number. For the moment coefficients, the rolling moment dynamic derivatives for roll, C_{l_p}, and yaw rate, C_{l_r}, the pitch rate dynamic derivative, C_{m_q}, and the yawing moment dynamic derivatives for roll, C_{n_p}, and yaw rate, C_{n_r}, are computed and normalized with $\frac{pb_{\text{ref}}}{2V}$, $\frac{qc_{\text{ref}}}{2V}$ and $\frac{rb_{\text{ref}}}{2V}$, respectively. At last, there are the derivatives of the coefficients, $C_{S_\beta}, C_{l_\beta}, C_{n_\beta}$, that can be multiplied with the sideslip angle, β, to get the actual coefficient value.

Determination of the Aerodynamic Coefficients

Previously, the aerodynamic coefficients for a space plane have been presented. For the winged-cone configuration, the coefficients are known and given in the technical report by Shaughnessy et al. (1990). The determination is done with numerical methods, of which a large number of programs exist. In the case of the NASP, APAS was used. Other programs that achieve a similar goal are the Panel Aerodynamics (PANAIR)[2] (Mooij, 2019a), Digital Datcom (DATCOM)[3] or CART3D[4].

As mentioned earlier, the force and moment coefficients are dependent on Mach number, surface deflection and angle of attack. The Mach number determines the flow regimes, which are the sub-, trans-, super- and hypersonic flow. In Table 4.2, the Mach number corresponding to the flow regimes can be seen. Based on the flow regimes, the method to determine the coefficients might differ. However, first, a number of definitions have to be introduced. The four important terms are the compressibility, viscosity, rotationality and steadiness of the flow. The first is the compressibility of the flow, where for flow velocities below Mach 0.3, the flow is assumed to be incompressible. This means that it is assumed that the density of the flow does not vary when traversing the vehicle surface. Above Mach 0.3 this assumption no longer holds and the density of the flow will vary. Secondly, the viscosity of the flow is defined by (Anderson, 2010) as *"A flow where the effects of viscosity, thermal conduction and mass diffusion is important"*. The viscosity effects deal with the no-slip condition, where the flow velocity at the surface of a vehicle is zero, which creates friction. Furthermore, this friction creates a situation where the flow is separated from the surface at some point, which results in pressure drag. Due to the no-slip condition, the velocity of the flow is reduced, which means that the energy lost in terms of kinetic energy is found in terms of heat *i.e.*, internal energy (Anderson, 2010). This heat can be transferred to the surface of the body, which is especially important for the super- and hypersonic flow regimes. Last to mention, the mass diffusion is important for the hypersonic flow regime, where the flow can dissociate, due to the high temperatures, and can chemically react (Mooij, 2019a). Thirdly, the flow can be rotational, which can be a result in shear stresses between flow layers if the velocity differs. These shear stresses causes the particles in the flow to rotate. Anderson (2010) states that the flow is irrotational for *"subsonic flow over airfoils, supersonic flow over slender bodies at small angle of attack, and subsonic-supersonic flow through nozzles"*. For these cases, a boundary layer exists with viscous and rotational flow, while the flow outside of the boundary layer is irrotational. Last to mention, is the steadiness of the flow. Here it is assumed that the flow does not vary with time, meaning that if a vehicle is placed in a flow, the flow would remain constant over time (Anderson, 2010).

The method of solving the aerodynamic coefficients all depends on the assumptions that are made about the flow. When not simplifying the flow *i.e.*, not assuming inviscid incompressible irrotational flow, complicated

[2]Public Domain Aeronautical Software (PDAS), PANAIR, accessed on 9 Jun 2021, `https://www.pdas.com/panair.html`

[3]PDAS, Digital Datcom, accessed on 9 Jun 2021, `https://www.pdas.com/datcom.html`

[4]National Aeronautics and Space Administration (NASA), Cart3D Documentation, accessed on 9 Jun 2021, `https://www.nas.nasa.gov/publications/software/docs/cart3d/`

Computational Fluid Dynamics (CFD) models need to be used, which are computationally expensive (Mooij, 2019a). Compressibility cannot be neglected and is therefore still taken into account for APAS. It makes use of a theory called the panel method, where the velocity over the surface of numerous panels is computed. With the flow velocity over the surface, a pressure coefficient, which is normal to the surface can be computed. The panels together will form the shape of the vehicle and the resultant pressure coefficient is used to determine the aerodynamic coefficients. Typically, the panel method (Anderson, 2010) is used for subsonic and supersonic flow, while for the hypersonic flow local inclination methods are used (Anderson, 2006). These methods have also been applied for the NASP and are available to be used in the investigation of the optimization of a space plane (Shaughnessy et al., 1990).

4.2.2. Thrust Forces and Moments

Typically, a conventional rocket engine will have a constant specific impulse, which can be used in combination with the change in mass, $\dot{m}$, to get the thrust, as can be seen in Equation 2.4. However, as has been seen in Chapter 2, the specific impulse, I_{sp}, for an air-breathing engine changes depending on the Mach number. The NASP uses a theoretical air-breathing engine, where a thrust coefficient has been computed, C_T, which has been tabulated and depends on the Mach number, fuel equivalence ratio and dynamic pressure (Shaughnessy et al., 1990). The fuel equivalence ratio, which can be varied, is used as a way to throttle the thrust. The specific impulse has been determined in a similar way and are tabulated to be used for the ascent trajectory. When using a thrust coefficient, the thrust can be computed with:

$$T = C_T \frac{1}{2} \rho V^2, \tag{4.22}$$

with the thrust and specific impulse, the mass rate can be computed with Equation 2.4 in the following form:

$$\dot{m} = \frac{T}{I_{sp} g_0}. \tag{4.23}$$

It is possible for the thrust to also induce a moment. This is, for instance, the case when thrust vectoring is used to trim the vehicle. The thrust-induced moment is also expressed in the B-frame, where the thrust force, $\mathbf{F}_{T,P}$ is transformed with transformation matrix $\mathbf{C_{B,P}}$ from the P- to the B-frame. The moment can be expressed as:

$$\mathbf{M}_{T,B} = \mathbf{r}_T \times \mathbf{F}_{T,B}, \tag{4.24}$$

where $\mathbf{r}_T$ is the distance between the CoG and location of the thrust force. If multiple engines are present, the moment for each can be computed separately and summed together to get the resultant thrust-induced moment (Mooij, 1994). In the study done by Mooij (1998), Thrust Vector Control (TVC) has been used to reduce the required propellant during the ascent trajectory. In his study, a Center of Thrust (CoT) has been defined, which is located along the x_B-axis at 19.1 m from the moment reference center. Furthermore, a maximum thrust vector angle of ± 25 deg has been assumed. The implementation of the TVC will be further discussed in Chapter 6.

4.2.3. Aerodynamic Heating

Throughout parts of the ascent, the vehicle will be subjected to super- and hypersonic flow velocities. These velocities will result in heat transfer between the flow behind shock waves and the surface of the vehicle. Typically, a maximum dynamic pressure constraint is imposed to ensure that aerodynamic heating is not an issue. In the study done by Mooij (1998), the maximum dynamic pressure of $95,000$ N/m^2 was defined. Furthermore, also a constraint for the maximum heat flux is imposed. Calculation of the heat flux can be done with the Navier-Stokes equations (Anderson, 2006). Using the Navier-Stokes equations is however computationally expensive, which was the reason to assume inviscid, irrotational flow. It is infeasible to both optimize the ascent trajectory and implement these equations. Therefore, engineering methods should be applied to assess the stagnation heat flux. The maximum heat flux can be computed with Chapman's equation, which compute the stagnation heat flux. In the lecture notes by Mooij (2019a), the maximum heat flux equation for a laminar flow has been given by:

$$q_{c,\text{lam}} = \frac{c^*_{\text{lam}}}{\sqrt{R_N}} \sqrt{\rho_\infty} V_\infty^3, \tag{4.25}$$

where a 'cold wall' and rounded nose, with radius $R_N = 0.1$ m, are assumed. In the equation, V_∞ is defined as the free stream flow and ρ_∞ the free stream density. The coefficient, c^*_{lam}, is according to Hankey (1988) $c^*_{\text{lam}} \approx 18$.

For the theoretical reference vehicle NASP, no details are known about the edges of the nose and the wings. In previous studies, a rounded edge of 0.1 m was assumed for the leading edge of the wing (Mooij, 1998; Spillenaar Bilgen, 2017). It was also assumed that the rounding of the nose was higher. It is therefore not necessary to also assess the aerodynamic heating at the nose since these heat flux values will always be higher due to the higher nose radius.

4.2.4. Vehicle Model Overview & Limitations

The NASP is a theoretical space plane that has aerodynamic coefficients, thrust coefficients, specific impulse, Center of Gravity (CoG) and moments of inertia given in graphs (Shaughnessy et al., 1990). These parameters are all in some way dependent on the angle of attack, Mach number, equivalence ratio, dynamic pressure or vehicle mass. The information given in these graphs is converted into look-up tables, where each parameter is dependent on a number of variables. In Table 4.3 the parameters are listed with their dependencies. Furthermore, the dependencies itself and their limitations are listed in Table 4.4. It can be seen that for the angle of attack and Mach number extrapolation is applied whenever these parameters are out of the tabulated range. For the angle of attack, only a small range is allowed outside of the tabulated range. The Guidance and Control (G&C) module has been designed to only command the space plane to angles of attack that do not require extrapolation. However, it can occur that when the space plane is commanded to the tabulated limit an overshoot occurs. In these situations extrapolation is applied, where it is assumed that the aerodynamic coefficients are still accurate. For the Mach number, no limit is applied by the G&C system. However, it is assumed that extrapolation still yields valid results.

Table 4.3: Overview of the dependencies of the vehicle.

Vehicle Parameter	Dependencies	Symbols
Vehicle Body Aero. Coeff.	Angle of Attack, Mach Number	α, M
Elevons Aero. Coeff.	Angle of Attack, Mach Number, Deflection Angle	$\alpha, M, u_{de,l}/u_{de,r}$
Rudder Aero. Coeff.	Angle of Attack, Mach Number, Deflection Angle	α, M, u_{dr}
Canard Aero. Coeff.	Angle of Attack, Mach Number, Deflection Angle	α, M, u_{dc}
Thrust Coeff.	Mach Number, Dynamic Pressure, Equivalence Ratio	$M, \bar{q}, \phi$
Specific Impulse	Mach Number, Dynamic Pressure, Equivalence Ratio	$M, \bar{q}, \phi$
Moments of Inertia	Vehicle Mass	m
Center of Gravity	Vehicle Mass	m

Table 4.4: Overview of the limitations of the dependencies.

Dependency	Range	Additional Notes
Angle of Attack [deg]	$[-1, 12]$	Extrapolated between $[-2, -1]$ and $[12, 13]$
Mach Number [-]	$[0, 24.2]$	Extrapolated above Mach 24.2
Elevon Deflection [deg]	$[-20, 20]$	G&C system limited to this range
Rudder Deflection [deg]	$[-20, 20]$	G&C system limited to this range
Canard Deflection [deg]	$[-10, 10]$	G&C system limited to this range
Dynamic Pressure [N/m^2]	$[0, 239, 401]$	G&C system ensures that range is not exceeded
Equivalence Ratio [-]	$[0, 10]$	Range never exceeded
Vehicle Mass [kg]	$[59, 968, 136, 079]$	Range never exceeded

5

Optimization

In Section 2.4, the use of a Single-Stage-To-Orbit (SSTO) launch vehicle, that could reach a Low Earth Orbit (LEO), has been investigated. It has become apparent that SSTO access to space is possible with an air-breathing engine, due to the increased engine performance. However, air-breathing engines have lower (T/W) ratios compared to conventional rocket engines, necessitating the use of a horizontally launched space plane that can generate lift. A horizontally launched space plane has a different ascent trajectory compared to a vertically launched rocket, due to the lifting capabilities. This also means that a space plane can more easily change the heading angle, which can be used to increase the launch window.

The optimization of an ascent trajectory is an optimal control problem. For such a problem, the control profile is determined in such a way that certain objectives are minimized. One of these objectives can be the minimization of the fuel used during the ascent and consequently maximizing the payload that can be transported. Another objective could be the minimization of the orbital elements of the final orbit, compared to a target orbit. In Section 5.1 the general formulation of an optimal control problem is given and an explanation is given how that is converted into a NonLinear Programming (NLP) problem. Furthermore, global and local optimization methods will be described, which will be used to find the fuel-optimal ascent trajectory of a space plane. In Section 5.2 the initial problem definition will be described. It will also discuss the results that this problem definition yielded and what changes were made to the optimization due to convergence issues. Finally, in Section 5.3 the improved problem definition will be described for the optimization of the ascent trajectory that can also include lateral motion, to also optimize for an extended launch window. The improved problem definition is used to obtain the results, presented in Chapter 8.

5.1. Optimization Theory

Optimization methods can be catergorized into indirect and direct optimization methods. The indirect method tries to analytically solve the control problem by using the first-order optimality conditions from variational calculus (Rao, 2014). The direct methods convert the optimal control problem into a NLP problem. The indirect method presents a number of issues, such as the necessity to derive a number of equations, that represent the control equations, the constraints of the problem and the fitness function. Furthermore, the indirect method requires knowledge of the initial costate variables, which are unknown and lack physical significance. The optimal control problem is sensitive to the estimation of these variables due to the nonlinearity of the problem (Conway, 2010; Betts, 2010). Because of these reasons, it is chosen to use direct optimization techniques to find the fuel-optimal trajectory for the space plane.

The direct optimization method converts an optimal control problem, with the continuous control function $\mathbf{u}(t)$, into an NLP problem with a sequence of points, along which the control variables and/or state variables are defined. The problem is optimized by assessing the objective function directly (Betts, 2010). This means that the necessary conditions, used for the indirect optimization methods, are not needed. This converts the problem essentially into a parameter optimization problem with a distinct number of parameters. These parameters can be formulated in a decision vector $\mathbf{z}$. For the optimization of the ascent trajectory of a space plane, it is chosen to optimize the control parameters only, which is called control parameterization method (Rao, 2014). Based on the decision vector the cost function, which is to be minimized, becomes:

$$\min \mathbf{f}(\mathbf{z}) = \min[f_1(\mathbf{z}), \cdots, f_n(\mathbf{z})]. \tag{5.1}$$

The objective function is subject to equality constraints:

$$\mathbf{g}(\mathbf{z}) = \mathbf{0}, \tag{5.2}$$

and inequality constraints

$$\mathbf{h}(\mathbf{z}) \leq \mathbf{0}. \tag{5.3}$$

The optimal control problem is converted into an NLP problem with a transcription method. It is chosen to use a direct shooting method, which can be categorized as a control parametrization method. The control function can be defined as:

$$\mathbf{u}(t) \approx \sum_{i=1}^{m} \mathbf{z}_i \psi_i(t), \tag{5.4}$$

where the parameters to be determined are $\mathbf{z}_i$, and ψ_i are known functions (Rao, 2014). Typically, the control function is dependent on the time. However, the launch time will be varied, and the capabilities of the space plane to manipulate the Right Ascensions of the Ascending Node (RAAN) is analyzed. This means that it is not desirable to have a control function dependent on time. Instead, a control function dependent on the altitude is constructed:

$$\mathbf{u}(h) \approx \sum_{i=1}^{m} \mathbf{z}_i \psi_i(h). \tag{5.5}$$

With the control function, the objective function, subject to both equality and inequality constraints, is evaluated whenever the simulation is terminated.

With the transcription of the optimal control problem into an NLP problem, a numerical method can be used to solve the NLP problem. The first method is the use of gradient methods, which can be classified as a local optimization method. This method can accurately find the local minimum of an optimization problem by following the gradient. However, these methods have the tendency of finding local optima. This means that local optimization methods cannot guarantee that the global minimum is found. In contrast, global optimization methods are good at finding the global optimum. However, global optimization cannot guarantee that the actual global minimum is found, due to the iterative nature of these algorithms.

5.1.1. Global Optimization

There are various objectives that can be minimized with the use of optimization techniques for a space plane ascent trajectory. For instance, the fuel used during the ascent, and the difference in orbital elements between the space plane and the target orbit at the end of the ascent can be defined as objective functions. In reality, the ascent trajectory should not be optimized for a single objective but for multiple objectives. One should optimize the fuel used during the ascent, while also minimizing the difference between the orbital elements. There are even situations where more than two objectives should be used. Besides the fuel used and the final orbit, also the inequality constraints could be used as an objective. There are several global optimization techniques that only deal with a single optimization objective, such as Differential Evolution (DE), Particle Swarm Optimizer (PSO) and Simulated Annealing (SA)[1]. If multiple objectives need to be optimized, the single objective global optimizers require to sum objectives with weights attached to each objective, in such a way that the sum of the weight equals one. In most situations, these objectives will conflict with each other, creating a situation where a trade-off needs to be made between the different objectives. Since the relation between these objectives is not known, it is more beneficial to use global optimization techniques that can yield a range of optimal solutions, taking into account the different objectives. One of the multi-objective approaches is Pareto-based, where a Pareto front is formed from a set of solutions that are not dominated by other solutions. This means that such solution can not be further improved in one objective without sacrificing in another[2]. A visualization of this can be seen in Figure 5.1, where the optimal solutions form a Pareto front.

In general, the global optimization can be classified as a Genetic Algorithm (GA), with many different variations. The algorithm starts with an initial population where each member of the population has a randomly generated decision vector. For each member within the population the objective function is assessed. Based on the outcome of the objective function the population undergoes three natural processes: selection, combination, mutation. Through the selection process the worst members of the population are removed and it is also possible for the best members to survive into the next generation, which is called elitism. The remaining

[1] Pagmo, Heuristic Global Optimization Capabilities, accessed on 18 Jun 2021, `https://esa.github.io/pagmo2/overview.html`.

[2] IGI Global, What is Pareto Front, accessed on 18 Jun 2021, `https://www-igi-global-com.tudelft.idm.oclc.org/dictionary/pareto-front/21878`.

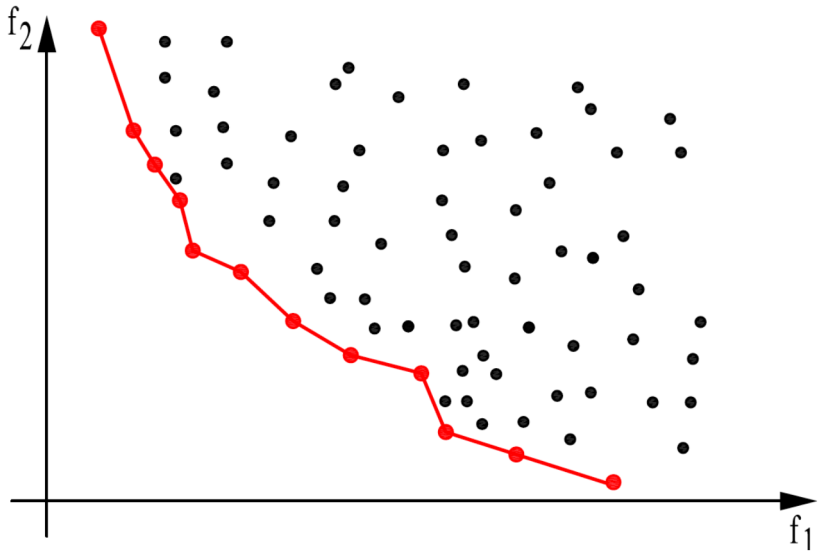

Figure 5.1: Graph showing the Pareto front in red, where it can be seen that the Pareto-optimal solutions are nondominated (Mooij and Dirkx, 2020).

members of the population are used as parents to create new members with a combined decision vector. From the newly created members, it is also possible to mutate a small portion of their decision vector, which might introduce unique elements to the vector. Using these three processes, a new generation is formed. For the new generation again the objective function is assessed and the natural process is repeated. This is done until either a fixed number of generations has been formed or if the best member of the generation has not changed for a certain number of iterations. Due to the iterative nature, there is not a guarantee that the actual global minimum of the problem will be found (Conway, 2010). Usually, a refinement is done to assess the accuracy of the found minimum. This can be done with a local optimization method.

There exists a C++ library for both single- and multi-objective optimization called Parallel Global Multi-objective framework for Optimization (PaGMO) (Biscani and Izzo, 2020). The multi-objective optimization techniques present are the Non-dominated Sorting Genetic Algorithm (NSGA2), Multi-Objective Evolutionary Algorithm with Decomposition (MOEA/D), Multi-Objective Hypervolume-based Ant Colony Optimizer (MHACO) and Non-dominated Sorting Particle Swarm Optimizer (NSPSO). These techniques are unconstrained optimizers, which means that the constraints present for an ascent trajectory need to be formulated in an objective. An alternative is to use constraints as termination conditions, which will lead to solutions that are infeasible. An example termination condition is the altitude. Whenever the altitude of the launch vehicle is less than zero *i.e.*, the launch vehicle has crashed, the termination should be stopped.

5.1.2. Local Optimization

For gradient methods, an initial guess is made of the unknown decision vector $\mathbf{z}$, which is used in Equations 5.1, 5.2 and 5.3. For each k^{th} iteration, a search direction, $\mathbf{p}_k$, is determined, which provides a direction along which to change the decision vector $\mathbf{z}$. Additionally, a step length, α_k, is defined, which yields the magnitude of the change to the decision vector (Rao, 2014). The update for the decision vector is given by:

$$\mathbf{z}_{k+1} = \mathbf{z}_k + \alpha_k \mathbf{p_k}. \tag{5.6}$$

For the minimization of the objective function, a search direction is chosen, which decreases the objective function according to:

$$f(\mathbf{z}_{k+1}) \leq f(\mathbf{z}_k) + K\alpha_k \nabla f^{\top}(\mathbf{z}_k)\mathbf{p}_k, \tag{5.7}$$

where K is a parameter between 0 and 1.

5.2. Initial Problem Definition

The problem definition for the optimization of the ascent trajectory has been changed over time to address convergence issues with the optimization algorithms. The reasons for the slow convergence is discussed in this

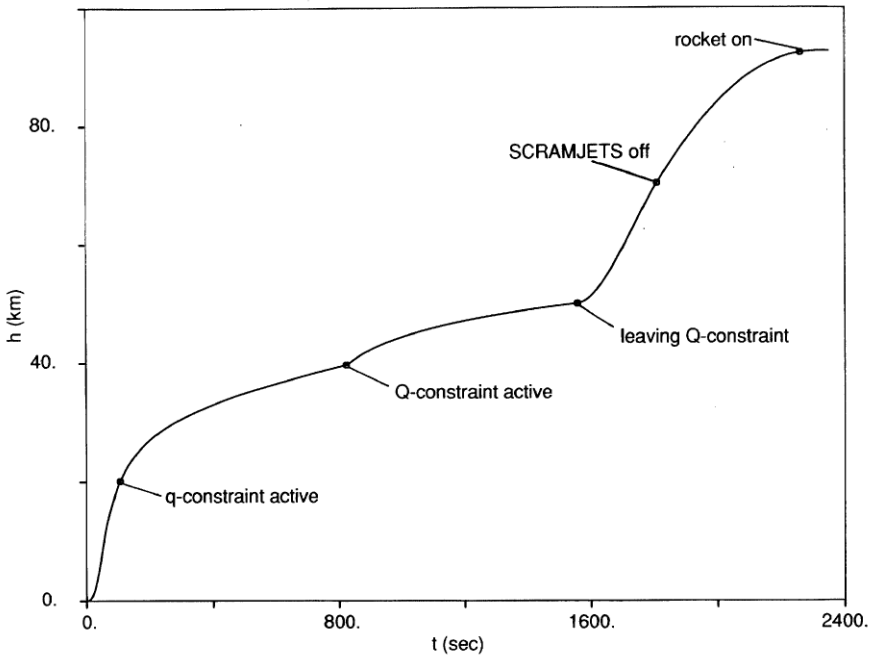

Figure 5.2: Plot showing the altitude as a function of time for the ascent of the NASP (Lu, 1993).

section. First of all, the initial problem definition is explained to give the reader insight and to understand the changes that have been made to improve the convergence.

5.2.1. Transcription

To find the fuel-optimal trajectory of a space plane, it is decided to optimize velocity , V, and flight path angle, γ, trajectory parameters. These can be characterized as the velocity and the direction in the longitudinal plane. It is chosen not to optimize for the position of the space plane to simplify the optimization when a launch window extension is included. Furthermore, to only optimize the longitudinal ascent, the heading angle of the space plane is fixed to 90 degrees, such that the space plane is launched due east.

In order to convert the optimal control problem, a specific number of nodes are used at which the velocity and flight path angle are defined. These nodes can be defined in time as is the case in the ascent trajectory optimization paper by Pescetelli et al. (2012). Another solution is to define the nodes with altitude. In this case, the velocity of the space plane and its direction will only dependent on the altitude of the space plane. Since constraints such as the heat flux and dynamic pressure are dependent on altitude, it is chosen to transcribe the optimal control problem in terms of nodes defined at specific altitudes.

By investigating previous articles about the ascent of the National Aero-Space Plane (NASP), it became apparent that the NASP would go through three different stages during the ascent. The first phase would be the initial ascent and acceleration phase, followed by the pull up phase, where the angle of attack would be increased to increase the flight path angle. The ascent would be concluded by the coasting phase, where the engines would be turned off (Mooij, 1998; Lu, 1993; Powell et al., 1991). From these articles it is not entirely certain at which altitudes these phases transition. This means that the pull up altitude and engine cut off altitude should be included in the optimization as optimization parameters. An indication of the pull up altitude and engine cut off altitude can be obtained by observing the altitude plot of the ascent trajectory in Figure 5.2 by Lu (1993). Based on these indications the nodes can be defined, taking into account that the pull up and Main Engine Cut-Off (MECO) altitude are uncertain. The resulting nodes and the search space for the velocity and flight path angle are shown in Table 5.1.

5.2.2. Objective Formulation

The objectives to be optimized are defined as the fuel used throughout the ascent to reach the target orbit and the reached orbit compared to the target orbit. For the initial longitudinal ascent, only the semi-major axis

Table 5.1: Overview of the number of nodes and at which altitude these are defined.

Node #	Altitude [km]	Velocity [m/s]	Flight Path Angle [deg]
1	0	[170, 8000]	[0, 90]
2	10	[170, 8000]	[0, 90]
3	20	[170, 8000]	[0, 90]
4	30	[170, 8000]	[0, 90]
5	40	[170, 8000]	[0, 90]
6	[40, 60]	[170, 8000]	[0, 90]
7	60	[170, 8000]	[0, 90]
8	[60, 80]	[170, 8000]	[0, 90]
9	80	[170, 8000]	[0, 90]
10	100	[170, 8000]	[0, 90]
11	120	[170, 8000]	[0, 90]

and the eccentricity of the final orbit are used as a target. The inclination and RAAN cannot be influenced with longitudinal maneuvers and are therefore not considered.

The fuel objective is defined by the amount of fuel used at the moment that the propagation of the ascent trajectory is terminated. This is found by comparing the initial mass of the space plane with the termination mass. Subsequently, the fuel objective is normalized to ensure that the range of the fuel objective is between zero and one. The equation that obtains the fuel objective is formulated as:

$$f_1 = f_{\text{normalized fuel used}} = \frac{m_{\text{MTOW}} - m_{\text{termination}}}{m_{\text{MTOW}} - m_{\text{OEW}}}, \tag{5.8}$$

where m_{MTOW} is the Maximum TakeOff Weight (MTOW) and m_{OEW} is the Operating Empty Weight (OEW), and m_{final} is the termination mass.

During initial investigations of the behavior of the target orbit objective, the semi-major axis and the eccentricity were compared between the final and target orbit. It became apparent that a situation occurred where the semi-major axis was reached below the target altitude, with only minimal difference in the eccentricity of the orbit. In this scenario, the optimization would tend to converge to this solution, discarding any individuals that would reach a higher altitude, due to a higher fuel demand. This meant that the optimization would get 'stuck' at this altitude and would not find a suitable solution where the final orbit would have an altitude of 120 km. In order to eliminate this issue, it was decided that the semi-major axis would be replaced by the altitude, and the velocity would be included to reward solutions that reached both a high altitude as well as velocities close to the target circular orbital velocity. It was theorized that this would enable the optimization to converge faster to solution that would reach the target altitude, while also accelerating towards the correct target velocity.

The target orbit objective was defined as the Root Mean Square (RMS) of the altitude, velocity and eccentricity:

$$f_2 = f_{\text{target orbit}} = \sqrt{\frac{f^2_{\text{normalized altitude}} + f^2_{\text{normalized velocity}} + f^2_{\text{eccentricity}}}{3}}, \tag{5.9}$$

where the eccentricity was taken as is, since it ranges between zero and one. The altitude and velocity were normalized with:

$$f_{\text{normalized altitude}} = \frac{h_{\text{target}} - h_{\text{termination}}}{h_{\text{target}} - h_{\text{initial}}}, \tag{5.10}$$

$$f_{\text{normalized velocity}} = \frac{V_{\text{target}} - V_{\text{termination}}}{V_{\text{target}} - V_{\text{initial}}}. \tag{5.11}$$

5.2.3. Constraint Formulation

In previous studies of the ascent of a space plane, a number of inequality constraints have been formulated that the space plane should comply to. In the research done by Lu (1993), the dynamic pressure and heat flux have been formulated as constraints. In the study done by Mooij (1998), the axial acceleration of the space plane is limited in addition to the two aforementioned inequality constraints. For this study, the constraints

Table 5.2: Inequality constraints defined for the space plane.

Inequality constraint	Symbol	Value	Unit
Maximum Dynamic Pressure	$\bar{q}_c$	95,000	[N/m^2]
Maximum Heat Flux	$\dot{Q}_c$	8,000	[kW/m^2]
Maximum Axial Acceleration	n_{a_c}	1	[g$_0$]

Table 5.3: Equality constraints defined for the space plane.

Equality constraint	Symbol	Termination Condition	Unit
Altitude	h_{min}	< 0	[km]
	h_{max}	> 120	[km]
Space Plane Mass	m	$< m_{\text{OEW}}$ $(58.968e3)$	[kg]
Time	T	$> t_0 + 4000$	[s]
Angle of Attack	α_{min}	< -2	[deg]
	α_{max}	> 13	[deg]
Dynamic Pressure	$\bar{q}_{2c}$	$> 190,000$	[N/m^2]
Heat Flux	$\dot{Q}_{2c}$	$> 16,000$	[kW/m^2]
Axial Acceleration	n_{2c}	> 2	[g$_0$]

formulated by Mooij (1998) will be followed, such that the results found in this study can be verified by the results obtained by Mooij (1998). The inequality constraints are summarized in Table 5.2.

The space plane has to adhere to a number of equality constraints in addition to the inequality constraints. Whenever equality constraints are exceeded, the propagation of the space plane is terminated and the objective functions are evaluated. The first equality constraint is the altitude, where the altitude should not be lower than 0 km and higher than 120 km. The second equality constraint is based on angle of attack of the space plane. The NASP has information about the aerodynamic coefficients between -1 and 12 degrees. The guidance module will command the space plane to an angle of attack that is within this bound. The control module will orient the space plane to adhere to the given commands by the guidance module. However, it might occur that a small overshoot occurs. For this reason, it is allowed for the space plane to achieve an angle of attack below 13 degrees or above -2 degrees. During the simulation a small overshoot is allowed, where it is assumed that extrapolation of the aerodynamic coefficients still yield accurate aerodynamic coefficients. However, whenever the angle of attack goes above 13 degrees and below -2 degrees the simulation is terminated. Besides the angle of attack and altitude, also the simulation time is used as an equality constraint. During the initial investigation of the behavior of the objective functions, it became apparent that the fuel and target orbit objective functions were achieved at the cost of the inequality constraints. Sometimes these values were exceed by a factor of 10 or more. This was obviously not intended behavior, and exceeding these constraints by that much was not desirable. It was therefore chosen to also include the dynamic pressure, heat flux and axial acceleration constraint as equality constraints. Whenever one of these was exceeded by twice the amount, the simulation would also be terminated. The equality constraints are summarized in Table 5.3, where the dynamic pressure, heat flux and axial acceleration equality constraints are denoted by $\bar{q}_{2c}$, $\dot{Q}_{2c}$ and n_{2c}, respectively.

For global optimization methods included in PaGMO, only unconstrained optimization is possible. This means that the inequality constraints are bundled and defined as the RMS of the maximum dynamic pressure, heat flux and axial acceleration during the ascent:

$$f_3 = f_{\text{ineq. constr.}} = \sqrt{\frac{f^2_{\text{norm. max dyn. press.}} + f^2_{\text{norm. max. heat flux}} + f^2_{\text{norm. max. axial acc.}}}{3}}, \tag{5.12}$$

where the normalized inequality constraints are expressed by:

$$f_{\text{norm. max dyn. press.}} = \begin{cases} 0 & \text{if } \bar{q}_{\max} < \bar{q}_c, \\ \frac{\bar{q}_{\max} - \bar{q}_c}{\bar{q}_{2c} - \bar{q}_c} & \text{else,} \end{cases} \tag{5.13a}$$

$$f_{\text{norm. max. heat flux}} = \begin{cases} 0 & \text{if } \dot{Q}_{\max} < \dot{Q}_c, \\ \frac{\dot{Q}_{\max} - \dot{Q}_c}{\dot{Q}_{2c} - \dot{Q}_c} & \text{else,} \end{cases} \tag{5.13b}$$

Table 5.4: Overview of the initial translational state of the space plane, defined in spherical elements.

Spherical Element	Value	Unit
Distance	R_E	[km]
Longitude	23.433	[deg]
Latitude	0.0	[deg]
Velocity	170.0	[deg]
Flight Path Angle	5.0	[m/s]
Heading Angle	90.0	[deg]

Table 5.5: Overview of the elements required to define the initial rotational state of the space plane.

Element	Value	Unit
Angle of Attack	5.0	[deg]
Angle of Sideslip	0.0	[deg]
Bank Angle	0.0	[deg]
ω_{x_I}	0.0	[deg/s]
ω_{y_I}	0.0	[deg/s]
ω_{z_I}	$4.18e-3$	[deg/s]

$$f_{\text{norm. max. axial acc.}} = \begin{cases} 0 & \text{if } n_{a_{\max}} < n_{a_c}, \\ \frac{n_{a_{\max}} - n_{a_c}}{n_{a_{2c}} - n_{a_c}} & \text{else.} \end{cases} \tag{5.13c}$$

The last set of constraints is related to the initial state. The initial state defines both the rotational and translational state of the space plane. The translational state is defined in spherical elements, which allows for better interpretation of the initial state. The initial position of the space plane is chosen to be on the equator, with a random longitude and an altitude of 0 km above the Earth surface. The initial velocity of the space plane is roughly based on the study done by Mooij (1998). However, the emphasis of the velocity is to ensure that the space plane generates a lift force that enables the space plane to maintain a positive flight path angle. The heading angle of the space plane, which defines the direction of the velocity on the local horizontal plane, is chosen to be 90 degrees. This corresponds with a launch due east. Table 5.4 gives an overview of the initial translational state. The position of the space plane is defined in the rotational frame, where the distance is considered the mean Earth radius, R_E. The velocity is defined in the vertical reference frame. The position and velocity are converted to Cartesian coordinates, and transformed to the inertial reference frame, with the basic transformation discussed in Section 3.1.

The rotational state, is defined partly by the spherical elements, and completed by defining the aerodynamic angles of the space plane. With the aerodynamic angles, the angles used for the translational state, the angular velocity of the Earth about the z_I-axis and the time since the R- and I-frame have coincided, a transformation matrix can be constructed that defines the attitude of the space plane with respect to the I-frame. The transformation matrix is used by TU Delft Astrodynamics Toolbox (TUDAT) to convert the orientation of the space plane to quaternions. The angular velocity of the space plane is assumed to be zero when considering the angular velocity of the space plane with respect to the rotating planetocentric reference frame. When considering the angular velocity with respect to the inertial reference frame, only the rotation of the Earth has to be considered. Equation 3.25, shows how the rotation of the Earth is converted to describe the angular velocity of the space plane with respect to the I-frame, expressed in components along the body axes. Table 5.5 shows the initial aerodynamic angles and angular velocity of the Earth.

5.2.4. Results

The search space shown in Table 5.1, reveals that the search space for the velocity and flight path angle is large. Prior to starting to optimize the ascent trajectory, it was attempted to reduce the search space. Using Sobol sequences, a large number of decision variable vectors were generated, which were used to identify any correlations between particular decision variables and the capability of the space plane to reach an altitude of 120 km. In Figure 5.3 it can be seen that a correlation was found between the velocity of the first node and the capability of reaching target altitude. By reducing the search space for the velocity at the first node and rerunning the sobol analysis, a correlation could also be found at the second node, see Figure 5.4. In a similar

Table 5.6: Overview of the number of nodes and at which altitude these are defined.

Node #	Altitude [km]	Velocity [m/s]	Flight Path Angle [deg]
1	0	[170, 360]	[0, 90]
2	10	[170, 1000]	[0, 90]
3	20	[800, 2500]	[0, 90]
4	30	[170, 8000]	[0, 90]
5	40	[170, 8000]	[0, 90]
6	[40, 60]	[170, 8000]	[0, 90]
7	60	[170, 8000]	[0, 90]
8	[60, 80]	[170, 8000]	[0, 90]
9	80	[170, 8000]	[0, 90]
10	100	[170, 8000]	[0, 90]
11	120	[170, 8000]	[0, 90]

fashion, a correlation was found at the third node, see Figure 5.5. Besides velocity at the first three nodes, no further correlation was found between the decision variables and the capabilities to reach the target altitude. This can be explained by the lack of individuals reaching the final altitude. It could be that many individuals already terminated before the space plane reached the 30 km mark. Due to the analysis, the search space was reduced, which are summarized in Table 5.6.

Based on the reduced search space, an initial optimization was done to assess the capabilities to converge to a solution. It was found that the optimization had difficulties to converge and penalties were imposed on the objective functions. The penalty to the objectives functions were imposed if the inequality constraints reached twice their value, whenever the altitude became lower than the Earth surface, and if the angle of attack reached a value outside of the allowed range. In these cases, the objective functions were set to one:

$$f_1 = f_2 = f_3 = 1.0. \tag{5.14}$$

The optimization of the NLP problem has been done with both NSGA2 and MOEA/D, two optimization algorithms included in PaGMO. Both of these algorithms are multi-objective unconstrained optimization algorithms. The optimization toolpackage PaGMO allows for changes to the algorithm such as the mutation rate or crossover. However, it was chosen to use the default values for the algorithms. Additionally, it was chosen to use 300 individuals per generation, to evolve these generations 250 times, and to use three different seeds $(100, 200, 300)$. The results of the optimization can be seen in Figure 5.6 and Figure 5.7.

The figures reveal that both algorithms had difficulty converging to solutions that would reach a target orbit objective close to zero, with a propellant objective lower than one. It was therefore chosen to investigate if a reduced search space would support a faster convergence. It was chosen to reduce the search space for the flight path angle to a maximum of 45 degrees, which is still far above the largest value the flight path angle obtained in results by Mooij (1998). With the reduced search space, convergence was possible for the MOEA/D algorithm, as can be seen in Figure 5.8. However, the NSGA2 algorithm was still not able to converge, see Figure 5.9.

The results obtained by the MOEA/D algorithm, shows that the orbital element objective can be reduced to zero. Furthermore, it can be seen that the propellant objective and the constraint objective are conflicting, which means that a trade-off should be made between using more fuel, or allowing the space plane to exceed a number of constraints. However, Figure 5.8 also shows that currently no individual exists that has a propellant objective lower than one, without also exceeding at least one inequality constraint. Figure 5.10 shows the dynamic pressure and heat flux history for a single simulation that has a propellant objective close to one. Here it can be seen that both the heat flux and the dynamic pressure constraint have been exceeded for an extended period of time.

The ascent trajectory can be further inspected to find another interesting phenomena. The optimization finds a solution for the space plane with an initial pull up followed by a shallow ascent, where the velocity of the space plane is increased to a magnitude close to that of the orbital velocity, see Figure 5.11. After about 1200 seconds, when the velocity of the space plane is increased, the space plane initiates the final pull up to reach the target orbit. At this point, it can be seen that the commanded velocity and flight path angle are not followed by the space plane anymore. Inspecting the aerodynamic angle time history, in Figure 5.12, yields insight into the behavior of the space plane to increase the flight path angle. It shows that the angle of attack

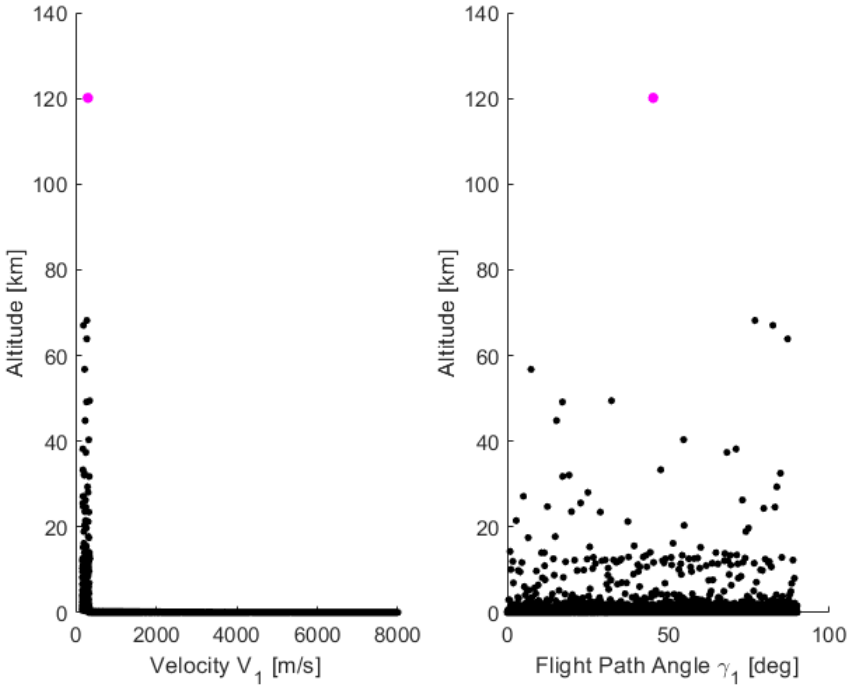

Figure 5.3: Results Sobol analysis decision variables at node 1.

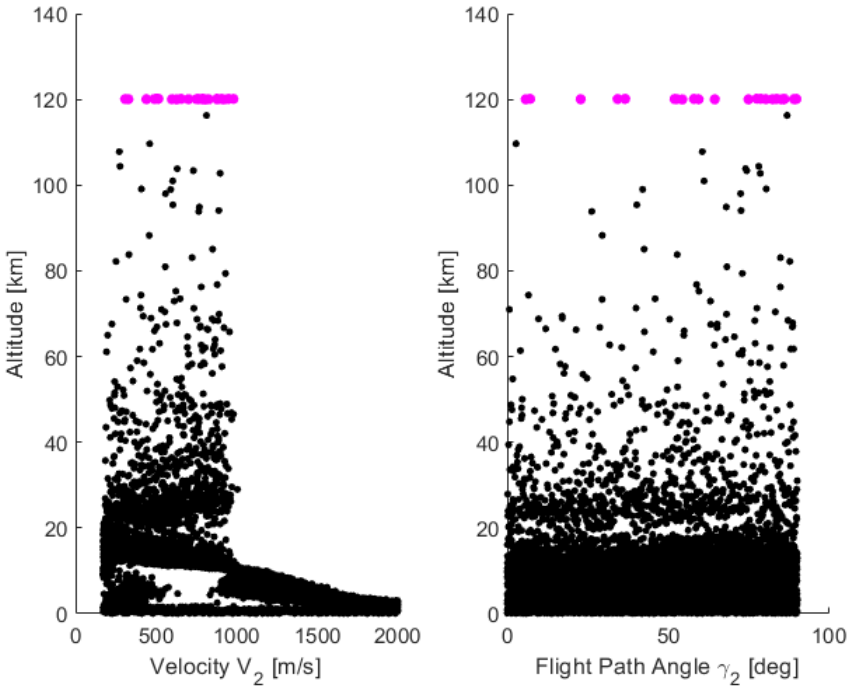

Figure 5.4: Results Sobol analysis decision variables at node 2.

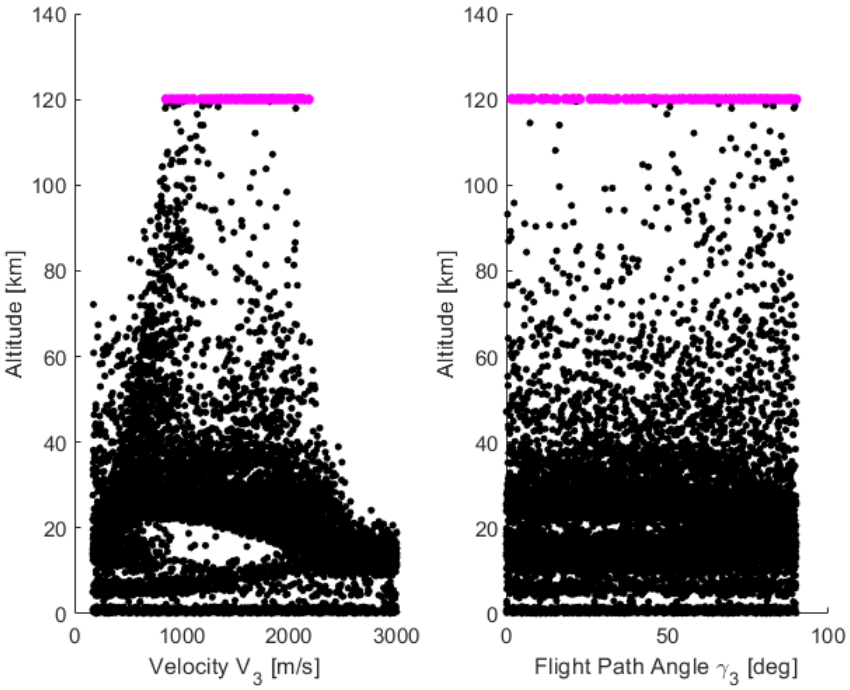

Figure 5.5: Results Sobol analysis decision variables at node 3.

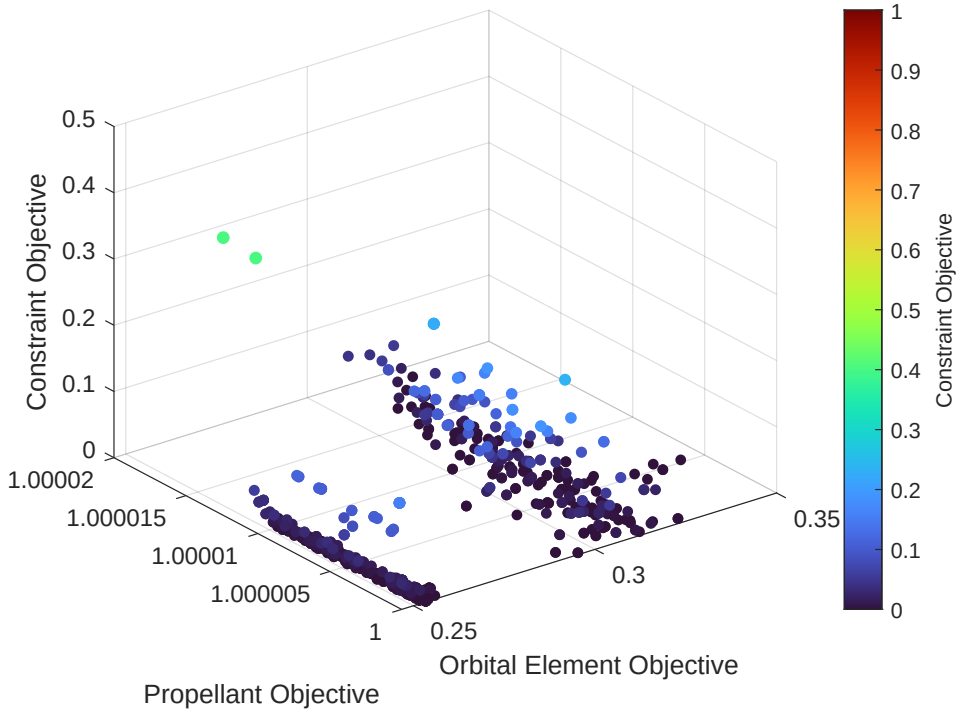

Figure 5.6: Optimization results for the ascent trajectory using MOEA/D.

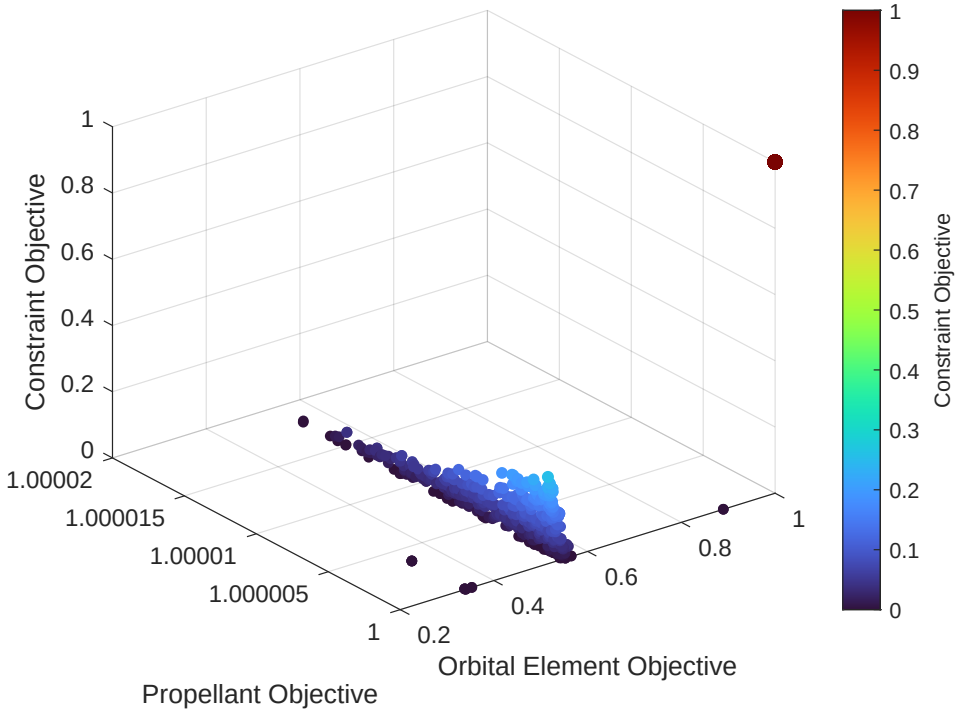

Figure 5.7: Optimization results for the ascent trajectory using NSGA2.

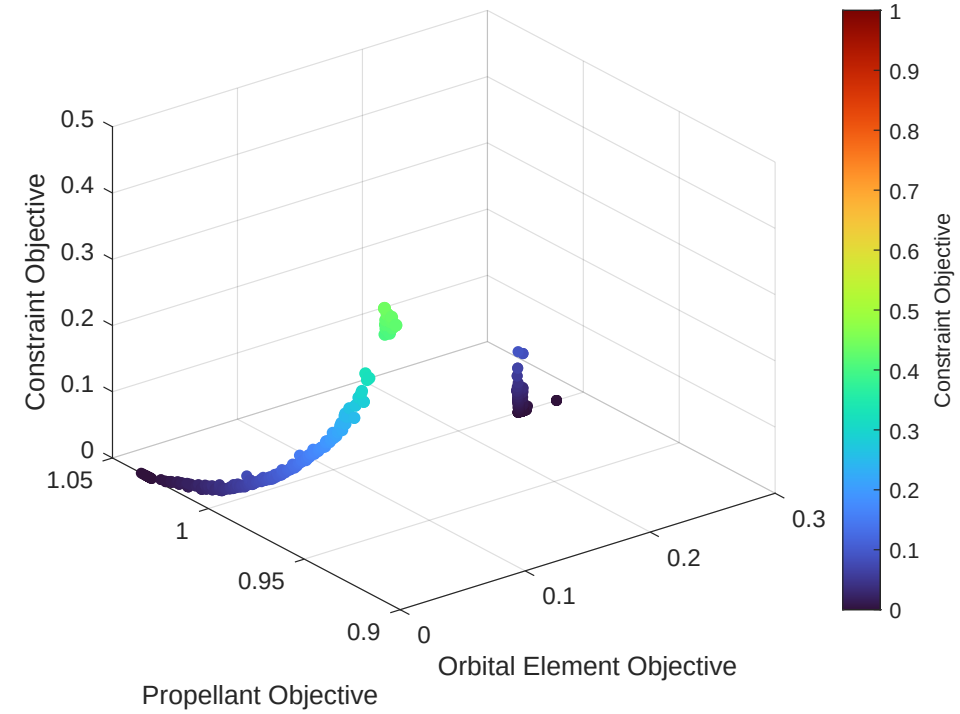

Figure 5.8: Optimization results for the ascent trajectory using MOEA/D with a smaller search space.

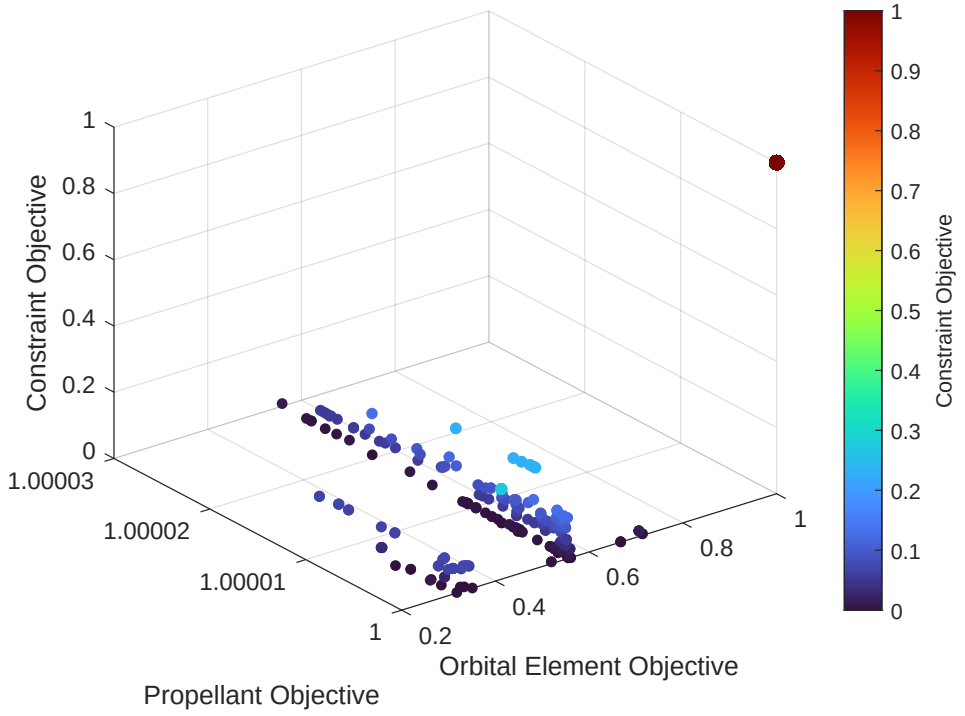

Figure 5.9: Optimization results for the ascent trajectory using NSGA2 with a smaller search space.

is increased to the maximum value, before dropping to the lowest allowed value in order to reduce the flight path angle again. This behavior is undesirable, since the space plane at this velocity is unstable for a large angle of attack (Powell et al., 1991). It is, therefore, necessary to have finer control over the angle of attack when the final pull up occurs.

The results of the optimization algorithm gives insight in the behavior of the space plane and allows for changes to the transcription in order to ensure that faster convergence of the optimization algorithm is achieved. First of all, the guidance module, that controls the flight path angle and velocity, has dificulties controlling these parameters to the commanded value when the pull up altitude is reached. Furthermore, the control module, tied to the guidance module reacts heavily on changes in the commanded flight path angle, which could make the space plane unstable. Besides the performance of the Guidance and Control (G&C) module, it can also be included that the transcription of the velocity is not refined enough to ensure that the dynamic pressure and heat flux constraint are not exceeded. Lastly, the optimization algorithms converge slowly to the optimal solution, which can contributed to the large search space and large number of optimization parameters. Even though both algorithms converge slowly, it can be seen in Figures 5.8 and 5.9 that the MOEA/D algorithm has faster convergence compared to the NSGA2 algorithm.

First of all, the guidance module, that controls the flight path angle, is stopped whenever the pull up altitude is reached. From that point on, not the flight path angle of the space plane, but the angle of attack is controlled. Allowing finer control of the orientation of the space plane, such that the space plane does not become unstable. Furthermore, the constraint values are easily exceeded and inhibit the ability of the optimization algorithm to converge. This is solved by removing the velocity of the space plane as an optimization parameter. Instead, the space plane is allowed to accelerate with maximum throttle, only reduced whenever the maximum dynamic pressure, heat flux or axial acceleration would be crossed. This reduces the search space significantly by removing the velocity itself as an optimization parameter. It is replaced only by the maximum equivalence ratio that the space plane is allowed to use.

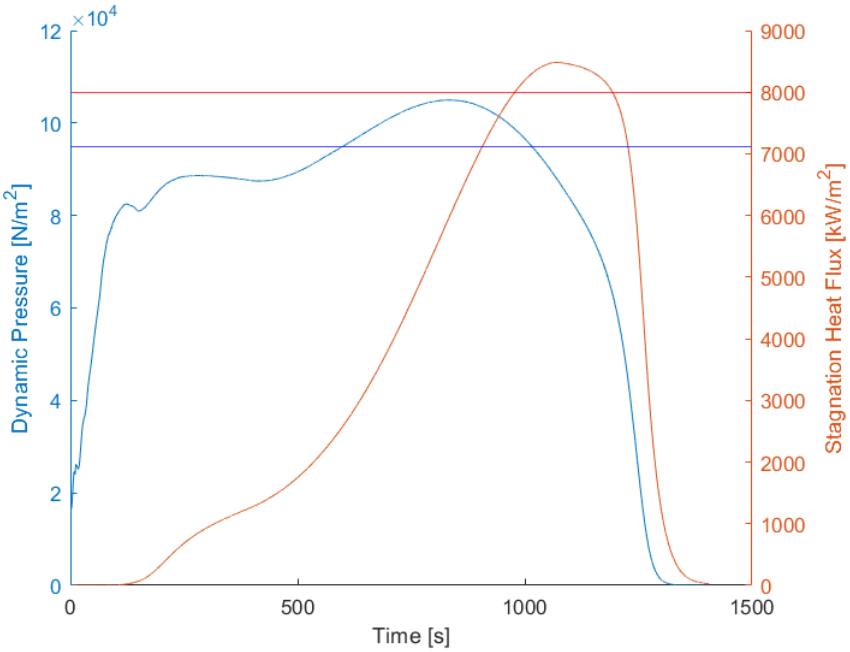

Figure 5.10: Time history of the dynamic pressure and heat flux constraint that the space plane has experienced during the ascent.

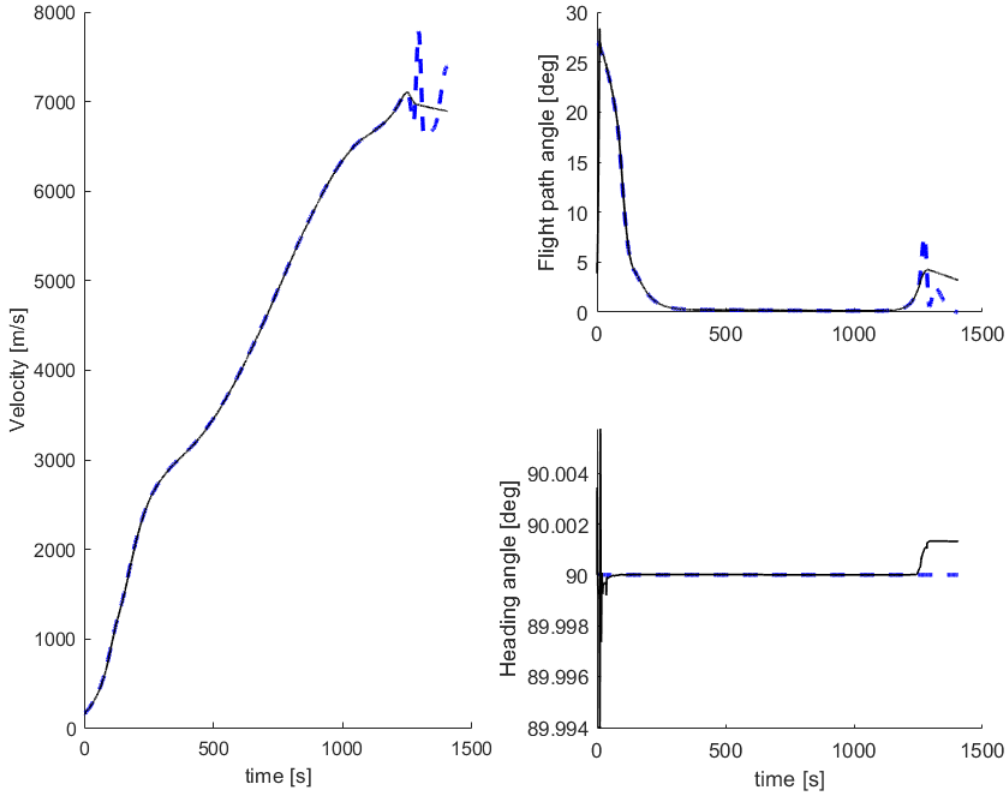

Figure 5.11: Time history of the trajectory parameters. The blue dashed lines indicate the reference, while the black continuous lines indicate the actual value obtained during the ascent.

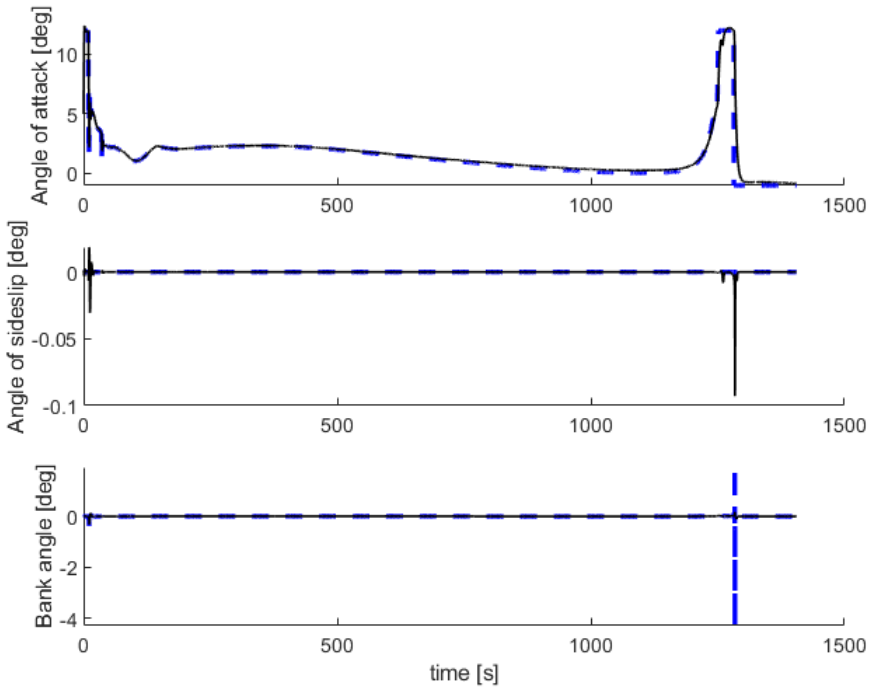

Figure 5.12: Time history of the aerodynamic angles. The blue dashed lines indicate the reference, while the black continuous lines indicate the actual value obtained during the ascent.

5.3. Final Problem Definition

The results from the initial problem definition have yielded results, which prompted changes to the method that the optimal control problem was transcribed. First of all, the velocity parameter is removed from the optimization to reduce the search space. Instead, active constraint control is added to the G&C system to ensure that the space plane does not exceed inequality constraints. Second of all, the space plane shall be commanded by the flight path angle until the pull up altitude is reached. Afterwards, the flight path angle of the space plane is no longer controlled directly, and instead the orientation of the space plane is controlled. The angle of attack is used as an optimization parameter to determine the most efficient way to initiate the pull up to reach the target orbit.

5.3.1. Transcription for the Ascent Excluding Lateral Motion

The optimal control problem is converted in an NLP problem by once again defining a number of points in terms of altitude at which either the flight path angle or the angle of attack of the space plane is defined. In Figure 5.13 it can be seen along which parts of the trajectory the angle of attack or the flight path angle is controlled. The angle of attack is only optimized until the moment that the coasting phase starts. During coast, the angle of attack is commanded to zero to reduce the amount of drag. The change in angle of attack is accomplished by Reaction Control System (RCS) thrusters, which are not actually modeled. To ensure that the space plane does not becomes unstable just before the RCS thrusters take over, the maximum angle of attack during the pull up phase is limited to 4 degrees. Further explanation into this phenomenon can be found in Section 6.3. Additionally, the minimum angle of attack during the pull up phase is set to 1 degree to ensure that flight path angle increases at the pull up altitude. It was found that the angle of attack just before the pull up altitude was lower than 1 degree. Thus, setting the minimum angle of attack to 1 degree will ensure the increase in flight path angle.

The velocity of the space plane is controlled by the maximum equivalence ratio that is allowed in combination with the guidance module that ensures that the constraints for the dynamic pressure, heat flux and axial acceleration are not exceeded. The maximum equivalence ratio is an optimization parameter, but the velocity itself is removed from the optimization. The altitude at which the pull up phase and coasting phase starts are still included in the optimization process. The parameters that need to be optimized are summarized in

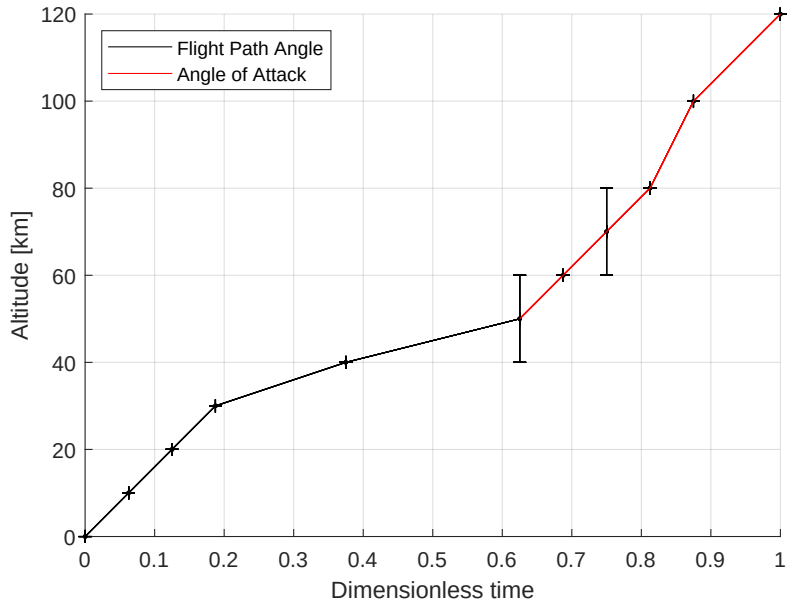

Figure 5.13: Showcase of the transcription that is performed to convert the optimal control problem into an NLP problem.

Table 5.7: Overview of the optimization parameters and their search space for the longitudinal ascent.

Optimization Parameter	# of Parameters	Search Space	Unit
Flight Path Angle	6	[0, 90]	[deg]
Angle of Attack	3	[1, 4]	[deg]
Pull Up Altitude	1	[40, 60]	[km]
Engine Cut-Off Altitude	1	[60, 80]	[km]
Maximum Equivalence Ratio	1	[0, 10]	[-]

Table 5.7. Lastly, it should be noted that the heading angle is not included in the longitudinal optimization and the bank angle is commanded to remain zero throughout the flight. Instead, an initial launch heading angle is computed based on the target orbital inclination. The initial heading angle in combination with the commanded bank angle and angle of sideslip, which are commanded to be zero, will results in a final orbit that will be close to the target orbital inclination. The initial heading angle is computed, if the rotation of the Earth is not considered, with:

$$\chi_{\text{inertial}} = \sin^{-1}\left(\frac{\sin i_{\text{target}}}{\cos \delta_{\text{launch}}}\right), \tag{5.15}$$

where i_{target} is the target orbit inclination, δ_{launch} is the launch latitude and χ_{inertial} is the launch heading angle if the rotation of the Earth is zero. Since the Earth is rotating, the heading angle with respect to the ground can be computed if the velocity of the surface of the Earth is known with respect to the inertial frame. With this velocity the heading angle can be expressed in the rotational frame, if the target orbit is circular, with:

$$\chi_{\text{rotational}} = \tan^{-1}\left(\frac{V_x}{V_y}\right) = \tan^{-1}\left(\frac{V_{\text{circ}} \sin \chi_{\text{inertial}} - V_E \cos \delta_{\text{launch}}}{V_{\text{circ}} \cos \chi_{\text{inertial}}}\right), \tag{5.16}$$

where V_{circ} is the target orbital circular velocity and V_E is the velocity of the Earth surface at the equator due to the rotation of the Earth. With this method, the launch heading angle can be computed, with which the space plane can launch into the target orbit.

5.3.2. Objective Formulation for the Ascent Excluding Lateral Motion

The switch to active constraints control means that the number of objectives is reduced to two. The two remaining objectives are the propellant used during the ascent and the RMS of the difference in altitude,

Table 5.8: Overview of the target altitude, velocity and eccentricity that define the target orbit.

Target Orbit	Altitude [km]	Velocity [m/s]	Eccentricity [-]
Value	120.0	7836.3	0.0

velocity and eccentricity that the space plane achieved compared to the target orbit. These objectives have not changed, but are repeated for the readers sake.

$$f_1 = f_{\text{normalized fuel used}} = \frac{m_{\text{MTOW}} - m_{\text{termination}}}{m_{\text{MTOW}} - m_{\text{OEW}}}, \tag{5.17}$$

$$f_2 = f_{\text{target orbit}} = \sqrt{\frac{f^2_{\text{normalized altitude}} + f^2_{\text{normalized velocity}} + f^2_{\text{eccentricity}}}{3}}, \tag{5.18}$$

with:

$$f_{\text{normalized altitude}} = \frac{h_{\text{target}} - h_{\text{termination}}}{h_{\text{target}} - h_{\text{initial}}}, \tag{5.19}$$

$$f_{\text{normalized velocity}} = \frac{V_{\text{target}} - V_{\text{termination}}}{V_{\text{target}} - V_{\text{initial}}}. \tag{5.20}$$

The target orbit is chosen to be a circular orbit at an altitude of 120 km above the Earth surface, assuming a spherical Earth. The target altitude, velocity and eccentricity are shown in Table 5.8. The target velocity is computed with:

$$V_{\text{target}} = V_{\text{circular}} = \sqrt{\frac{\mu_E}{(R_E + h_{\text{target}})}}, \tag{5.21}$$

where μ_E is the gravitational parameter of the Earth and R_E is the mean Earth radius.

In the study done by Mooij (1998), a similar target orbit was used. In that study a circularization maneuver was implemented when the target altitude was reached, with a velocity lower than the velocity for a circular orbit. In this research, a similar maneuver is implemented for when the target altitude is reached. The ΔV required to obtain the circular velocity is computed by comparing the velocity of the space plane in the inertial frame, with the circular velocity required to have a circular orbit at 120 km altitude. Assuming a typical rocket engine with a specific impulse of 465 s, the required propellant for the maneuver is computed with:

$$m_{\text{final}} = \frac{1}{\exp\left(\frac{\Delta V_{\text{req}}}{I_{sp} g_0}\right)} m_{\text{termination}}, \tag{5.22}$$

where m_{final} is the mass after the circularization maneuver, $m_{\text{termination}}$ is the mass just before the circularization maneuver, ΔV_{req} is the required ΔV to circularize, I_{sp} is the specific impulse, and g_0 is the standard gravity. If the circularization maneuver requires more propellant than is available, the maximum possible ΔV is computed and added to target orbit objective with:

$$\Delta V = I_{\text{sp}} g_0 \ln\left(\frac{m_{\text{termination}}}{m_{\text{EOW}}}\right). \tag{5.23}$$

The circularization maneuver requires to update the final mass of the space plane, as well as the final velocity and Kepler elements. These are then used in the objective functions to evaluate the simulation.

5.3.3. Transcription for the Ascent Including Lateral Motion

The optimization that includes lateral motion is done to investigate the possibility to manipulate the RAAN to allow for a larger launch window. In order to manipulate either the RAAN or inclination, a change in heading angle is required. During the ascent optimization that excludes lateral motion, either the space plane has flown due east, as was done for the initial problem definition, or the launch heading angle was determined based on the target orbit. Fortunately, Equation 5.16 can be used for more then to compute to launch heading angle. The heading angle of any object in an orbit around the Earth can be computed using the aforementioned equations, if the object resides in the northern hemisphere and the change in latitude is positive. The equations becomes:

$$\chi_{\text{inertial}} = \sin^{-1}\left(\frac{\sin i_{\text{target}}}{\cos \delta}\right), \tag{5.24}$$

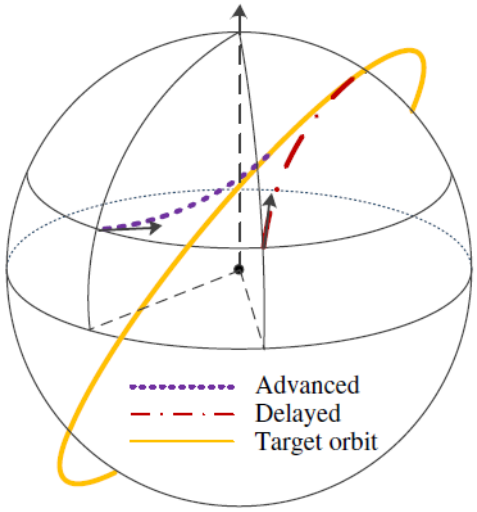

Figure 5.14: A general example of an advanced and delayed orbit insertion (Zhou, Wang, and Cui, 2020).

$$\chi_{\text{rotational}} = \tan^{-1}\left(\frac{V_x}{V_y}\right) = \tan^{-1}\left(\frac{V_{\text{circ}}\sin\chi_{\text{inertial}} - V_E\cos\delta}{V_{\text{circ}}\cos\chi_{\text{inertial}}}\right). \tag{5.25}$$

Since the space plane is launching from the equator and launches with a heading angle between the 0 and 90 degrees, these equations can be used to compute a commanded heading angle until the latitude derivative becomes zero or negative. During an initial investigation, it became apparent that for the entire duration that the flight path angle of the space plane is commanded, the maximum latitude is not yet reached, and Equation 5.16 can be used to command the space plane to the correct heading angle and subsequent correct inclination. When the pull up is initiated, the flight path angle and heading angle are no longer commanded. Instead, the bank angle and angle of sideslip are commanded to zero, which does not adversely effects the ability of the space plane to reach the correct orbit inclination. Furthermore, the angle of attack is directly commanded as part of the optimization problem.

In a previous study by Zhou, Wang, and Cui (2020), the RAAN was manipulated by commanding the space plane to a deviated inclination angle for part of the ascent. An example of how the ascent trajectory would look like can be seen in Figure 5.14. Here it can be seen that, with a delayed launch, the inclination is initially higher than the target orbit inclination and slowly converges to the target incliniation. In that study, the deviation in orbit inclination was a linear function of range. For this study, it was chosen to not use range, but use altitude instead as to be coherent with the optimization of the flight path angle. Furthermore, the function that computes the deviation in orbit inclination is a sigmoid function:

$$\Delta i = \left(1 - \frac{1}{\left(1 + \frac{(x^r)}{(1+x^r)}\right)^{-b}}\right)\Delta i_0, \tag{5.26}$$

where Δi_0 is the initial deviation in inclination, x is the ratio between the current altitude h_{current} of the space plane and the pull up altitude, $h_{\text{pull up}}$:

$$x = \frac{h_{\text{current}}}{h_{\text{pull up}}}. \tag{5.27}$$

The steepness of the sigmoid function is determined by b, and r is a variable that is used to define the altitude at which the deviation in inclination is exactly half:

$$r = -\frac{\log 2}{\log x_{1/2}}, \tag{5.28}$$

where $x_{1/2}$ is the altitude ratio at which the deviation should be exactly half. Equation 5.26 gives control over the moment when the deviation in inclination should be half, the steepness of the half way point and the

Table 5.9: Overview of the lateral optimization parameters and the search space.

Optimization Parameter	# of Parameters	Search Space	Unit
Δi_0	1	[-45, 45]	[deg]
Steepness, b	1	[2, 5]	[-]
$x_{1/2}$	1	[0.1, 0.9]	[-]

magnitude of the deviation. The deviation in inclination can be included in Equation 5.24 to compute the inertial heading angle:

$$\chi_{\text{inertial}} = \sin^{-1}\left(\frac{\sin(i_{\text{target}} + \Delta i)}{\cos\delta}\right), \tag{5.29}$$

which in turn can be used in Equation 5.25 to compute the heading angle with respect to the ground.

With these expressions, the lateral motion of the space plane is transcribed, such that the heading angle can be computed until the pull up altitude is reached. Afterwards, the flight path angle and heading angle are no longer commanded, and the angle of sideslip and bank angle are commanded to zero. The NLP problem in this scenario includes a control function for the flight path angle and heading angle until the pull up altitude, and a control function for the angle of attack from the pull up altitude to the main engine cut-off altitude. In Table 5.9 the search space is shown for the three optimization parameters that govern the lateral motion.

5.3.4. Objective Formulation for the Ascent Including Lateral Motion

For the optimization that includes a change in launch window, it is necessary to once again minimize the required propellent, while still reaching a correct orbit. This means that the propellant objective is still present. The space plane is capable of manipulating the inclination and RAAN of the target orbit due to the inclusion of the lateral motion. This means that the target orbit objective needs to include a target inclination and RAAN. Thus the target orbit objective is expressed by:

$$f_2 = f_{\text{target orbit}} = \sqrt{\frac{f_h^2 + f_V^2 + f_e^2 + f_i^2 + f_\Omega^2}{5}}, \tag{5.30}$$

with:

$$f_h = f_{\text{normalized altitude}} = \frac{h_{\text{target}} - h_{\text{termination}}}{h_{\text{target}} - h_{\text{initial}}}, \tag{5.31}$$

$$f_V = f_{\text{normalized velocity}} = \frac{V_{\text{target}} - V_{\text{termination}}}{V_{\text{target}} - V_{\text{initial}}}, \tag{5.32}$$

$$f_e = f_{\text{eccentricity}}, \tag{5.33}$$

$$f_i = f_{\text{normalized velocity}} = \frac{i_{\text{target}} - i_{\text{termination}}}{i_{\text{target}}}. \tag{5.34}$$

For the RAAN an if statement is used to normalize it in one of two ways, depending on the value of the RAAN that has been achieved in the final orbit. During the longitudinal ascent optimization it became apparent that the achieved RAAN was approximately 306 degrees, which is taken as the target value for the RAAN. Using the fact that a RAAN of 0 degrees is closer to the target value than 100 degrees, the following distinction is made:

$$f_\Omega = f_{\text{normalized RAAN}} = \begin{cases} \frac{\Omega_{\text{target}} - \Omega_{\text{termination}}}{\pi} & \text{if } \Omega_{\text{termination}} \geq \Omega_{\text{target}} - \pi \\ \frac{\Omega_{\text{target}} - (\Omega_{\text{termination}} + 2\pi)}{\pi} & \text{if } \Omega_{\text{termination}} < \Omega_{\text{target}} - \pi \end{cases}, \tag{5.35}$$

where the RAAN, Ω, is expressed in radians. With the normalized values, the second objective is normalized in such a way that the objective ranges between zero and one.

Since the optimization that excludes lateral motion showed that the space plane achieves a RAAN of 306 degrees, this value is used for the target RAAN. For the inclination, it is chosen to target an inclined orbit of 45 degrees. This value is slightly arbitrary, but should allow the space plane to investigate both delayed and advanced launches. Furthermore, the altitude, velocity and eccentricity are the same as for the optimization that does not include lateral motion. Table 5.10 gives an overview of the target orbit.

Similarly to the longitudinal optimization, a circularization maneuver is performed when the target altitude is reached. The final mass, velocity, and Kepler elements are updated and used in the objective functions to evaluate the fitness of the objectives.

Table 5.10: Overview of the target altitude, velocity, eccentricity, inclination and RAAN that define the target orbit.

Target Orbit	Altitude [km]	Velocity [m/s]	Eccentricity [-]	Inclination [deg]	RAAN [deg]
Value	120.0	7836.3	0.0	45.0	306.0

5.3.5. Constraint Formulation

The constraint formulation is similar for both the ascent that excludes lateral motion or includes lateral motion. The inequality constraints are all based on the velocity or its derivative, which means that the inequality constraints are eliminated by including these in the G&C system. What remains is the equality constraints, which were also defined for the initial problem definition. The equality constraints related to the dynamic pressure, heat flux and axial acceleration are removed. What remains are the minimum and maximum altitude, space plane mass, time and angle of attack. An overview of the equality constraints are shown in Table 5.11.

The initial state is also defined as a constraint, see Table 5.12. The initial translational state is similar to that of the initial problem definition. However, the state differs for the heading angle, since the space plane is not launched due east to ensure that the final orbit reaches an orbital inclination of 45 degrees. The heading angle is computed with Equations 5.15 or 5.29, which depends if lateral motion is included in the optimization problem, and Equation 5.16. Due to these equations, the initial heading angle can vary between 0 and 90 degrees. The initial rotational state of the space plane has not been changed for the final problem definition. For convenience, an overview of the initial rotational state has been given in Table 5.13. The method of conversion from spherical to Cartesian elements, and the conversion of the attitude to quaternions can be found in Section 5.2.3

Table 5.11: Overview of the equality constraints defined for the space plane.

Equality constraint	Symbol	Termination Condition	Unit
Altitude	h_{min}	< 0	[km]
	h_{max}	> 120	[km]
Space Plane Mass	m	$< m_{\text{OEW}}$ $(58.968e3)$	[kg]
Time	T	$> t_0 + 4000$	[s]
Angle of Attack	α_{min}	< -2	[deg]
	α_{max}	> 13	[deg]

Table 5.12: Overview of the initial translational state of the space plane, defined in spherical elements.

Spherical Element	Value	Unit
Distance	R_E	[km]
Longitude	23.433	[deg]
Latitude	0.0	[deg]
Velocity	170.0	[m/s]
Flight Path Angle	5.0	[deg]
Heading Angle	$[0.0, 90.0]$	[deg]

Table 5.13: Overview of the elements required to define the initial rotational state of the space plane.

Element	Value	Unit
Angle of Attack	5.0	[deg]
Angle of Sideslip	0.0	[deg]
Bank Angle	0.0	[deg]
ω_{x_I}	0.0	[deg/s]
ω_{y_I}	0.0	[deg/s]
ω_{z_I}	$4.18e-3$	[deg/s]

6

Guidance and Control

For the ascent trajectory optimization of the space plane, a Guidance and Control (G&C) system is designed that commands the space plane to follow the reference trajectory. The reference trajectory is a control function, $\mathbf{u}(h)$, which follows from the NonLinear Programming (NLP) problem as described in Chapter 5. Typically, a navigation module is used in conjunction with the G&C system to determine the position and orientation of the space plane. For the optimization of the ascent trajectory, a navigation module is not included. Thus, it is assumed that the translational and rotational state of the space plane is known exactly, which reduces the complexity of the G&C system. This means that estimation errors in the position and orientation of the space plane do not influence the performance of the space plane to follow the reference trajectory, which is important for finding the optimal ascent trajectory.

6.1. Control Algorithms

In order to effectively control the space plane, a control algorithm needs to be designed. Conventionally, algorithms to control aircraft and spacecraft linearize the nonlinear Equations of Motion (EoM) and apply gain scheduling to effectively control the vehicle throughout its flight envelope (Zhang and Jiang, 2008). Alternatively, a nonlinear control algorithm can be used, which removes the necessity to linearize the EoM and the gain scheduling (Lu, 2016).

The nonlinear control algorithms used by the G&C system are based on a combination of Non-linear Dynamic Inversion (NDI) and Incremental Non-linear Dynamic Inversion (INDI) controllers to determine the required change in thrust throttle, thrust elevation angle, and control surface deflection of the elevons and rudder. The NDI controller follows an onboard dynamics model to achieve the commanded dynamics. However, the onboard model does not take into account model uncertainties, which will compromise the controller's ability to correctly control the vehicle (Mooij, 2019a). Whenever uncertainties exist in the dynamics an INDI controller is used, which reduces the dependency of the onboard dynamics model (Sieberling, Chu, and J. A. Mulder, 2010).

6.1.1. Non-linear Dynamic Inversion Theory

Non-linear Dynamic Inversion (NDI) is a technique that uses the EoM of the system to formulate a control law. Consider the following general expression for the EoM:

$$\dot{\mathbf{x}} = \mathbf{f}(\mathbf{x}) + \mathbf{G}(\mathbf{x})\mathbf{u}, \tag{6.1}$$

where $\mathbf{f}(\mathbf{x})$ is part of the EoM that are not influenced by the actuators. In contrast, $\mathbf{G}(\mathbf{x})$, is the part of the EoM that is influenced by the actuators. The actuators itself are expressed by the vector $\mathbf{u}$. The expression can be inverted to obtain an expression for the actuators that are a function of the state derivative, $\dot{\mathbf{x}}$:

$$\mathbf{u} = \mathbf{G}^{-1}(\mathbf{x})(\dot{\mathbf{x}} - \mathbf{f}(\mathbf{x})). \tag{6.2}$$

Additionally, the state derivative can be replaced by a virtual control vector, which represents the difference between the actual and reference value multiplied by a proportional gain:

$$\dot{\mathbf{x}} = \boldsymbol{\nu} = \mathbf{K}_p\mathbf{e} = \mathbf{K}_p(\mathbf{x}^{\text{ref}} - \mathbf{x}). \tag{6.3}$$

The NDI method can be applied when the dynamics of the systems are known and when matrix $\mathbf{G}(\mathbf{x})$ is invertible. Furtermore, the method can be extended to incorporate the measured state, $\mathbf{y}$, instead of the actual state, $\mathbf{x}$. However, it suffices to use the actual state for the optimization of the ascent trajectory.

6.1.2. Incremental Non-linear Dynamic Inversion Theory

Equation 6.2 clearly shows the reliance of the NDI algorithm on the dynamics of the system. When the dynamics are uncertain, the Incremental Non-linear Dynamic Inversion (INDI) method can be applied. The method uses a Taylor series expansion to obtain an incremental form of the EoM:

$$\dot{\mathbf{x}} = \dot{\mathbf{x}}_0 + \frac{\partial}{\partial \mathbf{x}}[\mathbf{f}(\mathbf{x})]\Delta\mathbf{x} + \frac{\partial}{\partial \mathbf{u}}[\mathbf{G}(\mathbf{x})]\Delta\mathbf{u}, \tag{6.4}$$

where $\dot{\mathbf{x}}_0$ represents the state derivative, $\mathbf{x}_0$ the state and $\mathbf{u}_0$ the control vector, an incremental instance in time before $\dot{\mathbf{x}}$, $\mathbf{x}$ and $\mathbf{u}$. Additionally, the second term on the right hand side of Equation 6.4 can be neglected by assuming that for incremental time steps it is smaller than the third term on the right hand side. This is explained by the fact that the change in the state, $\Delta\mathbf{x}$, is considered to be smaller and only changing due to the state derivative itself, while the change in the control vector, $\Delta\mathbf{u}$, is assumed to be instantaneous (Sieberling, Chu, and J. A. Mulder, 2010). The initial state derivative is expressed by:

$$\dot{\mathbf{x}}_0 = \mathbf{f}(\mathbf{x_0}) + \mathbf{G}(\mathbf{x})\mathbf{u}_0, \tag{6.5}$$

and Equation 6.4 becomes:

$$\dot{\mathbf{x}} = \dot{\mathbf{x}}_0 + \frac{\partial}{\partial \mathbf{u}}[\mathbf{G}(\mathbf{x})]\Delta\mathbf{u}. \tag{6.6}$$

The required change in the actuators can be found by inverting the equation and by replacing the state derivative, $\dot{\mathbf{x}}$, by a virtual control vector, $\boldsymbol{\nu}$:

$$\Delta\mathbf{u} = \frac{\partial}{\partial \mathbf{u}}[\mathbf{G}^{-1}(\mathbf{x})](\dot{\mathbf{x}} - \dot{\mathbf{x}}_0) = \frac{\partial}{\partial \mathbf{u}}[\mathbf{G}^{-1}(\mathbf{x})](\boldsymbol{\nu} - \dot{\mathbf{x}}_0). \tag{6.7}$$

With the required change of the actuators, the actuators can simply be updated with:

$$\mathbf{u} = \mathbf{u}_0 + \Delta\mathbf{u}. \tag{6.8}$$

As can be seen, the INDI method is based on the same principle as the NDI method. This means that the matrix, $\frac{\partial}{\partial \mathbf{u}}\mathbf{G}(\mathbf{x})$, needs to be invertible. Furthermore, the INDI method uses a derivative of the original matrix, $\mathbf{G}(\mathbf{x})$, which means that the derivative needs to be non-zero. In other words, the matrix, $\mathbf{G}(\mathbf{x})$, needs to be dependent on the variables that exist in the vector, $\mathbf{u}$.

6.2. Guidance and Control System

The G&C system of the space plane can be divided in two parts. The first part is the guidance module, which relates to the control of the position and/or velocity of the space plane. The optimization of the ascent trajectory relates to the optimization of the velocity of the space plane in combination with the flight path and heading angle, which are a function of altitude. These parameters determine the direction and magnitude of the velocity of the space plane. Thus, the guidance module is used to only command the velocity of the space plane. The guidance module will compute the required equivalence ration, which is used as a thrust throttle, and aerodynamic angles, the latter are sent to the control module. The control module controls the orientation of the space plane by computing the change in deflection angles of the control surfaces of the space plane. The G&C system presented and discussed in this section is based on the G&C system designed by Lu (2016).

6.2.1. Guidance module

The guidance module takes as an input the reference trajectory parameters *i.e.,* the flight path angle, γ^{ref}, and heading angle, χ^{ref}, which are defined by the control function $\mathbf{u}(h)$. Furthermore, the maximum allowable velocity is computed based on the dynamic pressure and heat flux constraint for the current altitude. The guidance module compares the reference trajectory and maximum velocity with the current trajectory parameters and computes a virtual control vector, $\boldsymbol{\nu}_{\text{traj}}$. The virtual control vector is computed with:

$$\boldsymbol{\nu}_{\text{traj}} = \begin{bmatrix}\nu_V & \nu_\gamma & \nu_\chi\end{bmatrix}^\top = \mathbf{K}_{\text{traj}}\mathbf{e}_{\text{traj}} = \begin{bmatrix}K_{\dot{V}} \\ K_{\dot{\gamma}} \\ K_{\dot{\chi}}\end{bmatrix} \begin{bmatrix}V^{\max} - V \\ \gamma^{\text{ref}} - \gamma \\ \chi^{\text{ref}} - \chi\end{bmatrix}, \tag{6.9}$$

where $\mathbf{K}_{\text{traj}}$ is a proportional gain and $\mathbf{e}_{\text{traj}}$ is the error in the trajectory parameters. The maximum allowable velocity is found by assessing the dynamic pressure and heat flux constraint. Depending on the altitude, the maximum velocity changes. The maximum velocity that corresponds to the dynamic pressure is found by:

$$V^{\max} = \sqrt{\frac{2\bar{q}_c}{\rho_\infty}}, \tag{6.10}$$

where $\bar{q}_c$ is the dynamic pressure constraint and ρ_∞ is the current free stream dynamic pressure. For the maximum velocity due to the heat flux constraint, Chapman's equation is used:

$$V^{\max} = \left(\frac{\dot{Q}_c}{c^*_{\text{lam}}} \frac{\sqrt{R_N}}{\rho_\infty} \right)^{\frac{1}{3}}, \tag{6.11}$$

where $\dot{Q}_c$ is the heat flux constraint, c^*_{lam} is a constant used for laminar flow and R_N is the nose radius. From both equations, the lowest maximum velocity is taken to compute the virtual control for the velocity. Additionally, the virtual control value is limited to a maximum of 9.2 m/s^2 to comply to the axial acceleration constraint. The value is not set to the limit of 9.81 m/s^2 since large changes in the control surface deflection angle can increase the axial acceleration above the constraint value. The virtual control vector is used in conjunction with an onboard dynamics model to compute the desired thrust throttle, angle of attack and bank angle. Thus, an expression needs to be found that relates the derivative of the trajectory parameters with the thrust throttle, angle of attack and bank angle *i.e.,* the control variables of the guidance module.

The basis for these equations comes from the EoM in terms of spherical components. According to Mooij (1994), the derivative of the velocity, flight path angle and heading angle can be expressed by:

$$\dot{V} = \frac{F_V}{m} + \omega_{cb} r \cos\delta(\sin\gamma\cos\delta - \cos\gamma\sin\delta\cos\chi), \tag{6.12a}$$

$$\dot{\gamma} = \frac{F_\gamma}{mV} + 2\omega_{cb}\cos\delta\sin\chi + \frac{V}{r}\cos\gamma + \omega^2_{cb}\frac{r}{V}\cos\delta(\cos\delta\cos\gamma + \sin\gamma\sin\delta\cos\chi), \tag{6.12b}$$

$$\dot{\chi} = \frac{F_\chi}{mV\cos\gamma} + 2\omega_{cb}(\sin\delta - \cos\delta\tan\gamma\cos\chi) + \frac{V}{r}\cos\gamma\tan\delta\sin\chi + \omega^2_{cb}\frac{r}{V\cos\gamma}\cos\delta\sin\delta\sin\chi, \tag{6.12c}$$

where V is the velocity of the space plane, r is the distance of the space plane with respect to the center of the Earth, δ is the latitude and m is the mass of the space plane. Furthermore, the forces F_V, F_γ and F_χ are the aerodynamic, thrust and gravitational forces combined expressed in the trajectory frame. However, it should be noted that due to the definition of the flight path angle, the forces in the direction of the z-axis are positive pointing upwards.

Due to the inclusion of the thrust and aerodynamic forces, uncertainties exist in the dynamics model. The thrust and aerodynamic forces can be expressed as a function of thrust throttle and angle of attack. However, it is not possible to find an expression in terms of the bank angle. Thus, the desired bank angle is computed with an NDI control algorithm, while the desired thrust throttle and angle of attack are found with an INDI control algorithm. An overview of the guidance module can be seen in Figure 6.1.

Desired Bank Angle

The computation of the desired bank angle follows from the derivatives of the flight path angle and the heading angle. First, the trajectory forces, F_γ and F_χ, are decomposed in terms of components along the body axes. For these expressions it is assumed that the angle of sideslip is small along the ascent trajectory and that the non-radial gravitational components can be neglected. With these assumptions, the trajectory forces can be expressed by:

$$F_\gamma = -F_{A_y}\sin\sigma - [(F_{A_x} + T\cos\epsilon_T)\cos\alpha - (F_{A_z} + T\sin\epsilon_T)\sin\alpha]\cos\sigma - mg_r\cos\gamma, \tag{6.13a}$$

$$F_\chi = -F_{A_y}\cos\sigma + [(F_{A_x} + T\cos\epsilon_T)\cos\alpha - (F_{A_z} + T\sin\epsilon_T)\sin\alpha]\sin\sigma, \tag{6.13b}$$

where F_{A_x}, F_{A_y} and F_{A_z} are the aerodynamic forces expressed in the body reference frame. T is the thrust force and ϵ_T is the thrust elevation angle, which combined yield the thrust direction in the body reference frame for small angles of sideslip. α and σ are the angle of attack and bank angle respectively, and g_r is the radial component of the gravitational acceleration.

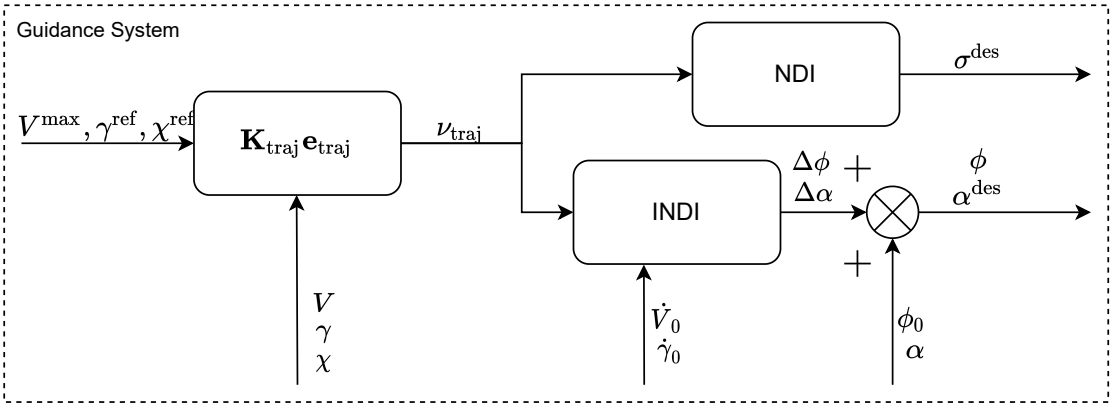

Figure 6.1: Diagram of the guidance module.

According to Lu (2016) the desired bank angle can be computed by dividing the flight path angle and heading angle derivatives. This is done by combining the flight path angle and heading angle derivative of Equation 6.12 with the decomposed trajectory forces of Equation 6.13. For the computation of the desired bank angle it is assumed that the rotation of the Earth, ω_{cb}, is small compared to the aerodynamic, thrust and gravitational forces. With these assumptions the desired bank angle can be found with:

$$\frac{[(F_{A_x}+T\cos\epsilon_T)\cos\alpha-(F_{A_z}+T\sin\epsilon_T)\sin\alpha]\sin\sigma}{[(F_{A_x}+T\cos\epsilon_T)\cos\alpha-(F_{A_z}+T\sin\epsilon_T)\sin\alpha]\cos\sigma}=\frac{F_{A_y}\cos\sigma+mV\cos\gamma\dot{\chi}-m\frac{V^2}{r}\cos^2\gamma\tan\delta\sin\chi}{-(F_{A_y}\sin\sigma+mg_r\cos\gamma+mV\dot{\gamma}-m\frac{V^2}{r}\cos\gamma)}, \tag{6.14}$$

which can be simplified to:

$$\sigma=\arctan\left[\frac{F_{A_y}\cos\sigma+mV\cos\gamma\dot{\chi}-m\frac{V^2}{r}\cos^2\gamma\tan\delta\sin\chi}{-(F_{A_y}\sin\sigma+mg_r\cos\gamma+mV\dot{\gamma}-m\frac{V^2}{r}\cos\gamma)}\right]. \tag{6.15}$$

The flight path angle and heading angle derivative can be replaced with the virtual control vector components, ν_γ and ν_χ, which represent the error between the actual and reference value of these parameters. By replacing the actual derivatives, an expression is found that computes the desired bank angle:

$$\sigma^{\text{des}}=\arctan\left[\frac{F_{A_y}\cos\sigma+mV\cos\gamma\nu_\chi-m\frac{V^2}{r}\cos^2\gamma\tan\delta\sin\chi}{-(F_{A_y}\sin\sigma+mg_r\cos\gamma+mV\nu_\gamma-m\frac{V^2}{r}\cos\gamma)}\right]. \tag{6.16}$$

It should be noted that the bank angle is also present in the right hand side of the equation. However, on the right hand side the bank angle represents the current value, not the desired value.

Desired Angle of Attack and Thrust Throttle

The desired angle of attack and thrust throttle can be computed with an INDI control algorithm, since it is possible to express the aerodynamic and thrust forces in terms of a derivative with respect to the angle of attack and thrust throttle, respectively (Lu, 2016). Similarly to the definition of Equation 6.13, it is assumed that the angle of sideslip, β, is small and that the non-radial components of the gravitational accelerations can be neglected. The forces can be expressed in the trajectory reference frame by:

$$F_V=\bar{q}(C_{T_\phi}\phi\cos\epsilon_t\cos\alpha-C_{T_\phi}\phi\sin\epsilon_T\sin\alpha-(\bar{C}_{D_0}+\bar{C}_{D_\alpha}\alpha)S_{\text{ref}})-mg_r\sin\gamma, \tag{6.17a}$$

$$F_\gamma=\bar{q}(-C_Y S+C_{T_\phi}\phi\cos\epsilon_t\sin\alpha\cos\sigma+C_{T_\phi}\phi\sin\epsilon_t\cos\alpha\cos\sigma+(\bar{C}_{L_0}+\bar{C}_{L_\alpha}\alpha)S_{\text{ref}}\cos\sigma)-mg_r\cos\gamma, \tag{6.17b}$$

where

$$\bar{C}_{D_0}=C_{D_{a_0}}, \tag{6.18a}$$

$$\bar{C}_{D_\alpha} = C_{D_{\alpha_a}} + C_{D_{\alpha_{de,l}}} + C_{D_{\alpha_{de,r}}} + C_{D_{\alpha_{dr}}} + C_{D_{\alpha_{dc}}}, \tag{6.18b}$$

$$\bar{C}_{L_0} = C_{L_{a_0}}, \tag{6.18c}$$

$$\bar{C}_{L_\alpha} = C_{L_{\alpha_a}} + C_{L_{\alpha_{de,l}}} + C_{L_{\alpha_{de,r}}} + C_{L_{\alpha_{dc}}}. \tag{6.18d}$$

The derivative of the drag and lift coefficients, $\bar{C}_{D_\alpha}$ and $\bar{C}_{L_\alpha}$, come from the left and right elevon, de, l and de, r, the rudder, dr, the canard dc, and the body coefficient, a. Furthermore, C_{T_ϕ} is the thrust throttle derivative of the thrust coefficient, ϕ is the thrust throttle itself, C_Y is the side force coefficient, S_{ref} is the reference area of the space plane and $\bar{q}$ is the dynamic pressure.

The expressions obtained in Equation 6.18 can be applied to the derivatives of the velocity and flight path angle of Equation 6.12. The resulting equations can be used in combination with the INDI algorithm to obtain an expression for the required change in angle of attack and thrust throttle:

$$\dot{V} = \dot{V}_0 + \frac{d}{d\phi}[G_V(\mathbf{x})]\Delta\phi, \tag{6.19a}$$

$$\dot{\gamma} = \dot{\gamma}_0 + \frac{d}{d\alpha}[G_\gamma(\mathbf{x})]\Delta\alpha, \tag{6.19b}$$

where

$$\frac{d}{d\phi}[G_V(\mathbf{x})] = \frac{\bar{q}}{m}(C_{T_\phi}\cos\epsilon_T\cos\alpha - C_{T_\phi}\sin\epsilon_T\sin\alpha) \tag{6.20a}$$

$$\frac{d}{d\alpha}[G_\gamma(\mathbf{x})] = \frac{\bar{q}S_{\text{ref}}}{mV}\bar{C}_{L_\alpha}\cos\sigma \tag{6.20b}$$

By inverting Equation 6.19a and 6.19b, and applying the virtual control vector, an expression is obtained that computes the required change in thrust throttle and angle of attack:

$$\Delta\phi = \frac{d}{d\phi}[\mathbf{G}_V(\mathbf{x})]^{-1}(\nu_V - \dot{V}_0), \tag{6.21a}$$

$$\Delta\alpha = \frac{d}{d\alpha}[\mathbf{G}_\gamma(\mathbf{x})]^{-1}(\nu_\gamma - \dot{\gamma}_0). \tag{6.21b}$$

With the required change in thrust throttle and angle of attack, the required thrust throttle and desired angle of attack are computed with:

$$\phi = \phi_0 + \Delta\phi, \tag{6.22a}$$

$$\alpha^{\text{des}} = \alpha + \Delta\alpha, \tag{6.22b}$$

where ϕ_0 is the initial thrust throttle, and α is the current angle of attack.

6.2.2. Control module

The guidance module produces desired angle of attack and bank angle. These desired angles are fed into the control module, with which the desired control surface deflection can be computed. The control module is separated into two parts. The first of which, computes a desired angular velocity that the space plane should achieve. This angular velocity is based on the desired angle of attack and bank angle that has been computed in the guidance module in combination with a reference angle of sideslip. Due to the assumptions made in the guidance module, this angle is always set to zero. These angles are used to form a virtual control vector, which is used in combination with an NDI control algorithm. The result of the loop is a desired angular velocity expressed in terms of the roll, pitch and yaw rate of the space plane. A diagram of the computation of the desired angular velocity can be seen in Figure 6.2.

The second part of the control module takes the desired angular velocity and creates a virtual control vector, which represents the desired angular acceleration. The virtual control vector is used with an INDI control algorithm to obtain the required control surface deflection in order to achieve the desired angular acceleration. A diagram of this part of the control module can be seen in Figure 6.3.

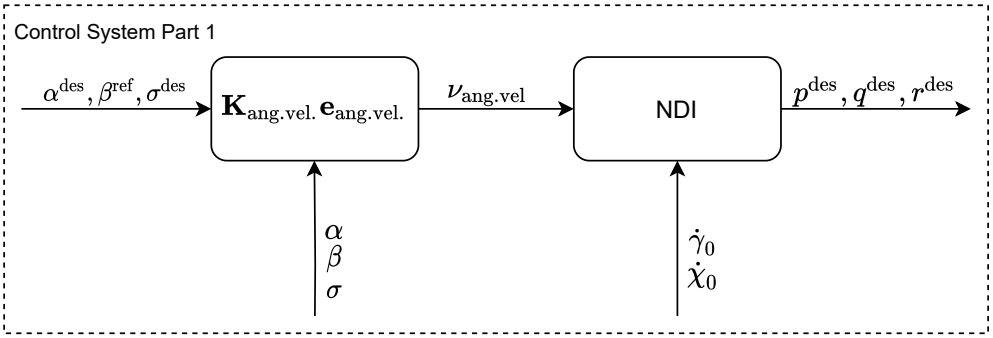

Figure 6.2: Diagram of the NDI control algorithm of the control module.

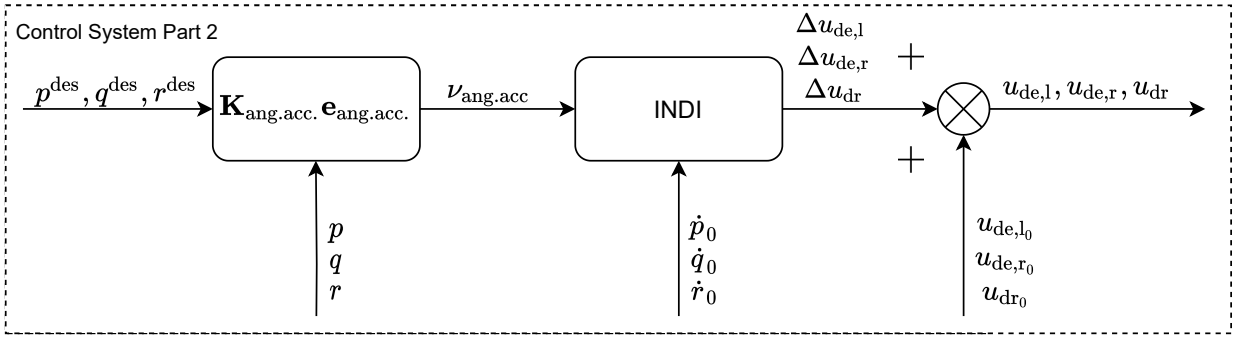

Figure 6.3: Diagram of the INDI control algorithm of the control module.

Angular Velocity Control

The NDI control algorithm, that is applied for the angular velocity, relates the roll, pitch and yaw rate of the space plane to the difference in desired and current aerodynamic angles. The virtual control vector for the angular velocity is defined by:

$$\boldsymbol{\nu}_{\text{ang.vel.}} = \begin{bmatrix} \nu_\sigma & \nu_\alpha & \nu_\beta \end{bmatrix}^\top = \mathbf{K}_{\text{ang.vel.}}\mathbf{e}_{\text{aero}} = \begin{bmatrix} K_{\dot{\sigma}} \\ K_{\dot{\alpha}} \\ K_{\dot{\beta}} \end{bmatrix} \begin{bmatrix} \sigma^{\text{des}} - \sigma \\ \alpha^{\text{des}} - \alpha \\ \beta^{\text{ref}} - \beta \end{bmatrix}. \tag{6.23}$$

The roll, pitch and yaw rate define the rotation of the space plane with respect to the inertial frame. This angular velocity can be decomposed into the rotation of different reference frames with respect to each other, as has been discussed in Section 3.1.3. The rotation of the space plane with respect to the inertial frame, expressed in components along the body axes, can be defined by:

$$\boldsymbol{\Omega}^B_{B,I} = \mathbf{C}_{\mathbf{B},\mathbf{I}}\boldsymbol{\Omega}^I_{E,I} + \mathbf{C}_{\mathbf{B},\mathbf{E}}\boldsymbol{\Omega}^E_{V,E} + \mathbf{C}_{\mathbf{B},\mathbf{T}}\boldsymbol{\Omega}^T_{T,V} + \mathbf{C}_{\mathbf{B},\mathbf{A}}\boldsymbol{\Omega}^A_{A,T} + \mathbf{C}_{\mathbf{B},\mathbf{A}}\boldsymbol{\Omega}^A_{B,A}. \tag{6.24}$$

This expression can be simplified by, first of all, assuming that the rotation of the Earth, and the change in longitude and latitude is small compared to the change in flight path angle, heading angle and change in the aerodynamic angles. Second of all, by investigating the axes of rotation as seen in Figure 3.8, it can be seen that the rotation due to the change in bank angle is about the x_T-axis, which is equal to the x_A-axis. This means that this rotation can also be expressed along the body axes with transformation matrix $\mathbf{C}_{\mathbf{B},\mathbf{A}}$. The resulting expression becomes:

$$\boldsymbol{\Omega}^B_{B,I} = \mathbf{C}_{\mathbf{B},\mathbf{T}}\boldsymbol{\Omega}^T_{T,V} + \mathbf{C}_{\mathbf{B},\mathbf{A}}\boldsymbol{\Omega}^A_{A,T} + \mathbf{C}_{\mathbf{B},\mathbf{A}}\boldsymbol{\Omega}^A_{B,A}, \tag{6.25a}$$

$$= \mathbf{C}_{\mathbf{B},\mathbf{A}}\boldsymbol{\Omega}^A_{B,T} + \mathbf{C}_{\mathbf{B},\mathbf{T}}\boldsymbol{\Omega}^T_{T,V}. \tag{6.25b}$$

In Figure 3.8 the definition of the angle of sideslip and bank angle are considered positive, while the angle of attack is considered negative. In a similar way, the definition of the flight path angle and heading angle are investigated. It can be seen in Figure 6.4 that the heading angle derivative is a rotation about the z_V-axis,

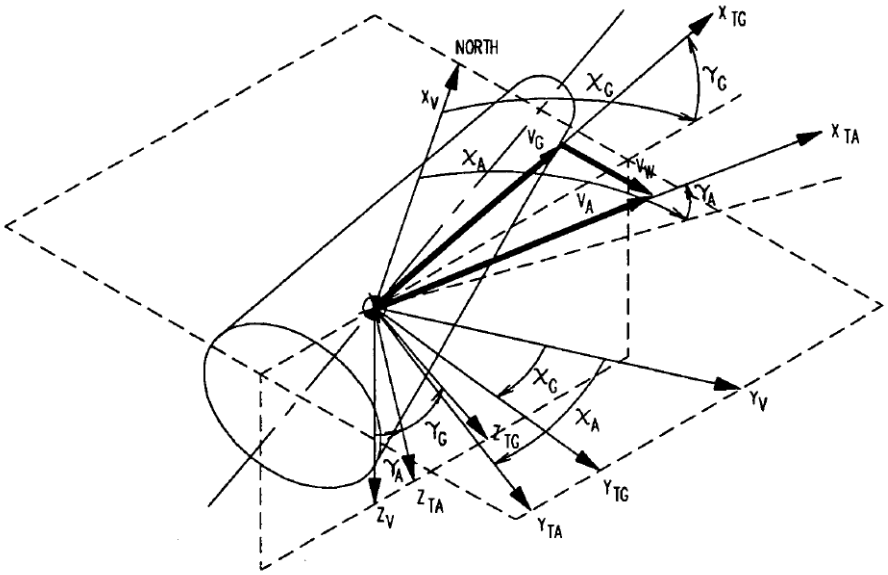

Figure 6.4: Relation between the V-frame and the TA- and TG-frame (Mooij, 1994).

while the flight path angle derivative is a rotation about the y_T-axis. Due to the definitions of the angles and the axes, the roll, pitch and yaw rate are expressed by:

$$\begin{bmatrix} -p \\ q \\ -r \end{bmatrix} = \mathbf{C_{B,A}} \begin{bmatrix} \dot{\sigma} \\ \dot{\alpha} \\ \dot{\beta} \end{bmatrix} + \mathbf{C_{B,T}} \begin{bmatrix} -\dot{\chi} \sin\gamma \\ \dot{\gamma} \\ -\dot{\chi} \cos\gamma \end{bmatrix}, \tag{6.26}$$

where the flight path and heading angle derivatives are computed using Equation 6.12.

The derivatives of the aerodynamic angles are replaced by the virtual control vector of Equation 6.23 to obtain an expression for the desired roll, pitch and yaw rate:

$$\begin{bmatrix} -p^{\text{des}} \\ q^{\text{des}} \\ -r^{\text{des}} \end{bmatrix} = \mathbf{C_{B,A}} \begin{bmatrix} \nu_\sigma \\ \nu_\alpha \\ \nu_\beta \end{bmatrix} + \mathbf{C_{B,T}} \begin{bmatrix} \dot{\chi} \sin\gamma \\ \dot{\gamma} \\ -\dot{\chi} \cos\gamma \end{bmatrix}. \tag{6.27}$$

Angular Acceleration Control

The objective of the angular acceleration control is to compute the required control surface deflections of the elevons and the rudder of the space plane to achieve the desired angular accelerations. The angular acceleration is defined by a virtual control vector, which found by comparing the actual and desired angular velocity of the space plane:

$$\nu_{\text{ang.acc.}} = \begin{bmatrix} \nu_p \\ \nu_q \\ \nu_r \end{bmatrix} = \mathbf{K}_{\text{ang.acc}} \mathbf{e}_{\text{ang.acc.}} = \begin{bmatrix} K_{\dot{p}} \\ K_{\dot{q}} \\ K_{\dot{r}} \end{bmatrix} \begin{bmatrix} p^{\text{des}} - p \\ q^{\text{des}} - q \\ r^{\text{des}} - r \end{bmatrix}, \tag{6.28}$$

where it is assumed that the current angular velocity of the space plane is known.

The control surfaces deflection changes are computed with an INDI control algorithm. According to Sieberling, Chu, and J. A. Mulder (2010), the derivative of the roll, pitch and yaw can be expressed in the following form:

$$\dot{\boldsymbol{\omega}} = \dot{\boldsymbol{\omega}}_0 + \frac{\partial}{\partial \mathbf{u}} [\mathbf{I}^{-1} \mathbf{M}_c] \Delta \mathbf{u} = \dot{\boldsymbol{\omega}}_0 + \mathbf{I}^{-1} \frac{\partial}{\partial \mathbf{u}} [\mathbf{M}_c] \Delta \mathbf{u}, \tag{6.29}$$

where the initial derivative of the angular velocity, $\dot{\boldsymbol{\omega}}_0$, is computed using Equation 3.33 and $\mathbf{I}$ is the moments of inertia matrix. The derivative matrix of the moments due to the control surfaces, containing the left and

right elevons, and the rudder can be expressed by:

$$(\mathbf{M}_c)_{\mathbf{u}} = \bar{q}S_{\text{ref}} \begin{bmatrix} b_{\text{ref}}C_{l_{\delta e,l}} & b_{\text{ref}}C_{l_{\delta e,r}} & b_{\text{ref}}C_{l_{\delta r}} \\ c_{\text{ref}}C_{m_{\delta e,l}} & c_{\text{ref}}C_{m_{\delta e,r}} & c_{\text{ref}}C_{m_{\delta r}} \\ b_{\text{ref}}C_{n_{\delta e,l}} & b_{\text{ref}}C_{n_{\delta e,r}} & b_{\text{ref}}C_{n_{\delta r}} \end{bmatrix}, \tag{6.30}$$

where the subscripts $\delta e, l$, $\delta e, r$ and δr denotes the derivative of the control surface deflection for the roll coefficient, C_l, pitch coefficient, C_m, and yaw coefficient C_n. The derivatives of the coefficients are not easily estimated, since not all coefficients have a linear derivative. Thus, it is assumed that the derivative of the yaw rate is only influenced by the rudder and that the pitching moment is not influenced by the rudder. Furthermore, the effect of a change in force coefficient due to a change in control surfaces is included. The resulting derivative matrix becomes:

$$(\mathbf{M}_c)_{\mathbf{u}} = \bar{q}S_{\text{ref}} \begin{bmatrix} b_{\text{ref}}C_{l_{\delta e,l}} & b_{\text{ref}}C_{l_{\delta e,r}} & b_{\text{ref}}C_{l_{\delta r}} \\ c_{\text{ref}}C_{m_{\delta e,l}} - C_{Z_{\delta e,l}}x_{cg} & c_{\text{ref}}C_{m_{\delta e,r}} - C_{Z_{\delta e,r}}x_{cg} & 0 \\ 0 & 0 & b_{\text{ref}}C_{n_{\delta r}} + C_{Y_{\delta r}}x_{cg} \end{bmatrix}, \tag{6.31}$$

where C_Y is the side force coefficient and C_Z is the force coefficient in the z_B-axis direction. Additionally, C_D is the drag force coefficient and C_L is the lift force coefficient. The force coefficient in the z_B-axis, C_Z, can be expressed, when assuming a small angle of sideslip, by:

$$C_{Z_{\delta e,l}} = -C_{D_{\delta e,l}} \sin\alpha - C_{L_{\delta e,l}} \cos\alpha, \tag{6.32a}$$

$$C_{Z_{\delta e,r}} = -C_{D_{\delta e,r}} \sin\alpha - C_{L_{\delta e,r}} \cos\alpha. \tag{6.32b}$$

$$\tag{6.32c}$$

After inversion and by applying the virtual control vector, $\nu_{\text{ang.acc.}}$ an expression is found for the change in control surface deflections:

$$\begin{bmatrix} \Delta u_{\text{de,l}} \\ \Delta u_{\text{de,r}} \\ \Delta u_{\text{dr}} \end{bmatrix} = \mathbf{I}\frac{\partial}{\partial \mathbf{u}}[\mathbf{M}_c]^{-1}(\nu_{\text{ang.acc.}} - \dot{\boldsymbol{\omega}}_0), \tag{6.33}$$

where $\Delta u_{\text{de,l}}$, $\Delta u_{\text{de,r}}$ and Δu_{dr} represent the required change in the left and right elevon, and rudder, respectively.

With the required change computed, the actual control surface deflection is simply found with:

$$\mathbf{u} = \mathbf{u}_0 + \Delta\mathbf{u}. \tag{6.34}$$

6.2.3. Trim Control module

In studies done by Mooij (1998) and Shaughnessy (1992), it was found that Thrust Vector Control (TVC) and a canard should be used to trim the space plane in order to reduce drag losses. A trimmed space plane, means that the natural pitching moment is zero *i.e.*, the pitching moment due to the body of the space plane itself does not impose a change in pitch angle. It is therefore needed to include trim module, consisting of control of the canard or TVC. The canard is used to trim the space plane during the subsonic parts of the ascent, since aerodynamic data for the canard is only available up to Mach 0.9. Afterwards, the TVC takes over to trim the space plane, with a maximum thrust elevation angle of ± 25 degrees Mooij (1998). A diagram of the trim control module can be seen in Figure 6.5.

Trim Control during Subsonic Flight

For the control with the canard an INDI control algorithm is applied. For subsonic parts of the flight, the required change in canard deflection is computed with:

$$\Delta u_{\text{dc}} = I_{yy}\frac{\partial}{\partial u_{\text{dc}}}[M_{y_{dc}}]^{-1}(-\dot{q}_0) = I_{yy}[\bar{q}S_{\text{ref}}C_{m_{\delta c}}]^{-1}(-\dot{q}_0), \tag{6.35}$$

where the initial derivative of the pitch rate, $\dot{q}_0$, is computed with Equation 3.33b, I_{yy} is the moment of inertia about the y_B-axis and $C_{m_{\delta c}}$ is the pitching moment coefficient derivative of the canard. It should be noted

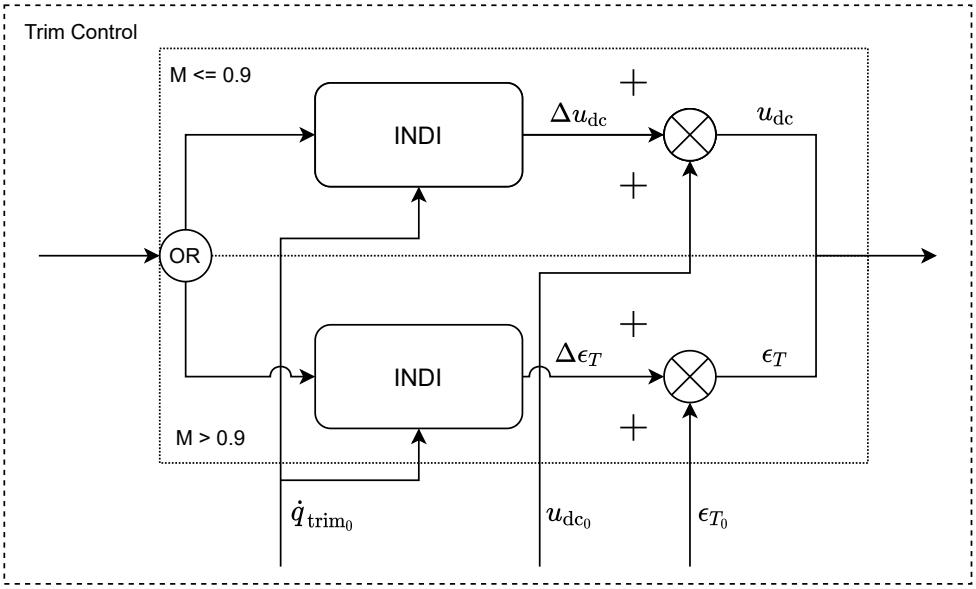

Figure 6.5: Diagram of the trim control module.

that the computation of the pitch rate derivative requires the moment about the corresponding axis. In this case, about the y_B-axis. The moment that is used to compute the pitch rate derivative is only the contribution of the space plane body, M_{y_a}, and canard, M_{y_c}:

$$M_{\mathrm{trim}} = M_{y_a} + M_{y_{dc}}, \tag{6.36}$$

where

$$M_{y_a} = \bar{q} C_{m_{\mathrm{a}}} S_{\mathrm{ref}} \bar{c}_{\mathrm{ref}}, \tag{6.37a}$$

$$M_{y_{dc}} = \bar{q} S_{\mathrm{ref}} \bar{c}_{\mathrm{ref}} \left(C_{m_{\mathrm{dc}}} - C_{Z_{\mathrm{dc}}} \frac{x_{\mathrm{cg}}}{\bar{c}_{\mathrm{ref}}} \right). \tag{6.37b}$$

This ensures that the trim control module only counteracts the natural pitching moment

In the aforementioned equations $C_{m_{\mathrm{a}}}$ and $C_{m_{\mathrm{dc}}}$ signify the pitching moment coefficient of the body and canard, respectively. $C_{Z_{\mathrm{dc}}}$ denotes the force coefficient of the canard along the positive z_B-axis. Furthermore, x_{cg} is the location of the Center of Gravity (CoG) with respect to the aerodynamic reference point and $\bar{c}_{\mathrm{ref}}$ is the chord length of the wing.

Once again, after the required change in canard deflection is computed, the canard deflection itself is computed with:

$$u_{\mathrm{dc}} = u_{\mathrm{dc}_0} + \Delta u_{\mathrm{dc}}. \tag{6.38}$$

Trim Control during Higher than Subsonic Flight

When transonic and higher Mach numbers are reached, the canard is retracted and the TVC is used to trim the space plane (Shaughnessy, 1992). An INDI control algorithm can be used by linearizing the thrust induced moment about the y_B-axis. It is assumed that the thrust elevation angle is small, which allows the use of the small angle approximation. This means that there is a linear relation between the TVC induced control moment and the thrust off-set angle, which is required for the INDI. The linearized thrust induced moment is given by:

$$M_{y_{\mathrm{tvc}}} = -\bar{q} C_T \epsilon_T x_{\mathrm{ct}}. \tag{6.39}$$

With the linearized thrust moment an equation can be set up to compute the required change in thrust elevation angle:

$$\Delta \epsilon_T = I_{yy} \frac{\partial}{\partial \epsilon_T} [M_{y_{\mathrm{tvc}}}]^{-1} (-\dot{q}) = I_{yy} [-\bar{q} C_T x_{\mathrm{ct}}]^{-1} (-\dot{q}_0), \tag{6.40}$$

where the computation of the pitch rate, $\dot{q}_0$ is done with the trim moment:

$$M_{\mathrm{trim}} = M_{y_a} + M_{y_{\mathrm{tvc}}}, \tag{6.41a}$$

$$M_{y_a} = \bar{q} C_{m_\mathrm{a}} S_\mathrm{ref} \bar{c}_\mathrm{ref}, \tag{6.41b}$$

$$M_{y_\mathrm{tvc}} = -\bar{q} C_T \sin\epsilon_T x_\mathrm{ct}. \tag{6.41c}$$

In the above equations M_{y_tvc} is the pitching moment due to the thrust in z_B-direction, ϵ_T is the thrust elevation angle and x_{ct} is the Center of Thrust (CoT) with respect to the CoG.

The required change in thrust elevation angle is used to update the thrust elevation angle with:

$$\epsilon_T = \epsilon_{T_0} + \Delta\epsilon_T. \tag{6.42}$$

6.3. Guidance and Control Architecture & Performance

The G&C systems performance has been investigated before and during the initial optimization. Based on the investigation a number of changes have been implemented to ensure that the system is able to effectively guide and control the space plane. Additionally, the transcription method discussed in Chapter 5, requires a G&C system that is capable of switching off partly depending on the ascent phase.

6.3.1. Performance

During the initial optimization, which is discussed in Section 5.2, the performance of the G&C system has been investigated. The main issue that came up with the system was the difficulty to control the velocity and flight path angle of the space plane during the pull up phase. For this reason, it was chosen to remove the velocity as an optimization parameter and to control the angle of attack of the space plane directly from the moment that the pull up phase starts. Another issue that came up during that investigation, was that the control surface deflection oscillates heavily from the moment that the dynamic pressure drops due to the increasing altitude, which is around the same time as the start of the pull up phase. Figure 6.6 shows these oscillations. It was hypothesized that during the pull up phase the dynamic pressure drops considerably, which caused these oscillations. Another hypothesis was that these oscillations occurred due to the interactions between the trim module and the control module. The main reason for these oscillations was not found, which necessitated the minimization of these oscillations.

Oscillations

In order to minimize the oscillations, a maximum change in control surface deflection angle was introduced. The maximum change in control surface deflection angle was set to ± 40 degrees per second, ± 4 deg per time step of the integrator. Whenever the pull up phase would start, the maximum change in deflection angle would be limited with the following expression:

$$\dot{u}_\mathrm{max} = 4.0 \frac{\bar{q}}{\bar{q}_c}, \tag{6.43}$$

where $\dot{u}_\mathrm{max}$ is the maximum change in deflection angle, $\bar{q}$ is the current dynamic pressure, and $\bar{q}_c$ is the dynamic pressure constraint. In this way, the oscillations that occurred, would be minimized. Additionally, the gains of the first part of the control module, which controls the angular velocity of the space plane, change when the pull up altitude starts. Finally, the oscillations during the last phase where removed by assuming that the space plane would control its orientation by using Reaction Control System (RCS) thrusters. The use of these thrusters were first introduced in the study by Mooij (1998), since the dynamic pressure during the last phase of the ascent is close to zero. The implementation of the thrusters itself is not considered, instead a simple INDI algorithm is used to define moment coefficients that simulate the use of RCS thrusters. The computation of these coefficients is based on Equation 6.33, where the deflection angle is replaced by these moment coefficients:

$$\begin{bmatrix} \Delta C_\mathrm{RCS,x} \\ \Delta C_\mathrm{RCS,y} \\ \Delta C_\mathrm{RCS,z} \end{bmatrix} = \mathbf{I} \frac{\partial}{\partial \mathbf{u}} [\mathbf{M}_\mathrm{RCS}]^{-1} (\nu_\mathrm{ang.acc.} - \dot{\boldsymbol{\omega}}_0), \tag{6.44}$$

where the thruster coefficients, C_RCS are expressed about the body axes of the space plan. The derivative matrix of the moment, $\frac{\partial}{\partial \mathbf{u}}[\mathbf{M}_\mathrm{RCS}]$ is defined by:

$$\frac{\partial}{\partial \mathbf{u}} [\mathbf{M}_\mathrm{RCS}] = \begin{bmatrix} \bar{q} S_\mathrm{ref} b_\mathrm{ref} & 0 & 0 \\ 0 & \bar{q} S_\mathrm{ref} c_\mathrm{ref} & 0 \\ 0 & 0 & \bar{q} S_\mathrm{ref} b_\mathrm{ref} \end{bmatrix}. \tag{6.45}$$

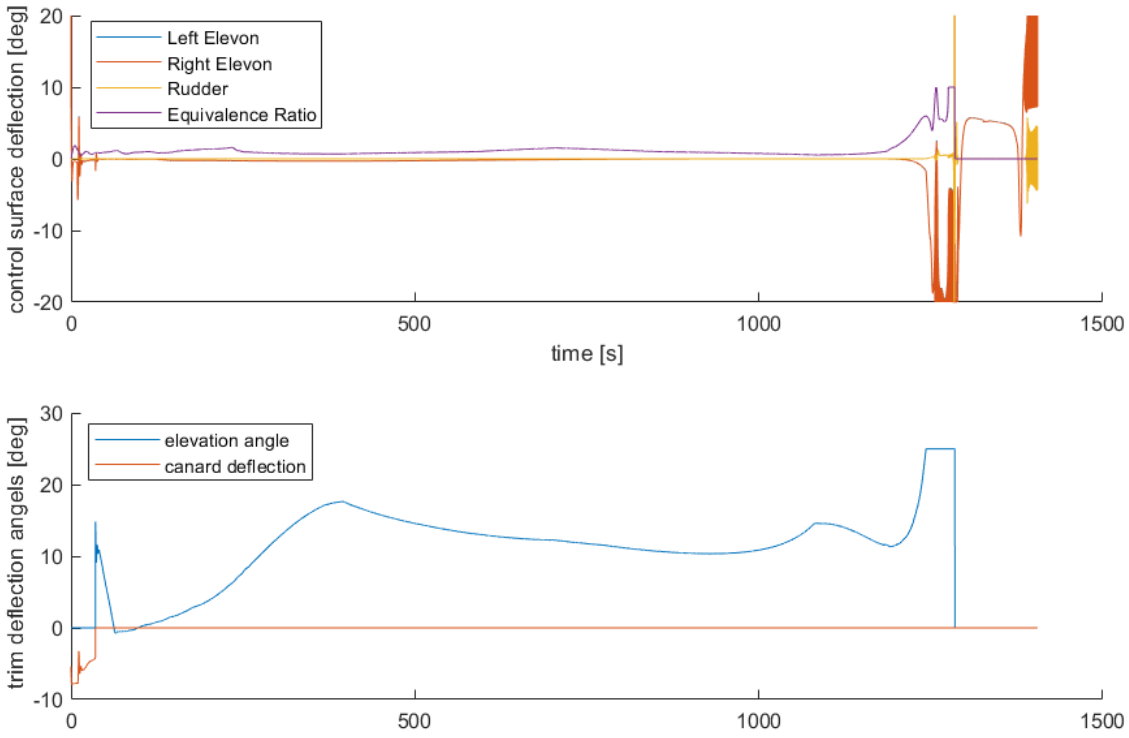

Figure 6.6: Time history of the control surface deflection angles, equivalence ratio, and thrust elevation angle.

The RCS thruster coefficients are updated by:

$$\begin{bmatrix} C_{\mathrm{RCS,x}} \\ C_{\mathrm{RCS,y}} \\ C_{\mathrm{RCS,z}} \end{bmatrix} = \begin{bmatrix} C_{\mathrm{RCS,x}_0} \\ C_{\mathrm{RCS,y}_0} \\ C_{\mathrm{RCS,z}_0} \end{bmatrix} + \begin{bmatrix} \Delta C_{\mathrm{RCS,x}} \\ \Delta C_{\mathrm{RCS,y}} \\ \Delta C_{\mathrm{RCS,z}} \end{bmatrix}, \tag{6.46}$$

where the subscript 0 denotes the current coefficient values. The updated coefficients are used to find the moments induced by the thrusters with:

$$\begin{bmatrix} M_{\mathrm{RCS,x}} \\ M_{\mathrm{RCS,y}} \\ M_{\mathrm{RCS,z}} \end{bmatrix} = \bar{q} S_{\mathrm{ref}} \begin{bmatrix} b_{\mathrm{ref}} C_{\mathrm{RCS,x}} \\ c_{\mathrm{ref}} C_{\mathrm{RCS,y}} \\ b_{\mathrm{ref}} C_{\mathrm{RCS,z}} \end{bmatrix}. \tag{6.47}$$

The thrusters that are simulated are not based on any actual thrusters, and the performance limit of these is not implemented. During the coasting phase, the angle of attack is commanded to zero, which reduces the aerodynamic force induced moments. A potential issue could occur during the pull up phase when the space plane is commanded to a large angle of attack. The optimization algorithm could find a solution with a coast phase altitude, such that the RCS thrusters are enabled when the space plane is right on the cusp of becoming unstable. In order to mitigate this risk, a maximum angle of attack during the pull up phase is enforced. In the study done by Mooij (1998) the pull up phase had a constant angle of attack of 6 degrees. For this study, the maximum angle of attack is set to 4 degrees, and a refinement will be performed when the optimization algorithm finds a fuel-optimal solution with an angle of attack close to the maximum.

Bank Angle

The desired bank angle is computed with an NDI algorithm. It was not possible to use the INDI algorithm, since the aerodynamic coefficients cannot be expressed as a function of the bank angle. Typically, NDI is

applied when the dynamics of the system are known exactly. For the bank angle, which is influenced by the aerodynamic forces, this is not the case. Since the desired bank angle is not changed incrementally, large changes in the desired bank angle can occur. It was found that large changes in the bank angle occurred when the flight path angle is close to zero. When the flight path angle is close to zero, the forces that act on the space plane are in equilibrium. It was found that the flight path angle would slightly oscillate in these occurrences around the commanded flight path angle. Since the flight path angle oscillates around the commanded value, the virtual control for the flight path angle, ν_γ, changes sign with the oscillations. This virtual control is included in the determination of the desired bank angle, as can be seen in Equation 6.16. Since the forces are in equilibrium, the virtual control has a large influence on the computation of the desired bank angle. In order to mitigate the oscillations in bank angle, the value of the virtual control of the flight path angle is limited by expressing the desired bank angle with:

$$\sigma^{\text{des}} = \arctan\left[\frac{F_{A_y}\cos\sigma + mV\cos\gamma\nu_\chi - m\frac{V^2}{r}\cos^2\gamma\tan\delta\sin\chi}{-(F_{A_y}\sin\sigma + mg_r\cos\gamma + 0.01mV\nu_\gamma - m\frac{V^2}{r}\cos\gamma)}\right]. \tag{6.48}$$

Determination of the Gains

Since the NDI and INDI algorithms are used to guide and control the space plane, linearization of the EoM was not necessary. This in turn means that gain scheduling is not necessary. The gains for the different virtual control vectors are determined by trial and error. For the guidance module the gains are:

$$\mathbf{K}_{\text{traj}} = \begin{bmatrix} K_{\dot{V}} & K_{\dot{\gamma}} & K_{\dot{\chi}} \end{bmatrix}^\top = \begin{bmatrix} 4.0 & 0.8 & 0.4 \end{bmatrix}^\top. \tag{6.49}$$

The heading angle gain is low due to the fact that the desired bank angle, which results from the commanded heading angle, is computed with an NDI algorithm. As mentioned previously, the NDI algorithm does not change the desired value incrementally. Thus, the commanded change in heading angle should not be too large to ensure that the bank angle does not start to oscillate.

For the commanded angular velocity of the space plane, which is computed with the first part of the control system, two gains are defined. The two gains are used for initial phase of the ascent and pull up phase, where the pull up phase requires finer control over the angular velocity. This necessitates a small gain for the second phase. The gain vectors are:

$$\mathbf{K}_{\text{ang.vel.phase.1}} = \begin{bmatrix} K_{\dot{\sigma}} & K_{\dot{\alpha}} & K_{\dot{\beta}} \end{bmatrix}^\top = \begin{bmatrix} 2.0 & 2.0 & 2.0 \end{bmatrix}^\top, \tag{6.50a}$$

$$\mathbf{K}_{\text{ang.vel.phase.2}} = \begin{bmatrix} K_{\dot{\sigma}} & K_{\dot{\alpha}} & K_{\dot{\beta}} \end{bmatrix}^\top = \begin{bmatrix} 0.5 & 0.5 & 0.5 \end{bmatrix}^\top. \tag{6.50b}$$

The reduced values for the gain vector during the pull up phase ensures that the overshoot is reduced, which means that the space plane will not becoming unstable as quickly.

For the second part of the control module a single gain vector is defined by:

$$\mathbf{K}_{\text{ang.acc.}} = \begin{bmatrix} K_{\dot{p}} & K_{\dot{q}} & K_{\dot{r}} \end{bmatrix}^\top = \begin{bmatrix} 3.0 & 3.0 & 3.0 \end{bmatrix}^\top. \tag{6.51}$$

Effects of the Changes

With the changes to mitigate the oscillations in the flight path angle and the bank angle. A stable enough system is developed, which can be used to optimize the ascent trajectory of a space plane. In Figures 6.7 and 6.8 the effect of these changes can be seen for a launch time of $t_0 = 0$ s and $t_0 = 3600$ s. These results come from the optimization that will be discussed in Chapter 8. It can be seen that the elevon deflections still oscillate just before the pull up maneuver. The reason why these oscillations occurred became apparent during the sensitivity analysis. A more detailed discussion in this phenomenon can be read in Section 9.2.

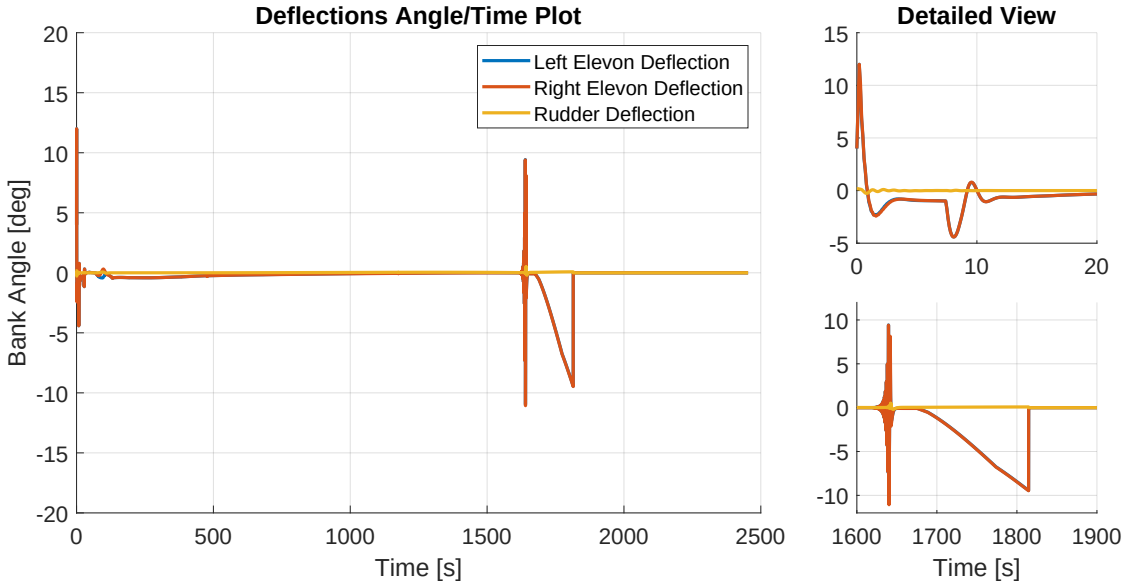

Figure 6.7: Showcase of the time history of the deflection angles of the space plane for a launch time of $t_0 = 0$ s.

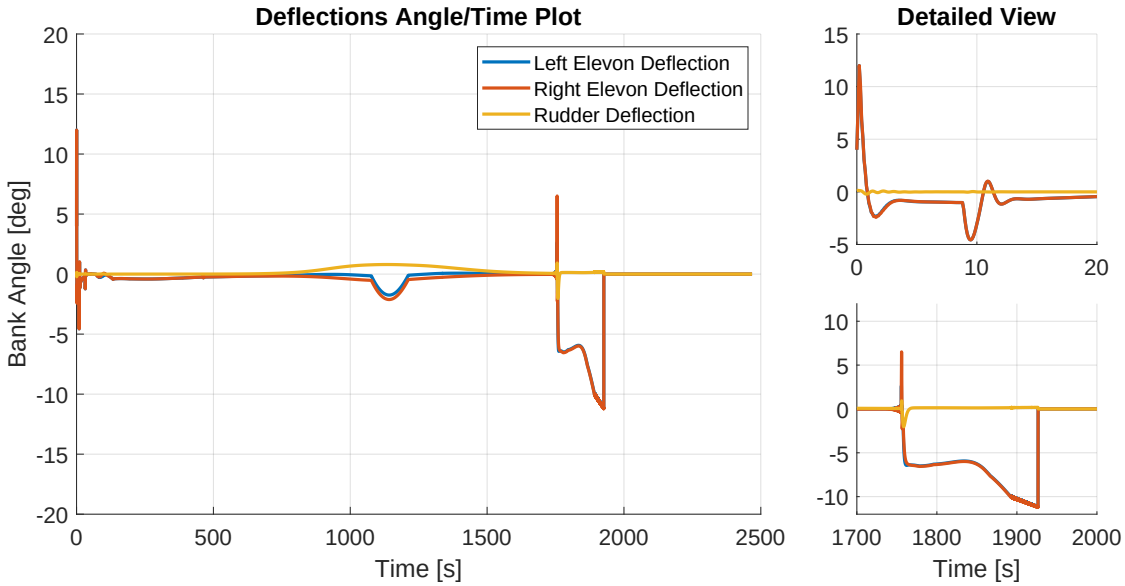

Figure 6.8: Showcase of the time history of the deflection angles of the space plane for a launch time of $t_0 = 3600$ s.

6.3.2. Guidance and Control Architecture

The ascent phases and the differing ways of controlling the space plane during these phases requires a G&C system that is modular and capable of switching of parts of the system. In Figure 6.9 an overview is given of the architecture of the system. During the first phase, the full G&C system is utilized, as described in Section 6.2. During this phase, the velocity, flight path angle and heading angle is directly commanded. Afterwards, the part of the guidance module that controls the flight path angle and heading angle is turned off. The thrust throttle is still updated and the TVC is active. However, the bank angle and sideslip angle are commanded to zero and the reference angle of attack comes from the optimization parameters. During the last phase of the ascent, the coasting phase, the engine is turned off, which also means that the TVC module is turned off. In this phase the RCS thrusters are used to ensure that the angle of attack is, in addition to the angle of sideslip

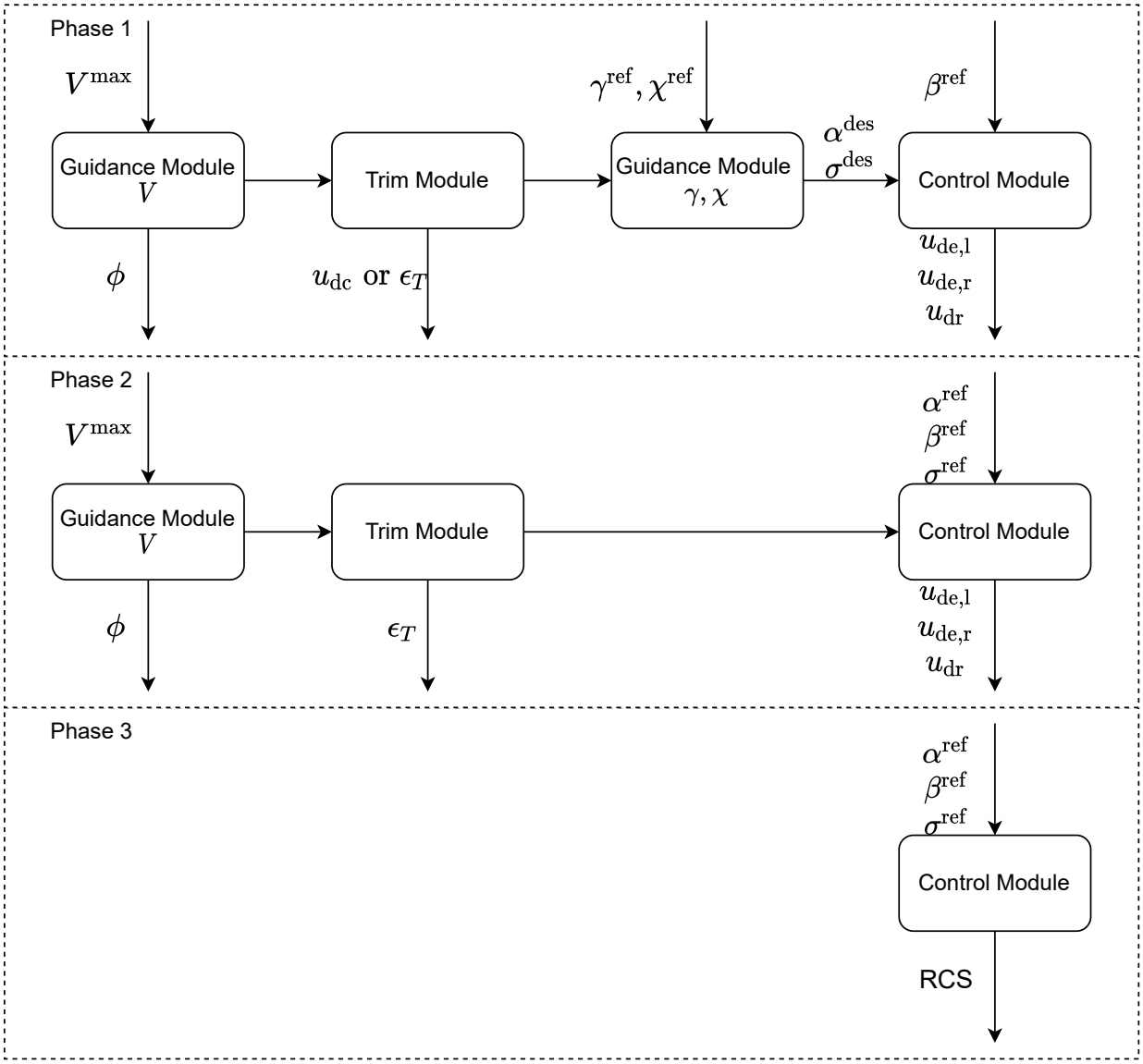

Figure 6.9: Overview of the G&C system architecture.

and bank angle, returned to zero.

7

Software

In this chapter the use of the software packages and several numerical methods will be discussed, which are necessary for the optimization of an ascent trajectory. In Section 7.1 the numerical methods that are used in the simulation are discussed. This includes the use of an integrator to propagate the state of the space plane, interpolation to evaluate the aerodynamic coefficients and the construction of a reference trajectory based on the optimization parameters. In Section 7.2 the entire architecture behind the simulation of the ascent trajectory and the optimization of that trajectory is explained. Furthermore, it is explained, which parts of the simulation are built from scratch and which parts are used from existing software packages.

7.1. Numerical Methods

In this section an overview is given of the numerical methods that have been used for the simulation of the ascent trajectory, with reasoning why these methods have been used.

7.1.1. Integration

The Equations of Motion (EoM) derived in Section 3.2 need to be solved numerically. A number of integrators are available in TU Delft Astrodynamics Toolbox (TUDAT) to solve the EoM. The most well-known integrator is the Runge-Kutta multi-stage integrator. The Runge-Kutta 4 (RK4) integrator uses four function evaluations for a single time step (Dirkx and Cowan, 2019). Other more intricate integrators are also available, that either use more function evaluation to increase the accuracy of the integrator, or use a variable step size. The variable step size integrators use two different orders, for instance, a fourth and fifth order Runge-Kutta integrator, and compare the difference to assess the Local Truncation Error (LTE) (Dirkx and Cowan, 2019). Based on the LTE, the step size is varied and used by the lowest order integrator. The use of a variable step size integrator has seen benefits for elliptical orbits, where the dynamics of the orbit might be fast or slow depending on the place in the orbit. However, the inclusion of Incremental Non-linear Dynamic Inversion (INDI) algorithms to guide and control the space plane creates a risk when using the variable step size integrators. An important assumption that enables the use of the algorithm is that the step size is small, which enables the reduction of the EoM. The variable step size integrators might result in a large time step, which could result in a poor performing Guidance and Control (G&C) system. For this reason, variable step size integrators will not be used to solve the EoM.

For the fixed step size integrators, a trade-off was done to determine, which integrator should be used. As was mentioned previously, the fixed step size integrators can have a number of function evaluations. More function evaluation will result in a more accurate solution of the EoM, at the cost of a longer simulation time. A trade-off can be made between the accuracy of the solution and the simulation time. However, it was found by investigating the performance of the G&C system that it would greatly be reduced when considering a time step larger than 0.1 seconds. For this reason, the step size of 0.1 seconds was considered non-negotiable. Instead, a trade-off was made between the different fixed step-size integrators, where RK4 was the integrator considered with the lowest amount of function evaluations. It became apparent that even by using RK4 the simulation that would reach the target altitude would result in a simulation time of 7 seconds. Considering the fact that the optimization algorithm might need to simulate an ascent possibly more than 200 times per generation, with an unknown number of generations, it is imperative to reduce the simulation time of a single

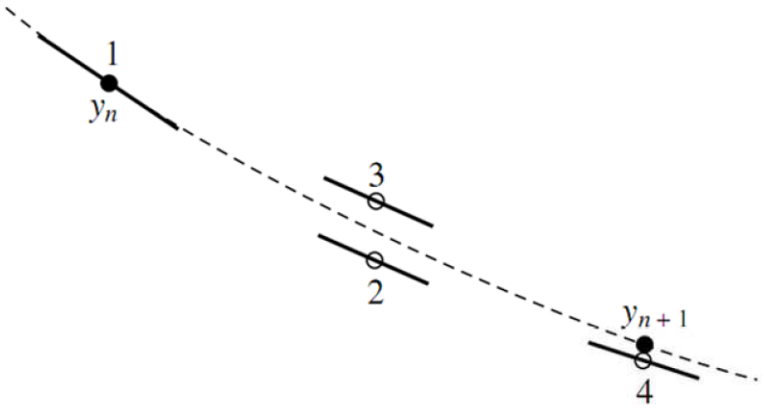

Figure 7.1: Illustration of the Runge-Kutta 4 intermediate steps (Noomen, 2019).

ascent as much as possible. For instance, with 200 individuals in a single generation, 500 generations in total and an average simulation time of 3.5 seconds, the total simulation time would become 350,000 seconds, which is four entire days that the optimization algorithm requires to find the solution for a fuel-optimal ascent trajectory. For this reason, RK4 was selected as the integrator to be used to solve the EoM numerically.

With the choice to use *RK4* as integrator, a small overview is given of the equations that are used to find the state of the next time step. The integrator defines the state at the next step with:

$$\mathbf{k}_1 = \Delta t \mathbf{f}(\mathbf{x}, t), \tag{7.1a}$$

$$\mathbf{k}_2 = \Delta t \mathbf{f}(\mathbf{x} + \frac{1}{2}\mathbf{k}_1, t + \frac{1}{2}\Delta t), \tag{7.1b}$$

$$\mathbf{k}_3 = \Delta t \mathbf{f}(\mathbf{x} + \frac{1}{2}\mathbf{k}_2, t + \frac{1}{2}\Delta t), \tag{7.1c}$$

$$\mathbf{k}_4 = \Delta t \mathbf{f}(\mathbf{x} + \mathbf{k}_3, t + \Delta t), \tag{7.1d}$$

$$\mathbf{x}(t + \Delta t) = \mathbf{x} + \frac{1}{6}(\mathbf{k}_1 + 2\mathbf{k}_2 + 2\mathbf{k}_3 + \mathbf{k}_4), \tag{7.1e}$$

where $\mathbf{k}_1$, $\mathbf{k}_2$, $\mathbf{k}_3$ and $\mathbf{k}_4$ represent the function evaluations of the integrator, which are used together to compute the state derivative. In Figure 7.1 an overview is given of the function evaluations.

7.1.2. Interpolation

Interpolation is needed to find the aerodynamic and thrust coefficients, as well as the mass and moments of inertia of the National Aero-Space Plane (NASP). Shaughnessy et al. (1990) has graphs that define the aerodynamic coefficients for various Mach numbers, angles of attack and deflection angles of the control surfaces. The thrust coefficients and specific impulse are determined for various dynamic pressure values, Mach numbers and fuel equivalence ratios, ϕ. Lastly, the moment of inertia and the Center of Gravity (CoG) are defined for a number of weights. The graphs have been tabulated, which are used to interpolate the coefficients, CoG and moments of inertia. It is assumed that linear interpolation can be used to determine these values. For this study, the graphs have been converted into look-up tables that can be used within the TUDAT environment. With the following interpolation methods these look-up tables are called upon to find the correct value.

Standard Linear Interpolation

For the CoG and moments of inertia, standard linear interpolation is used to determine the values. The value for either can be found with:

$$y = y_0 + (x - x_0)\frac{y_1 - y_0}{x_1 - x_0}, \tag{7.2}$$

where x is the weight of the space plane and y is the CoG or I_{xx}, I_{yy}, I_{zz}. The subscripts 0 and 1 define the known neighboring elements *i.e.*, the values that have been tabulated.

Bilinear Interpolation
For the aerodynamic and thrust coefficients, the interpolation is less straight forward. In the case that the coefficient is dependent on two variables, bilinear interpolation is needed. For instance, the yawing moment dynamic derivative for the roll rate, C_{n_p}, is dependent on the current Mach number and angle of attack. In this case, first the yawing moment dynamic derivative for the current angle of attack is found for the two neighboring Mach numbers via linear interpolation. After that, the yawing moment dynamic derivative is found for the current Mach number. Mathematically, the interpolation can be described with:

$$C_{n_{p_0}} = C_{n_{p_{00}}} + (\alpha - \alpha_0)\frac{C_{n_{p_{01}}} - C_{n_{p_{00}}}}{\alpha_1 - \alpha_0}, \tag{7.3a}$$

$$C_{n_{p_1}} = C_{n_{p_{10}}} + (\alpha - \alpha_0)\frac{C_{n_{p_{11}}} - C_{n_{p_{10}}}}{\alpha_1 - \alpha_0}, \tag{7.3b}$$

$$C_{n_p} = C_{n_{p_0}} + (M - M_0)\frac{C_{n_{p_1}} - C_{n_{p_0}}}{M_1 - M_0}, \tag{7.3c}$$

where M is the Mach number and α is the angle of attack. Subscript 00 and 01 denotes the yawing moment dynamic derivatives for the the lower neighboring Mach number for the lower and upper neighboring angle of attack. Similarly, subscript 10 and 11 are the yawing moment dynamic derivatives for the the higher neighboring Mach number for the lower and upper neighboring angle of attack. Thus, subscript 0 and 1 denotes the yawing moment dynamic derivatives for the current angle of attack, and the lower and upper neighboring Mach number.

Trilinear Interpolation
Several coefficients exist that are dependent on three different variables. One of these is the yawing moment coefficient due the the rudder, $C_{n,dr}$, which is dependent on the angle of attack, the deflection angle of the rudder and the Mach number. In this case, first $C_{n,dr}$ is found for the current deflection angle, for the two neighboring angle of attacks and for the two neighboring Mach numbers. After that $C_{n,dr}$ is found for the current angle of attack and for the two neighboring Mach numbers. Finally, the current $C_{n,dr}$ is found. Mathematically, this can be written by:

$$C_{n,dr_{00}} = C_{n,dr_{000}} + (\delta_{\mathrm{dr}} - \delta_{\mathrm{dr}_0})\frac{C_{n,dr_{001}} - C_{n,dr_{000}}}{\delta_{\mathrm{dr}_1} - \delta_{\mathrm{dr}_0}}, \tag{7.4a}$$

$$C_{n,dr_{01}} = C_{n,dr_{010}} + (\delta_{\mathrm{dr}} - \delta_{\mathrm{dr}_0})\frac{C_{n,dr_{011}} - C_{n,dr_{010}}}{\delta_{\mathrm{dr}_1} - \delta_{\mathrm{dr}_0}}, \tag{7.4b}$$

$$C_{n,dr_{10}} = C_{n,dr_{100}} + (\delta_{\mathrm{dr}} - \delta_{\mathrm{dr}_0})\frac{C_{n,dr_{101}} - C_{n,dr_{100}}}{\delta_{\mathrm{dr}_1} - \delta_{\mathrm{dr}_0}}, \tag{7.4c}$$

$$C_{n,dr_{11}} = C_{n,dr_{110}} + (\delta_{\mathrm{dr}} - \delta_{\mathrm{dr}_0})\frac{C_{n,dr_{111}} - C_{n,dr_{110}}}{\delta_{\mathrm{dr}_1} - \delta_{\mathrm{dr}_0}}, \tag{7.4d}$$

$$C_{n,dr_0} = C_{n,dr_{00}} + (\alpha - \alpha_0)\frac{C_{n,dr_{01}} - C_{n,dr_{00}}}{\alpha_1 - \alpha_0}, \tag{7.4e}$$

$$C_{n,dr_1} = C_{n,dr_{10}} + (\alpha - \alpha_0)\frac{C_{n,dr_{11}} - C_{n,dr_{10}}}{\alpha_1 - \alpha_0}, \tag{7.4f}$$

$$C_{n,dr} = C_{n,dr_0} + (M - M_0)\frac{C_{n,dr_1} - C_{n,dr_0}}{M_1 - M_0}, \tag{7.4g}$$

where M is once again the Mach number and α is the angle of attack. Additionally, the deflection of the rudder is denoted by δ_{dr}.

7.1.3. Derivative Coefficient Approximation

In Section 6.2 the determination of the desired angle of attack, required equivalence ratio that is used as a means to throttle the engine, and required deflection angles of the control surfaces has been discussed. The determination of these control parameters was possible when the derivative of certain aerodynamic coefficients and the thrust coefficient were defined with respect to the angle of attack, control surface deflection or equivalence ratio, respectively. The derivative of the coefficients is not given in the technical report by Shaughnessy

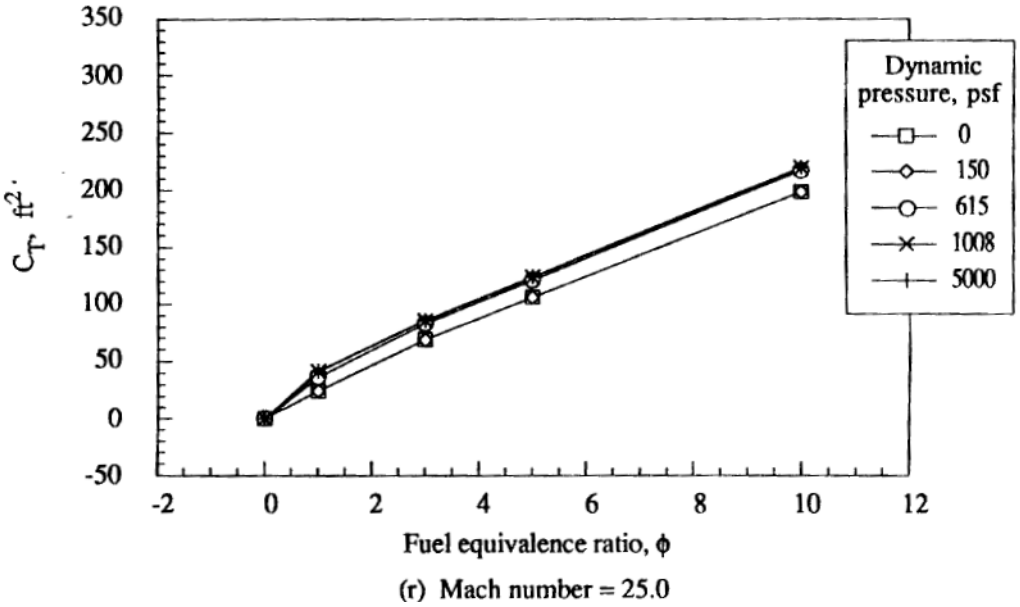

Figure 7.2: Example of a graph that gives information about the thrust coefficient of the NASP (Shaughnessy et al., 1990).

et al. (1990). Instead, the derivative of the coefficients is approximated using numerical differentiation methods. In Figure 7.2, an example is given of the graphs provided for the NASP. In this figure, it can be seen that the thrust coefficient is dependent on the equivalence ratio, dynamic pressure, and Mach number. The derivative of the thrust coefficient with respect to the equivalence ratio can be approximated by using forward, backward or central difference methods (Klees and Dwight, 2014). Additionally, not all coefficient vary linearly between the minimum and maximum angle of attack, deflection angle of the control surface or equivalence ratio. For this reason, it is chosen to approximate the derivative of the coefficients at each node and to use trilinear interpolation to find the derivative of the coefficient for the current angle of attack, deflection angle of the control surface or equivalence ratio.

As an example, the method to obtain the thrust coefficient derivative with respect to the equivalence ratio is explained. For the first node, which corresponds to an equivalence ratio of zero, the derivative is approximated by using forward difference:

$$C_{T_{\phi_0}} = \frac{C_{T_1} - C_{T_0}}{\phi_1 - \phi_0}, \tag{7.5}$$

where $C_{T_{\phi_0}}$ is the derivative of the thrust with respect to the equivalence ration at the first node, and C_{T_0} and C_{T_1} are the thrust coefficient at the first and second node. Similarly, ϕ_0 and ϕ_1 denote the equivalence ratio at the first and second node. For the derivative at the last node backward difference is used:

$$C_{T_{\phi_4}} = \frac{C_{T_4} - C_{T_3}}{\phi_4 - \phi_3}. \tag{7.6}$$

For the nodes in the middle central difference is used. For example for the third node:

$$C_{T_{\phi_3}} = \frac{C_{T_4} - C_{T_2}}{\phi_4 - \phi_2}. \tag{7.7}$$

With these methods the derivative of the thrust coefficient with respect to the equivalence ratio is defined for each node. As was mentioned earlier, the derivatives are defined for each node, and are still dependent on the Mach number, dynamic pressure and equivalence ratio. Thus, in order to retrieve the derivative, trilinear interpolation is used to determine the derivative of the coefficient during flight for a specific Mach number and dynamic pressure, and equivalence ratio. The derivative of the aerodynamic coefficients with respect to the angle of attack and control surface deflections, which are discussed in Section 6.2.1, are found in a similar fashion.

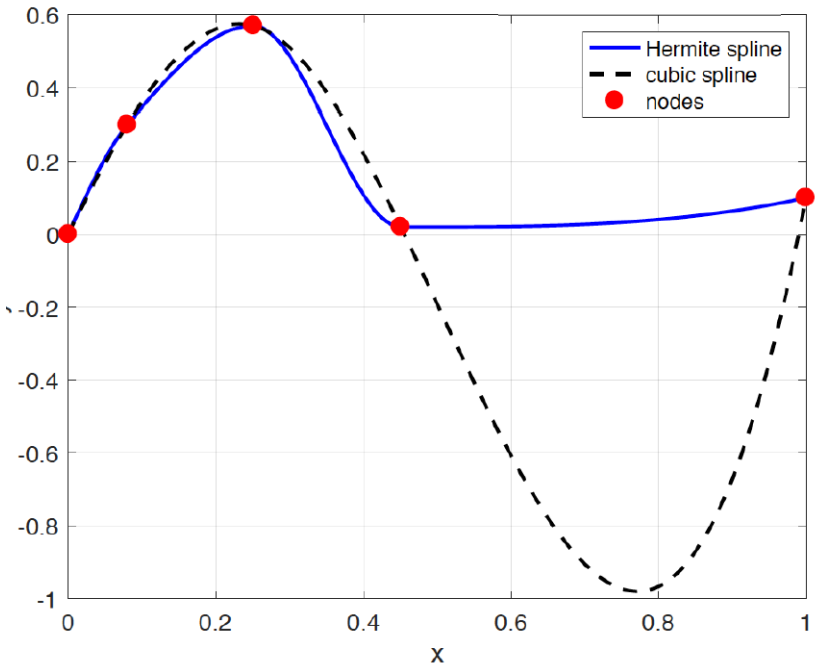

Figure 7.3: Demonstration of the performance of a Hermite spline compared to a cubic spline (Mooij and Dirkx, 2020).

7.1.4. Reference Trajectory

In Chapter 5 it was explained that the optimal control problem is converted into a NonLinear Programming (NLP) problem. Nodes would be defined at which the control parameters would be defined. To define a reference trajectory based on the control parameter at these nodes, an interpolation method is needed. The interpolation will result in a continuous function *i.e.*, the control parameters are defined along the entire ascent trajectory.

For the reference trajectory, a continuous function needs to be defined. Using linear interpolation introduces discontinuities in the gradient, at the control nodes (Mooij and Dirkx, 2020). Thus, a spline could be used to remove the discontinuity. However, using a cubic spline might introduce large oscillations in the reference trajectory, see Figure 7.3. Instead, a Hermite spline is used, which does not have oscillations. The cubic Hermite polynomial for a given interval is given by:

$$\begin{aligned} p_i(x) = y_i\left(1+2\frac{x_i-x}{x_i-x_{i+1}}\right)\left(\frac{x-x_{i+1}}{x_i-x_{i+1}}\right)^2 + y_{i+1}\left(1+2\frac{x_{i+1}-x}{x_{i+1}-x_i}\right)\left(\frac{x-x_i}{x_{i+1}-x_i}\right)^2 \\ +d_i(x-x_i)\left(\frac{x-x_{i+1}}{x_i-x_{i+1}}\right)^2 + d_{i+1}(x-x_{i+1})\left(\frac{x-x_i}{x_{i+1}-x_i}\right)^2, \end{aligned} \tag{7.8}$$

where d_i and d_{i+1} are the derivatives of the two nodes, and x and y denote the input and output values. The derivative can be influenced by introducing a derivative that is weighted (Mooij and Dirkx, 2020). The weighting of the derivative ensures a smooth transition of the derivative from node to node. The computation of the weighted derivative is in this case divided into three separate situations. In the first situation both the left and right slope δ_k and δ_{k+1} are positive. The weighted derivative is in this situation expressed by:

$$d_k = \begin{cases} \dfrac{\delta_k + \frac{\delta_k+\delta_{k+1}}{2}}{2} & \text{if } \delta_k < \delta_{k+1} \\ \dfrac{\delta_{k+1} + \left(\frac{\delta_k+\delta_{k+1}}{2}\right)}{2} & \text{if } \delta_{k+1} \geq \delta_k \end{cases}. \tag{7.9}$$

In the situation where both slopes are negative the derivative is computed with:

$$d_k = \begin{cases} \dfrac{\delta_k + \dfrac{\delta_k + \delta_{k+1}}{2}}{2} & \text{if } \delta_k > \delta_{k+1} \\ \dfrac{\delta_{k+1} + \left(\dfrac{\delta_k + \delta_{k+1}}{2}\right)}{2} & \text{if } \delta_{k+1} \leq \delta_k \end{cases}. \tag{7.10}$$

Finally, when the left and right slope of the node are opposite in sign, the derivative is set to zero:

$$d_k = 0.0, \tag{7.11}$$

which ensures that no overshoot occurs at the node (Mooij and Dirkx, 2020).

With the Hermite interpolation method two different continuous function are constructed. The first defines the flight path angle as a function of altitude between 0 km altitude, which is the launch altitude, until the altitude where the pull up phase starts. The second defines the angle of attack as a function of altitude between the altitude where the pull up is initiated and the altitude where the engine is turned off.

During the investigation of the performance of the reference trajectory, simulations were observed where the reference flight path angle would become negative. The negative flight path angle caused a decrease in altitude, which would mean that the flight path angle would become positive again. This resulted in the space plane oscillating around the altitude where the reference flight path angle would go negative. It was noted that this scenario could occur due to the weighted derivative that has been described previously. In order to mitigate the chance of this occurrence, it is chosen to not weight the derivative of the flight path angle when the reference flight path angle becomes smaller than 5 degrees. In these cases, the derivative of the reference flight path angle is computed with:

$$d_k = \begin{cases} \delta_k & \text{if } \delta_k > 0 \wedge \delta_{k+1} > 0 \\ \delta_{k+1} & \text{if } \delta_k \leq 0 \wedge \delta_{k+1} \leq 0 \\ 0.0 & \text{else} \end{cases}. \tag{7.12}$$

7.2. Simulation Architecture

The software used for the simulation of the ascent trajectory is a combination of a software package called TUDAT and newly implemented modules. According to the TUDAT website: *The TU Delft Astrodynamics Toolbox (TUDAT) is a powerful set of C++ libraries that support astrodynamics and space research. One of the key strengths within TUDAT is its ability to combine such libraries in a powerful simulator framework. Such framework can be used for a wide variety of purposes, ranging from the study of reentry dynamics to interplanetary missions.*[1]

The TUDAT software package has already implemented a number of models and methods that have been explained thus far. First of all, the environmental models that have described in Section 4.1 are present in TUDAT. Second of all, the numerical methods that are used to integrate the state, interpolate the vehicle data, and interpolate the reference trajectory that have been described in the previous section are also present. Last of all, the reference frames and transformation matrices between the reference frame, that have been discussed in Section 3.1, the transformations between Cartesian, spherical and Kepler elements, and a method to compute all necessary angles for the transformation matrices is present. What is missing in TUDAT is the entire vehicle model, which includes the aerodynamics, thrust and mass models, and the G&C system. Additionally, the optimization toolbox Parallel Global Multiobjective framework for Optimization (PaGMO) is integrated in TUDAT. This means that after integration of the vehicle model, the simulation and optimization of the ascent can be done by TUDAT and PaGMO, respectively.

7.2.1. Vehicle Model Integration

The vehicle model that has been integrated in the TUDAT package is a conceptual vehicle, called the National Aero-Space Plane (NASP) (Shaughnessy et al., 1990). The vehicle model, as explained in Section 4.2, has details about the aerodynamics, thrust and mass of the vehicle. The vehicle model provides information about the aerodynamic and thrust forces and moments, and the G&C and moments of inertia. The objective of the vehicle model is to provide information about the vehicle that is necessary to compute the state derivative, which is used to propagate the translational, rotational and mass state. An overview of the vehicle model is

[1] Tudat, Tudat Space: Documentation, accessed on 23 Jun 2021 `https://tudat-space.readthedocs.io/en/latest/`

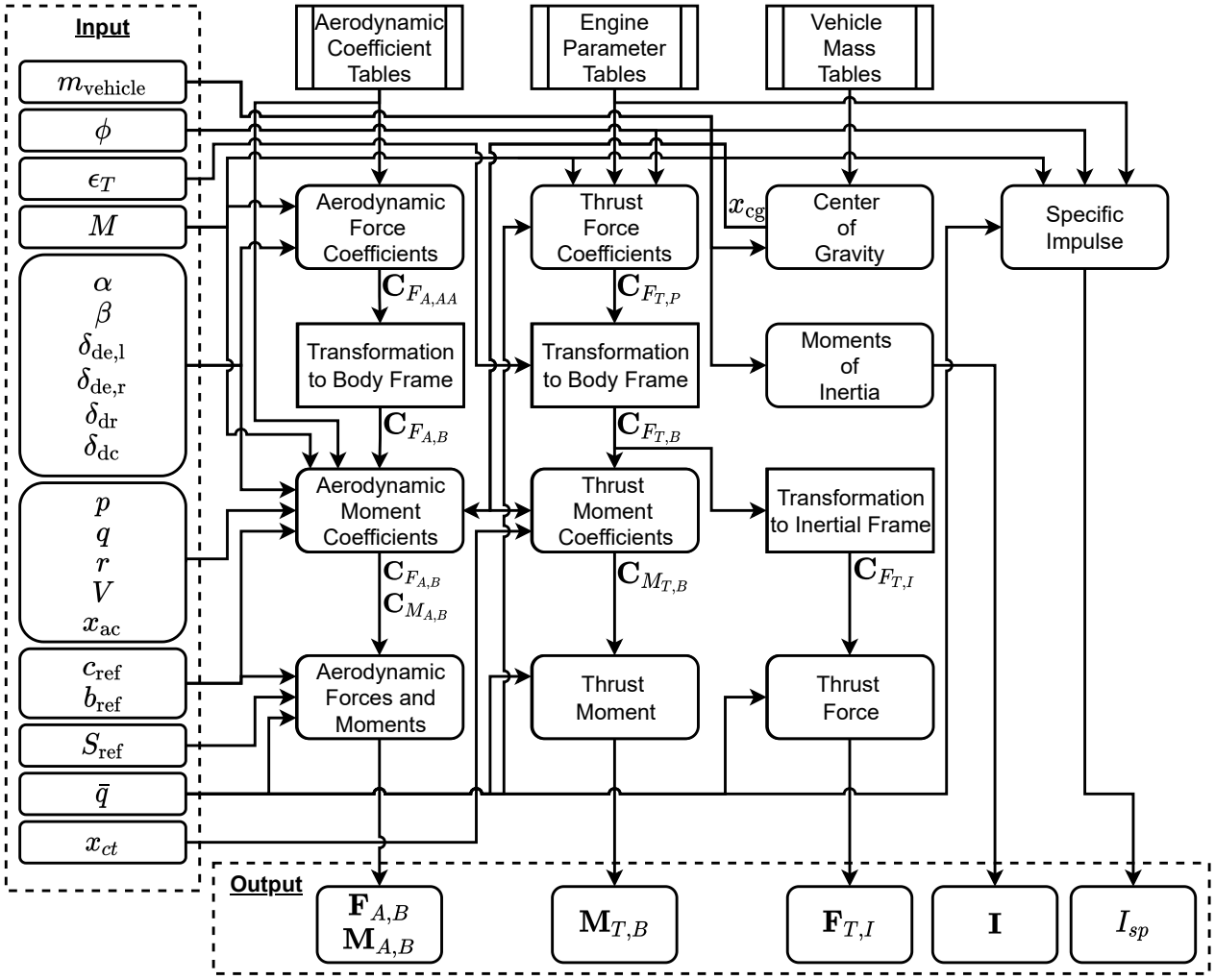

Figure 7.4: Overview of the inputs and outputs of the space plane model.

seen in Figure 7.4. The vehicle model takes information about the state of the vehicle, such as the orientation, angular velocity, translational velocity and mass of the space plane. Additionally, atmospheric information such as the dynamic pressure, which is a function of the altitude, and the Mach number, which is a function of the velocity and altitude of the space plane, are provided. Furthermore, vehicle system information is needed to compute the outputs of the vehicle model. Some of these are constants, such as the chord length, c_{ref}, reference span, b_{ref}, and reference area, S_{ref}. Other variables are the control surface deflection, δ and equivalence ratio, ϕ, which are computed and updated by the G&C system.

The resulting model uses all that information to compute the aerodynamic forces and moments, expressed in the body reference frame. The aerodynamic forces need to be expressed in the inertial frame to be used in the EoM. However, TUDAT transforms these forces by itself and requires the forces to be expressed in the same frame as the aerodynamic moments. The thrust forces are not inherently transformed by TUDAT to the inertial reference frame. Thus, the thrust force vector is first expressed in the propulsion frame, where it is assumed that the thrust is acting along the x_P-axis. Then the vector is transformed to the body frame with the thrust elevation angle if the Thrust Vector Control (TVC) is active. Finally, the thrust force is transformed to the inertial reference frame with a transformation matrix that is already available in TUDAT. The retrieval of the thrust coefficient and specific impulse require the same variables. Namely, the dynamic pressure, Mach number and equivalence ratio. For this reason, the retrieval of these two parameters are handled together in the engine module of vehicle model. The specific impulse is retrieved and used to compute the mass rate of the fuel used by the engine to propagate the mass of the vehicle. The thrust moment is computed with the thrust coefficient vector expressed in the body reference frame. TUDAT does not have a simple method to

include a moment induced by the engine. Thus, the thrust moment coefficient is computed in the aerodynamic coefficient interface. The interface usually retrieves the aerodynamic forces and moments, expressed in the body frame. In the vehicle model presented, the thrust moment coefficients are added to the interface, which is normalized to ensure that the typical aerodynamic moment equations still apply. Within the coefficient interface, also the moments of inertia are updated based on the mass of the vehicle. The moments of inertia together with the aerodynamic and thrust moments are used to compute the derivative of the angular velocity of the space plane.

7.2.2. Guidance and Control (G&C) System Integration

In the previous subsection it became apparent that the vehicle model requires information about the vehicle, such as the deflection angles of the control surfaces. Furthermore, the equivalence ratio of the engine is needed, which is used to throttle the engine. In Chapter 6 the architecture of the G&C system has been explained in detail, including the algorithms that are used. In this section, the goal is to give the reader insight into the integration of the G&C system together with the vehicle model and how that is further integrated in TUDAT.

The G&C system requires information about the forces and moments that are acting on the space plane. This means that the G&C system requires information about the vehicle, while the vehicle requires information from the G&C system to properly guide and control the vehicle. It is therefore important to understand that both the model and system cannot simply be sequentially integrated. Any changes to the vehicle model will influence the outputs of the G&C system and vice versa. For this reason, the G&C system is integrated directly in the coefficient interface, that has been mentioned previously. An overview of the integration of the vehicle model with the G&C system can be seen in Figure 7.5.

At the start of a time step, the aerodynamic forces and moments and thrust moments are retrieved together with the moments of inertia. The G&C system uses this information, together with an approximation of the gravitational forces acting on the space plane, to initially compute the required equivalence ratio. The change in equivalence ratio means that the thrust coefficient has changed, which influences the EoM. For this reason, the thrust force and moment are updated in the vehicle model and retrieved by the G&C system whenever these are needed. After the equivalence ratio is computed and the thrust moment is retrieved, the thrust elevation angle or canard deflection angle is computed in the trim module. The trim module introduces the second change to the vehicle. Either the deflection angle of the canard is changed or the thrust elevation angle is changed. The dynamics of the changes in control surface deflection or thrust elevation is not taken into account, which means that the changes made will have an immediate impact on the thrust and aerodynamic forces and moments. Thus, after the changes are made by the trim module, the aerodynamic and moments, and the thrust forces and moments are retrieved from the vehicle model. It is assumed that a change in deflection angle of the canard does not necessitate an update of the aerodynamic forces. With the updated thrust forces, the total forces acting on the space plane, where the gravitational forces are approximated, are expressed in the trajectory frame. These are used in the second part of the guidance module where the current and reference flight path and heading angle are assessed. The output are the reference sideslip angle, and desired angle of attack and bank angle, which does not necessitate an update to the forces and moments. From there the first part of the control module computes the desired angular velocities of the space plane. Since the output of the module are not physical changes to the system, no updates are necessary. The last part of the G&C system takes the desired angular velocities and computes the required angular acceleration. The module is the most intricate part of the system, with the most inputs required. The module takes the updated aerodynamic and thrust moments to compute the angular acceleration before the elevons or rudder have changed their deflection angle. With that information the required change in deflection angle of the control surfaces are computed to properly orient the space plane. The output of that module is the updated control surface deflections.

The overview of the integration, Figure 7.5, also gives insight in how the G&C system is used to control the velocity, flight path angle, or angle of attack, depending on the ascent phase. During the first phase the entire G&C system is used, where the maximum allowable velocity together with the reference flight path and heading angle are used to guide the space plane along the trajectory parameters. During the pull up phase, the reference flight path and heading angle are no longer used. Instead, the aerodynamic angles are used as reference, where only the angle of attack is optimized for. The other two reference angles are set to zero. For the final phase, only the orientation of the space plane is controlled, where all reference aerodynamic angles are set to zero.

In summary, the G&C system computes required changes of up to six physical parameters of the space plane that influence the EoM. These parameters are capable of both guiding and controlling the space plane. Furthermore, they are stored in a vehicle system object, which can be retrieved from anywhere within TUDAT.

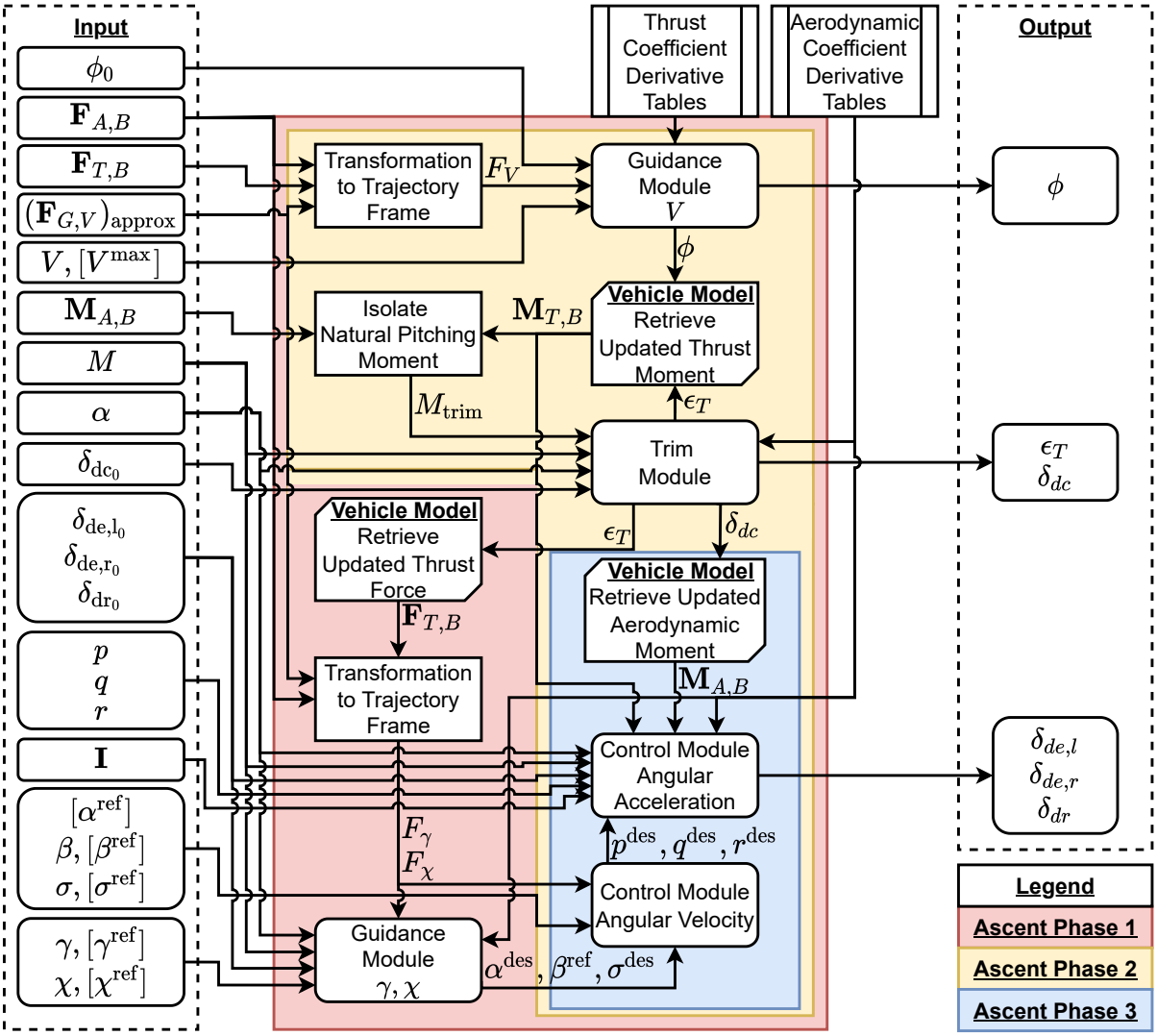

Figure 7.5: Overview of the integration of the Guidance and Control (G&C) system with the vehicle model.

Since the six parameters have been updated, the thrust and aerodynamic forces and moments have been changed. This necessitates the retrieval of them before the state derivative is constructed. This means that after the G&C system has updated the vehicle system, the vehicle model is called upon again to compute all aerodynamic and thrust forces and moments before the state derivative is constructed by TUDAT.

7.2.3. Simulation Overview

With the integration of the vehicle model and the G&C system explained, the final step is to explain the integration into TUDAT. In essence, TUDAT takes the forces and moments that are influenced by the vehicle, computes gravitational forces by itself, constructs environmental models, and integrates and propagates the state until a termination condition is met. The simulation of the ascent trajectory is done mostly by TUDAT. However, a single implementation issue has not been discussed. The integration of the G&C system with the vehicle model would normally mean that the chosen integrator, which is implemented in TUDAT, would compute required changes to the vehicle parameters every intermediate time step. As was discussed previously, the RK4 integrator computes the state derivative four times and combines that to compute the actual state derivative. The G&C system is a computationally heavy part of the entire software, which would result in more than a doubled simulation time. Furthermore, the changes that have been implemented for each intermediate time step would not be recorded by TUDAT, which makes it impossible to assess what was occurring. For these reasons, it was necessary to ensure that the G&C system only computes required changes before the state is integrated. Fortunately, at the start of a new time step a large number of variables are updated. This includes

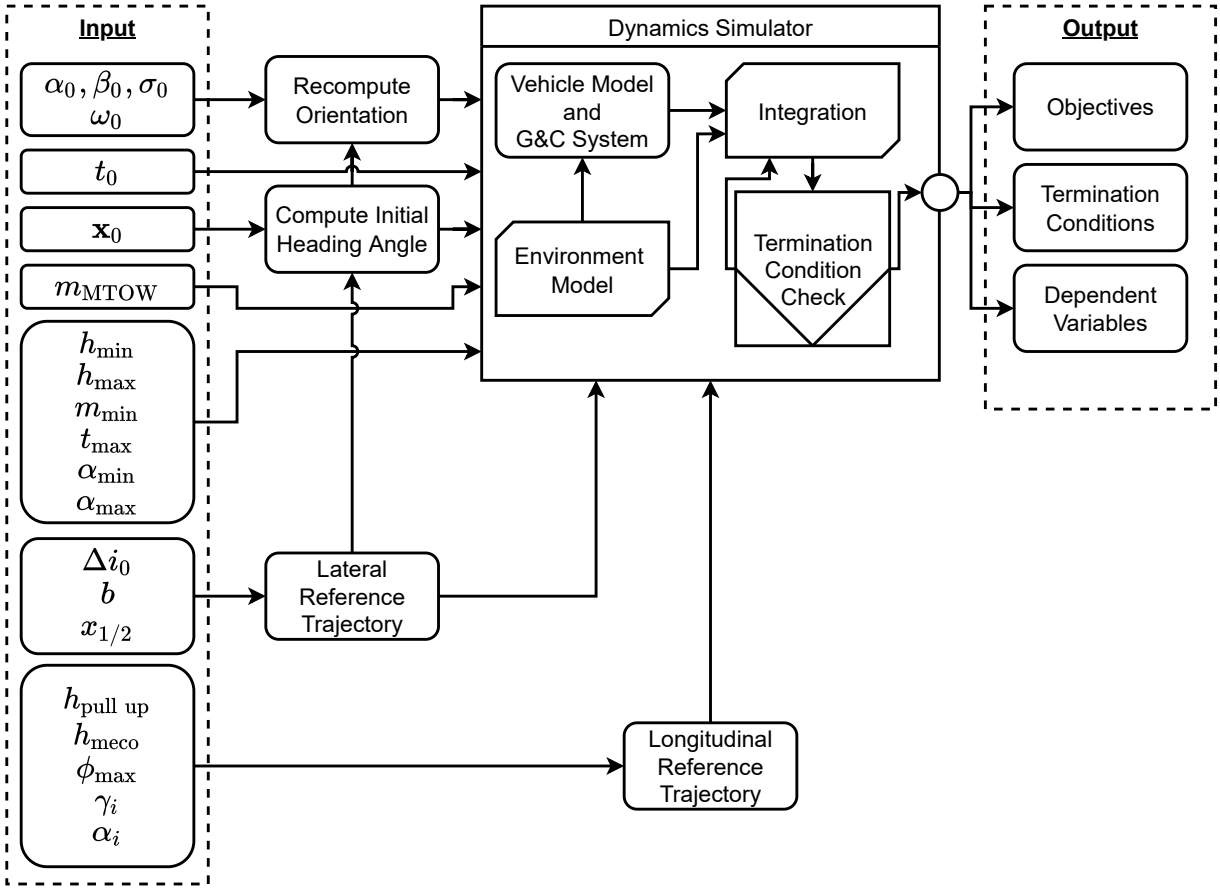

Figure 7.6: Simulation overview with the integration of the vehicle model and G&C system within TUDAT.

all variables that are required for the simulation, which would have changed due to the new state. When these variables are updated, also the coefficient interface is accessed to update the aerodynamic force and moment coefficients. Thus, when this update occurs the G&C system is accessed to compute the required changes to the vehicle. The additional times, that the coefficient interface is accessed to compute the intermediate time steps, the G&C system is not active *i.e.*, the vehicle parameters are not recomputed.

With the aforementioned implementation issue resolved, the total simulation architecture can be explained. A simplified overview can be given of the simulation architecture, with details about the integration of the vehicle model within TUDAT, see Figure 7.6. The goal of the simulation is to propagate the state to a termination condition. The entire initial state is constructed from the initial translational, rotational and mass state. Furthermore, the initial time is used as an input, since a change in initial time will change the angle between the rotational frame with respect to the inertial frame. A change of initial time can be used to simulate a delayed or advanced launch, in Chapter 8 this phenomena will be discussed in a more detailed manner. The initial state will be altered since the initial heading angle will change due to the initial target inclination, which can vary due to the transcription method described in Section 5.3. With the new initial heading angle, also the initial orientation of the space plane will have to be reconstructed. The new orientation can be found by constructing the transformation matrix between the inertial and body frame. The entire transformation matrix can be decomposed to give flexibility over intermediate angles, such as the aerodynamic angles (α, β, σ) and trajectory angles (γ, χ). With the recomputed translational and rotational state, the dynamics simulator can be started. The dynamics simulator takes the aforementioned vehicle model, with integrated G&C system, and the environmental model to construct the state derivative of the state. The state derivative is used to propagate the state until a termination condition is reached. Afterwards, the objectives and termination conditions are computed and stored, together with various dependent variables that can be used to investigate the ascent trajectory.

7.2.4. Optimization Overview

The global and local optimization of the ascent trajectory, which can also include a delayed or advanced launch, is done by the optimization library PaGMO. The library has many optimization algorithms included for global and local optimization. The optimization investigates a population of decision vectors, that is composed of a number op optimization parameters. The simulation, discussed previously, simulates the ascent of the space plane and computes the objective values. This means that each individual in a population is 'scored'. With the objectives values, the population is evolved using selection processes discussed in Section 5.1. The population is evolved for a predetermined amount of time, where for each generation the objective values and population decision vectors are stored.

An overview of the integration of the optimization and simulation software can be seen in Figure 7.7. Here it can be seen that an initial population is generated based on the search space for the different optimization parameters. Afterwards, the population information is used by the simulation software to compute the objective values, which in turn are used to assess the current generation of the population. After the maximum generation is reached, the objective and population information is stored, which can be used to assess the individuals in the population. Furthermore, all generations are stored, which can be used to assess the history of the 'best' individual. This information can be valuable to assess if the best individual has recently been improved upon or not.

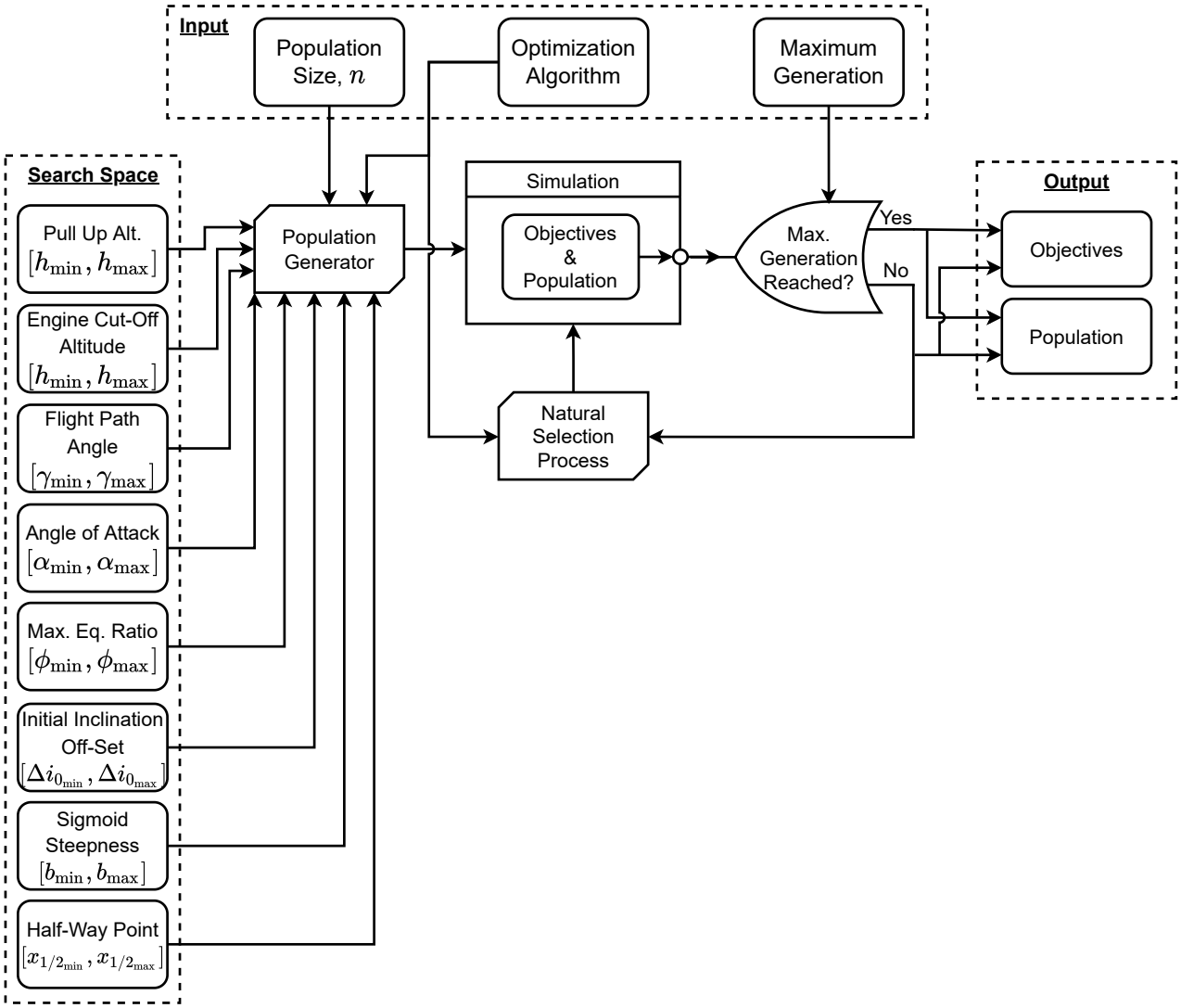

Figure 7.7: Overview of the integration of the optimization and simulation software.

8

Results

In this chapter the results that have been obtained will be discussed. First of all, a brief summary is given of the optimization strategy and settings that have been used, and the initial state that has been used to start the simulation of the ascent. Second of all, the optimization of the longitudinal ascent is presented. The results from this optimization will serve as a baseline for the lateral optimization. Third of all, the results from the lateral motion optimization is presented, where both global optimization and local refinement are discussed. Finally, the results are analyzed, by computing the ΔV obtained by the space plane, and compared to a simple Right Ascensions of the Ascending Node (RAAN) change by a satellite.

8.1. Optimization Strategy

The optimization of the ascent trajectory of the space plane is divided into two parts. The first part will only analyze the space plane, defined in six Degrees of Freedom (DoF), where the optimization parameters exclude the lateral motion parameters. In essence, this means that the space plane is only optimized for longitudinal motion, where bank angle and sideslip angle are commanded to be zero throughout the entire ascent. Initially, an investigation was made in the capabilities of the Guidance and Control (G&C) system to follow the reference flight path angle. The results from this investigation showed that the search space for the flight path angle could be reduced, which improves convergence of the optimization algorithm.

In the second part, the bank angle is no longer commanded to zero. Instead, the lateral motion is defined using a transcription method, which uses the formulas described in Section 5.3. The transcription method produces a reference heading angle, which results in a commanded bank angle to steer the space plane to that heading angle. With the space plane free to maneuver, the launch time can be manipulated to change the rotation of the Earth with respect to the inertial frame. By changing the initial launch time, without changing the launch longitude and latitude, the space plane can be considered to have a delayed or advanced launch.

8.1.1. Optimization Settings

For both the longitudinal ascent, as well as the ascent that includes lateral motion, similar optimization settings will be used. This means that the optimization algorithm, its settings and the population size and maximum number of generations is not changed. The optimization algorithm settings are summarized in Table 8.1.

The methods of obtaining the translational and rotational initial state have been described in Section 5.3. The initial state of the space plane will be changed as little as possible. The only changes made to the initial state is to the initial time and the initial heading angle. The latter change means that the orientation of the space plane with respect to the inertial planetocentric reference frame is changed as well. The change in heading angle ensures that the space plane does not have to initiate a bank maneuver at the start of the simulation. Thus, it is assumed that the space plane is free to have a launch heading angle anywhere

Table 8.1: Optimization algorithm settings.

Optimization Algorithm	Population Size	Maximum Generations	Seeds
MOEA/D	300	500	$(100, 200, 300)$

Table 8.2: Overview of the initial translational state of the space plane, defined in spherical elements.

Spherical Element	Value	Unit
Distance	R_E	[km]
Longitude	23.433	[deg]
Latitude	0.0	[deg]
Velocity	170.0	[m/s]
Flight Path Angle	5.0	[deg]
Heading Angle	[0.0, 90.0]	[deg]

Table 8.3: Overview of the elements required to define the initial rotational state of the space plane.

Element	Value	Unit
Angle of Attack	5.0	[deg]
Angle of Sideslip	0.0	[deg]
Bank Angle	0.0	[deg]
ω_{x_I}	0.0	[deg/s]
ω_{y_I}	0.0	[deg/s]
ω_{z_I}	$4.18 \cdot 10^{-3}$	[deg/s]

Table 8.4: Overview of the initial time range, space plane take-off weight and vehicle control parameters

Element	Value	Unit
Time	$[-7200.0, 7200.0]$	[s]
Take-Off Weight	$133,800$	[kg]
Canard Deflection Angle	0.0	[deg]
Left Elevon Deflection Angle	0.0	[deg]
Right Elevon Deflection Angle	0.0	[deg]
Rudder Deflection Angle	0.0	[deg]
Equivalence Ratio	0.0	[-]
Thrust Elevation Angle	0.0	[deg]

between 0 and 90 degrees, depending on the initial inclination off-set. The elements that are necessary to define the transliation and rotation initial state is repeated in Tables 8.2 and 8.3. Part of defining the initial state in the inertial frame is defining the initial time, which relates the inertial planetocentric frame with the rotational planetocentric frame. The initial time, as stated previously, is varied to investigate the launch window extension. This investigation is limited to launches that are advanced or delayed by two hours. The range of the initial time, in combination with the space plane take-off weight and vehicle control parameters, are shown in Table 8.4.

The equality constraints that are defined as the termination settings in the simulation model do not vary depending on the inclusion of the lateral motion. However, the target orbit objective is varied to include a target inclination and RAAN. For this reason, the equality constraints are shown here, in Table 8.5, while the objective values will be shown in the respective sections of this chapter. The inequality constraints are not part of the optimization objectives. Instead, the G&C system ensures that the inequality constraints are no longer exceeded. The inequality constraints, which will not vary depending on the optimization, are repeated in Table 8.6.

8.2. Optimization of the Longitudinal Ascent

As mentioned previously, this section will first discuss the capabilities of the G&C system to follow the reference flight path angle. Based on the outcome, the search space for the reference flight path angle will be reduced. After the search space refinement, the results of the ascent trajectory optimization without lateral motion will be presented and discussed.

Table 8.5: Equality constraints defined for the simulation of the space plane ascent trajectory.

Equality constraint	Symbol	Termination Condition	Unit
Altitude	h_{min}	< 0	[km]
	h_{max}	> 120	[km]
Space Plane Mass	m	$< m_{OEW}\ (58.968 \cdot 10^{-3})$	[kg]
Time	T	$> t_0 + 4000$	[s]
Angle of Attack	α_{min}	< -2	[deg]
	α_{max}	> 13	[deg]

Table 8.6: Inequality constraints defined for simulation of the the space plane ascent trajectory.

Inequality constraint	Symbol	Value	Unit
Maximum Dynamic Pressure	$\bar{q}_c$	95,000	[N/m^2]
Maximum Heat Flux	$\dot{Q}_c$	8,000	[kW/m^2]
Maximum Axial Acceleration	n_{a_c}	1	[g_0]

Table 8.7: Overview of the reduced search space for the longitudinal ascent.

Optimization Parameter	# of Parameters	Search Space	Unit
Flight Path Angle	6	[0, 60]	[deg]
Angle of Attack	3	[1, 4]	[deg]
Pull Up Altitude	1	[40, 60]	[km]
Engine Cut-Off Altitude	1	[60, 80]	[km]
Maximum Equivalence Ratio	1	[0, 10]	[-]

8.2.1. Search Space Refinement

In order to assess the capability of the G&C system to follow the reference flight path angle, a Sobol sequence is used to assess all different combinations of flight path angles. The capability of the G&C system is measured with an objective function:

$$f_{\text{GC performance}} = \frac{\int_0^{t_f} (\gamma_{\text{ref}} - \gamma_{\text{actual}}) dt}{\int_0^{t_f} \frac{\pi}{2} dt}, \tag{8.1}$$

where t_f represents the termination time, γ_{ref} the reference flight path angle and γ_{actual} the actual flight path angle of the space plane. This function measures the average difference between the reference and actual flight path angle and relates it to the theoretical maximum flight path angle of 90 degrees. The resulting G&C system effectiveness for the Sobol sequence is shown in Figure 8.1. In the figure, it can be seen that all individuals are colored black. For the observant reader, any individuals of the Sobol sequence that reach the target altitude are colored magenta. Thus, it can be concluded that the Sobol sequence does not produce an individual where the target altitude can be reached. This can be explained by the changes made how the inequality constraints are handled. Previously, these constraints were measured instead of enforced. For the current optimization, these constraints are actively enforced by the G&C system. The figure also shows a correlation between the reference flight path angle at the first control node, γ_0, at 0 km. The figure shows a performance indicator that increases as the reference flight path angle is increased. It is safe to assume from the figure that the G&C system is unable to properly follow a reference flight path angle above 60 degrees. With this conclusion, the search space for the flight path angle can be reduced for the first control node. Furthermore, from the initial optimization done, which is presented in Section 5.2, it can be concluded that after an initial pull up, the flight path angle is reduced significantly to enable the space plane to accelerate at the altitude where the engine is most efficient. Thus, the search space of the subsequent control nodes is also limited to 60 degrees. In Table 8.7 the search space for the optimization of the longitudinal ascent is shown.

8.2.2. Global Optimization Results of the Longitudinal Ascent

With the reduced search space, the optimization of the longitudinal ascent can be performed. For the longitudinal ascent, as was mentioned previously, the guidance module only commands the flight path angle and velocity of the space plane. A reference heading angle is not considered and the bank angle is commanded to be

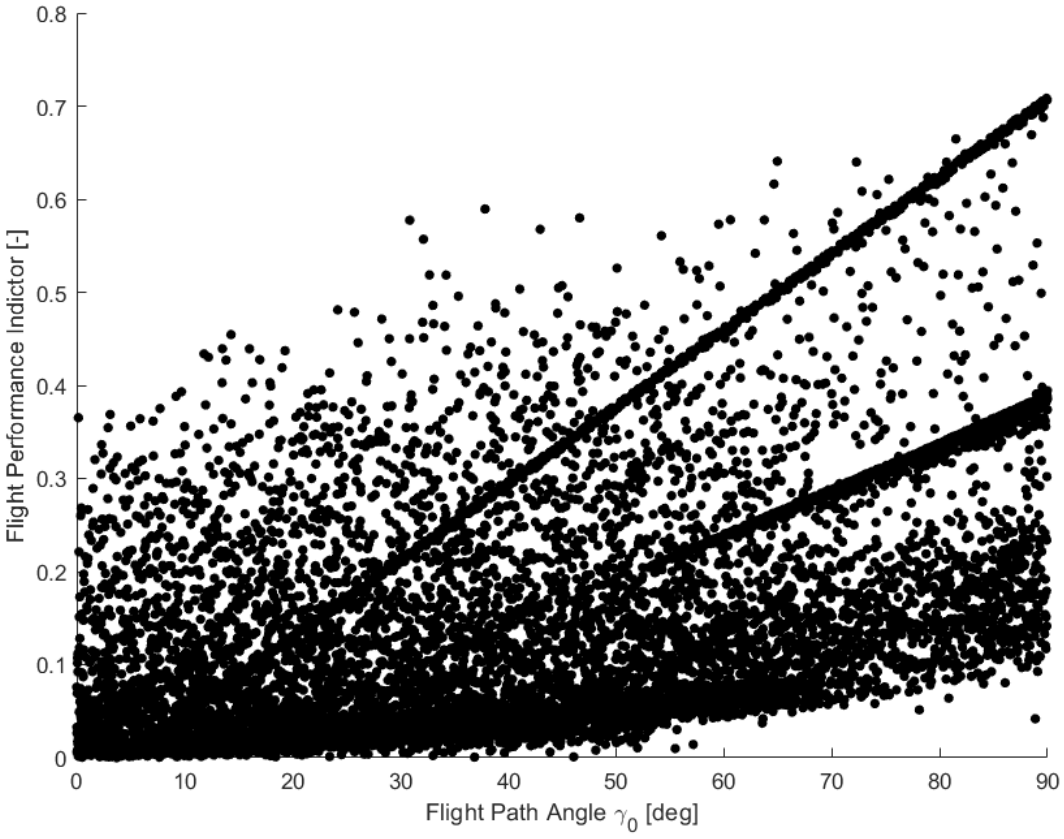

Figure 8.1: Indication of the G&C system performance to achieve the reference flight.

Table 8.8: Overview of the target altitude, velocity and eccentricity that define the target orbit.

Target Orbit	Altitude [km]	Velocity [m/s]	Eccentricity [-]
Value	120.0	7836.3	0.0

zero throughout the entire ascent. The objective of the longitudinal optimization is to find an objective value for the target RAAN, when an advanced or delayed launch is considered. Furthermore, the optimization when lateral motion is included will increase the search space by including the three lateral optimization parameters. Thus, the population of the longitudinal optimization is assessed to refine the search space of the longitudinal optimization parameters.

The optimization will target a circular orbit that is 120 km above the surface of the Earth. As was mentioned in Section 5.2, using the semi-major axis to assess the difference between the reached orbit and the target orbit could result in the optimization stalling around 50 km. Thus, the altitude and velocity are used instead of the semi-major axis, in combination with the eccentricity. The target values are listed in Table 8.8.

With the aforementioned initial state, constraints, target orbit and optimization settings, the optimization of the ascent trajectory that does not include lateral motion is done. Figure 8.2 shows the Pareto front, which is produced by the 500^{th} generation of the Multi-Objective Evolutionary Algorithm with Decomposition (MOEA/D) optimization algorithm. In this figure it can be seen that the propellant objective and the target orbit objective are competing. Reducing one inherently means an increase in the other objective value. Furthermore, a gap can be seen in the Pareto front. When the target altitude is reached an impulsive burn is initiated to attempt to circularize the orbit. The circularization maneuver is modeled as an impulsive shot, which instantly changes the velocity of the space plane and the orbital elements. Thus, it can be concluded that the gap in the Pareto front is caused by this circularization maneuver. The goal of the ascent trajectory is to reach an altitude of 120 km, which means that any individuals that do not reach that altitude should

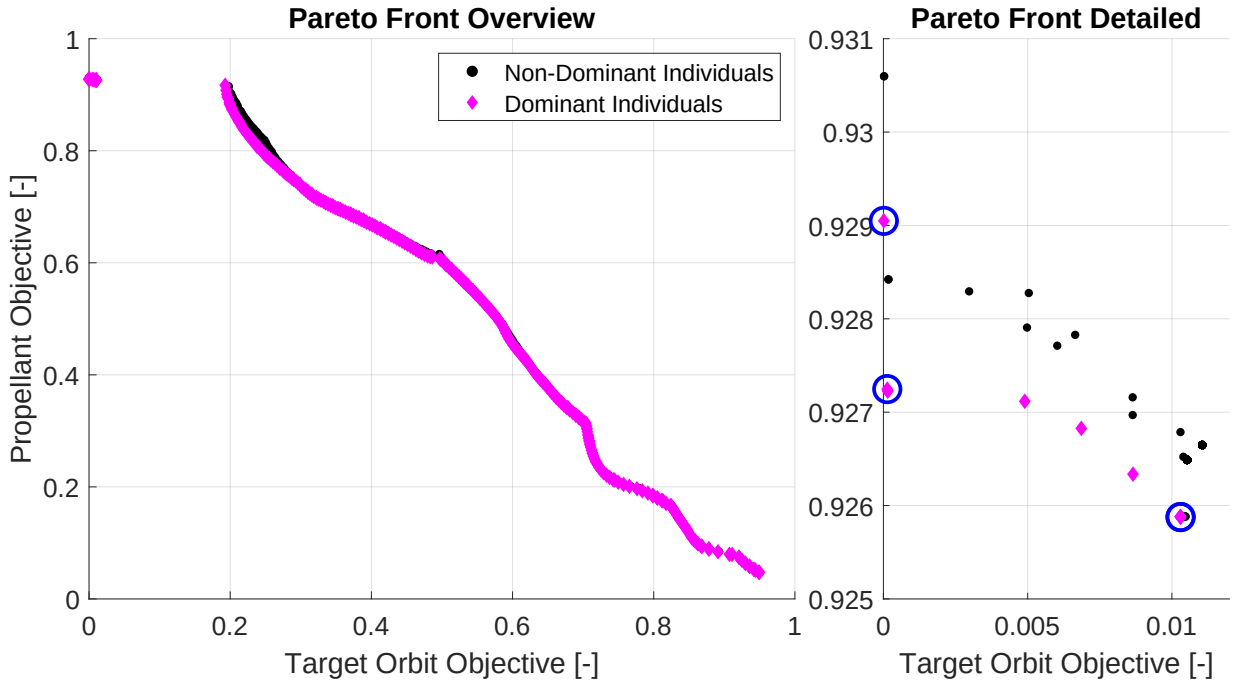

Figure 8.2: Pareto front of the optimization for the longitudinal ascent trajectory. The 500^{th} generation is considered, with all three seeds included in the Pareto front.

not be considered. On the right of the figure, a detailed view is shown with only individuals of the generation that reach the target orbit. Here it can be seen that the target orbit is improved significantly by increasing the used propellant up to a certain point. The figure shows two individuals that have a target orbit objective close to zero, while the propellant used increases significantly.

Figure 8.3 shows the altitude versus velocity plot of the ascent trajectory of three individuals. The first individual is the most efficient ascent trajectory *i.e.*, the ascent trajectory that reaches the target altitude with the least amount of fuel. The other two individuals have a target orbit objective very close to zero, but differ significantly in the amount of fuel used. The selected individuals are marked with a blue circle, which can be seen in Figure 8.2. The space plane is launched with the maximum take-off weight and any propellant not used is assumed to be available for payload. The available payload is computed with:

$$m_{\text{payload}} = (1 - f_1)(m_{\text{MTOW}} - m_{\text{OEW}}), \tag{8.2}$$

where m_{payload} signifies the available payload mass, m_{MTOW} the maximum take-off weight, and m_{OEW} the empty operating weight. In the figure depicting the velocity versus altitude plot, it can clearly be seen that the most efficient individual has a pull up altitude higher than the other two, which results in the space plane to be able to have a higher velocity, when the pull up is initiated, since the heat flux constraint allows a higher velocity. Due to the higher pull up velocity, the final circularization maneuver requires less fuel, which makes this individual more efficient compared to the other two individuals. This is explained by the difference in engine efficiency. The air-breathing engine is more efficient *i.e.*, has a higher specific impulse, than the pure rocket engine used for the circularization. The more efficient engine will use less propellant to achieve the same amount of change in velocity, which makes it beneficial to pull up at an altitude that allows a higher velocity due to the imposed constraints. The downside of the higher pull up velocity can be seen in Figure 8.4. Here it can be seen that the final flight path angle of the most efficient individual reaches the target orbit with a nonzero flight path angle. The circularization maneuver is done in the same direction as the velocity vector, since the angle of attack is zero, which means that a nonzero flight path angle will reduce the effectiveness of the maneuver. The other two individuals do have a flight path angle close to zero, which means that the maneuver ensures that especially the eccentricity goes to zero. This conclusion can also be seen in Figure 8.5, where the most efficient individual does not have a significant change in the eccentricity.

Figure 8.5 also shows the inclination and RAAN that the simulations achieve, when the target altitude is reached. To begin with, it is noted that these elements are not effected by the circularization maneuver. This

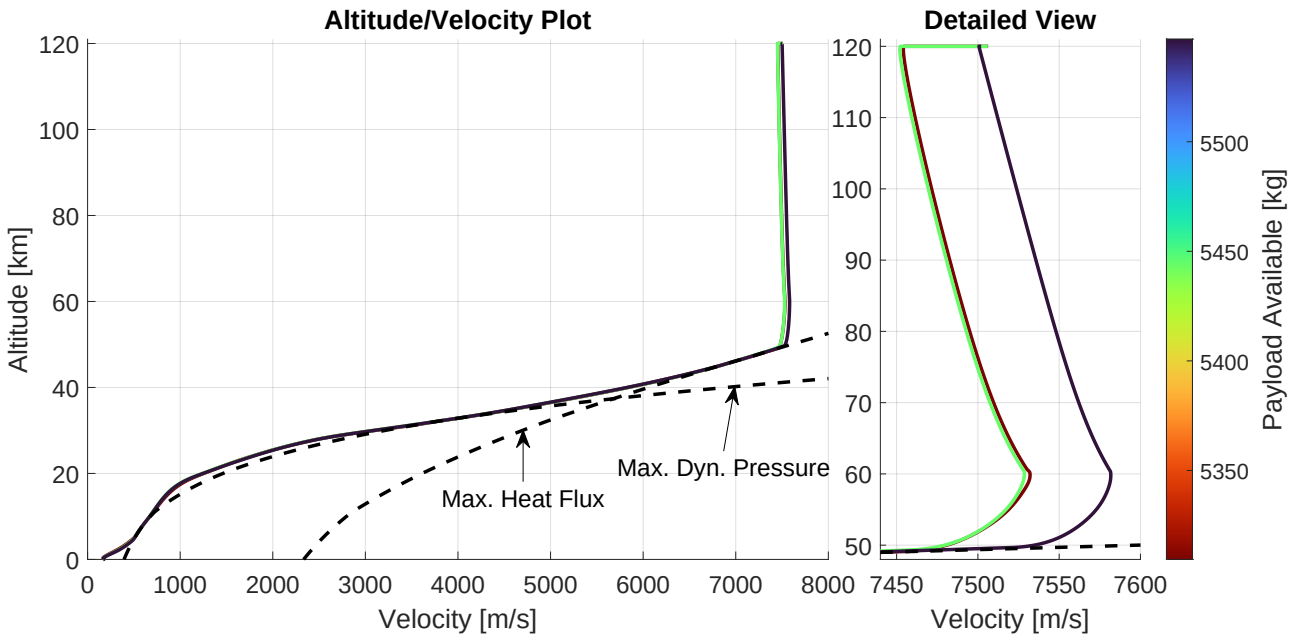

Figure 8.3: Altitude versus velocity plot of three simulations that reach the target orbit.

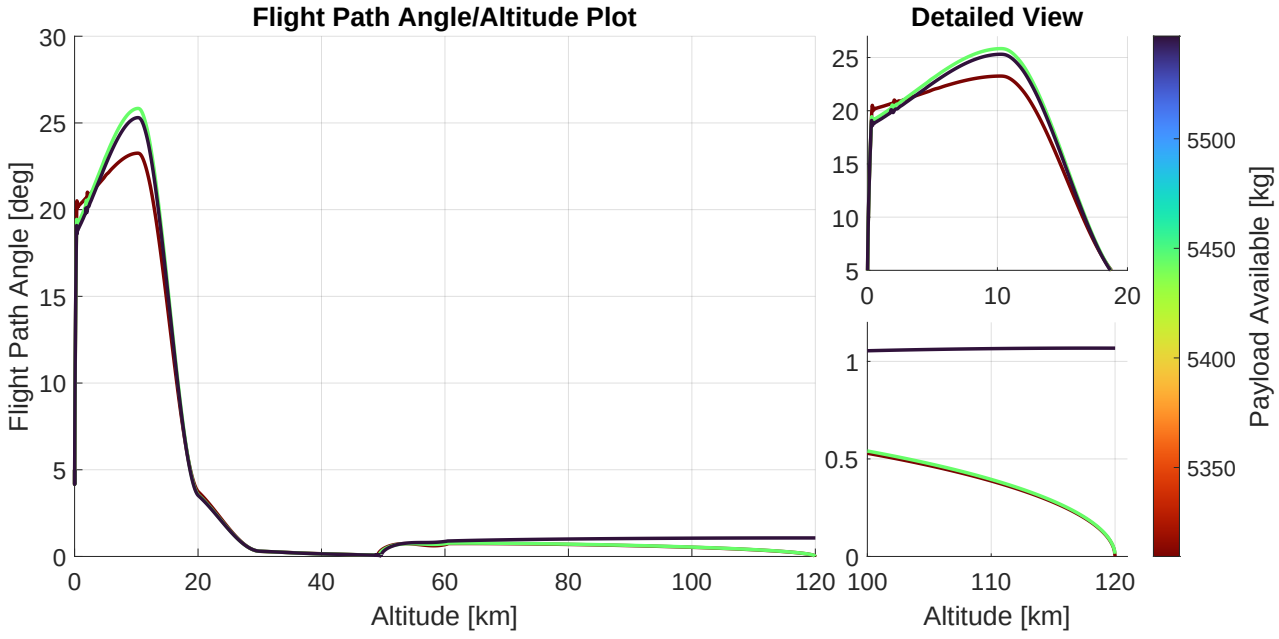

Figure 8.4: Altitude versus flight path angle plot of three simulations that reach the target orbit.

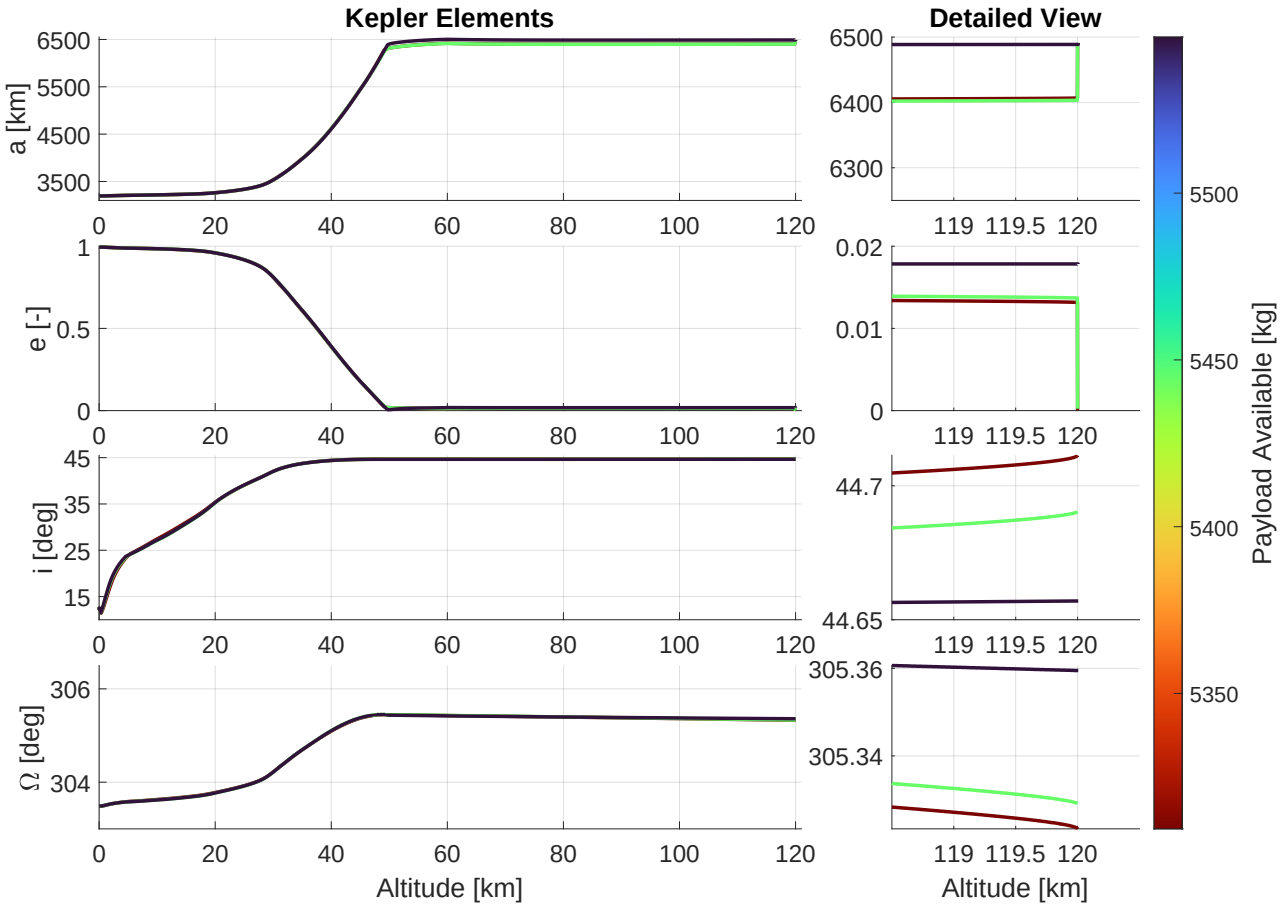

Figure 8.5: Overview of the Kepler elements as a function of altitude for three simulations that reach the target orbit.

is expected since the circularization maneuver is in the direction of the velocity vector. Additionally, the figure shows that the final inclination that the individuals reach is not exactly 45 degrees, which was intended by determining the launch heading angle. The guidance module does not compute a required bank angle, based on the difference between the actual and reference heading angle. Instead, the bank angle is commanded to zero throughout the entire ascent, which could mean that the ascent slightly deviates from the intended inclination angle. Thus, the results from this optimization cannot be used to determine the target RAAN, since both the inclination and RAAN are effected by lateral motion. Instead, it was chosen to use the reference heading angle without a deviation in inclination to determine the achieved RAAN, which can be used to determine the target RAAN when a delayed or advanced launch is considered. The methodology to find the target RAAN is discussed in Section 8.3.1.

In addition to the velocity, flight path angle and orbital elements, the angle of attack of the individuals was investigated. The altitude versus angle of attack plot is shown in Figure 8.6. In this plot two phenomena are depicted that are not intended. The first phenomena is the osciallations that occur just before the pull up maneuver is initiated, which is around 50 km altitude. This phenomena occurs due to improper gains for the flight path angle. Initially, the gain for the flight path angle, $K_{\dot{\gamma}}$ was set to 1.2. After the optimization results were investigated, the gain is tuned back to 0.8, which is also described in Section 6.3. Tuning the gain ensured that the oscillations were minimized. The second phenomena that can be seen is that the reference angle of attack peaks at the end of the pull up phase. However, after the pull up maneuver the orientation of the space plane is controlled theoretically by Reaction Control System (RCS) thrusters, which are not based on actual thrusters. Thus, it is unknown if practically these thrusters would be able to counteract the unstable pitching moment that could occur at higher angles of attack. For this reason, it was chosen to reformulate the reference angle of attack. In a similar fashion as the flight path angle at small angles, the derivative at the nodes is computed without weighting the derivatives itself, see Section 7.1. This ensured that the reference angle of

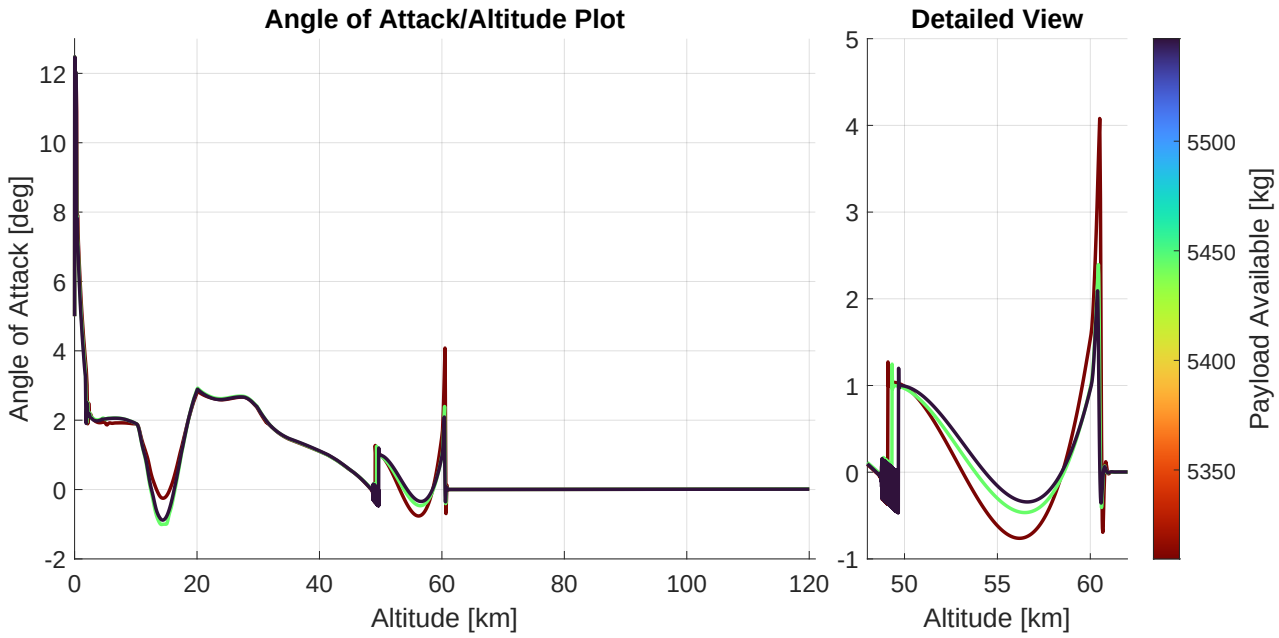

Figure 8.6: Overview of the angle of attack as a function of altitude for three simulations that reach the target orbit.

attack would increase more constantly and slower before the pull up phase would end, which would ensure that an unstable angle of attack would have to be counteracted by the elevons. If these would be unable to counteract the natural pitching moment, the simulation would be terminated before the RCS thrusters take over control of the orientation.

Population Overview

For the population that reach the target altitude, an overview of the population optimization parameters is given. Figure 8.7 shows the search space for the optimization parameters that reach the target altitude, where the optimization parameters are depicted with respect to the target orbit objective and the propellant objective. By depicting the optimization parameters in terms of both objectives, a relation can be discovered between the pull up altitude and the objectives. It can be seen that with a higher pull up altitude, the target orbit objective increases, while the propellant objective decreases. This conclusion was also described when investigating the altitude versus velocity plot in Figure 8.3. The figure gives good insight into the search space. In general, it can be seen that most optimization parameters have a small range, where all optimization parameters are clustered in a small part of the original search space. Based on these optimization parameters a new search space can be defined, which can be used for the optimization where lateral motion is included. However, it should be noted that the changes made to the reference angle of attack necessitate to reevaluate the original search space for these parameters. Additionally, the pull up and engine cut-off altitude have a large search space to ensure that the pull up phase can properly be optimized for. The entire search space, based on the outcome of the longitudinal optimization, can be seen in Table 8.9.

With the new search space, the original angle of attack search space is used. The angle of attack optimization parameters, depicted in Figure 8.7, shows that the angle of attack is very close to 1 degree, which is the border of the search space. This indicates that the search space of the angle of attack should be expanded. However, it is chosen not to expand the search space for the global optimization. Instead, a local refinement will be performed to investigate if expanding the search space for these optimization parameters will yield a better result. The reason to not include the expanded search space for the global optimization is to ensure that the correct pull up altitude is found. As was discussed, the start of the pull up phase is an important optimization parameter that can significantly impact the outcome of the two objective values. By keeping the lower bound of the search space to 1 degree, it is enforced that the pull up starts at the pull up altitude optimization parameter.

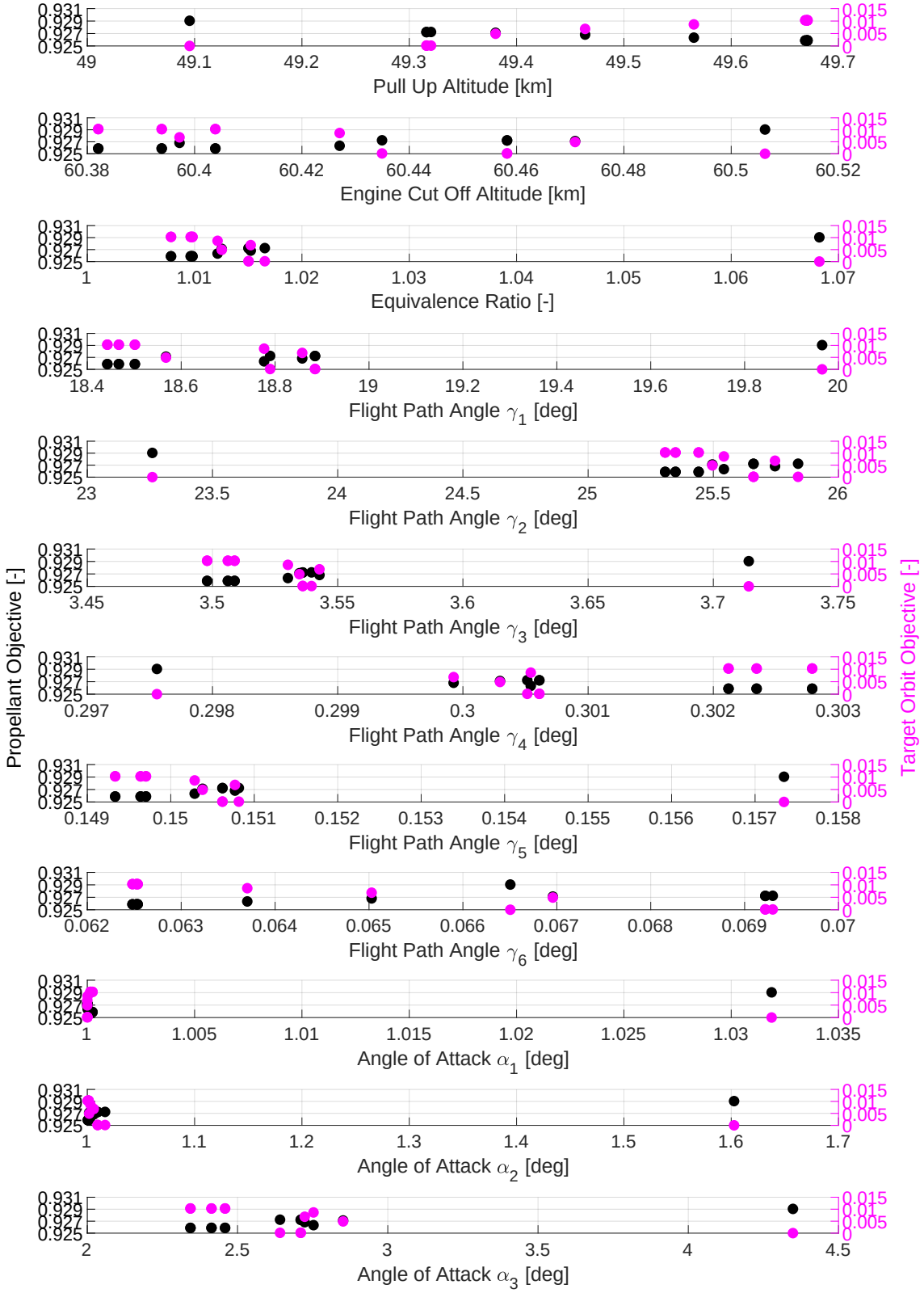

Figure 8.7: Overview of the optimization parameters search space for the individuals that reach the target altitude.

Table 8.9: Overview of the reduced search space for the optimization of the ascent that includes lateral motion.

Optimization Parameter	# of Parameters	Search Space	Unit
Flight Path Angle γ_1	1	[16.0, 24.0]	[deg]
Flight Path Angle γ_2	1	[22.0, 29.0]	[deg]
Flight Path Angle γ_3	1	[2.0, 5.5]	[deg]
Flight Path Angle γ_4	1	[0.0, 0.5]	[deg]
Flight Path Angle γ_5	1	[0.0, 0.5]	[deg]
Flight Path Angle γ_6	1	[0.0, 0.5]	[deg]
Angle of Attack	3	[1.0, 4.0]	[deg]
Pull Up Altitude	1	[45.0, 55.0]	[km]
Engine Cut-Off Altitude	1	[60.0, 80.0]	[km]
Maximum Equivalence Ratio	1	[0.9, 1.5]	[-]

8.3. Optimization of the Ascent with Lateral Motion

The results presented in this section will answer the question what a fuel-optimal trajectory is when a launch window extension is considered. First, the target orbit is determined based on a mock optimization, where the guidance module also steers the heading angle. Afterwards, the methodology to investigate the launch window is discussed. This is followed by the results from the global optimization that has been performed. Lastly, a comparison is made between a change in RAAN by the space plane, with a change in RAAN by the payload itself.

8.3.1. Determination of Target Orbit

As was discussed in the previous section, the final orbit found by the optimization has an inclination close to 45 degrees. However, with the inclusion of lateral motion, the final inclination and RAAN can be manipulated, which means that the guidance module is used to command the heading angle to ensure that the final orbital inclination achieved by an individual is closer to the target value. It is chosen to target an orbital inclination of 45 degrees to assess the capabilities of both an advanced and delayed launch. For this reason, a mock optimization is performed, where the guidance module also commands the heading angle to ensure that the target orbital inclination is achieved. The reference heading angle is computed with Equations 5.24 and 5.25, where the target orbital inclination and the latitudinal position of the space plane is used. It should be noted that the heading angle is not an optimization parameter. It is purely used to ensure that the final orbital inclination is closer to the target value of 45 degrees. Based on the results of the optimization, the RAAN that has been achieved will be used as an objective value, when the heading angle is part of the optimization.

The results of the mock optimization parameter are presented in Figure 8.8. Here the orbital elements of two individuals are shown that reach the target altitude. It can be seen that the inclination that has been achieved is much closer to the target value, compared to the results shown in Figure 8.5. From this it can be concluded that the guidance module is capable of guiding the space plane to the correct inclination. Furthermore, it can be seen that the RAAN that has been achieved has changed due to the inclusion of the reference heading angle. Based on these results, the target objective for the RAAN is selected to be 306 degrees.

8.3.2. Methodology

The extension of the launch window is investigated by advancing or delaying the launch of the simulation. This is done by changing the initial time, which is part of the initial state. By changing the initial time, the orientation of the rotational planetocentric reference frame with respect to the inertial planetocentric reference frame is changed, based on the rotation of the Earth. In essence, the orientation of the frame changes by approximately 15 degrees per hour. Since the launch location of the Earth does not change, the RAAN should also change by approximately 15 degrees. The goal for the optimization of the ascent trajectory that includes lateral motion is to find a trajectory, where the final orbit has the same semi-major axis, eccentricity, inclination and Right Ascensions of the Ascending Node (RAAN), irregardless of the time launched. In order to assess the capabilities of the National Aero-Space Plane (NASP), the initial time is changed ranging between plus and minus two hours, see Table 8.10. Based on the results, the difference in propellant used is compared to assess the added cost in terms of propellant to delay or advance a launch.

The transcription of the reference heading angle uses a deviation in inclination to compute the heading

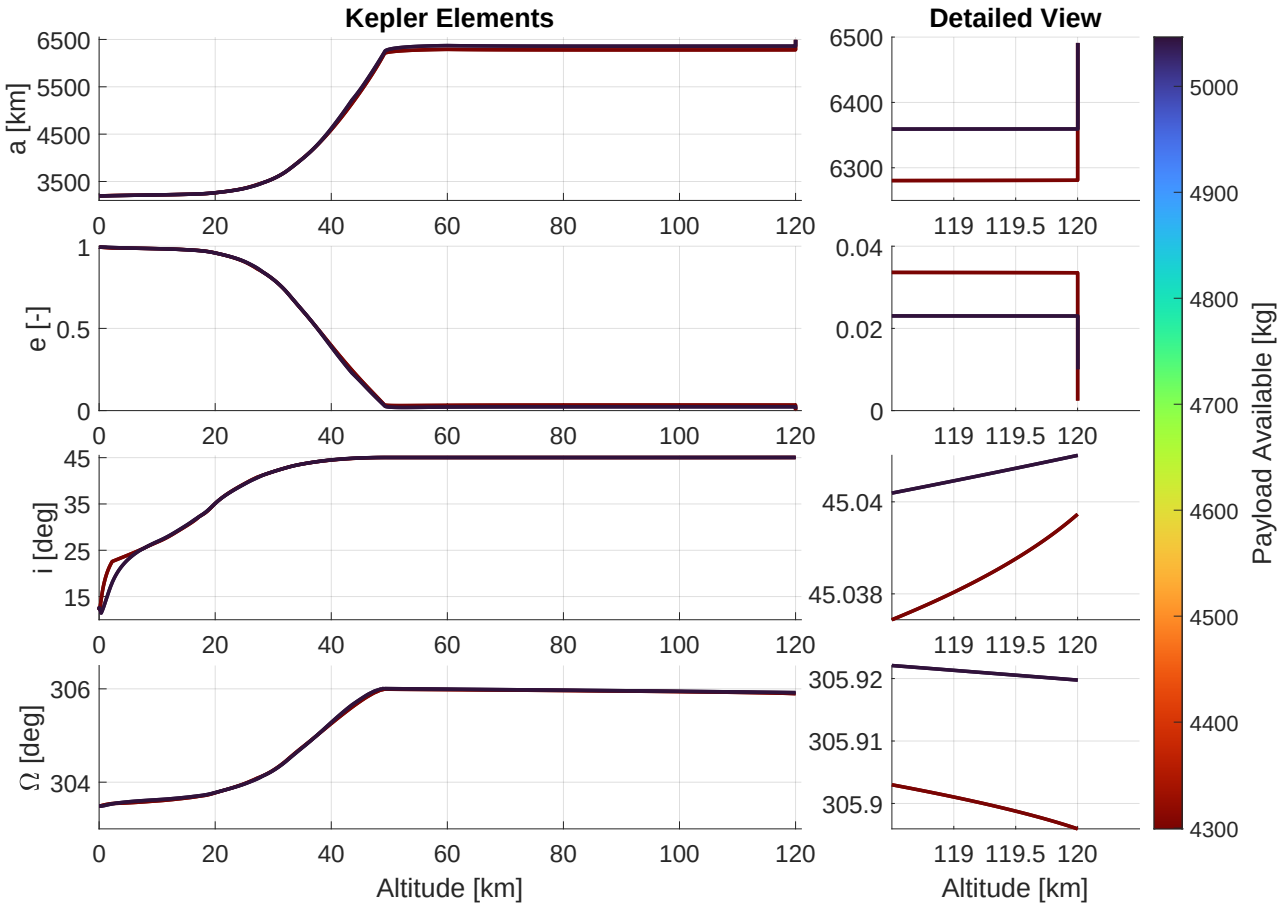

Figure 8.8: Overview of the Kepler elements a a function of altitude for the mock optimization to assess the target orbital inclination and RAAN.

Table 8.10: Overview of the launch times that the ascent trajectory has been optimized for.

Initial Time	$\Delta T0$ [s]	$\Delta T1$ [s]	$\Delta T2$ [s]	$\Delta T3$ [s]	$\Delta T4$ [s]	$\Delta T5$ [s]
Value	0	$\pm$600	$\pm$1200	$\pm$1800	$\pm$3600	$\pm$7200

Table 8.11: Overview of the target altitude, velocity, eccentricity, inclination and RAAN that define the target orbit.

Target Orbit	Altitude [km]	Velocity [m/s]	Eccentricity [-]	Inclination [deg]	RAAN [deg]
Value	120.0	7836.3	0.0	45.0	306.0

angle with respect to the current altitude of the space plane. As was discussed in Section 5.3, a sigmoid function is used to define the deviation in inclination. The sigmoid function varies the deviation in inclination, and ensures the the deviation is zero before the guidance module is turned off. This should ensure that the final inclination that ascent trajectories achieve is always 45 degrees. However, this cannot be guaranteed, since it is unknown what the capabilities are for the space plane to steer the plane to a certain heading angle. For instance, it could occur that the guidance module does not have enough time to steer the space plane to the correct heading angle when the deviation in inclination goes to zero. Thus, it is necessary to include both the inclination and RAAN in the target orbit objective. Based on the results from the mock optimization, the target objective values are presented in Table 8.11. The target orbit objective is computed with Equation 5.30, which includes the two new orbital elements.

The sigmoid function, Equation 5.26, has three variables that determine the shape and magnitude of the function. These variables are used as optimization parameters. The actual reference heading angle uses the

Table 8.12: Overview of the lateral optimization parameters and the search space.

Optimization Parameter	# of Parameters	Search Space	Unit
Δi_0	1	[-45, 45]	[deg]
Steepness, b	1	[2, 5]	[-]
$x_{1/2}$	1	[0.1, 0.9]	[-]

deviation in inclination to compute the inertial heading angle first with Equation 5.29, and transforms that to the rotational frame with Equation 5.25. The search space for the variables of the sigmoid function are shown in Table 8.12. The search space for the lateral motion together with the refined search space shown in Table 8.9 form the complete search space for the optimization of an ascent trajectory that includes a launch window.

8.3.3. Results of the Global Optimization

The results, where lateral motion is included, is split up into two parts. First, the results are discussed for an initial time of $t_0 = 0$ s. This is done to obtain the target orbital elements. The results are also used to obtain a general insight in the behavior of the ascent trajectory when lateral motion is included. Second, the initial time is varied and the results obtained from these optimizations is compared to the control trajectory where the initial time is $t_0 = 0$ s.

Results without Delayed or Advanced Ascent

The Pareto front for the ascent trajectory of a space plane is shown in Figure 8.9. The initial launch time is set to zero seconds, which is the same launch time as the optimization done for the longitudinal ascent. Once again, it can be seen that the two objectives are competing. Furthermore, it can be seen in the detailed view that the target orbit objective can be significantly improved by increasing the propellant used up to a certain point. Any further improvements can only be done by significantly increasing the amount of propellant used. It should be noted that the global optimization technique cannot guarantee that the global minimum of the problem is found (Conway, 2010). Due to the iterative nature of global optimization, it is important to check the convergence of the objective values and to improve upon the solutions with a deterministic optimization algorithm, which will be discussed later. The convergence can be confirmed by assessing the objective values per generation and to find how these have evolved. Figure 8.10 shows the evolution of the objective values. The figure shows that the global optimization technique has converged to a sub-optimal solution for both objectives. Here it can be seen that the minimum propellant objective is found close to the 100^{th} generation, while the minimum target orbit objective is found after approximately the 250^{th} generation. Similarly, the average of the objective values does have large variations after around the same amount of generations. Thus, it can be concluded that the global optimization has converged to the (sub-)optimal solution.

With these results the ascent trajectory can be analyzed. The analysis is done for three individuals, which are marked by a blue circle in the detailed view of Figure 8.9. The individuals selected are the most efficient and most accurate individual to reach the target altitude. Additionally, an individual is selected that reaches the target orbit with an acceptable accuracy, while using an efficient amount of propellant.

The altitude velocity plot, Figure 8.11, confirms that the altitude of the pull up maneuver is correlated with the amount of fuel used to obtain the the target orbit. Due to the constraint formulation, a higher altitude means a higher maximum allowable velocity, which reduces the amount of propellant necessary to circularize. However, the increased velocity results in a higher flight path angle when the target altitude is reached, which reduces the effectiveness of the circularization maneuver, see Figure 8.12.

The effect of the changes made to the flight path angle gain and the reference angle of attack can be seen in Figure 8.13. Here it can be seen that the oscillations that occurred just before the pull up phase are mostly eliminated. Furthermore, the reference angle of attack peaks less when the pull up phase is almost at an end, which was unwanted behavior observed in Figure 8.6. Instead, the angle of attack is constant during that phase for two individuals, while one individual has a steadily increasing angle of attack at the end of the phase. This eliminates the possibility that the space plane becomes unstable at the end of the pull up phase, as was mentioned in the previous section. Furthermore, the figure shows the angle of attack is close to the edge of the search space, which is set to 1 deg. This was also found to be the case for the longitudinal ascent in the previous section. This means that the fuel-optimal ascent trajectory is possibly not yet found. For this reason, a local refinement will be performed, where the search space for the angle of attack is extended.

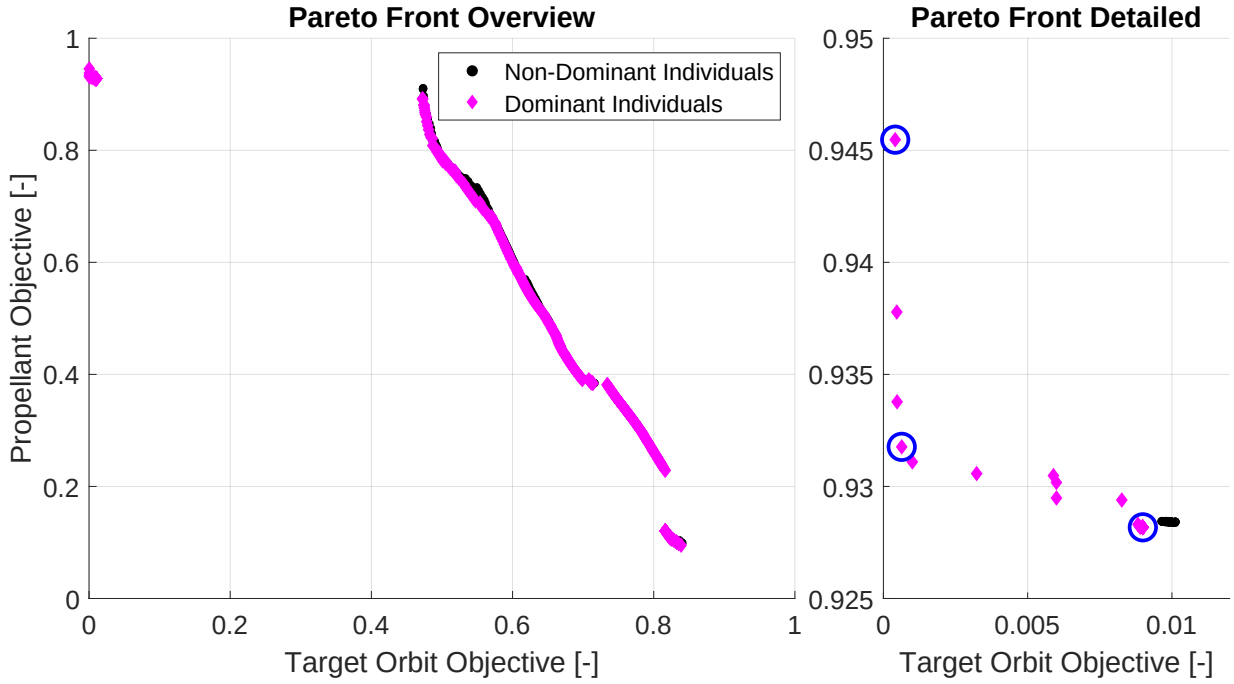

Figure 8.9: Pareto front of the optimization for the ascent trajectory with an initial time zero seconds. The 500^{th} generation is considered, with all three seeds included in the Pareto front.

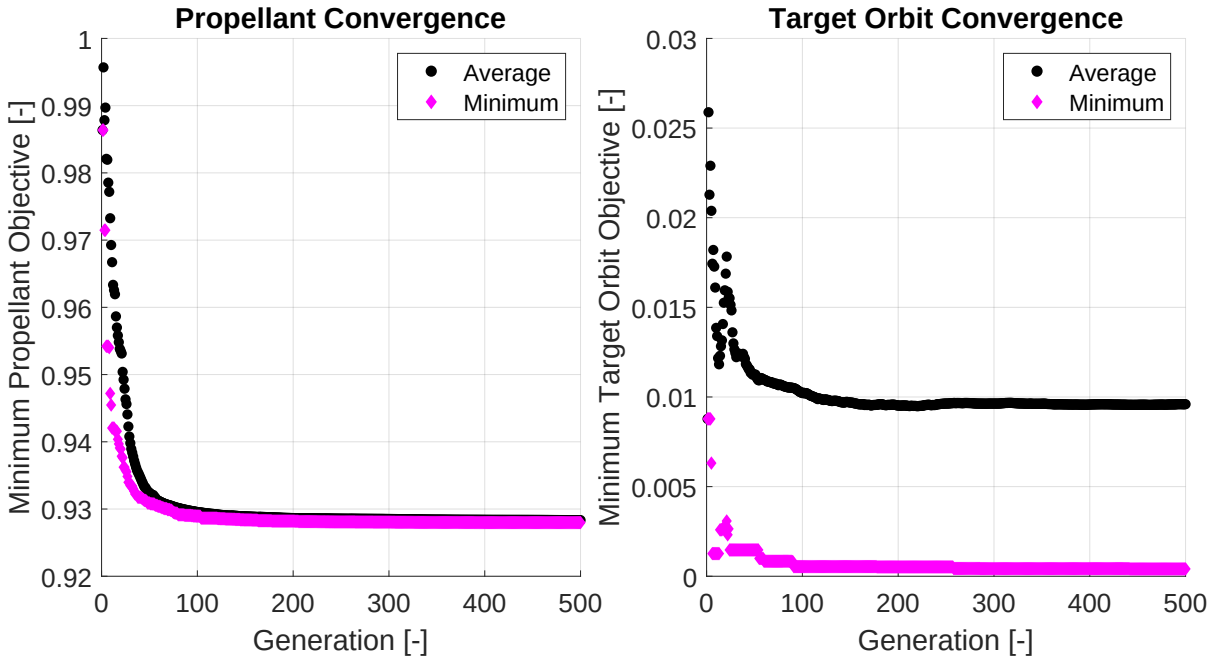

Figure 8.10: Evolution of the objective values for an initial time of $t_0 = 0$ s, where both the minimum and average of both objectives is shown per generation.

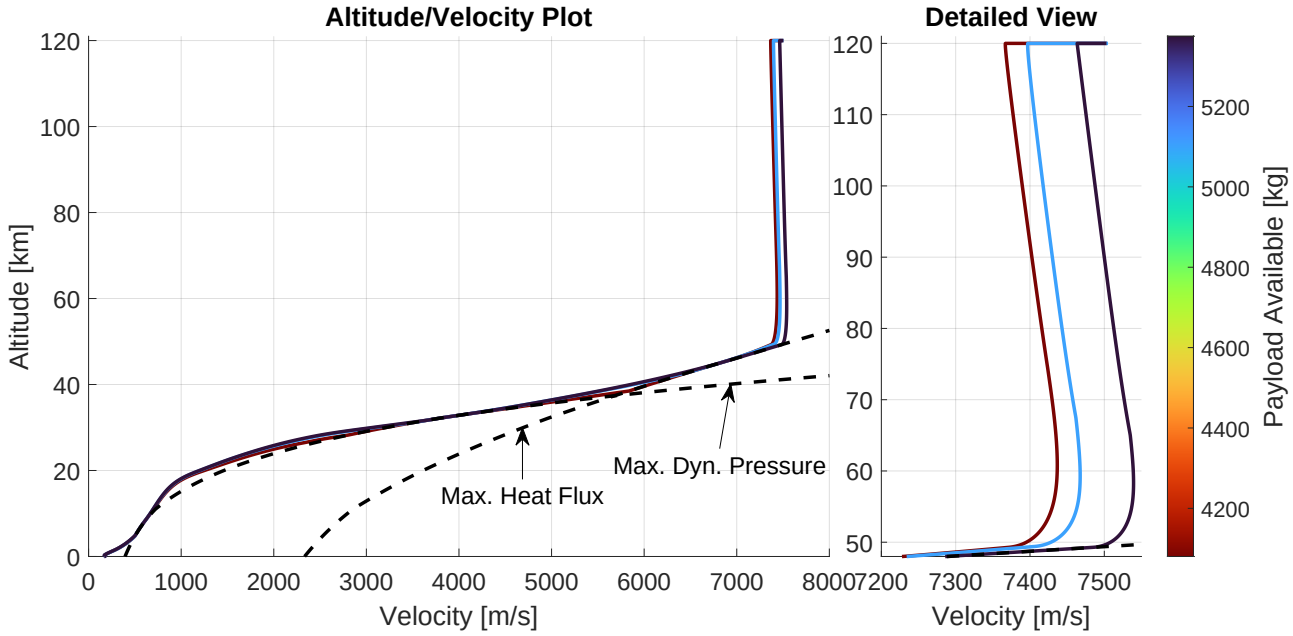

Figure 8.11: Altitude versus velocity plot of three simulations that reach the target orbit with initial time $t_0 = 0$ s.

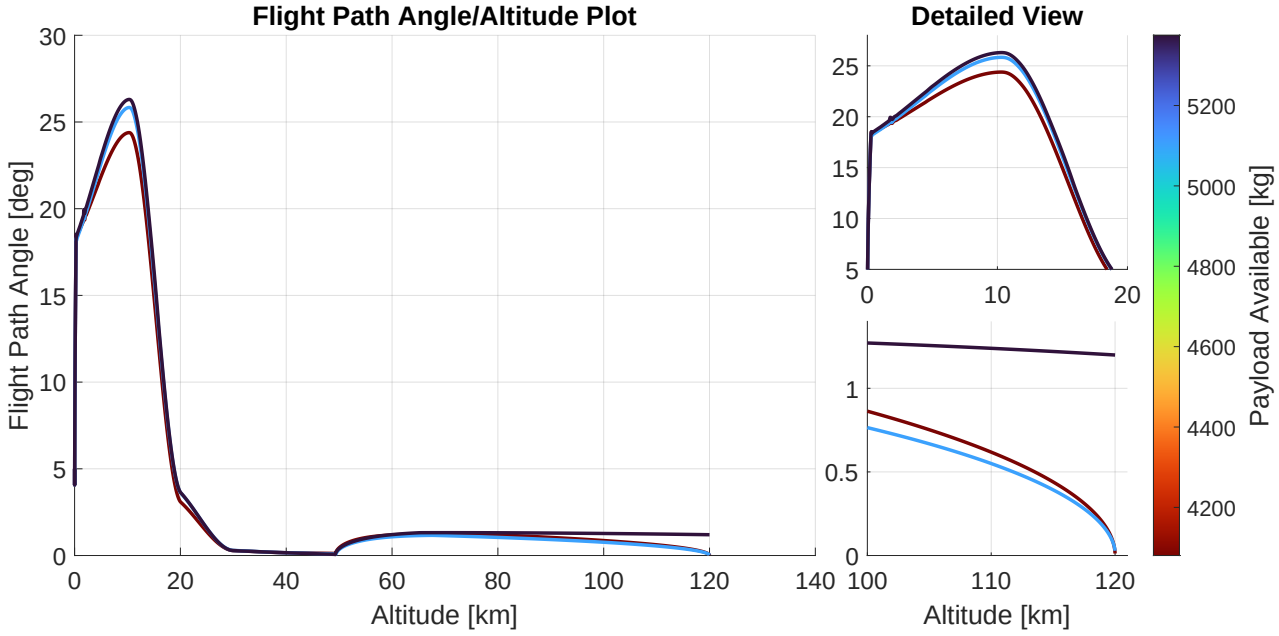

Figure 8.12: Altitude versus flight path angle plot of three simulations that reach the target orbit with initial time $t_0 = 0$ s.

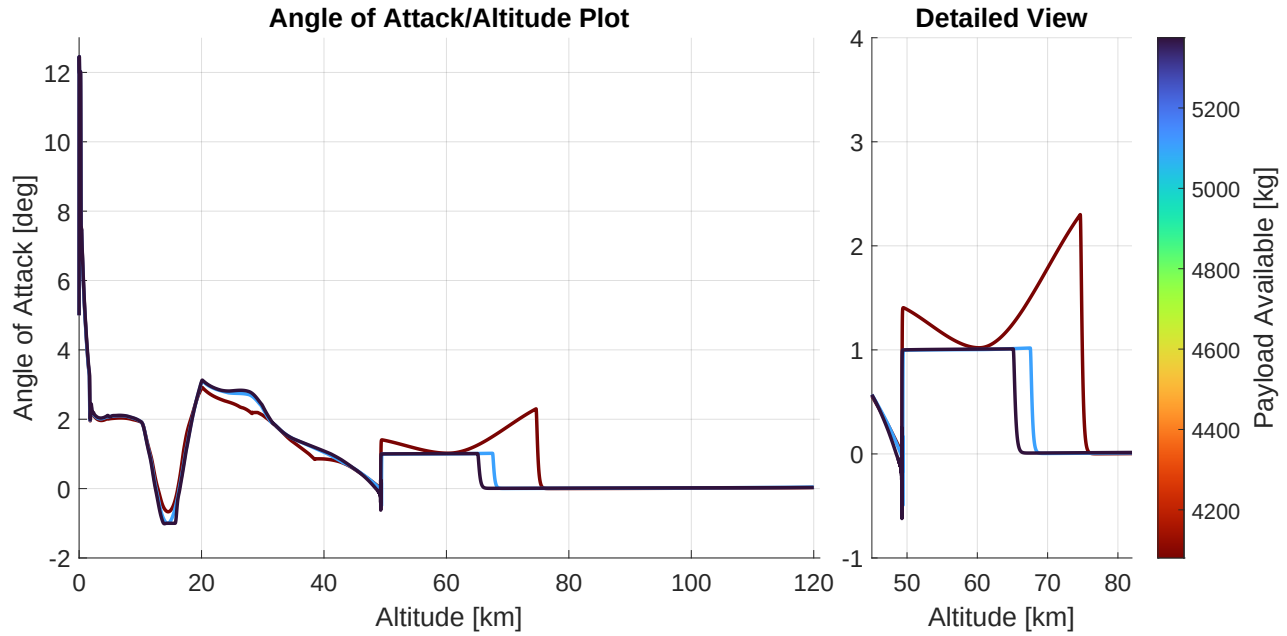

Figure 8.13: Overview of the angle of attack as a function of altitude for three simulations that reach the target orbit with initial time $t_0 = 0$ s.

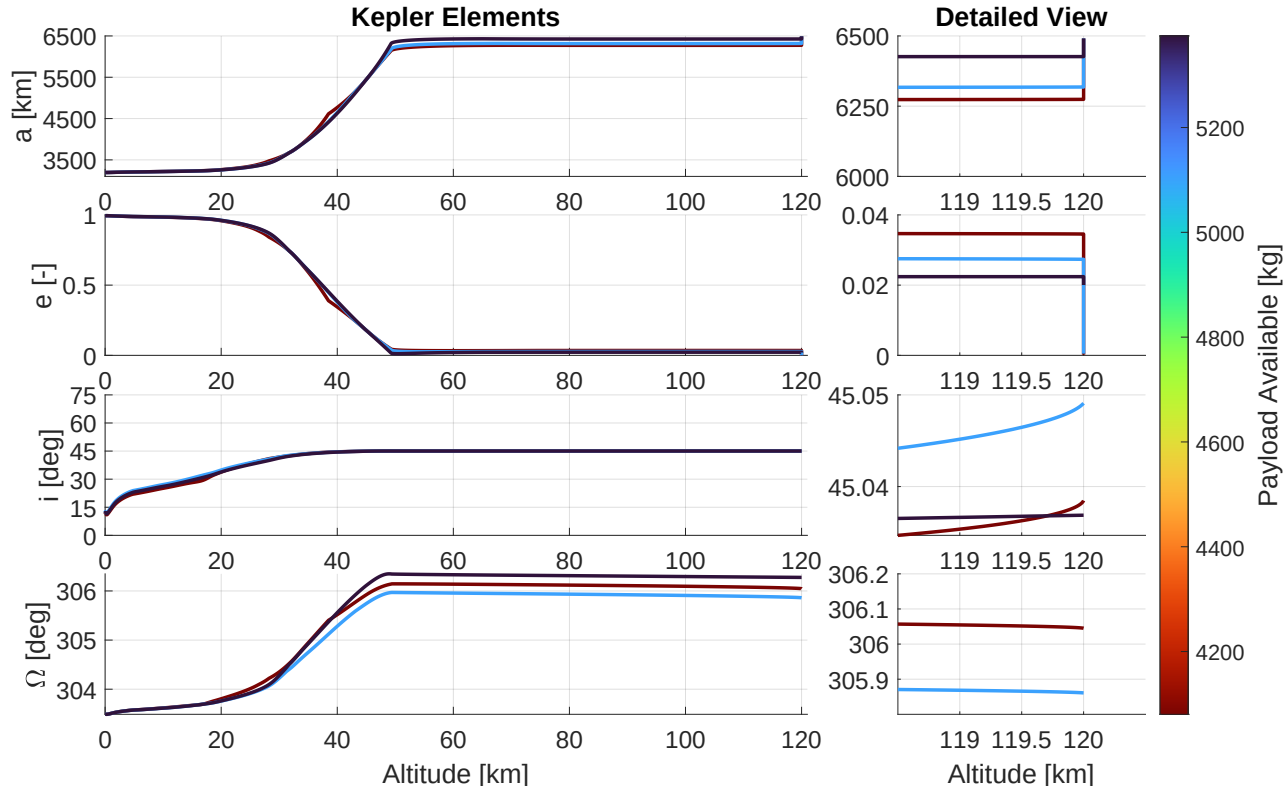

Figure 8.14: Overview of the Kepler elements as a function of altitude for three simulations that reach the target orbit with initial time $t_0 = 0$ s.

The target orbital elements can be seen in Figure 8.14, where the velocity and altitude target values are replaced with the semi-major axis. In this figure it can be seen that the simulations achieve the target semi-major axis and inclination accurately. The inclination, as was mentioned previously, is ensured by the G&C system that steers the space plane to the target inclination. The eccentricity is correlated with the flight path angle. It can be seen that the simulations that have a flight path angle close to zero at the target altitude can effectively reduce the eccentricity to zero. The RAAN that the three simulations achieve is relatively accurate to the target value of 306 degrees. It can be seen that the three individuals vary slightly, which is expected behavior. The reference heading angle steers the space plane to a target inclination, which can include a deviation in inclination. This means that the heading angle, which also influences the inclination and RAAN, does not steer the space plane to the target RAAN. This is also the reason why the ascent trajectory with lateral motion is an optimization problem. There is not a direct equation that relates the heading angle to the RAAN. However, it can be seen that for the control situation, where the initial time is set to $t_0 = 0$ s, the RAAN achieved is close to the target value.

Results with Delayed or Advanced Ascent

The optimization of an extended launch window was investigated for a variety of different initial times. By investigating a single initial time the characteristics can be observed about the Pareto front. For example, investigating an initial time that is delayed by one hour, $t_0 = 3600$ s, see Figure 8.15, it can be seen that the target objective ranges from 0 to 0.04, which is a larger range compared to the Pareto front for a launch which is not delayed or advanced, see Figure 8.9. Reviewing the orbital parameter plot, Figure 8.16, for the delayed launch reveals that the larger range is the result of the required change in RAAN. The most efficient individual in terms of propellant will not change the RAAN to the target value, which results in a higher target orbit objective value. Thus, it can be concluded that manipulating the RAAN results in more propellant used during the ascent. Additionally, the most accurate individual will have a pull up altitude lower than the other individuals, which results in a large amount of propellant needed during the circularization maneuver, see Figure 8.17. The most accurate individual and the most efficient individual both have their downsides for either the target orbit objective or the propellant objective, respectively. This means that there is a trade-off between the accuracy of the final orbit and the amount of propellant used. Similarly to the previous Pareto fronts shown, there exists a point where the target orbit objective value does not significantly improve anymore, while the propellant objective does significantly increase. This point, is considered to be of good accuracy while still being efficient with the amount of propellant used. As can be seen in Figure 8.16, all orbital elements are close to the target value, while that individual does significantly improve upon the amount of payload available compared to the most accurate individual.

For the sake of brevity, the Pareto fronts of the different launch times and the convergence of the optimizations are not discussed or shown in this section. Instead, one individual is selected for each launch time and discussed here. The selected individuals are at the point where the propellant used no longer significantly increases the target orbit objective. The Pareto fronts and the selection of the individuals, and the convergence of the optimizations can be found in Appendices A and B.

With the selection made, the results of the ascent trajectory with different initial launch times can be seen in Figure 8.18. The runs that have been selected all have a similar final semi-major axis and eccentricity, which can be considered the longitudinal maneuver parameters. It can be seen that throughout the ascent, these parameters progress in a similar fashion as the longitudinal ascent trajectory shown in Figure 8.5. On the other hand, the inclination and RAAN, which can be considered the lateral maneuver parameters, do vary compared to the longitudinal ascent trajectory. This is the effect of using a deviation in inclination angle to command the heading angle of the space plane. It can be seen that the RAAN of the different simulations have a different initial value, depending on the launch time. A launch which is not delayed or advanced has an initial RAAN of approximately 303 degrees, which differs slightly from the final RAAN found in the previous section due to the rotation of the Earth. When the launch is delayed or advanced by two hours, the initial RAAN is plus or minus 30 degrees, which corresponds with the angular rotation of the Earth of approximately 15 degrees per hour. The manipulation of the RAAN is done by launching at a different launch heading angle, which depends on the deviation in inclination. The effects of the deviation in inclination can be seen in Figure 8.18. It can be seen that a delayed launch will require a positive deviation in inclination, which is corrected for just before the pull up phase starts. Adversely, an advanced launch will require a negative deviation in inclination, followed by a similar correction. The initial heading angle and how the correction influences the heading angle can be seen in Figure 8.19. Here it can be seen that the delayed launch, which requires a positive deviation in inclination, launches almost due North, while an advanced launch requires a launch almost due East. The

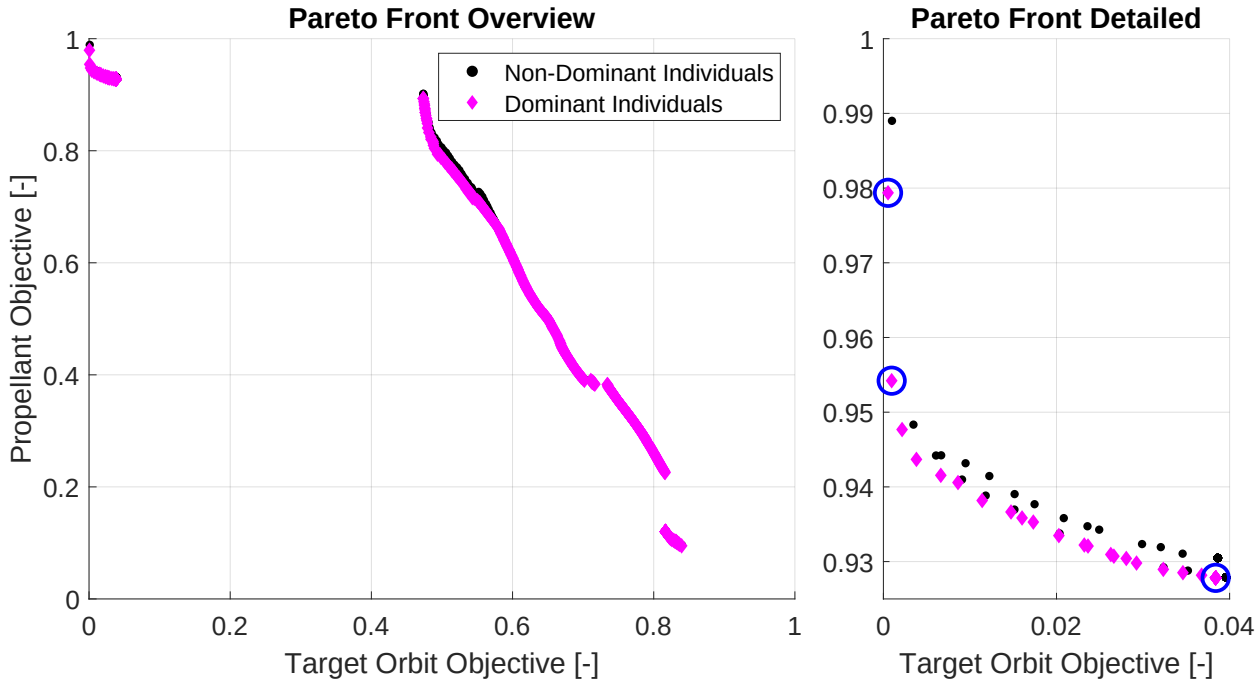

Figure 8.15: Pareto front of the optimization for the ascent trajectory with an initial time of 3600 seconds. The 500^{th} generation is considered, with all three seeds included in the Pareto front.

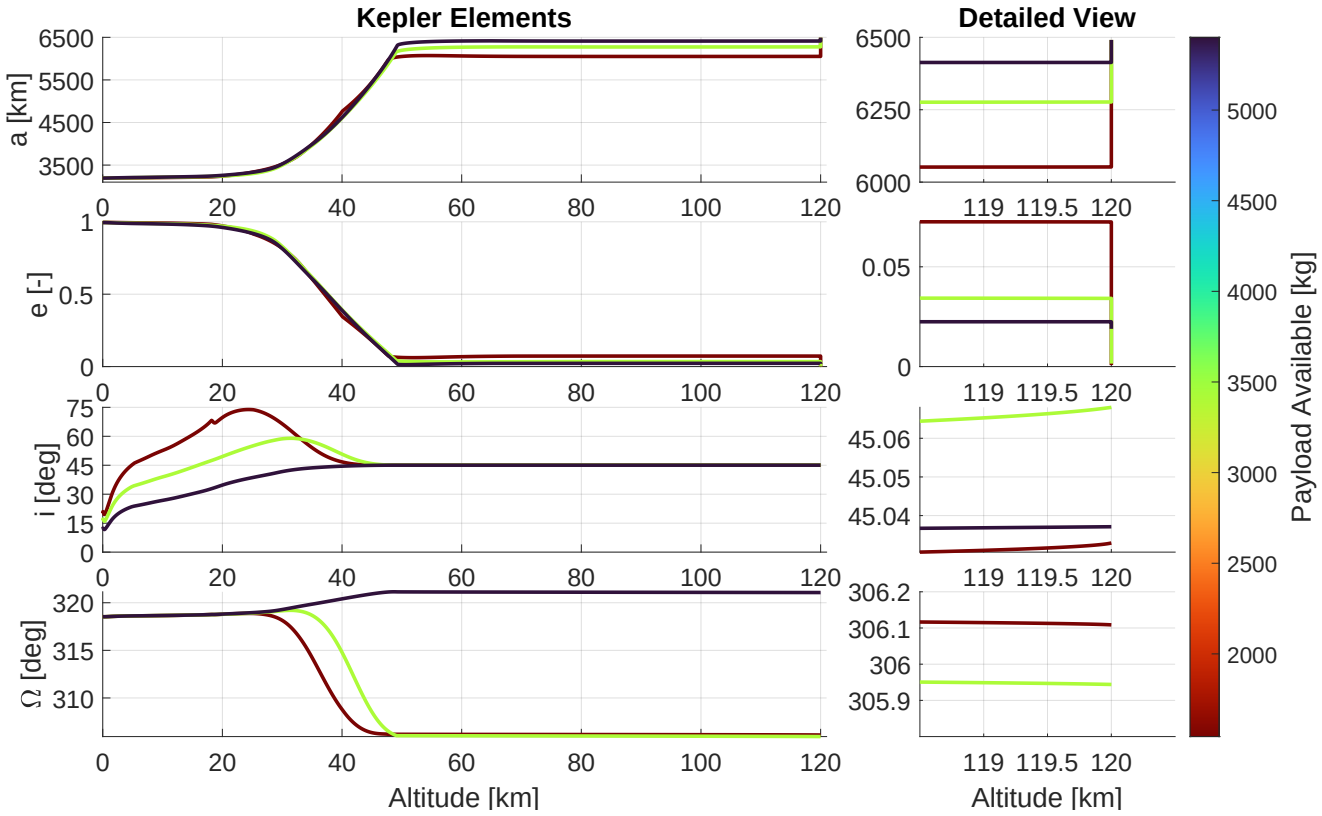

Figure 8.16: Overview of the Kepler elements as a function of altitude for three simulations that reach the target orbit with initial time $t_0 = 3600$ s.

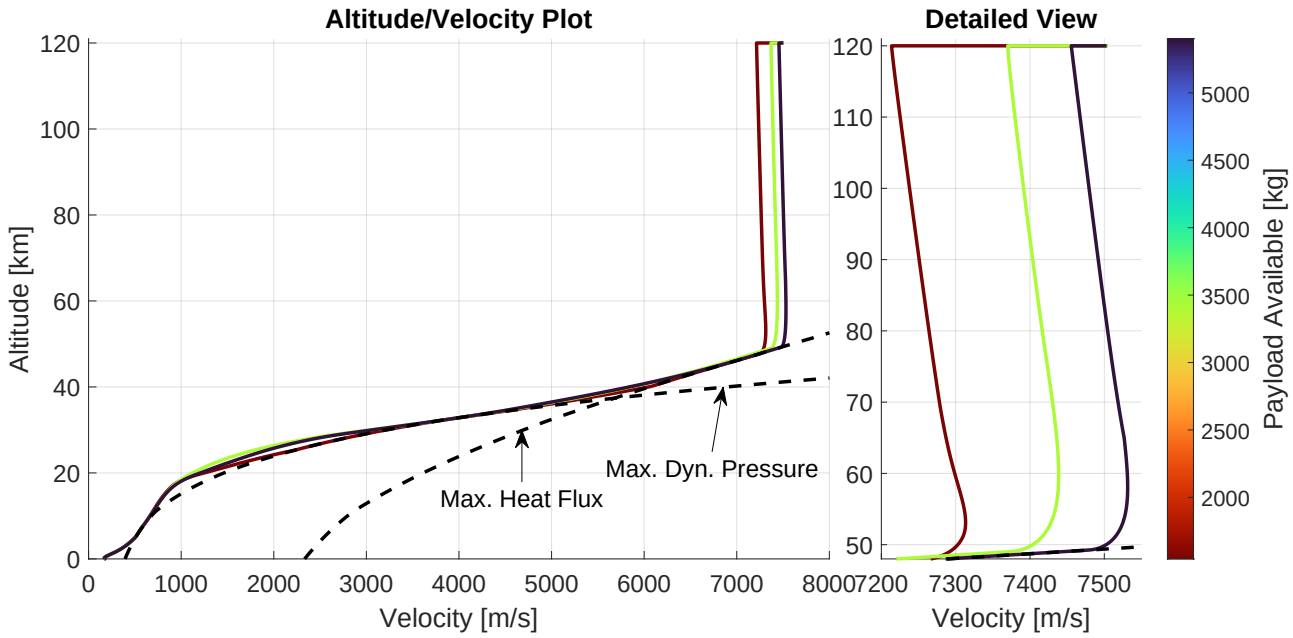

Figure 8.17: Altitude versus velocity plot of three simulations that reach the target orbit with initial time $t_0 = 0$ s.

heading angle correction occurs just before the pull up phase starts, which is around 50 km. Depending on the current latitude of the space plane when the pull up phase starts, the heading angle will vary. It can be seen that for the advanced launch, the required heading angle is smaller. This can be explained by visualizing the history of the longitude and latitude. This is done in Figure 8.20, where the history of the longitude and latitude are plotted on an inertial sphere. Depending on the launch time, the starting longitude will vary. It can be seen that all selected individuals, launched from the equator, have their own starting position in terms of inertial longitude. As the space plane ascents, the heading angle is varied to allign before the pull up phase to the correct heading angle. Afterwards, the semi-major axis, eccentricity, inclination and RAAN are nearly identical for all individuals, as can be confirmed by Figure 8.18. Furthermore, it can be seen that for an advanced launch, the latitude of the space plane progresses slowly, due to the large initial heading angle. When the pull up phase starts, the required heading angle is not close to 90 degrees yet. On the other hand, for the delayed launch, which launches with a small heading angle, it can be seen that at the start of the pull up phase the heading angle is almost 90 degrees. This means that the latitude of the space plane at the start of the pull up phase is almost 45 degrees, since the target inclination is 45 degrees. Due to the formulation of the reference heading angle, a limit exists at which latitudes the space plane can be commanded. When the space plane latitude is greater than the target inclination, the reference heading angle will produce an error. Thus, it can be concluded that a two hours delayed launch reaches the limit of what is possible with the current formulation of the reference heading angle.

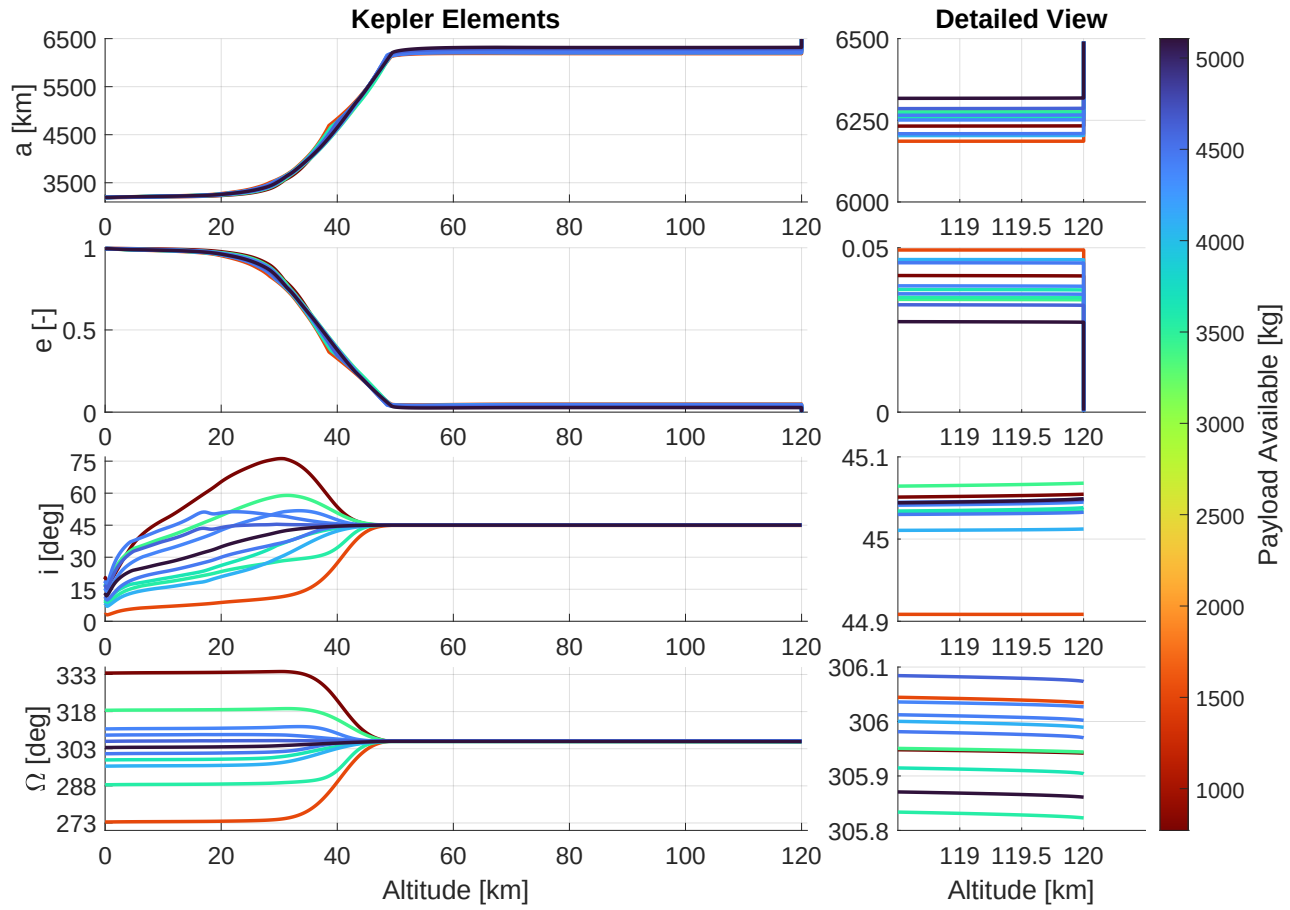

Figure 8.18: Overview of the Kepler elements as a function of altitude for the best simulation from each initial time that reaches the target orbit.

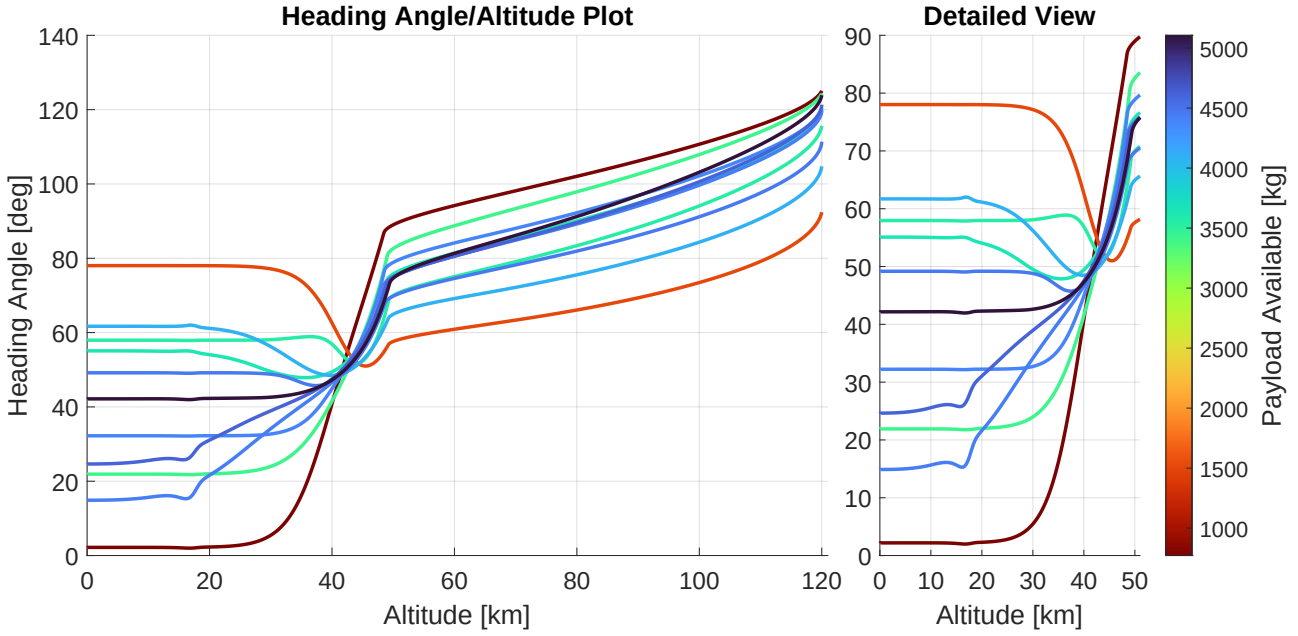

Figure 8.19: Overview of the heading angle as a function of altitude for the best simulation from each initial time that reaches the target orbit.

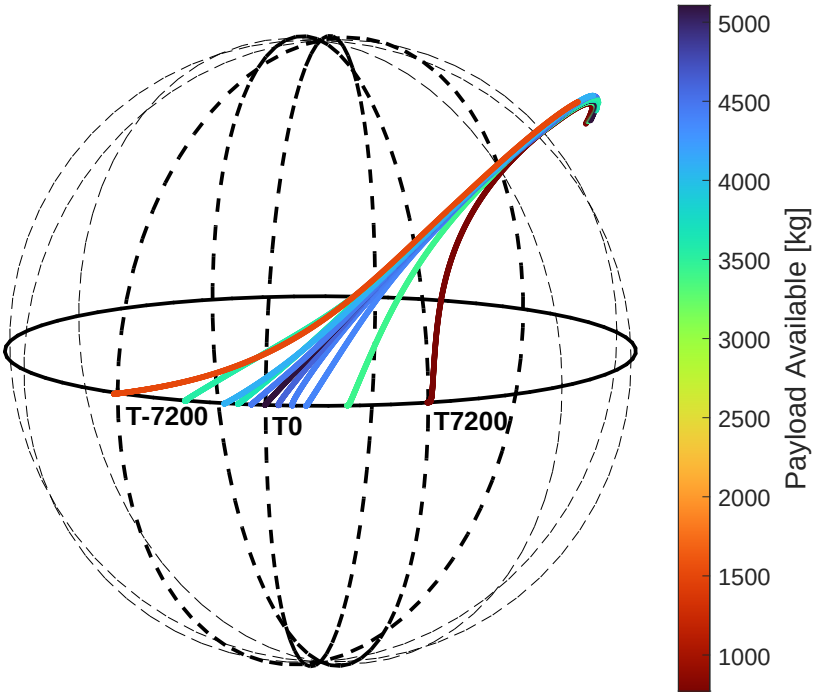

Figure 8.20: History of the longitude and latitude of the simulations with respect to an inertial sphere. The obtained altitude is enhanced to visually distinguish between the inertial sphere and the trajectory of the simulations.

The maneuver to correct the heading angle can also be seen in Figure 8.21, where the heading angle correction maneuver starts around 30 km. The heading angle correction requires a large banking maneuver, which enables the space plane to change the direction of the velocity to align with the desired inclination. An interesting phenomenon can be observed by comparing the delayed and advanced launches. In general it can be seen that a delayed launch, which uses a negative banking maneuver, starts slightly earlier and becomes less steep compared to the advanced launches. The advanced launches, which use a positive banking maneuver, reach a higher bank angle, which enables these simulations to start the bank angle maneuver later. It is theorized that this behavior can be contributed to the formulation of the reference heading angle. The reference heading angle can only be computed for a latitude smaller than the target inclination. All delayed launches will launch in some extent in northern direction, which means that for these individuals, the latitude progresses quicker compared to the advanced launch individuals. In order to ensure that the latitude does not exceed the target inclination value, the space plane needs initiate the banking maneuver earlier, while not needing to change the heading angle as sharply. This can also be confirmed by looking at the angle of attack versus altitude plot, see Figure 8.22. Due to the banking maneuver the angle of attack needs to be increased to ensure that the flight path angle does not drop due to the reduction in lift force. For the delayed launch, the angle of attack increases earlier compared to the advanced launch. This could also give an indication why the ascent trajectory for a delayed or advanced launch uses more propellant. An increased angle of attack induces more drag, which means that the drag losses for these simulations will be higher. After the local refinement, a detailed investigation is done to assess whether the drag losses are the reason for the reduced available payload.

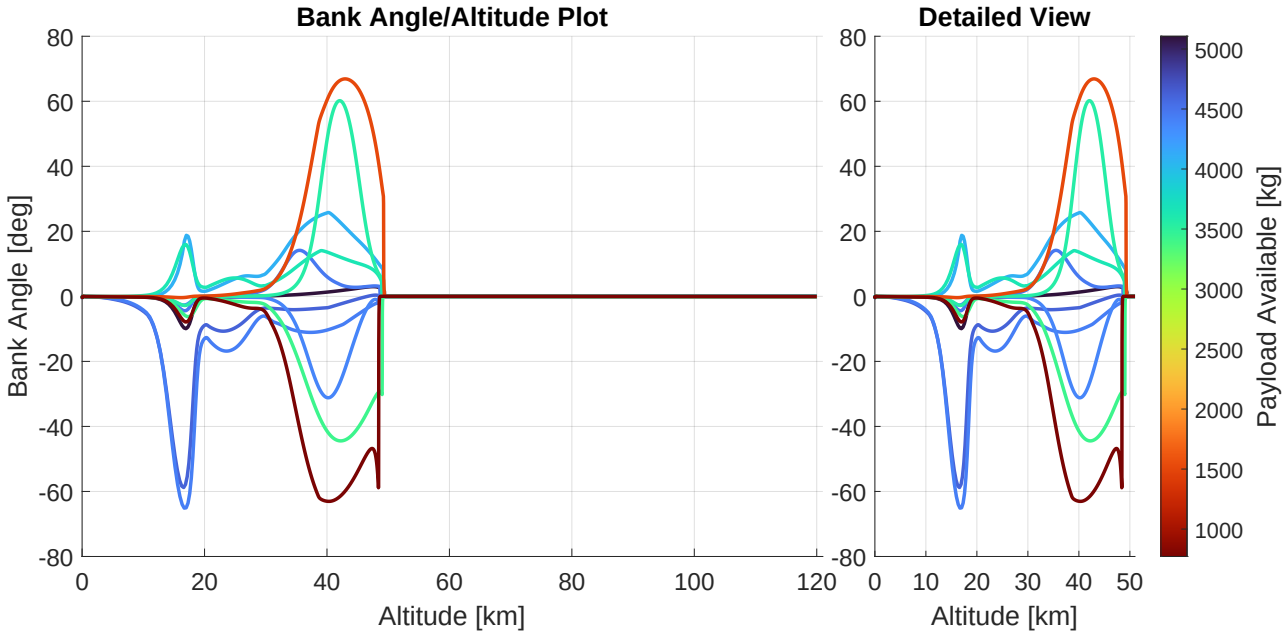

Figure 8.21: Overview of the bank angle as a function of altitude for the best simulation from each initial time that reaches the target orbit.

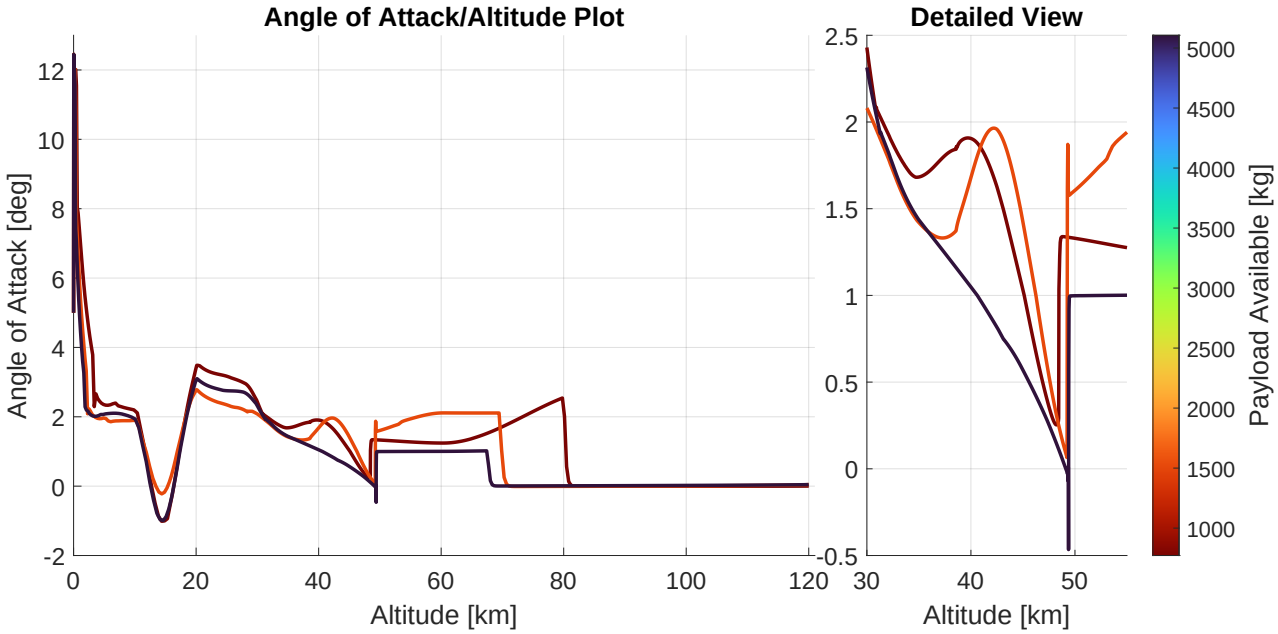

Figure 8.22: Overview of the angle of attack as a function of altitude for the best simulation, from $t_0 = 0, 7200, -7200$ s, that reaches the target orbit.

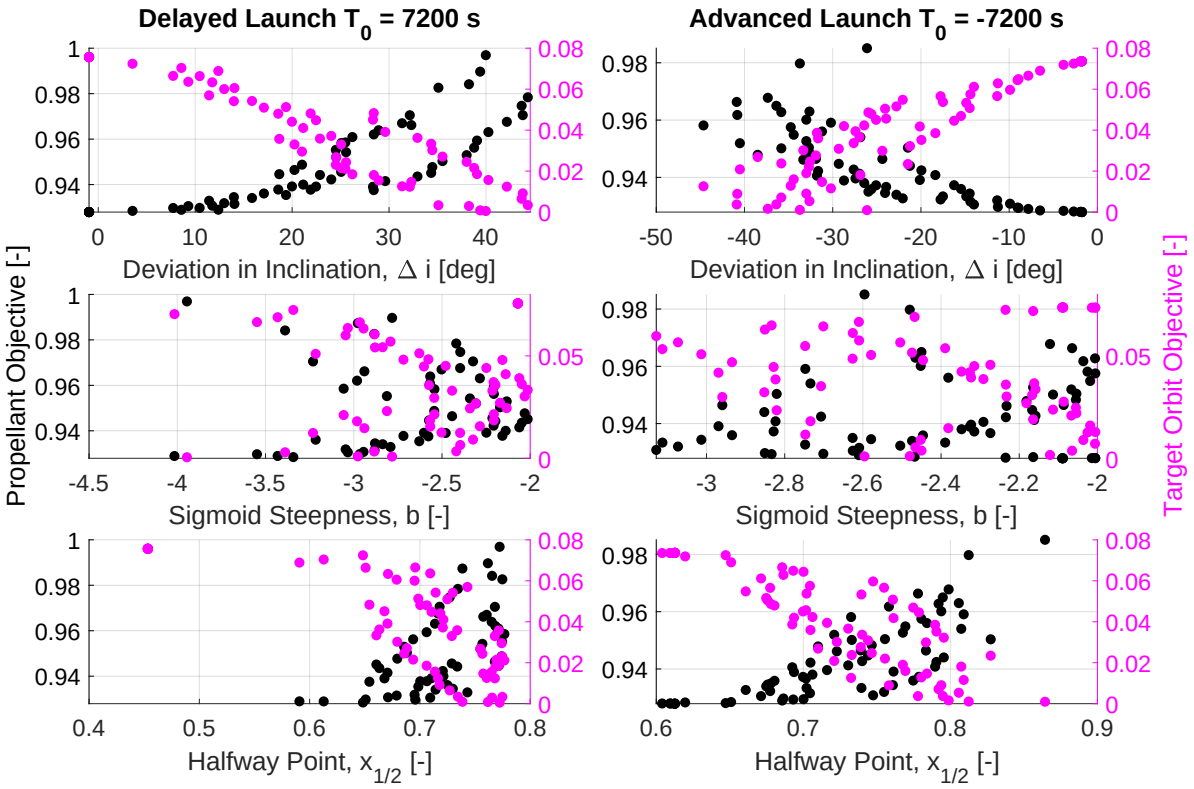

Figure 8.23: Overview of the lateral optimization parameters for an advanced and delayed launch that reach the target altitude.

Investigation of the Lateral Optimization Parameters

Previously, it was discussed that depending on a delayed or advanced launch the deviation in inclination was either positive or negative, respectively. In order to gain insight in the behavior of the lateral optimization parameters, a scatter plot is shown where the objectives are plotted versus these parameters, see Figure 8.23. In the figure only the optimization parameters are shown for a delayed or advanced launch by two hours. As was discussed previously, only the individuals that reach the target altitude are considered. As can be seen, there is a strong correlation between the deviation in inclination and the target orbit objective. Furthermore, it can be seen that the point that the sigmoid function reaches the half way point of the deviation in inclination increases as the target orbit objective becomes lower. An interesting difference between the advanced and delayed launch is that the half way point for an advanced launch is of higher value, which corresponds with a higher altitude. The reason why the advanced launch has a higher value is due to the definition of the reference heading angle. The delayed launch is limited due to the more northwards moving direction, which means that the latitude of these simulations increases more rapidly and approaches the limit of 45 degrees earlier. Thus, the banking maneuver to correct the heading angle needs to occur earlier. Decision variable insight for the other launch times can be seen in Appendix D.

8.3.4. Results of the Local Refinement

Previously, the global optimization results are shown for the different launch times. In the discussion of the results, a number of issues were identified, which required a refinement of the Pareto front. The first issue was the definition of the search space for the angle of attack, which should be extended. The second issue is that the global optimization is not guaranteed to find the optimal result. A local optimization can be used to either refine the Pareto front or confirm that the current Pareto front is indeed the optimum. This refinement is not done for all initial times. It was determined that the delayed or advanced launch by either 10 or 20 minutes did not add any significant details compared to the longer delayed or advanced launches.

The refinement of the Pareto front is done with a Sobol sequence, where a large number of combinations of the optimization parameter range is generated. The Sobol analysis, similar to how it previously was used,

Table 8.13: Refined search space of the longitudinal optimization parameters, used for the Sobol analysis.

Parameter	Search Space	Unit
γ_1	[15.2,24.6]	[deg]
γ_2	[21.2,28.8]	[deg]
γ_3	[2.2,3.5]	[deg]
γ_4	[0.0,0.5]	[deg]
γ_5	[0.0,0.5]	[deg]
γ_6	[0.0,0.5]	[deg]
α_1	[-1.0,4.0]	[deg]
α_2	[-1.0,4.0]	[deg]
α_3	[-1.0,4.0]	[deg]
$h_{\text{pull up}}$	[47.5, 49.8]	[km]
h_{MECO}	[60.0, 80.0]	[km]
ϕ_{max}	[1.0, 1.4]	[-]

Table 8.14: Refined search space of the lateral optimization parameters, used for the Sobol analysis.

Launch Time	Δi_0 [deg]	b [-]	$x_{1/2}$ [-]
$t_0 = 0$ s	[-4.0, 4.0]	[-5.0, -2.0]	[0.2, 0.8]
$t_0 = 1800$ s	[5.0, 25.0]	[-5.0, -2.0]	[0.6, 0.9]
$t_0 = -1800$ s	[-20.0, -10.0]	[-3.0, -2.0]	[0.6, 0.8]
$t_0 = 3600$ s	[10.0, 44.9]	[-4.0, -2.0]	[0.6, 0.9]
$t_0 = -3600$ s	[-44.9, -10.0]	[-4.0, -2.0]	[0.6, 0.9]
$t_0 = 7200$ s	[30.0, 44.9]	[-4.0, -2.0]	[0.6, 0.8]
$t_0 = -7200$ s	[-44.9, -25.0]	[-3.0, -2.0]	[0.7, 0.9]

will create pseudo-random sequences that enables the investigation of the entire search space.

Determination of the Search Space

With the results of the global optimization, the optimization parameters can be used to find a refined search space. The optimization parameter range from the individuals of the global optimization that reached the target altitude are used. For each parameter the minimum and maximum value are obtained and 10 % of its range is either subtracted or added to the minimum or maximum value, respectively. This defines the refined search space, which is used for both the local optimization and the Sobol analysis. Exception to this rule is the angle of attack. As was discussed during the results of the longitudinal ascent, the edge of the angle of attack search space should be extended significantly. For the angle of attack, the minimum value is extended to -1 degree. This is the minimum value for which the aerodynamic coefficients are tabulated. The refined search space can be seen in Table 8.13.

Additionally, for each launch time, the lateral optimization parameters are assessed and used to define a search space from which a Sobol sequence is generated. The lateral optimization parameters are determined for the different launch times. By investigating the lateral optimization parameters, as can be seen in Figure 8.23, a refined search space can be found to investigate the local refinement. This is done by only considering optimization parameters that have a target orbit objective below 0.02. Any value above this, will include solutions that do not properly manipulate the RAAN. By doing this for the different launch times, a refined search space is found that can be used to construct the Sobol sequence. The refined search space for the different launch times can be found in Table 8.14.

Results

The results of the Sobol analysis for an initial time of $t_0 = 0$ s can be seen in Figure 8.24. As can be seen, the Sobol analysis does not give any solutions that improve the Pareto front that was found by the global optimization algorithm. Similarly, the Sobol analyses for the other launch times did not find an improved Pareto front, see Appendix C. The reason for this could be that the global optimization solutions are already very close to the optimal solution. Alternatively, the inclusion of a wider search space for the angle of attack could necessitate a larger number of individuals in the Sobol sequence to find improvements upon the Pareto front. Besides the Sobol analysis, a local optimization could be done, which uses gradient based methods

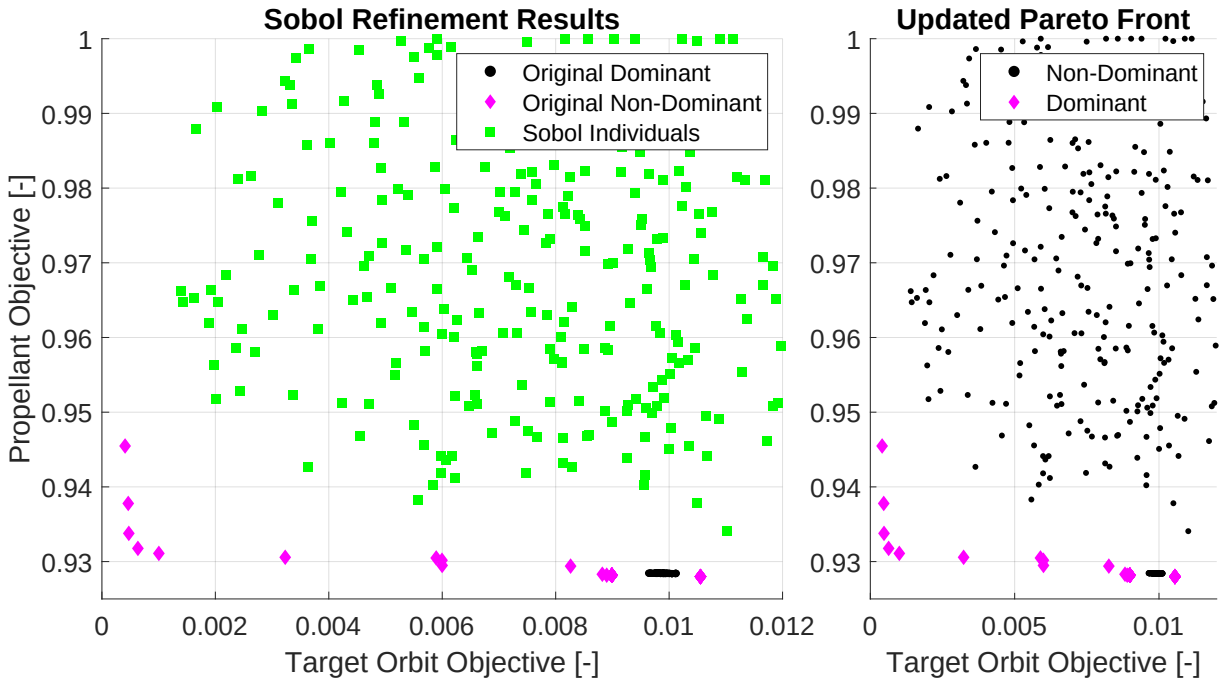

Figure 8.24: Pareto front with the Sobol analysis for an initial time of $t_0 = 0$ s.

Table 8.15: Overview of the selected individuals that reach the target orbit.

Launch Time	T0	T1800	T-1800	T3600	T-3600	T7200	T-7200
Available Payload [kg]	5106	4392	4089	3426	3554	772	1514

to find the optimal solution. Since the global optimization already indicates where the global minimum is located, a local optimization could be used to further improve upon the near-optimal solution found by the global optimization. Though this extended analysis would fall outside the scope of the MSc thesis. Instead, it is recommended as a future study.

8.4. Analysis of the Results

In the previous section the results of the optimization was presented. It has become clear that the space plane is capable of changing the Right Ascensions of the Ascending Node (RAAN) at the cost of propellant. In Figure 8.22, it was already seen that the banking maneuver requires an increased angle of attack to maintain the correct flight path angle, which increases the drag forces. The propellant used can be converted to available payload, by assuming that any propellant not used by the space plane can be used as payload up to the Operating Empty Weight (OEW). The resulting available payload, which was used to color code the different simulations, can be seen in Table 8.15. However, using the payload as a measure does not give enough information how the extra propellant is actually used. Therefore, a ΔV budget is computed for each simulation.

For the computation of the budget, three losses should be included. These losses occur due to the drag, gravity and misalignment of the thrust vector with respect to the velocity vector. The drag losses are computed with:

$$\Delta V_{\text{drag}} = \int_{t_0}^{t_f} D\text{dt}, \tag{8.3}$$

where D is the drag force, which is integrated between the initial time, t_0 and the final time, t_f. The gravity loss is computed with:

$$\Delta V_{\text{grav.}} = \int_{t_0}^{t_f} g_0 \sin\gamma \text{dt}, \tag{8.4}$$

Table 8.16: Overview of the selected individuals that reach the target orbit.

Launch Time	T0	T1800	T-1800	T3600	T-3600	T7200	T-7200
ΔV_{ideal} [m/s]	11289	11331	11172	11395	11560	11848	11781
ΔV_{circ} [m/s]	108	151	183	135	138	164	196
ΔV_{drag} [m/s]	3241	3284	3170	3295	3419	3564	3628
$\Delta V_{\text{grav.}}$ [m/s]	540	554	563	549	553	614	549
ΔV_{thrust} [m/s]	273	301	279	342	382	490	458
$\Delta V_{\text{initial}}$ [m/s]	170	170	170	170	170	170	170
ΔV_{total} [m/s]	7512	7514	7514	7514	7513	7514	7512

where g_0 is the gravity acceleration at sea level and γ is the flight path angle. Finally, thrust losses occur due to the misalignment of the thrust vector with respect to the velocity vector. Typically, the misalignment only occurs due to the angle of attack, assuming that the thrust vector points along the x_B-axis. For this study, a Thrust Vector Control (TVC) module is implemented, which introduces the thrust elevation angle, ϵ_T. If TVC would not be implemented, the thrust losses could be negelected. In a previous study by Powell et al. (1991), the thrust losses without TVC were determined to be approximately 16 m/s. The thrust losses are computed with:

$$\Delta V_{\text{thrust}} = \int_{t_0}^{t_f} T \sin(\epsilon_T + \alpha) \mathrm{dt}, \tag{8.5}$$

where α is the angle of attack and T is thrust magnitude.

Besides these losses, the space plane undergoes a circularization maneuver and has an initial velocity that should also be included in the ΔV budget. The circularization velocity change, ΔV_{circ}, was computed with Equation 5.23, where the specific impulse is assumed to be 465 s (Mooij, 1998). The initial velocity is 170 m/s and denoted with the symbol $\Delta V_{\text{initial}}$. Additionally, to compare all the simulations the ideal velocity change is computed with:

$$\Delta V_{\text{ideal}} = \int_{t_0}^{t_f} I_{sp} g_0 \ln \frac{M_0}{M_0 - \dot{m}} dt, \tag{8.6}$$

where

$$\dot{m} = \frac{T}{I_{sp} g_0}. \tag{8.7}$$

With the positive and negative change to the ΔV computed, the total ΔV budget for the ascent of a space plane can be computed with:

$$\Delta V_{\text{total}} = \Delta V_{\text{ideal}} + \Delta V_{\text{circ}} + \Delta V_{\text{initial}} - \Delta V_{\text{drag}} - \Delta V_{\text{grav.}} - \Delta V_{\text{thrust}}. \tag{8.8}$$

The complete budget for the different launch times can be seen in Table 8.16. It can be seen that the budget closes and that all velocity changes corresponds approximately with the achieved velocity, as can be seen in Figure 8.25. The overall trend that can be observed is that the drag and thrust losses increase as the launch is further delayed or advanced. It is believed that these increases occur due to the increased angle of attack. An increase in angle of attack induces a higher drag force, which increases the drag losses. Furthermore, the increase in angle of attack means that the natural pitching moment of the space plane is increased, which necessitates the TVC to trim the space plane more. The increase in thrust elevation angle means that the thrust vector misalignment with the velocity vector increases, which means that the thrust losses increase.

Now that the cost of changing the RAAN with a space plane is quantified, a similar analysis can be done for a satellite that would make this change in-orbit. Assuming that the space plane would not change the RAAN, a satellite could be launch with a mass of approximately 5100 kg. According to K. F. Wakker (2015) the required ΔV to make an in-orbit change of the RAAN, can be computed for a circular orbit with:

$$\Delta V = 2V_1 \sin i \sin(0.5\Delta\Omega), \tag{8.9}$$

where V_1 is the original orbital velocity, i is the inclination of the orbit and $\Delta\Omega$ is the change in the RAAN. Applying this equation to the target orbit yields a number of velocity changes, ΔV, which depend on the change in RAAN. The required propellant to make this change is computed with the rocket equation, modified

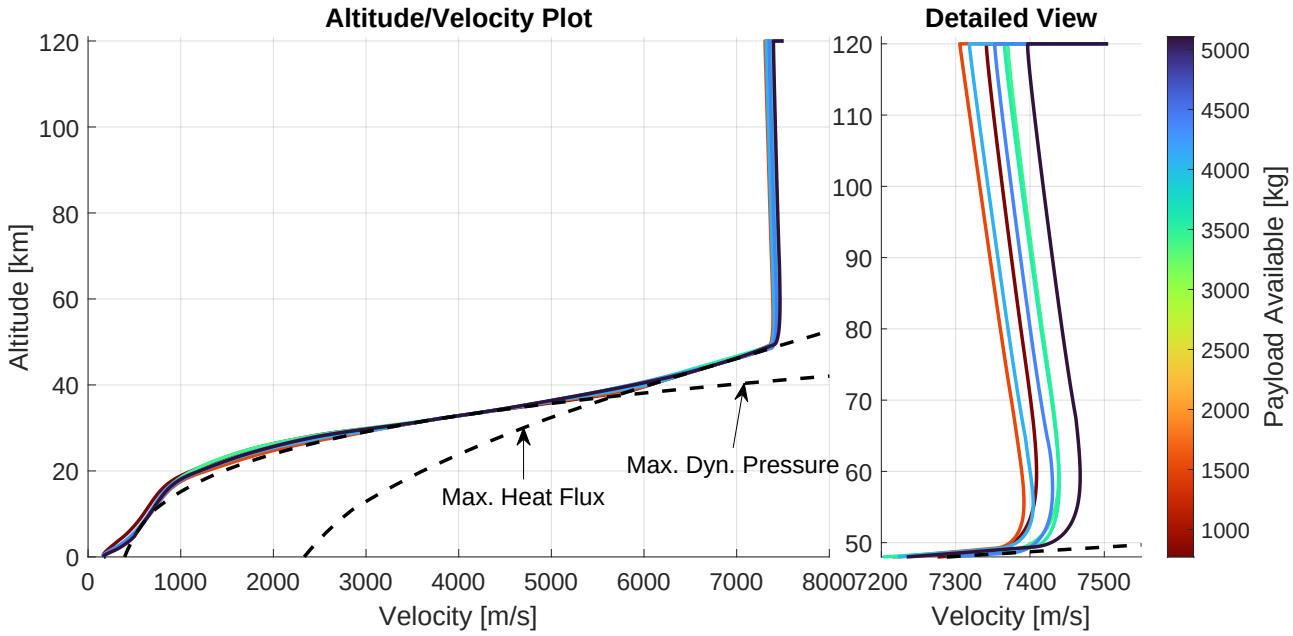

Figure 8.25: Altitude versus velocity of the simulation that reach the target orbit with varying initial times.

to determine the required propellant:

$$M_p = M_0 - M_f = M_0 \frac{1}{\exp\left(\frac{\Delta V}{I_{sp} g_0}\right)}, \tag{8.10}$$

where M_0 is the initial satellite mass, M_f is the final satellite mass, M_p is the required propellant mass to achieve the desired change in velocity, ΔV. In Figure 8.26 the required propellant for a satellite of 5100 kg to change the RAAN is shown. In this figure, it can be seen that, depending on the specific impulse of the engine, the required propellant changes. It can be seen that a theoretical impulsive shot to change the RAAN is more efficient when considering a delayed or advanced launch of two hours. However, when considering a delayed or advanced launch by an hour or less, the space plane is capable of efficiently changing the RAAN, which is on par with the impulsive shot for a rocket engine with a specific impulse of 450 s. This means that for satellite missions, where a change in RAAN is not taken into account, the space plane could effectively make this change instead. The possibility of such a change ensures that the launch window can be extended even if the final target orbit that needs to be achieved has high accuracy requirements. Furthermore, the launch window could be further extend if a more efficient air-breathing engine is developed. In a similar fashion, a space plane with a lower OEW could also increase the launch window by carrying more propellant.

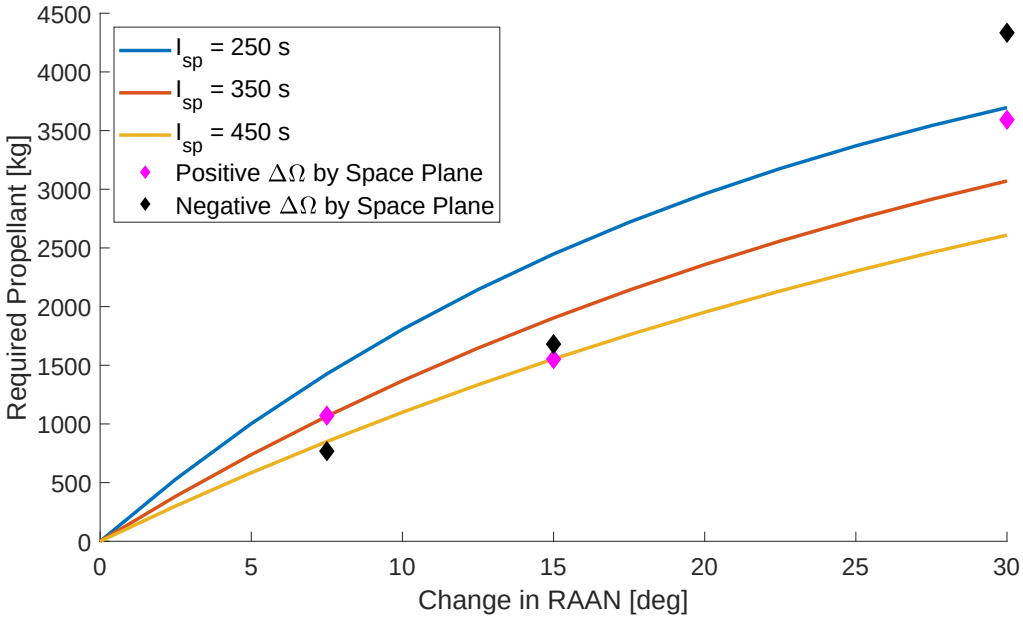

Figure 8.26: Overview of the required propellant to change the RAAN for a satellite and the space plane.

9

Verification & Sensitivity Analysis

In this chapter the verification process of the simulation model and the retrieved ascent trajectories are discussed. Afterwards, an analysis done into the robustness of the Guidance and Control (G&C) system and the obtained results by varying initial state, G&C system parameters and an optimization parameter.

9.1. Verification

The verification of the simulation is done in two parts. First of all, the implementation and integration of the vehicle model and the G&C system are verified. The verification process involves unit testing of the coefficients obtained by Shaughnessy et al. (1990). Furthermore, the implementation of the G&C system is verified by analyzing the reference values with the obtained values of the space plane.

After the optimization is done, the simulation that is obtained will be verified with results from previous studies. The longitudinal ascent will be verified with a study done by Mooij (1998). The lateral motion that is involved to manipulate the Right Ascensions of the Ascending Node (RAAN) is verified by comparing the results from Zhou, Wang, and Cui (2020) with the obtained results from the different delayed or advanced launches.

9.1.1. Verification of the Vehicle Model

The vehicle model is obtained from a study done by Shaughnessy et al. (1990). The vehicle model is comprised of mass, thrust and aerodynamic data. All of the data is given in graphs, which is obtained manually and ordered in tables. The tables correspond with the required look-up table format that TU Delft Astrodynamics Toolbox (TUDAT) uses to retrieve and interpolate the coefficient data. The acquirement of the tables is verified in two ways. First of all, when the tables are created, a number of data points are manually checked. This means that, for each variable that the data is dependent on, three values are assessed and compared to the graphs. For the implementation of these look-up tables in TUDAT another check is performed. The coefficient data is compared, for three values per dependent variable, with the graphs.

With these two checks, it is determined that both the data has been correctly converted from a graph to a table, and the tables are correctly implemented in TUDAT. The vehicle data is loaded in the existing custom aerodynamic coefficient interface and the thrust model. From here, TUDAT uses these models to compute and propagate the rotational, translational and mass state of the vehicle.

9.1.2. Verification of the Guidance and Control (G&C) System

The G&C system is a very complex system, with a variety of parts that work together to steer the space plane to the correct orbit. However, the purpose of the G&C system is very simple. In essence, the G&C system can be seen as a vehicle system computer. It computes six required vehicle parameters that should guide and control the vehicle to the correct trajectory parameters. These six parameters involve deflection angles of the elevons, rudder and canard, the equivalence ratio (thrust throttle), and thrust elevation angle. Based on the required vehicle system parameters the vehicle data is obtained by TUDAT. Thus, it can be concluded that the G&C systems does not directly influence the Equations of Motion (EoM). If the vehicle model is correctly implemented and the G&C system is effective in guiding and controlling the space plane to the correct orbit, the G&C system works.

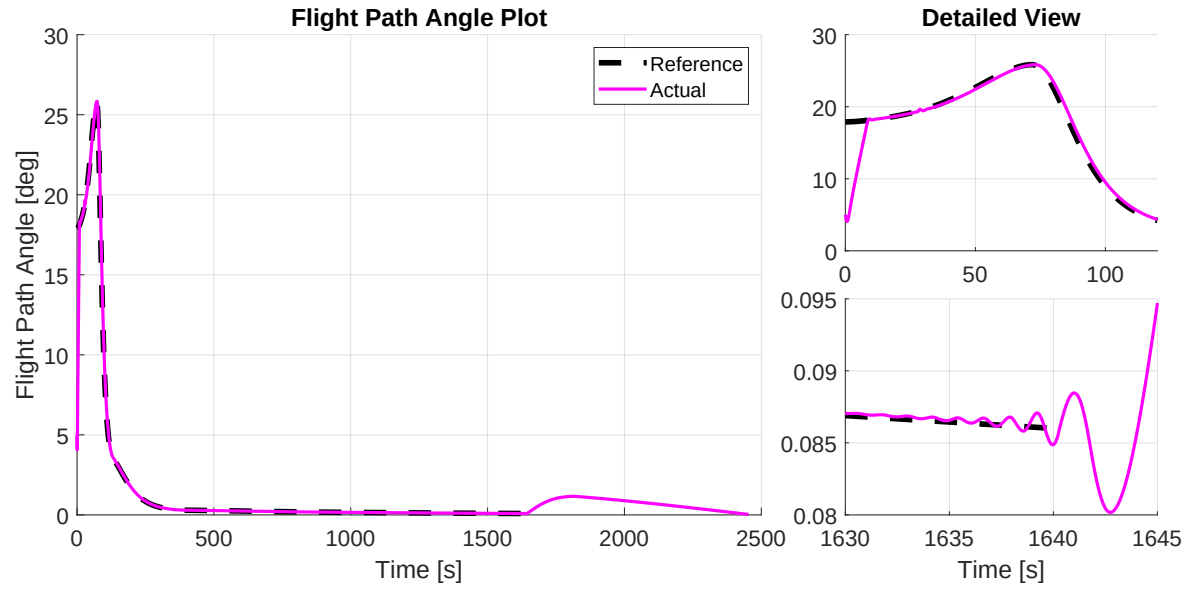

Figure 9.1: Verification of the G&C system to steer the space plane to the correct flight path angle. Simulation is shown for an initial launch time of $t_0 = 0$ s.

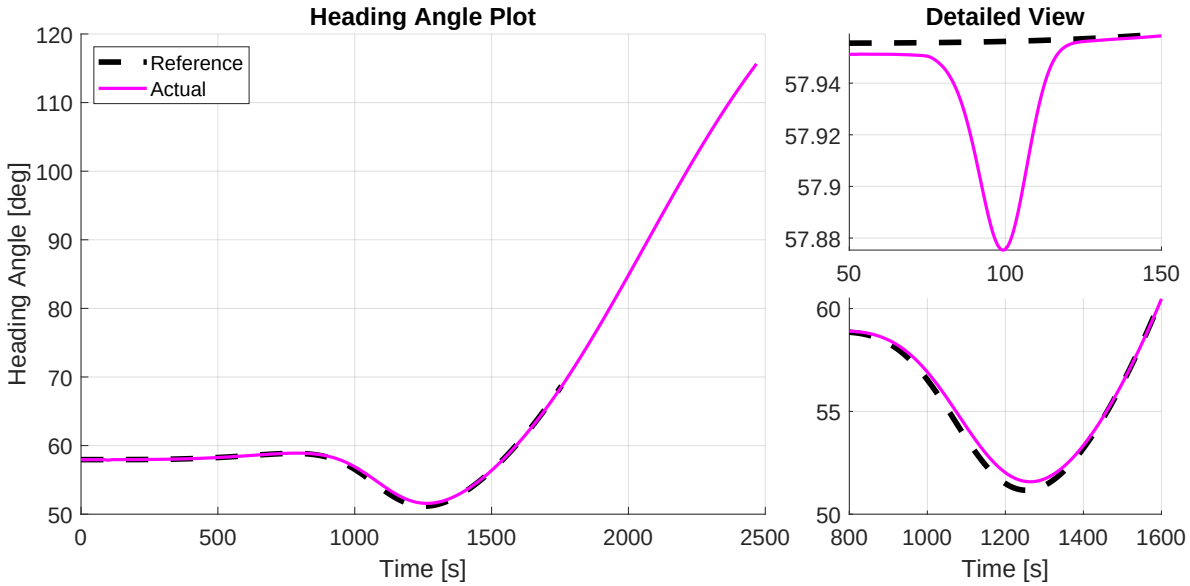

Figure 9.2: Verification of the G&C system to steer the space plane to the correct heading angle. Simulation is shown for an initial launch time of $t_0 = 3600$ s.

The G&C system is verified manually by inspecting the outcome of test simulations. In these tests, a guesstimate was done of the ascent trajectory. Based on the outcome of the simulation, the reference trajectory parameters, and desired aerodynamic angles were checked with the actual trajectory parameters and aerodynamic angles. In a similar fashion, the integration of the G&C system can be verified, with the obtained results, discussed in Chapter 8. In Figure 9.1, the reference flight path angle is shown up until the point that the guidance module steers the space plane to these reference parameters. Here it can be seen that, from the initial flight path angle of 5 degrees, the flight path angle rapidly is increased to the commanded flight path angle. After about 80 seconds, the flight path angle decreases again, where the guidance module has some trouble following the reference. Later when considering the aerodynamic angles, it will become apparent why this is the case. At the end of the first ascent phase, the flight path angle starts to oscillate slightly. As was mentioned earlier in Chapter 8, the flight path angle gain, $K_{\dot{\gamma}}$, was tuned to reduce these oscillations. As

can be seen, the oscillations are still present, albeit in reduced form due to the lower flight path angle gain. Figure 9.2 shows the reference and actual heading angle, where the reference angle is stopped at the end of the first ascent phase. Here it can be seen that the guidance module can effectively steer the space plane to the correct heading angle. Around 100 seconds, a small deviation is seen, which is caused due to the rapidly reducing flight path angle. This phenomenon will be discussed when considering the aerodynamic angles. The heading angle correction to insert in the target orbit, starts around 800 seconds. It can be seen that there is a difference between the reference heading angle and the actual angle. This can be contributed to a low heading angle gain, $K_{\dot{\chi}}$, which was chosen on purpose to limit the bank angle. At the end of the correction maneuver the actual heading angle has effectively been changed to match the reference.

In order to change the heading and flight path angle, desired aerodynamic angles are computed. Thus, to further verify the correct integration of the G&C system, the aerodynamic angles and their desired values should be analyzed. The angle of attack, Figure 9.3, is analyzed for an initial time of $t_0 = 0$ s, since the desired angle of attack is a direct result from the reference flight path angle. Here it can be seen that initially, the angle of attack is increased to increase the flight path angle. When the reference flight path angle decreases, the aerodynamic angle decreases as well. In order to follow the reference flight path angle the desired angle of attack becomes negative for a brief moment, where the lift force is negative. Afterwards, the flight path angle is followed, where the desired angle of attack slowly decreases due to the increasing velocity, which facilitates a lower aerodynamic angle to generate enough lift. When the pull up altitude is reached, where the oscillations were observed in Figure 9.1, also oscillations are seen for the desired angle of attack. Due to the reduced flight path angle gain, the angle of attack oscillations also remain somewhat limited. In the previous iteration of the gains, there was the tendency for the aerodynamic angle to increase to above 6 degrees, where the space plane was not able to trim itself anymore. For the pull up phase, it can be seen that the space plane is perfectly capable of following the aerodynamic angle until the engine cut-off altitude is reached.

For the desired bank angle, Figure 9.4, an initial time of $t_0 = 3600$ seconds is analyzed, which corresponds to the reference heading angle figure shown earlier. Here it can be seen that the desired bank angle is perfectly followed throughout the entire ascent. It can be seen that when the flight path angle has to be decreased, which necessitates a negative angle of attack, also a small banking maneuver is seen. This maneuver is due to the formulation of the desired bank angle, see Equation 6.48, where the desired change in flight path angle is included. When large changes in flight path angle are required, also a banking maneuver is initiated. This is in theory a correct maneuver, if the lift remains positive. However, due to the symmetric nature of the space plane, an aerodynamic angle below 0 degrees, means that the lift force is pointing downwards. Thus, the banking maneuver does indeed counteract the negative angle of attack, reducing the capability of the space plane to effectively change the flight path angle. This behavior is unintended and can be corrected by removing

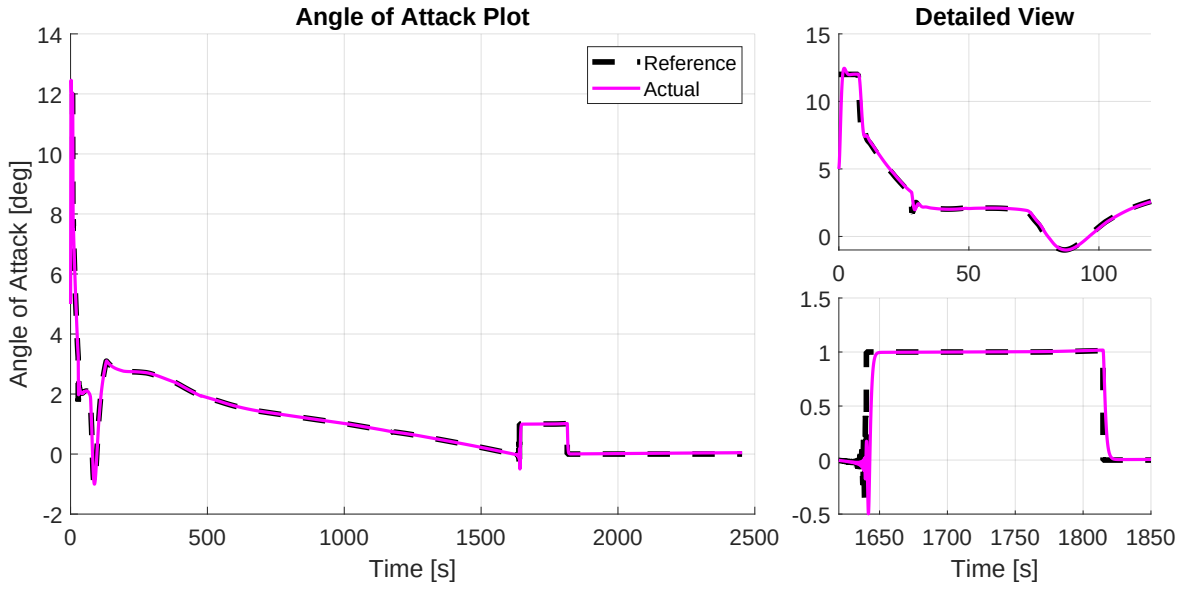

Figure 9.3: Verification of the G&C system to orient the space plane to the correct angle of attack. Simulation is shown for an initial launch time of $t_0 = 0$ s.

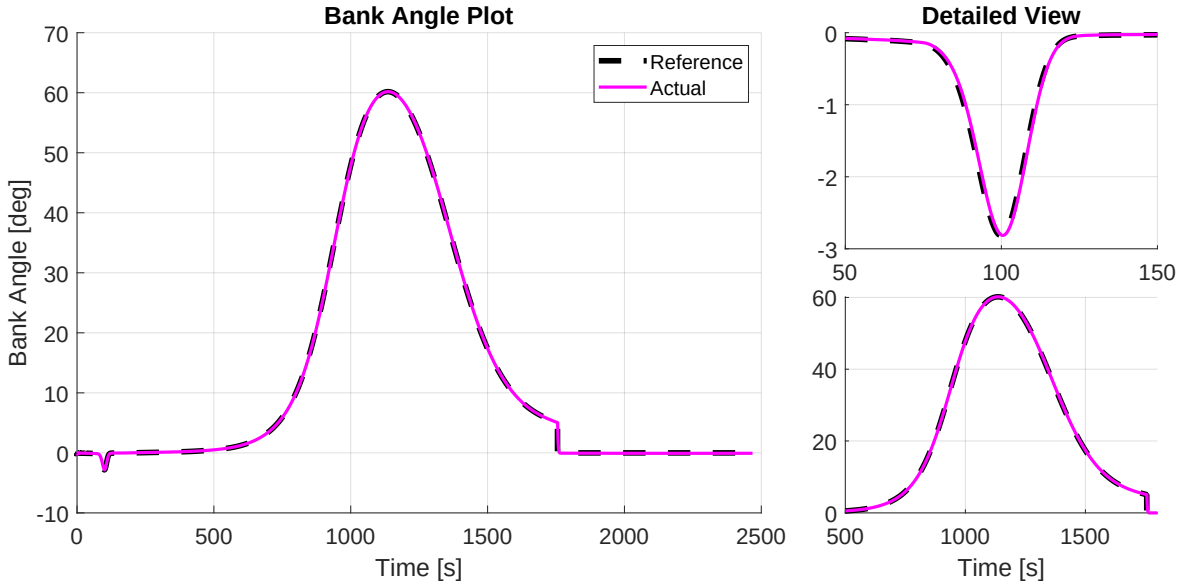

Figure 9.4: Verification of the G&C system to orient the space plane to the correct bank angle. Simulation is shown for an initial launch time of $t_0 = 3600$ s.

the flight path angle derivative virtual control value out of the aforementioned equation. However, this was not foreseen and changed when integrating the G&C system.

The last aerodynamic angle to be checked is the reference angle of sideslip. For the optimization of ascent trajectory, it was assumed that changing the heading angle should be done by the bank angle, setting the reference angle of sideslip to 0 degrees throughout the entire ascent. Figure 9.5 shows the reference and actual angle of sideslip for a launch time of $t_0 = 3600$ seconds. Here it can be seen that the angle of sideslip remains very close to zero, only varying slightly due to the changes in bank angle, as can be seen in the detailed view. As can be seen , changes in bank angle also have a small impact on the angle of sideslip.

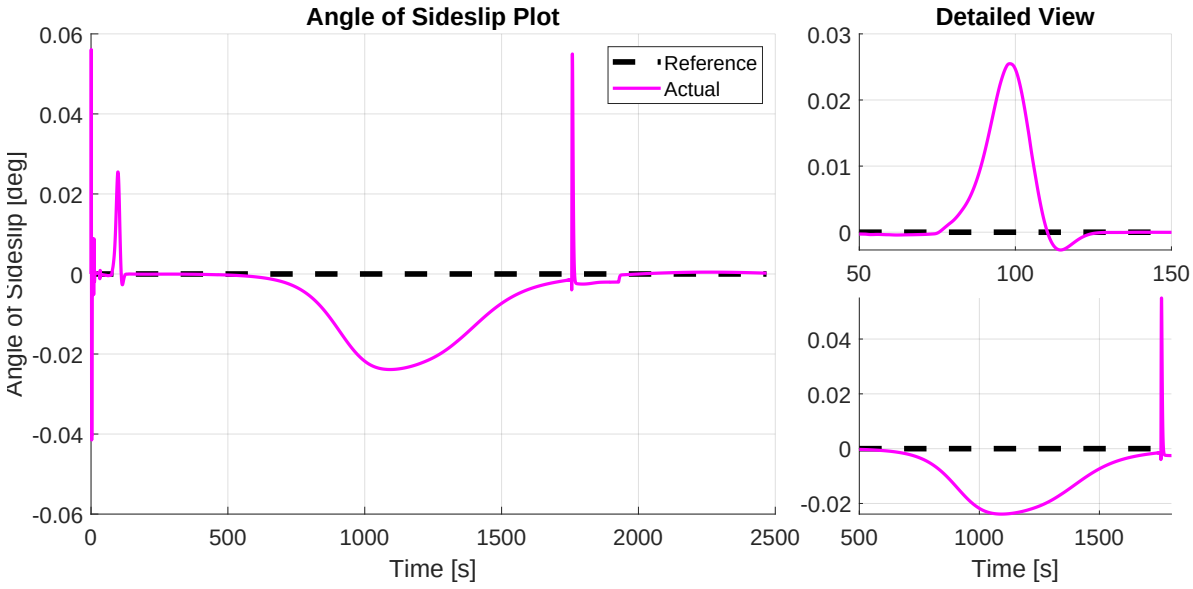

Figure 9.5: Verification of the G&C system to orient the space plane to the correct angle of sideslip. Simulation is shown for an initial launch time of $t_0 = 3600$ s.

With the analysis of the aerodynamic angles, it can be concluded that the G&C system is properly integrated. The space plane is capable of effectively following the reference trajectory angles and orienting itself to the desired aerodynamic angles. The oscillations that occur in the flight path angle and angle of attack are due to an unforeseen circumstance. Fortunately, the optimization algorithm was capable of finding solutions that would limit the impact of these oscillations. The cause of these oscillations will be explained during the sensitivity analysis.

9.1.3. Verification of the Longitudinal Motion

In the previous sections, the verification strategies were discussed to ensure that the vehicle model and G&C system were properly implemented in TUDAT. The obtained results from the optimization using TUDAT and Parallel Global Multiobjective framework for Optimization (PaGMO) can be verified with previous studies as was mentioned in the introduction of the section.

The first study that is used to verify the results will compare the obtained trajectory parameters, the constraints that were implemented, the angle of attack, drag and lift force, and equivalence ratio set by the G&C system to accelerate the space plane. The study is done by Mooij (1998), where the longitudinal ascent of the space plane was investigated. For this reason, the results obtained from an initial launch time of $t_0 = 0$ s is used as verification.

First of all, the flight path angle and angle of attack is compared, which can be seen in Figures 9.6 and 9.7. In the first figure, it can clearly be seen that the flight path angle is similar. The major difference is in the initial pull up, which occurs in the first 100 seconds. The results by Mooij (1998) show a more instantaneous increase of the flight path angle of 25 degrees, followed by an almost linear decrease afterwards. For the results obtained by this study show a somewhat later increase in the flight path angle, followed by a steeper decrease afterwards. This difference can be explained by the differences in the transcription of the optimal control problem. Due to the iterative nature of the global optimization, it is important to reduce the number of optimization parameters. Conversely, the verification results are manually found, which allows for a more discrete points at which the flight path angle can be defined. The difference in flight path angle is also reflected in the comparison for the angle of attack, where the verification results do not decrease below approximately 2 degrees. Since the results from this study require a faster change in flight path angle, a larger decrease in angle of attack is observed. The angle of attack comparison also shows the difference in how the pull up maneuver is done. This is once again a difference due to design choices, where for the verification results it was determined to perform the maneuver with a constant 6 degrees angle of attack. Due to the larger angle of attack, the flight path angle increase is slightly higher and drops more quickly due to the higher loss in velocity due to the increased drag, which will be shown later.

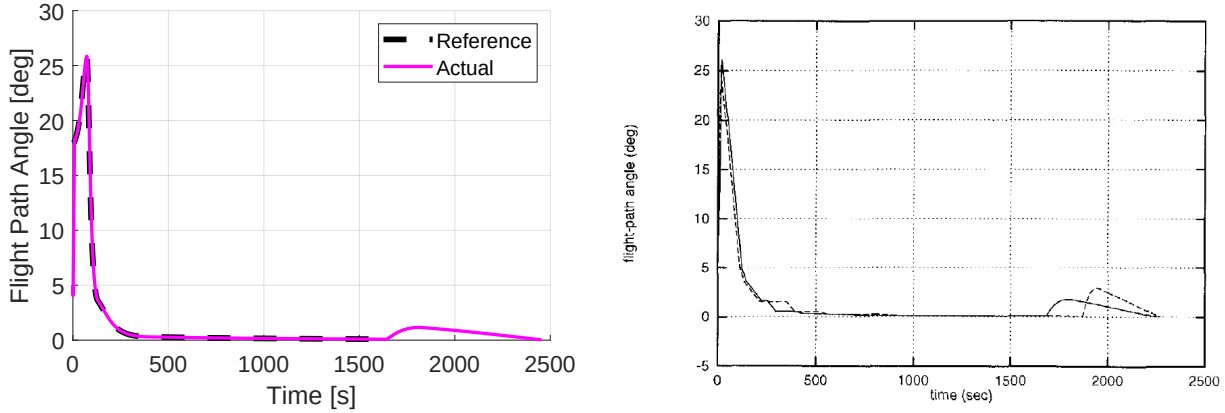

(a) Actual Results **(b)** Verification Results

Figure 9.6: Comparison of the flight path angle from this study and a previous study (Mooij, 1998).

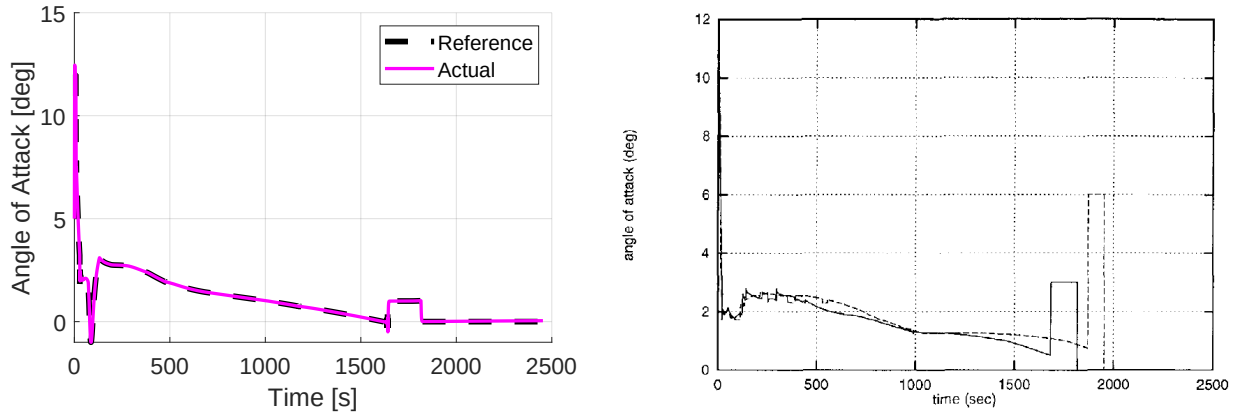

(a) Actual Results **(b)** Verification Results

Figure 9.7: Comparison of the angle of attack from this study and a previous study (Mooij, 1998).

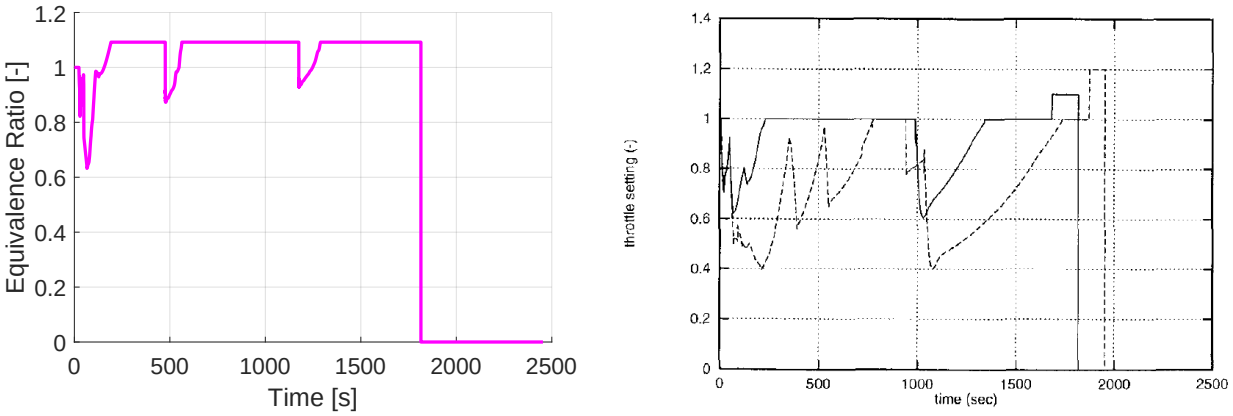

(a) Actual Results **(b)** Verification Results

Figure 9.8: Comparison of the equivalence ratio (thrust throttle) from this study and a previous study (Mooij, 1998).

The second part of the verification, is to show the equivalence ratio, used as thrust throttle, the dynamic pressure, and heat flux. The comparisons can be seen in Figures 9.8, 9.9 and 9.10. The study done by Mooij (1998) has used the same constraints, where the heat flux constraint is being computed with Equation 4.25. The equivalence ratio differs slightly due to the inclusion of a maximum equivalence ratio for the optimization of the NonLinear Programming (NLP) problem. Due to this difference, the dynamic pressure and heat flux reach the constraint at different times. However, the dynamic pressure and heat flux do drop significantly after the pull up phase starts, due to the rapidly increasing altitude. Additionally, it can be seen that the equivalence ratio is reduced whenever a constraint value is reached, which occurs for both the actual and the verification results.

The third part to verify is the drag and lift forces, which are generated by the space plane throughout the ascent. Figures 9.11 and 9.12 show the drag and lift for the results obtained in this study compared with the results obtained by Mooij (1998). By comparing these figures, it can be seen that the drag and lift force follow a similar pattern. However, it can be seen that both the drag and lift force obtained by this result has a higher peak at the start of the simulation. This can be explained by the different simulation settings. In this study, the angular velocity and angular acceleration are modeled, where the elevons are used to induce an angular acceleration in order to orient that space plane. In the verification study, the elevons are used only to trim the space plane for each time step. At the start of the simulation the angle of attack is increased to increase the flight path angle. The elevons are used to increase the angle of attack, which induce an increased drag and lift force. A detailed view of the drag and lift force for this study can be seen in Figure 9.13.

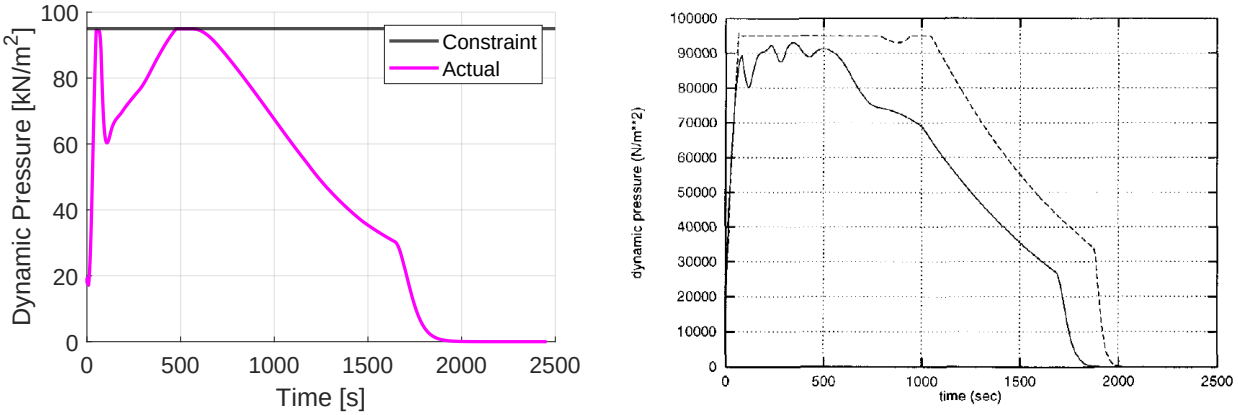

(a) Actual Results **(b)** Verification Results

Figure 9.9: Comparison of the dynamic pressure from this study and a previous study (Mooij, 1998).

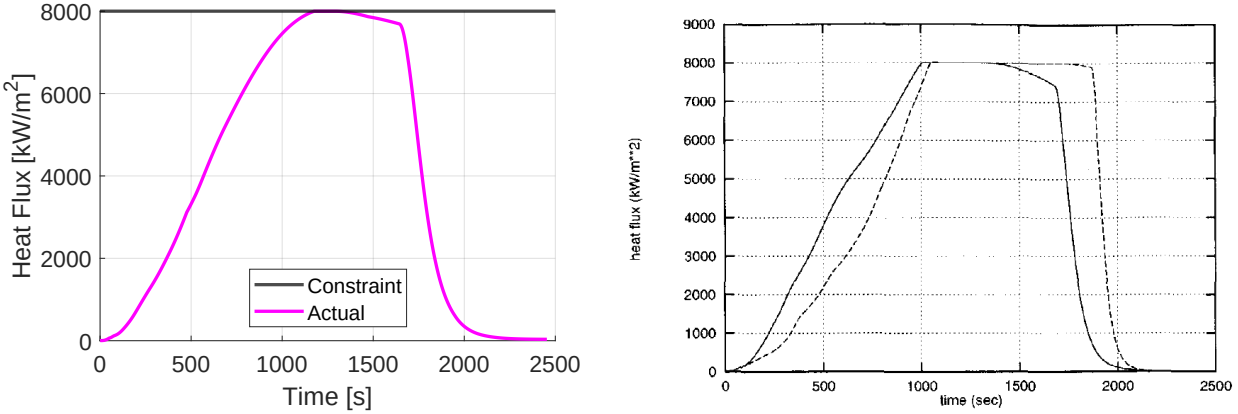

(a) Actual Results **(b)** Verification Results

Figure 9.10: Comparison of the heat flux from this study and a previous study (Mooij, 1998).

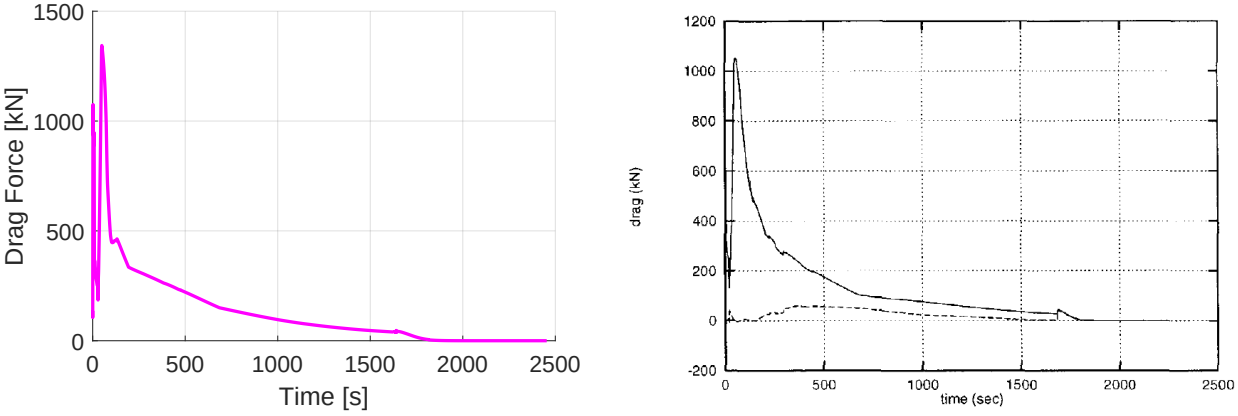

(a) Actual Results **(b)** Verification Results

Figure 9.11: Comparison of the drag force from this study and a previous study (Mooij, 1998).

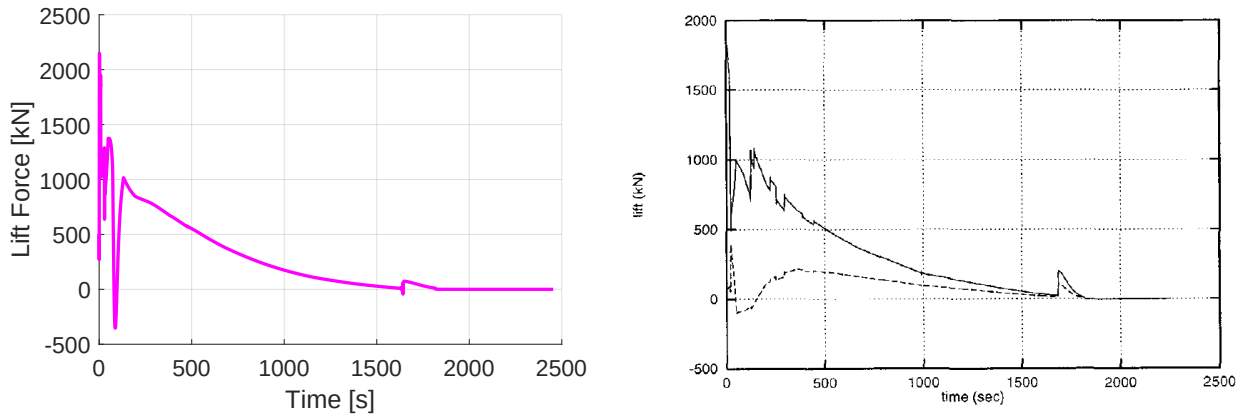

(a) Actual Results **(b)** Verification Results

Figure 9.12: Comparison of the lift force from this study and a previous study (Mooij, 1998).

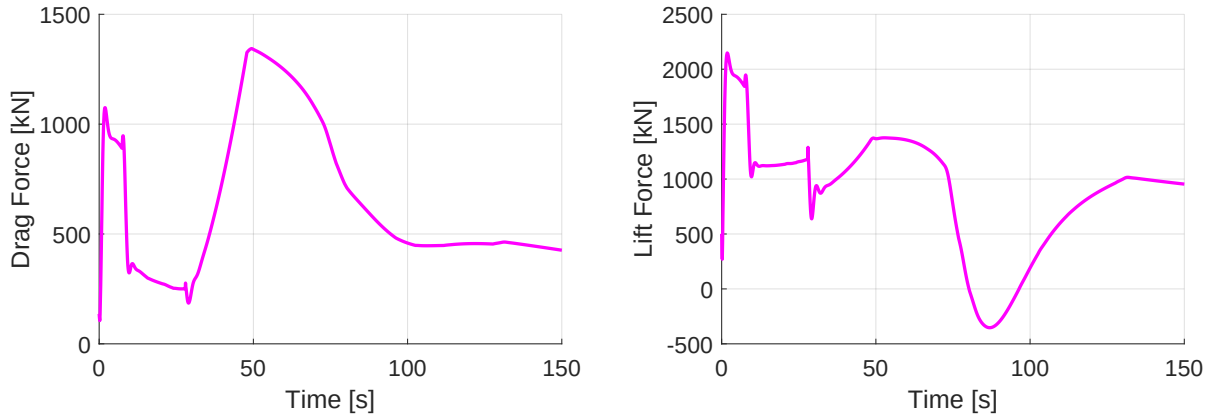

(a) Drag Force **(b)** Lift Force

Figure 9.13: Detailed view of the drag and lift force at the start of the simulation.

With the details of the ascent trajectory discussed, a general overview can be given of the ascent of a space plane. In the study by Mooij (1998), this is done by showing the altitude of the space plane as a function of velocity, where the dynamic pressure and heat flux constraints are also depicted. Figure 9.14, shows this plot, as well as the plot generated by the results from this study. Here it can be seen that the both results show a similar line, following along either the dynamic pressure constraint or the heat flux constraint up until the pull up phase. For the observant reader, it can be seen that the final velocity obtained by this study is higher. This can be explained by the fact that the space plane is inserted into an inclined orbit, whereas the verification study inserts into an equatorial orbit. Due to the inclination, the space plane benefits less from the rotation of the Earth that increases the inertial velocity. Thus, the velocity that the space plane needs to achieve, expressed in the rotational frame, is higher. Furthermore, it can be seen that the circularization maneuver changes the velocity by less, which is a result of the optimization of the pull up maneuver.

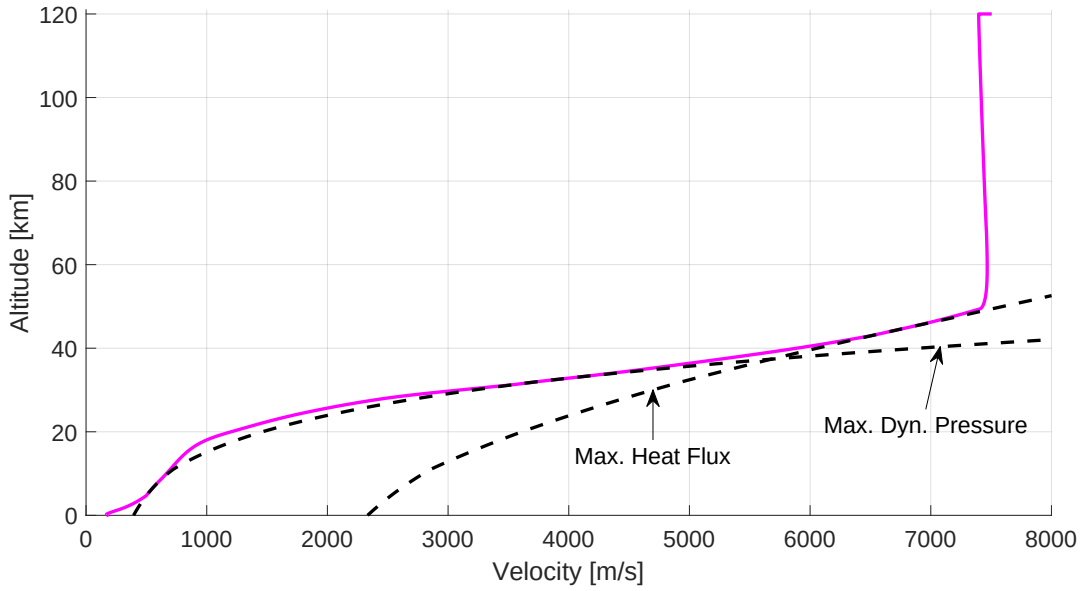

(a) Actual Result

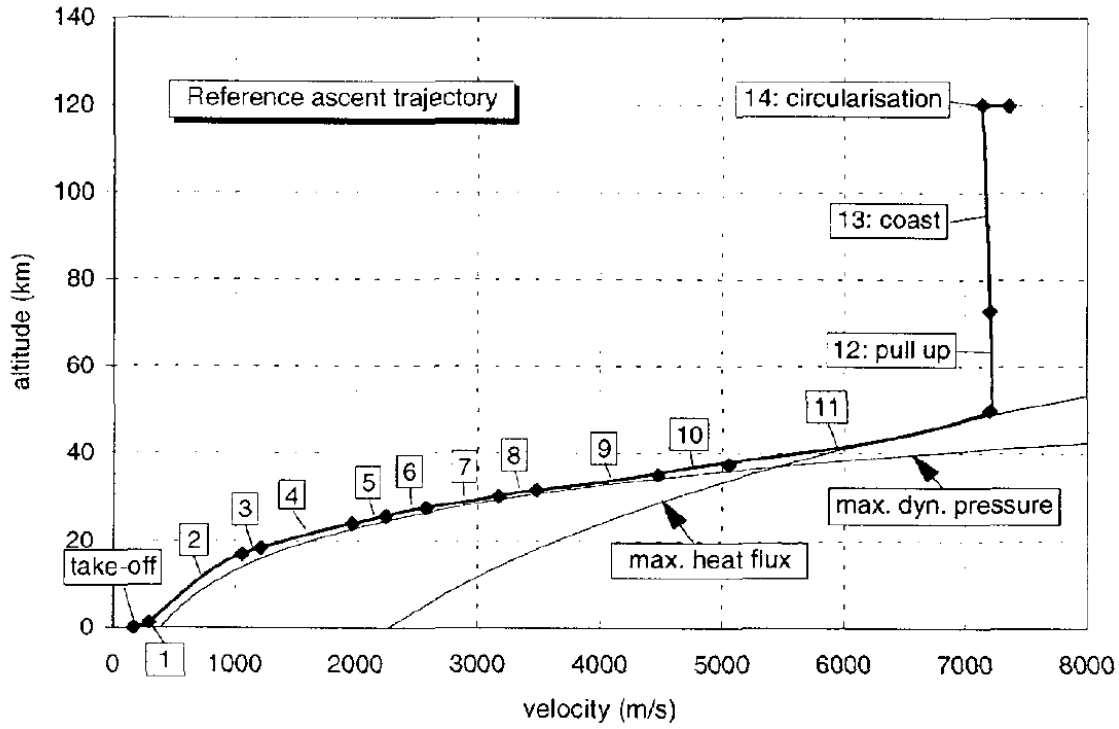

(b) Verification Result

Figure 9.14: Overview of the altitude versus velocity plot for the results of this study and the verification study (Mooij, 1998).

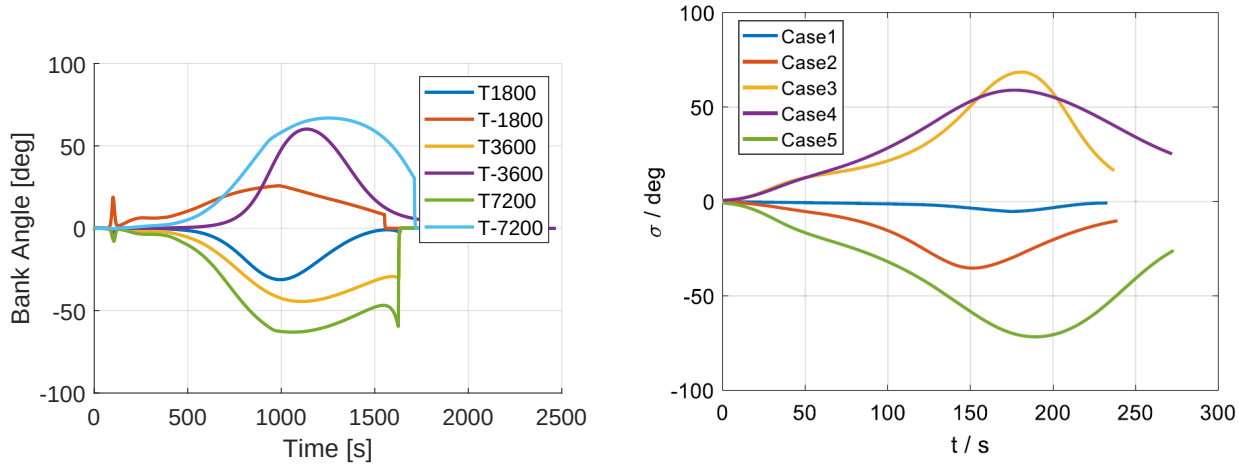

(a) Actual Result **(b)** Verification Result

Figure 9.15: Comparison of the dynamic pressure from this study and a previous study (Zhou, Wang, and Cui, 2020).

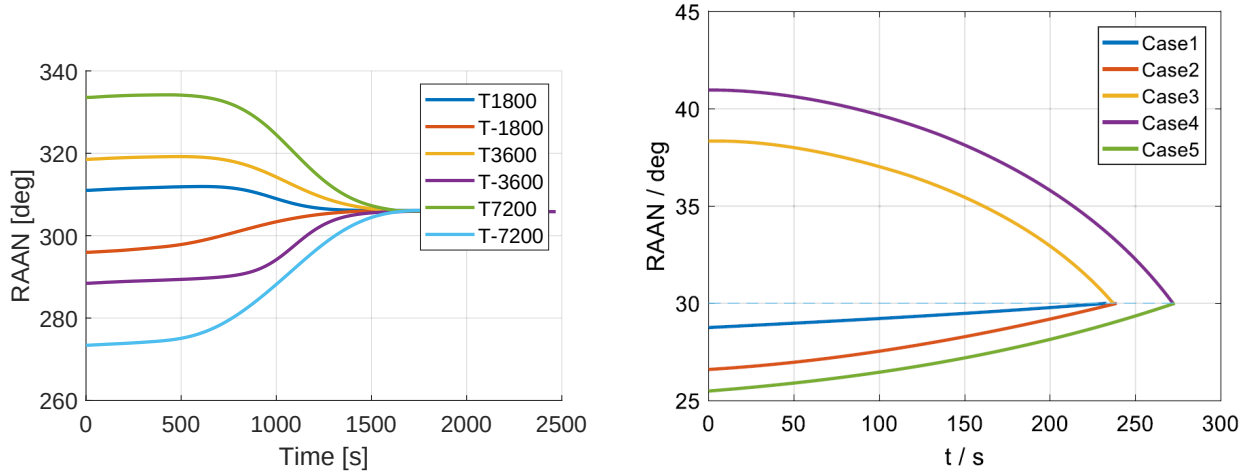

(a) Actual Result **(b)** Verification Result

Figure 9.16: Comparison of the dynamic pressure from this study and a previous study (Zhou, Wang, and Cui, 2020).

9.1.4. Verification of the Lateral Motion

The lateral motion is verified with the results obtained by Zhou, Wang, and Cui (2020). It should be noted that this study, only analyzed an ascent between 20 and approximately 55 km altitude, where the velocity at the termination altitude was 5000 m/s. Additionally, the study did have a higher flight path angle, which reduces the time of flight to approximately 250 seconds. Due to the small time of flight and low velocity, the bank angle maneuver is not as effective as was demonstrated in this study. Furthermore, the verification study did not present a heading angle time history. Thus, the verification can only be done based on the bank angle history and the change in RAAN that was accomplished by this banking maneuver. The study by Zhou, Wang, and Cui (2020) has investigated five different cases for which a change in RAAN is achieved. Cases one through four are for an orbital inclination of 20 degrees with a change in launch time of −300, −600, 1800, 2400 seconds, respectively. The fifth case is done for an orbital inclination of 80 degrees with a launch time of −1800 seconds.

In Figure 9.15, it can be seen what banking maneuver is performed, while Figure 9.16 shows how this maneuver changed the RAAN. Due to large differences in the verification study and this study, a proper verification of the results is not possible. However, it can be seen that both results show a similar banking maneuver, with a corresponding change in RAAN. In this study, the full ascent was studied, where the change

in RAAN would only start after a predetermined altitude is reached. The sigmoid function, that was used to determine the reference heading angle, gives great flexibility to when the banking maneuver should start and how aggressive this change should be. This explains the difference in how the RAAN is manipulated. Whereas the verification study shows a predictable change in RAAN irregardless of the launch time, this study shows a less predictable change.

9.1.5. Concluding Remarks with Regards to the Verification

The verification of the integration of the vehicle model and G&C system has been discussed and verified by comparing the results obtained by Mooij (1998) with the results presented in the study. It has been seen that the results presented in this study have large similarities for the longitudinal ascent. Additionally, by comparing the lateral maneuvers presented by Zhou, Wang, and Cui (2020) to the results obtained in this study, it can be seen that similar banking maneuvers were found to manipulate the RAAN. However, it should be noted that due to variations in the vehicle model, ascent trajectory choices and definition of the banking maneuver, a larger change in RAAN was found in this study compared to the study by Zhou, Wang, and Cui (2020).

9.2. Sensitivity Analysis

A partial sensitivity is performed and discussed in this section. First, impact on the results due to deviations in the initial state are analyzed. This is followed by a performance analysis of the G&C system. Lastly, a discovered issue is analyzed and discussed by varying an optimization parameter.

9.2.1. Sensitivity to the Initial State

In order to asses the sensitivity of the results to the initial state, a number of parameters that determine the initial state have been varied. The first parameters that are varied relate to the velocity vector. The velocity is varied by a percentage initial velocity of 170 m/s. The variation of the velocity can be seen in Figure 9.17. The flight path angle and heading angle are varied by a specific value, since the initial flight path angle is already quite small, and the heading angle varies depending on the deviation in inclination. The variation in these angles can be seen in Figures 9.18 and 9.19. In these figures, it can be seen that irregardless of the changes made to the initial state, the altitude time history would only change slightly. What can be observed that most individuals reach the target altitude or just miss it, before descending again. For the velocity, an exception is found for the negative change of 10%. The velocity is decreased by 17 m/s, which results in the space plane not generating enough lift to increase the altitude. Another exception is found in the variation in flight path angle, for the negative variations in flight path angle for an initial launch time of $t_0 = 0$ seconds. For this variation, the simulation stops just before the pull up altitude. By further inspection, this is caused by the oscillations that were found and discussed in Chapter 8. This indicates that the oscillations are still present and are capable of causing a termination of the simulation. For the variation in heading angle, it was found that either a positive or negative variation of 1 degree induces a banking maneuver, which causes the space plane to lose altitude. Since the initial altitude is 0 meters, the simulation is immediately terminated.

Besides the velocity vector parameters, the initial mass and altitude have been varied. The results of the variation in mass can be seen in Figure 9.20. Here it can be seen that for an initial time of $t_0 = 0$ seconds, once again a simulation is terminated around the pull up altitude due to the oscillations in the flight path angle. The other simulati do not terminate due to oonsscillations, but most solutions do not reach the target altitude. Interestingly, the negative variations for an initial time of $t_0 = -3600$ seconds still reach the target altitude. For a variation in the altitude, Figure 9.21, almost no difference is seen except for a variation in altitude by 1 km. It can be seen that the space plane is not capable of ascending to the target altitude, due to reference flight path angle, see Figure 9.22. It can be seen that the initial flight path angle can be followed, However, the reference flight path angle of 25 cannot be reached, and starts oscillating. It is theorized that the increased starting altitude means that the velocity required to obtain such a high flight path angle cannot be reached due to the axial acceleration constraint.

Lastly, the sensitivity of the results to initial aerodynamic angles have been analyzed. The variation of the angle of attack, angle of sideslip and bank angle did not yield any new information. The only issue that was found in the variation of these angles was that the target altitude was not reached, resulting in the space plane descending again. For this reason, the figures of these variations are not included.

It can be concluded that the sensitivity of the found solution to the final solution is limited. Any variation in the flight path and heading angle can be handled well by the guidance module, except for a few situations

due to oscillations in the flight path angle. Furthermore, the result is not sensitive to changes in altitude. Unless the altitude is too high for the space plane to generate enough lfit, it can be ensured that the space plane achieves the target altitude. However, the final result is more sensitive to variations that impact the velocity. The difference in velocity and mass causes the space plane to either miss the target altitude or reach the target orbit with a higher flight path angle. By including a minimum velocity before the pull up maneuver is initiated, it can be ensured that the target altitude is at least reached irregardless of the variation in initial velocity or mass.

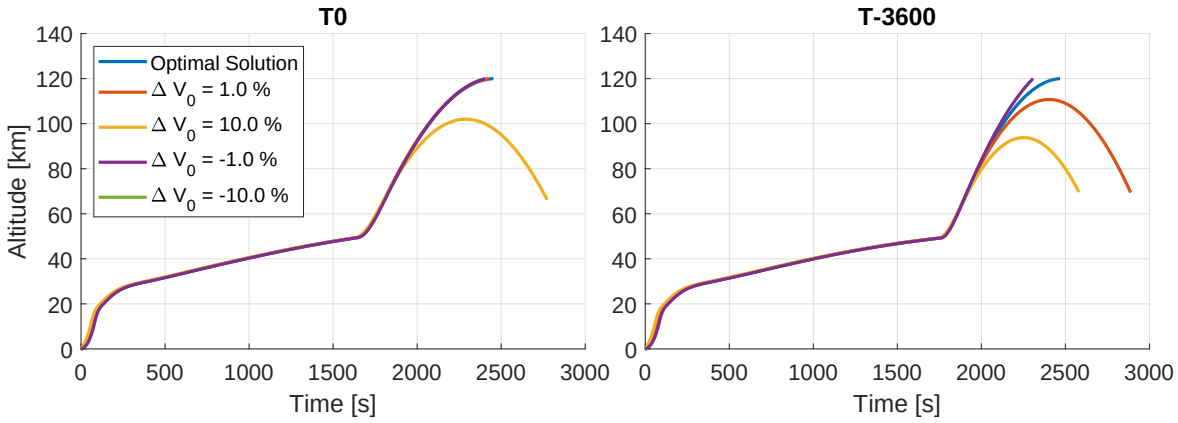

Figure 9.17: Time history of the altitude of the space plane for a variation in the initial velocity.

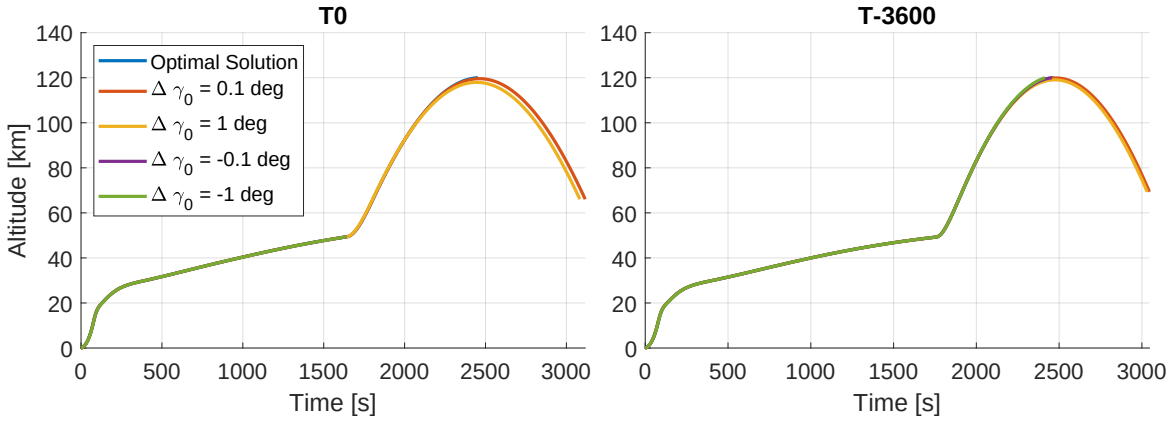

Figure 9.18: Time history of the altitude of the space plane for a variation in the initial flight path angle.

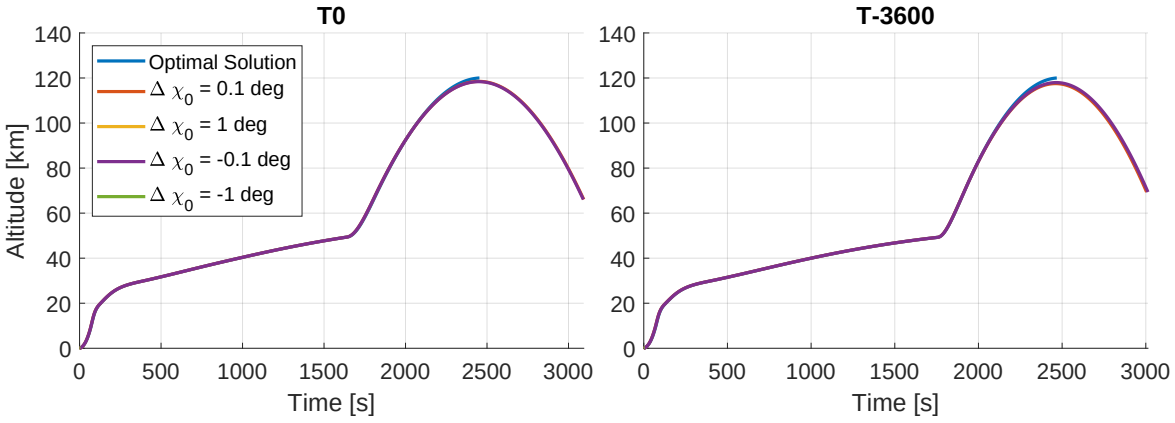

Figure 9.19: Time history of the altitude of the space plane for a variation in the initial heading angle.

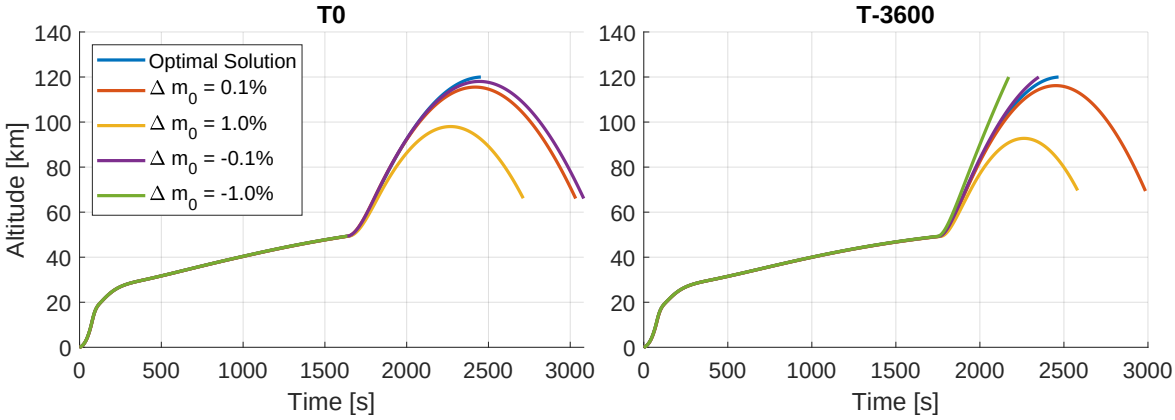

Figure 9.20: Time history of the altitude of the space plane for a variation in the initial mass.

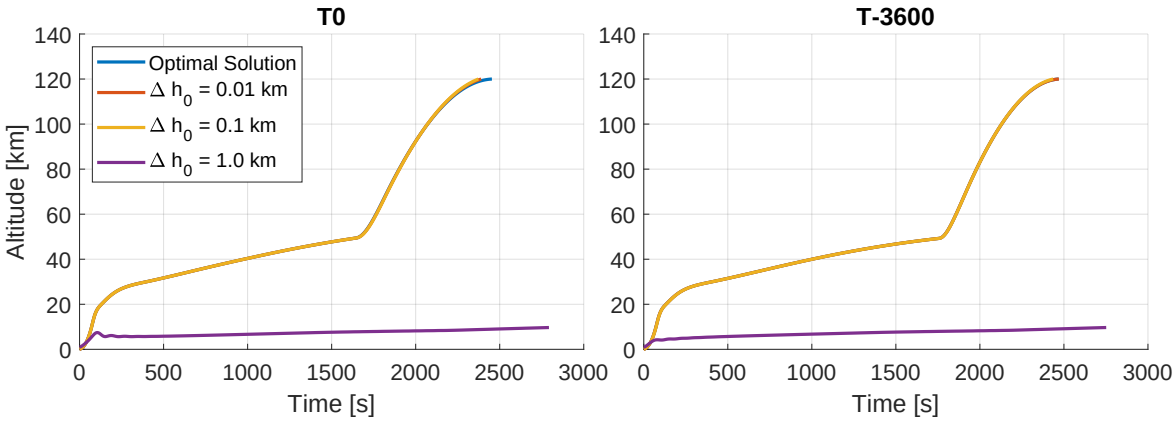

Figure 9.21: Time history of the altitude of the space plane for a variation in the initial altitude.

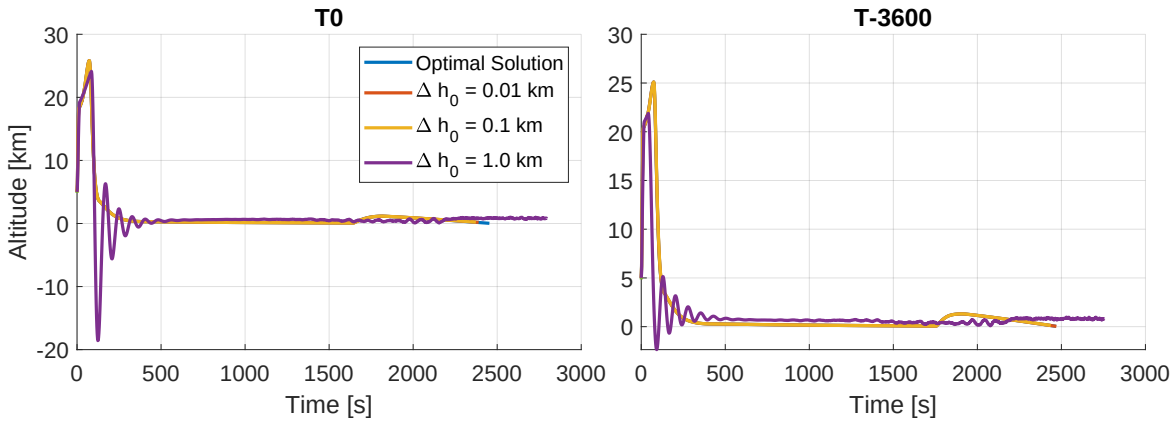

Figure 9.22: Time history of the flight path angle of the space plane for a variation in the initial altitude.

9.2.2. Sensitivity to Errors in the G&C System

The sensitivity of the obtained results to the G&C system is assessed by investigating the impact of an offset to the deflection angles. This is done for each control surface separately, where the time history of the altitude that the space plane achieves is used as comparison. The first offset is to the left elevon, with the results shown in Figure 9.23. Here it can be seen that the altitude history up to the pull up altitude is similar for all simulations. However, at the pull up altitude, a number of simulations are terminated due to the angle of attack boundary being exceeded. Furthermore, the simulation with an offset of 0.1 degree does not reach the target altitude. The time history for a deflection in the right elevon is seen in Figure 9.24, where the same issues occur as was seen for the offset in the left elevon deflection. Lastly, the rudder deflection angle is investigated, as can be seen in Figure 9.25. Here it can be seen that once again, the simulation either stops around the pull up altitude, the simulation misses the target altitude or the simulation is successful in reaching the target altitude. The last investigation is done with an offset to all three deflections at the same time, where the same offset is used for all control surfaces. The results can be seen in Figure 9.26, where once again the simulation is terminated due to one of the aforementioned issues.

Besides the offset in control surface angles, also an offset in thrust elevation angle and equivalence ratio is investigated. For the thrust elevation angle, the same offsets are used as for the control surfaces. The results of the thrust elevation angle can be seen in Figure 9.27, where the most interesting phenomenon can be seen around the 45 km altitude mark. Here it can be seen that the simulation is terminated for an offset in negative thrust elevation angle. This is caused for both launch times, where oscillations in the flight path angle occur. It is interesting to see that this only occurs for negative offsets in thrust elevation angle. Seeing this unexpected phenomenon only happens for a negative offset, might indicate that the interaction between the trim module and the control module causes oscillations in the flight path angle at high velocities. The variation in equivalence ratio can be seen in Figure 9.28. Here it can be seen that the negative variation of 0.1 results in simulations that are unable to maintain the altitude profile that the other simulations do have, which can be explained by the lack of acceleration due to the reduced equivalence ratio. Other than that, most runs once again either terminate due to oscillations in the flight path angle, reach the target altitude or just miss it.

It can be concluded that the reason why simulation are unsuccessful is either due to the oscillations that occur around the pull up altitude, or the space plane does not have enough velocity at the pull up altitude to reach the target orbit. This means that the results are sensitive to the control method to command the space plane for certain flight path angles at high velocities. It can be argued that the pull up altitude that was optimized for, is not a product of the optimal altitude, but the best altitude to transition to direct angle of attack control to ensure that the oscillations would stop before it became catastrophic. Furthermore, in order to ensure that the target altitude is reached, a minimum pull up velocity could be defined. The minimum velocity could be included in the optimization process to determine what this minimum velocity is. This could potentially eliminate the pull up altitude as an optimization parameter altogether. It is recommended to include such a condition to ensure that the target orbit is reached.

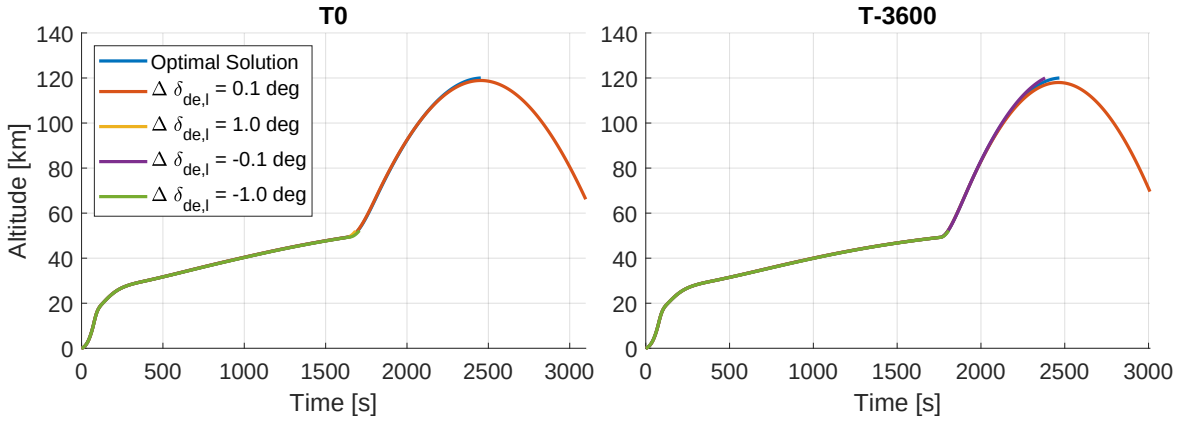

Figure 9.23: Time history of the altitude of the space plane for an offset in the left elevon deflection angle.

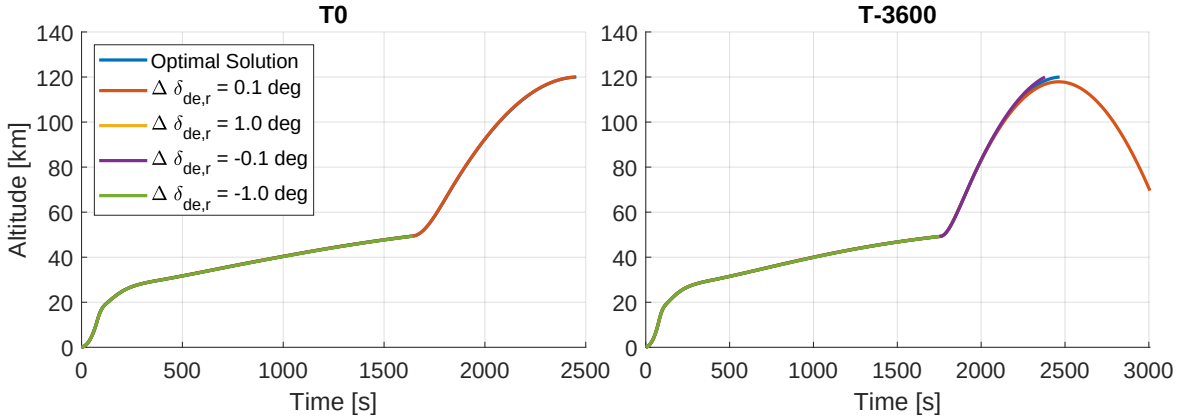

Figure 9.24: Time history of the altitude of the space plane for an offset in the right elevon deflection angle.

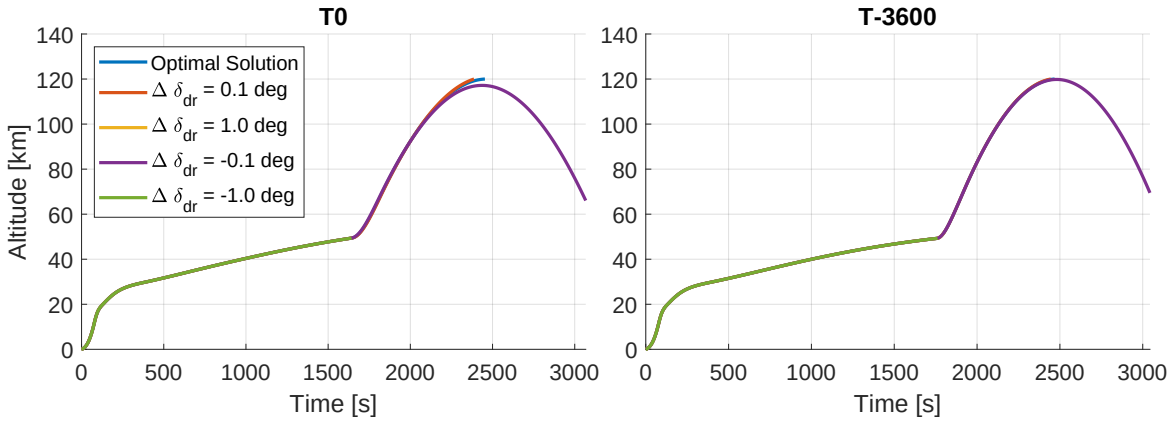

Figure 9.25: Time history of the altitude of the space plane for an offset in the rudder deflection angle.

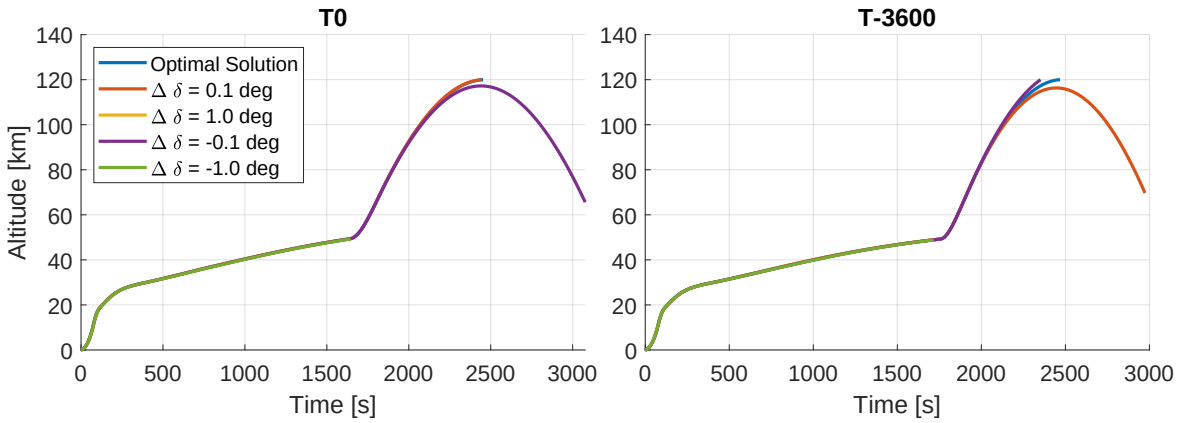

Figure 9.26: Time history of the altitude of the space plane for an offset in the elevons and rudder deflection angle.

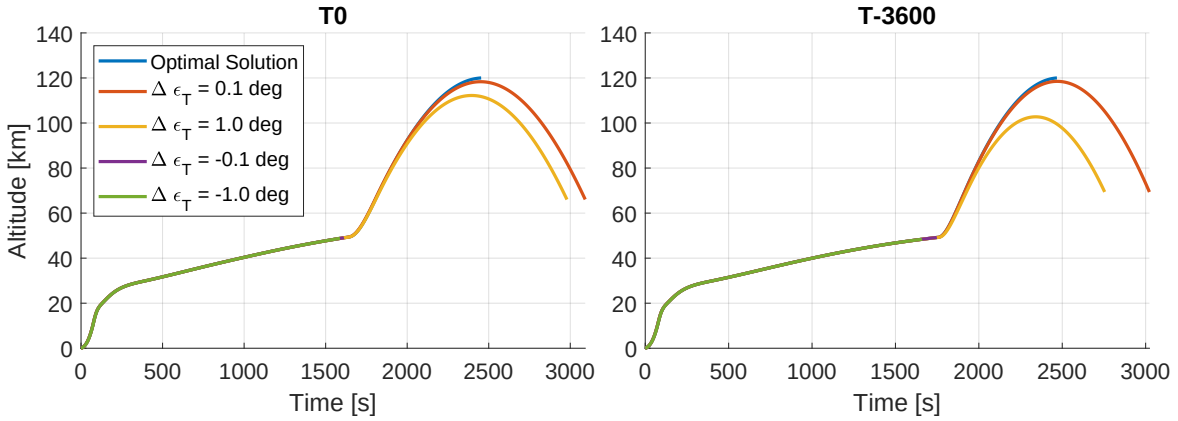

Figure 9.27: Time history of the altitude of the space plane for an offset in the thrust elevation angle.

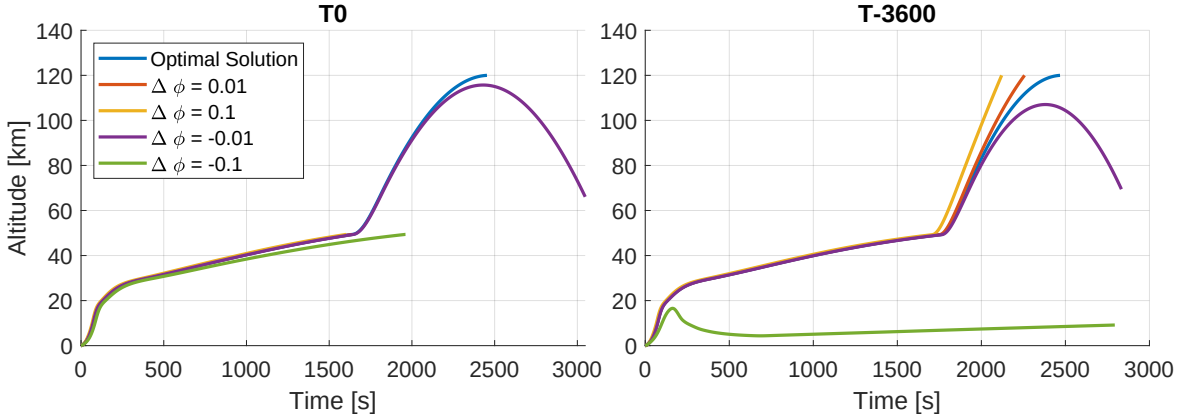

Figure 9.28: Time history of the altitude of the space plane for an offset in the equivalence ratio.

9.2.3. Sensitivity to the Optimization Parameters

It has been established that the G&C system has an issue to correctly steer the space plane to the flight path angle close to the pull up altitude, where the velocity of the space plane reaches velocities above 7000 m/s. Due to this issue, the optimization found results based on this issue *i.e.*, the solution accommodates for the flight path angle oscillations, trying to limit these to ensure that the space plane achieves the target altitude. Due to this issue, any changes to the flight path angle will most likely result in solutions that terminate around the pull up altitude. In order to confirm this suspicion, a sensitivity analysis is done for the pull up altitude optimization parameter. Furthermore, during the discussion of the results it became apparent that the point of the pull up altitude was an important optimization parameter that would enable the space plane to pull up at a velocity that, when the target orbit was reached, the space plane would have a flight path angle close to zero. The result of the variation in pull up altitude can be seen in Figure 9.29, where immediately it can be seen that a negative variation in the pull up altitude will result in the space plane not reaching the target altitude. This indicates that the found pull up altitude is indeed optimized for. The goal of the optimization was to find a solution that would reach the target orbit accurately with as little fuel as possible. A decrease in the pull up altitude will result in the space plane not achieving the proper velocity to achieve the target altitude. Conversely, an increase in pull up altitude will increase the pull up velocity, which results in a non zero positive flight path angle at the target altitude. The positive flight path angle will result in a circularization maneuver that is not perpendicular to the local horizontal plane, which means that the maneuver will be less effective. However, the space plane will use less fuel since it achieves a higher velocity with the more efficient air-breathing engine, and uses less to do the circularization maneuver. Thus, it can be concluded that the pull up altitude found for both launch times is the optimal altitude. The positive change in the pull up altitude will yield some results that reach the target orbit. For the initial launch time of $t_0 = 0$ seconds, a positive change of 10 meters will still result in a solution that reaches the target orbit. However, the positive change of 100 meters or more, will result in flight path oscillations that result in the termination of the simulation prematurely. Interestingly, the launch time of $t_0 = -3600$ seconds, does also give a good result for an increase in the pull up altitude of 100 meters. Throughout the previous analyses that have been performed for the sensitivity of the G&C system and initial state, this could also have been observed. Apparently, the solution found for the advanced launch time is less prone to these flight path oscillations.

The flight path oscillations dominate the results that are obtained with the sensitivity analysis. Further investigating the optimization parameters will result in most cases of the flight path angle starting to oscillate and terminate the simulation, which will yield no valid results to perform a sensitivity analysis on. For this reason, it is chosen to not further investigate the sensitivity of the results. Resolving the oscillations will enable sensitivity analysis of changes to the optimization parameters and how those changes impact the propellant and target orbit objective.

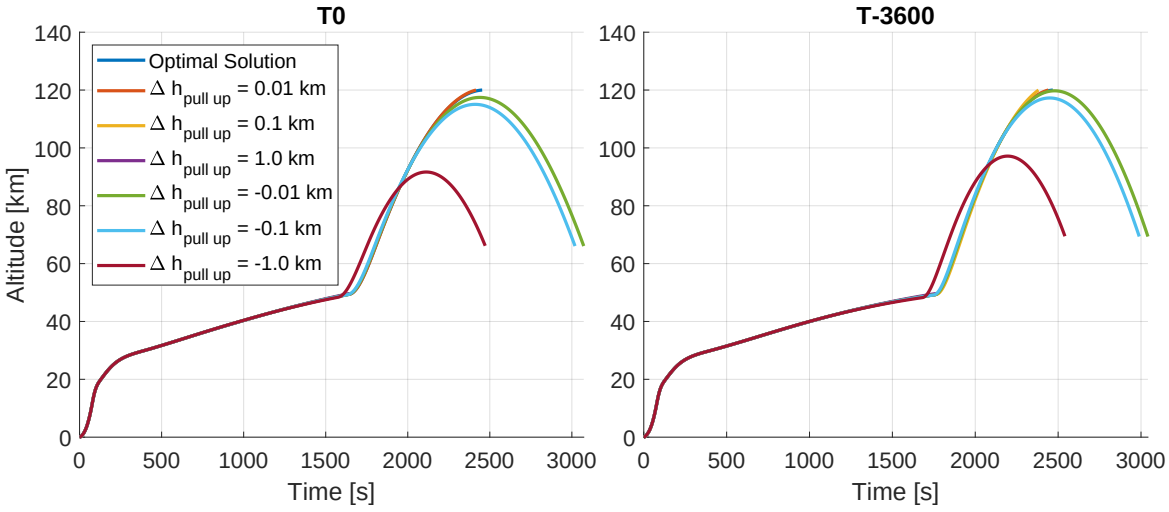

Figure 9.29: Time history of the altitude of the space plane for a variation in the pull up altitude.

9.2.4. Intermezzo to the Sensitivity Analysis

During the analysis of the flight path oscillations with respect to the optimization parameters, it became apparent that the oscillations start when the angle of attack of the space plane is close to zero. The angle of attack becomes zero at different time depending if a banking maneuver is performed. The reason that the oscillations occur is due to three factors occurring simultaneously. First of all, the flight path angle is close to zero and should only change slowly. Second of all, the angle of attack is close to zero, which means that the symmetric body does generate only small amounts of lift. Third and last of all, the velocity of the space plane is increasing, which increases the natural pitching moment of the space plane. At the pull up altitude, the natural pitching moment has increased to such magnitudes that the Thrust Vector Control (TVC) system is unable to compensate for the moment by itself. This means that the elevons are activated to reduce the remaining pitching moment to zero. The increase in the elevons deflection angle induces a lifting force in either positive or negative direction, which influences the flight path angle. The change in flight path angle, which the space plane tries to compensate for by changing the angle of attack. However, the space plane still has a small angle of attack, which means that a change in angle of attack is not effective enough compared to a change in deflection angle. This induces a back and forth, where desired computed angle of attack starts oscillating due to the deflection angles that continuously change. This hypothesis would also imply, that if the maximum thrust elevation angle was limited, these oscillations would occur earlier. As can be seen in Figure 9.27, the negative bias on the thrust elevation angle advances the moment that the flight path oscillations occur. Since the time that the natural pitching moment can no longer be overcome by the TVC is earlier.

9.2.5. Concluding Remarks with Regards to the Sensitivity Analysis

In the sensitivity analysis it has been seen that variations in initial state and variations to the parameters determined by the G&C system can be handled well. This can be explained by the use of the Incremental Nonlinear Dynamic Inversion (INDI) algorithm, which does not require the use of linearized equations. Typically, using linearized equations results in eigenmotions, which can cause unstable motions that cannot be damped by the linearized control algorithm. By using a nonlinearized algorithm these unstable motions are not present in the G&C system and are no issue when considering changes to the initial state and offsets imposed on the G&C system. Unfortunately, it became apparent that the results obtained are sensitivity due to an oversight in the G&C system, where the flight path angle would start to oscillate under specific circumstances. Luckily, the optimization process was able to find a solution that would reach the target orbit with a reasonable amount of propellant. However, the robustness of the solution cannot be fully established due to this oscillation issue. What can be established is that the found results are sensitive to the pull up altitude and the velocity at which this pull up maneuver is initiated. It is recommended to determine the required velocity before the pull up is initiated to ensure that the target orbit is achieved. In Section 10.2, a few hints will be given on how to determine this minimum velocity.

10

Conclusion and Future Recommendations

In this study, an investigation is done into the capabilities of a Horizontal Take-off and Horizontal Landing (HTHL) space plane to change the Right Ascensions of the Ascending Node (RAAN) of the target orbit. Something typically not capable by conventional rockets. By being able to change this parameter, an extended launch window can be established for which the space plane is capable of launching and still achieving the same orbit. The flexibility that this increased launch window gives can increase the reliability of a launch occurring. Launches can be canceled for a number of reasons, such as bad weather or technical malfunctions. Furthermore, the increased launch window can be used to replace satellites if there is a malfunction and an emergency replacement is necessary.

The change in the RAAN is possible by using lateral motion, which can also change the inclination of an orbit. The manipulation of these 'lateral' parameters has been investigated before in a limited capacity (Zhou, Wang, and Cui, 2020). In the previous study, only an ascent trajectory between 20 and approximately 55 km was considered. Furthermore, the cost of changing the RAAN in terms of propellant was not quantified. To add to this study, similar maneuvers are investigated and applied to the National Aero-Space Plane (NASP), a conceptual space plane, that has been used in previous studies to find an optimal longitudinal ascent trajectory (Shaughnessy et al., 1990; Powell et al., 1991; Mooij, 1998). By using this space plane, the results in this study can be verified and the possibility to change the RAAN can be quantified in terms of necessary propellant. Furthermore, the optimization parameters that have been used by Zhou, Wang, and Cui (2020) have been expanded upon. In that study, a deviation in inclination was introduced to manipulate the RAAN that would change linearly to zero. This approach has been expanded upon by introducing a sigmoid function that defines the deviation in target inclination. The sigmoid function, a function of altitude, enables to change both the point at which the deviation in orbital inclination changes, as well as the speed at which the change is done. Additionally, in this thesis a robust Guidance and Control (G&C) system was implemented. The inclusion of this system allowed for the elimination of eigenmotions, which made the space plane less sensitive to changes in initial conditions, changes in optimization parameters, and errors the deflection angles of the actuators.

The chapter is divided into two parts, where first the conclusions are presented for this study. This is followed by recommendations for future research.

10.1. Conclusion

In this section the conclusions that can be drawn with the obtained results are discussed in the context of the research question and the accompanying sub-questions. This study aimed to answer the research question:

Research Question: *What is the fuel-optimal ascent trajectory for a Horizontal Take-off and Horizontal Landing (HTHL) space plane, which includes a change in the Right Ascensions of the Ascending Node (RAAN) to extend the launch window?*

To support the answer to the research questions a number of Sub-Questions (SQ) have been defined. The sub-questions formulated will be used to support the answer to the main research question and show the significance of the findings.

SQ1 *What is the fuel-optimal ascent trajectory for a Horizontal Take-off and Horizontal Landing (HTHL) launch vehicle without considering a launch window?*

SQ2 *How does the required propellant during the ascent trajectory vary due to the inclusion of an extended launch window?*

SQ3 *How does the required propellant for a change in the Right Ascensions of the Ascending Node (RAAN) by a space plane compare to the same change in the right ascension of the ascending node by a traditional secondary stage?*

In addition to these research questions, a number of objectives were identified for the study. These objectives were identified to be:

AG1 Include the full six Degrees of Freedom (DoF) translational and rotational Equations of Motion (EoM).

AG2 Include a G&C system that can deal with the nonlinear translational and rotational Equations of Motion (EoM).

AG3 Include a vehicle model that has been used before to optimize the longitudinal ascent, which includes constraints.

Optimization of the Ascent without Launch Window

For the ascent trajectory without an extended launch window, it was found that a space plane can ascent with a payload of about 5100 kg into an inclined orbit of 45 degrees. It was identified that the ascent of the space plane consists of three phases. The first phase is called the acceleration phase. In this phase, the space plane lifts off, ascends to an altitude where the air-breathing engine is most efficient and from there starts to accelerate. During this phase, the constraints that are imposed on the space plane are most of the time active. It has been seen that these constraints dictate the velocity of the space plane. Both the dynamic pressure and heat flux are dependent on the density, which decreases as the altitude increases. This means that there is a balancing act between accelerating as fast as possible, to reduce drag, gravity and thrust losses, while ensuring that the space plane adheres to the imposed constraints. Additionally, the space plane air-breathing engine is more efficient at high Mach numbers for higher dynamic pressure (Shaughnessy et al., 1990). This means that the space plane wants to accelerate at an altitude that benefits the efficiency boost. For this reason, the ascent trajectory found for the space plane would closely follow the two aforementioned constraints until the correct velocity was achieved to reach the target altitude.

The second phase of the ascent is the pull up phase. Due to oscillation issues with the flight path angle, it was determined to switch over to direct angle of attack control in this phase, where it was ensured that the angle of attack would at least be 1 degree to initiate the pull up. It was identified that the start of the pull up phase was an important optimization parameter. An earlier pull up phase in terms of altitude would mean that the velocity at the start of the phase was lower due to the imposed constraints. The lower velocity would require a larger circularization burn to ensure that the target orbital velocity was reached, which would require more propellant due to the less efficient engine mode. Conversely, a later burn would mean that the flight path angle at the target altitude would be non zero, which made the circularization maneuver less efficient. The non zero flight path angle would mean that, while the target velocity was reached, the eccentricity that the space plane would achieve was not close to zero. It is clear from this discovery, that there is a trade-off between the amount of propellant used and the accuracy of the achieved orbit. Initiating the pull up will ensure a more efficient trajectory in terms of propellant used, while the final orbit will not be able to fully circularize.

After the pull up phase a coasting phase starts, where the engine of the space plane is turned off. For this study, the angle of attack was set to zero degrees during this phase, similarly to what was done in the study by Mooij (1998). However, further investigation in this phase could prove useful to ensure that the target orbit is reached, while the velocity at the start of the pull up phase can be increased. This will be further discussed in the recommendations section.

Cost Assessment of the Ascent with Launch Window

In order to optimize the ascent, where a launch window extension is considered, a novel transcription method is used to guide the space plane to the correct heading angle. In this study, it was discovered that a reference heading angle could be defined for the northern hemisphere only if the latitude of the space plane would increase. Using this reference heading angle made it possible to launch the space plane into the correct orbital inclination. Furthermore, the definition of the reference heading angle could be manipulated to allow for a

deviation in the inclination, which would serve as the basis of the manipulation of the RAAN. It was found that by having a positive deviation in the target inclination, a negative change in RAAN was possible. For a negative deviation, the reverse was found. The novel transcription method allowed for the launch window to be optimized for, while only including three extra optimization parameters compared to the optimization of the longitudinal ascent.

It was found that a launch window could be created of at least four hours, where there is a clear trade-off between the deviation in launch time and the amount of propellant used to ensure that the target orbit is reached. An analysis was done on the variation of the propellant used for the different launch times. It was found that for the delayed or advanced launch of one hour, an additional 1500 kg of propellant was necessary, which would mean that the available payload that could be delivered into orbit would be approximately 3600 kg. In addition to analysis of the difference in payload, also a ΔV analysis was done. In this analysis it was found that the extra propellant cost came from the increase in drag and thrust losses, which were caused by the banking maneuver. In order to correct for the deviation in inclination at the end of the pull up phase, a banking maneuver would be used to steer the space plane back to the heading angle that would correspond with an inclination of 45 degrees. This banking maneuver would decrease the lift component pointing upwards, which would mean that the flight path angle would decrease. In order to ensure this decrease would not occur, the angle of attack of the space plane was increased. This increase in angle of attack increases the drag losses due to an increased drag force. Furthermore, the higher angle of attack would also induce a higher pitching moment, which would be trimmed with the Thrust Vector Control (TVC) system. The increased thrust elevation angle to trim the space plane would increase the thrust losses, as was seen in Equation 8.5.

It can be concluded that a space plane is capable of changing the RAAN of the space plane by launching in a heading angle direction that corresponds with a deviated inclination. The cost of changing the heading angle back to the correct inclination comes from either drag losses alone, or drag and thrust losses depending on the usage of a TVC system to trim the space plane. It should be noted that the outcome of the delayed or advanced launch by two hours is highly different. It became apparent that for the delayed launches, the reference heading angle was poorly constructed. A delayed launch requires a positive deviation in inclination *i.e.*, the space plane wants to launch in the northern direction. Due to the more northern motion, the latitude of the space plane develops faster compared to the baseline launch or the advanced launches. The reference heading angle can only be computed if the latitude of the space plane is smaller than the target inclination. If the inclination of the space plane would not have a deviation, no issues could occur, where the maximum latitude that the space plane would achieve is 45 degrees. However, due to the deviation in inclination, a higher latitude is achieved, which limits the possible solutions that the delayed launch can find.

Optimization of the Ascent with Launch Window

The propellant requirements for the space plane to advance or delay the launch has been compared to a simple in-orbit RAAN changing maneuver. It was assumed that the satellite would have a mass of 5100 kg, the same value as was found for the ascent trajectory where no change in RAAN was considered. Depending on the engine efficiency of the satellite, the satellite would perform worse or comparable for a delayed launch up to one hour. For the delayed or advanced launch by two hours, the satellite was able to change the RAAN with less propellant used. The space plane would have to generate approximately an extra 500 m/s of ΔV to achieve the required change in RAAN. Even though the space plane is using a highly efficient engine compared to the satellite, the mass of the space plane is at least ten times higher, which means that large extra amounts of ΔV require more propellant, compared to a 'small' satellite.

Conclusion of the Objectives

The objectives of this study were identified to guide and find a robust answer to the research question. First of all, it was necessary to include the six Degrees of Freedom (DoF) Equations of Motion (EoM) to be able to define the lateral motion required to manipulate the RAAN. In previous studies, it was found that a G&C system that utilizes linearized EoM would experience eigenmotions that could make the space plane unstable (Mooij, 1998; Spillenaar Bilgen, 2017). By introducing a nonlinear G&C system it has been shown that these eigenmotions are not present anymore and that the solution found is robust to changes in the initial state and uncertainties in the G&C system itself. Unfortunately, this system has proven difficult to test, which was seen in the sensitivity analysis, see Section 9.2. The discovered issue with the system shows that the space plane is susceptible to flight path oscillations close to orbital velocities if the space plane angle of attack becomes close to zero.

In addition, it was chosen to use a space plane vehicle model that has been used before in studies to

optimize the longitudinal ascent. This objective has ensured that the results obtained in this study can be verified with the study done by Mooij (1998). It has been seen in Chapter 9, that this study was able to reproduce the results of that previous study, while a different G&C system was used.

Final Conclusion

With the sub-questions answered previously, the main research question can be answered. The fuel-optimal ascent trajectory with a launch window extension can be split up into two parts. The first part relates to the longitudinal ascent if a launch window is considered. It has been seen that the altitude velocity plots for the launch with a launch window extension do not vary compared to the ascent without an extended launch window. Due to the banking maneuver, a change in RAAN is possible, where the drag and thrust losses increase due to an increase in angle of attack. However, the longitudinal trajectory parameters *i.e.*, the velocity and flight path angle do not vary. The same constraints still apply for the ascent with launch window, and these are still leading, when considering the longitudinal ascent. Thus, the fuel-optimal ascent trajectory with a launch window only deviates from the ascent without launch window consideration due to the lateral motion. The lateral motion has been optimized with a transcription method that is capable of guiding the space plane towards a commanded inclination, where the inclination itself has been deviated. This means that there is no equation that relates the space plane to the correct RAAN directly. This is why optimization algorithms were used to identify how the inclination of the space plane should vary to accomplish a change in RAAN. It has been seen that with a larger delayed or advanced launch, the deviation in inclination is increased, which induces a larger banking maneuver when the deviation inclination returns to zero.

The found sub-optimal ascent trajectory has two known issues. The first is the flight path oscillations that inhibit the ability to properly use a local optimization method to find the optimal solution. The global optimization algorithm used is capable of finding the global optimum. However, due to the iterative nature of the process, it is not guaranteed to find the real optimal solution. Furthermore, the oscillations make the space plane unstable, prematurely terminating the simulation if these oscillations are not stopped in time. It is theorized that the sub-optimal solution found here is limited due to these oscillations. The second issue is the definition of the reference heading angle that does not take into account a situation where the latitude is higher than the commanded inclination. With a proper definition of the reference heading angle, that can take into account this issue, perhaps a better solution could be found for the delayed launches.

10.2. Recommendations

In the previous section it was concluded that the found ascent trajectory was sub-optimal and could be improved upon. In this section these issues are briefly discussed and a number of interesting new research topics are named.

Resolving of the Issues in this Study

It is recommended for future research, to apply the Incremental Non-linear Dynamic Inversion (INDI) algorithm to steer a space plane to the correct target orbit. It has been demonstrated that the algorithm is capable of dealing with large variations in both initial conditions and G&C uncertainties. By including a minimum velocity before the space plane initiates in the pull up maneuver, it can also be ensured that the target orbit is reached. The minimum velocity can be determined in a number of ways. First of all, the minimum velocity can be included in the optimization process. However, one can also try to find a minimum velocity by realizing that from the moment that the pull up maneuver is initiated, the space plane follows a somewhat parabolic path. It could be possible to determine in this way a minimum velocity if the drag losses during the last two phases of the ascent are negligible. Furthermore, by resolving the issues with the flight path oscillation and the reference heading angle, a better quantification can be made of the cost of the longitudinal ascent with or without lateral motion. If these issues are resolved, research can be dedicated to properly question the influence of the optimization parameters on the achieved orbit and the propellant used for the ascent trajectory.

The issue of the oscillations can be resolved in a number of ways. First of all, the gain that is used for the flight path angle can be made dependent on a variable. For instance, since it is known that the space plane is symmetric, the gain could become smaller in magnitude if the angle of attack is smaller. In this way, only smaller changes are commanded when the angle of attack is close to zero, which could resolve the oscillations. Second of all, the guidance module that commands the flight path angle can be defined which also precomputes the required changes of the deflection angles. This means that the difference in forces due to a change in deflection angle is already taken into account when computing the desired angle of attack. In

practice, this would probably translate into an iterative process, where the desired angle of attack would be tuned in such a way that the deflection angles of the elevons would be commanded to a value that would ensure that the space plane is steered to the correct flight path angle. Last of all, the issue could be solved by reducing the time step of the integrator. Although, this is a computationally expensive way of solving any issue.

For the reference heading angle, it should be possible to define the heading angle for four different scenarios. The first and second scenario is where the space plane is in the northern hemisphere, with either a positive or negative latitude derivative. The third and fourth scenario is for a situation where the space plane resides in the southern hemisphere with either a positive or negative latitude derivative. Clever trigonometry allows for a definition of the heading angle, where these four scenarios are taken into account. Additionally, a solution needs to be found whenever the latitude of the space plane exceeds the target orbital inclination. In this scenario, the equations used to define the reference heading angle 'break' and do not provide any valid value. Of course, an if statement could be set up to check for this scenario and a corrective heading angle could be defined. However, there might be a more elegant method by designing a formula that does not break whenever the latitude exceeds the target orbital inclination.

Inclusion of an Ellipsoidal Earth Shape Model

In Chapter 4, it was discussed that an ellipsoidal Earth would better represent the shape of the Earth compared to the spherical Earth model used in this study. A possible method of implementing this model, while using an altitude dependent NonLinear Programming (NLP) problem, is to use a normalized altitude variable. The normalized altitude would indicate the altitude for a specific latitude if a spherical model was used. In this way, the space plane would still be guided to the proper final altitude, while an ellipsoidal Earth shape model is used. The downside of the system is that the atmosphere would change depending on the actual altitude, which could negatively impact the performance of the air-breathing engine. Instead, the normalized altitude could be used only to compute the minimum velocity needed before the pull up to ensure that the correct semi-major axis is reached.

Assessment of the Integration Accuracy and G&C System on Step Size Changes

Due to the oscillations that occurred in the flight path angle. A proper assessment of the accuracy of the integrator was not possible. When the oscillation phenomenon is resolved, it is recommended to assess the accuracy of the integrator. Furthermore, it could be studied how a change in the update interval for the G&C system would influence the ability of the space plane to steer to the correct trajectory parameters. For the current system, it was found that an update every 0.1 seconds was the largest step for which the system was still capable of steering the space plane even at high velocities. However, when the flight path angle oscillations are resolved, it could be possible to reduce this, which could reduce the computational load. This could ensure that future optimizations will require less time to converge.

Lateral Motion for other Applications

It has been seen that lateral motion is capable of effectively changing the RAAN and inclination. Another application of this lateral motion is to steer a space plane at a later point to another inclination due to launch heading angle restrictions. An example of this is the restriction imposed for launches from Florida, where rockets are only allowed to fly to specific heading angles due to safety reasons. A space plane could be capable of adhering to these restrictions, while later starting a banking maneuver to change the inclination. This can be useful for polar orbits, where in-orbit changes might be more costly than using a space plane to make these changes.

Furthermore, the lateral motion could be used to launch from a higher latitude than the target inclination. Conventional rockets are only capable of inserting a satellite in an inclined orbit that is lower than the launch latitude. A space plane could be used to fly south, from the launch site, if a launch from the northern hemisphere is considered. When a certain latitude is reached, a banking maneuver is initiated to start a change in inclination. In this way, a space plane could be used to effectively change the inclination of the orbit, while still launching from a high latitude launch site.

Another possible application is the inclusion of multiple orbit insertions with a single launch. Currently, many companies are interested in constellations of satellites for a variety of reasons. With a space plane, it could be possible to insert one or multiple satellites into multiple different orbits in terms of inclination and RAAN. In this study, the circularization of the target orbit was done by the space plane. However, if the inserted satellite would be capable of doing this maneuver, the space plane would descend again to an altitude

where the space plane would be capable of changing the inclination or RAAN again. Afterward, the space plane could initiate another pull up maneuver and insert one or more satellites again. Since the space plane already has a velocity close to the orbital velocity, this could be an efficient method to insert a constellation of satellites. Of course, this does assume that the space plane is capable of resisting the heat involved in re-entering the atmosphere multiple times in a row. If a future study would focus on this topic, it is recommended to include the total heat load in combination with the maximum heat flux.

Appendices

A

Pareto Front Results

In this appendix the Pareto fronts are shown for the global optimization for a variety of launch times. From each front an individual is selected that represents a balanced individual in terms of accuracy of the achieved orbit, and efficiency in terms of propellant.

Pareto Front Global Optimization

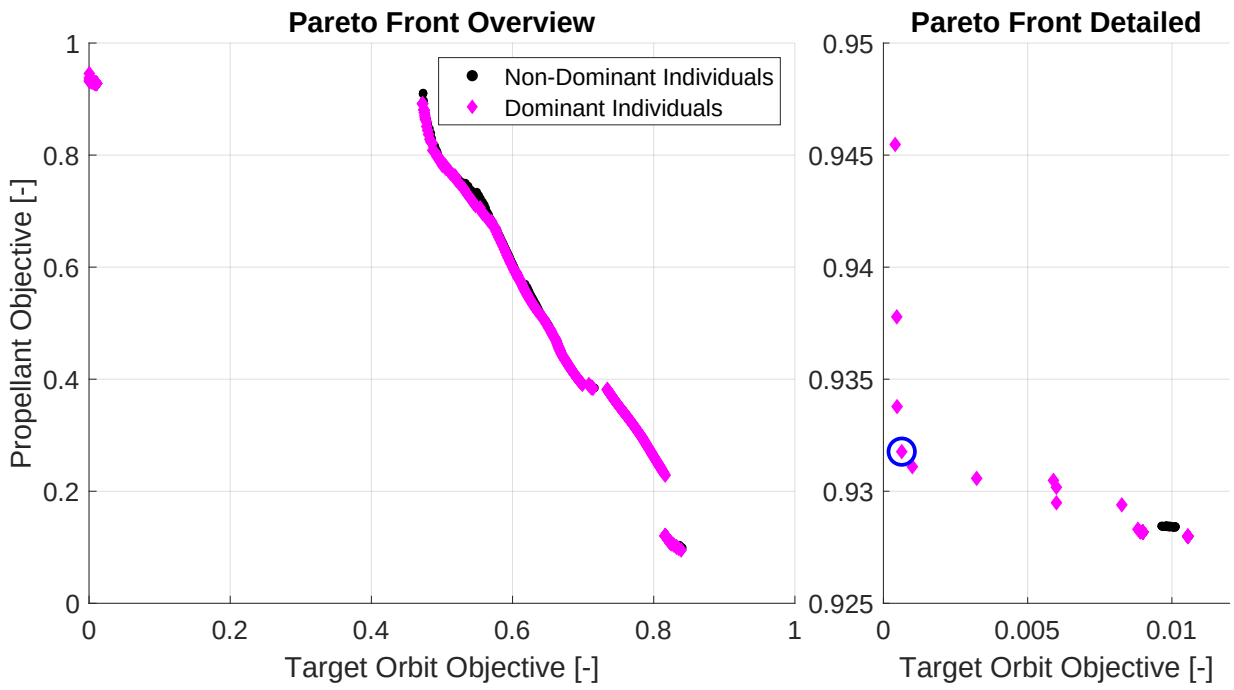

*

Pareto front of the optimization for the ascent trajectory with an initial time of 0 seconds. The 500^{th} generation is considered, with all three seeds included in the Pareto front.

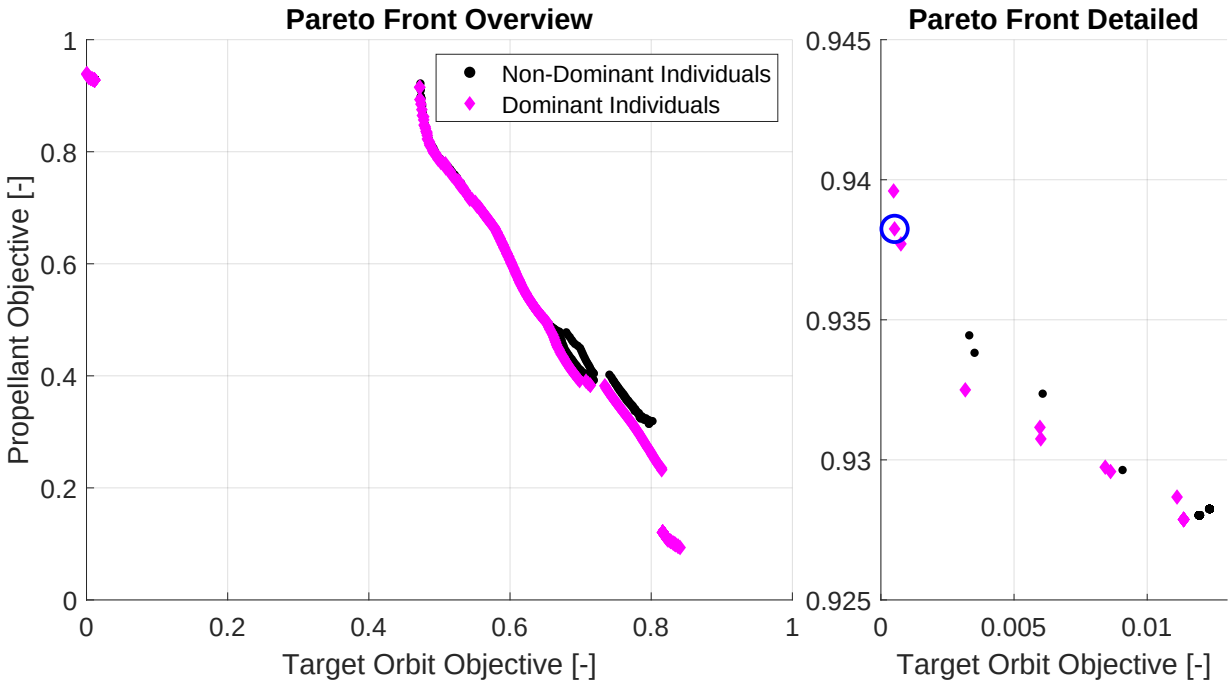

Pareto front of the optimization for the ascent trajectory with an initial time of 1800 seconds. The 500^{th} generation is considered, with all three seeds included in the Pareto front.

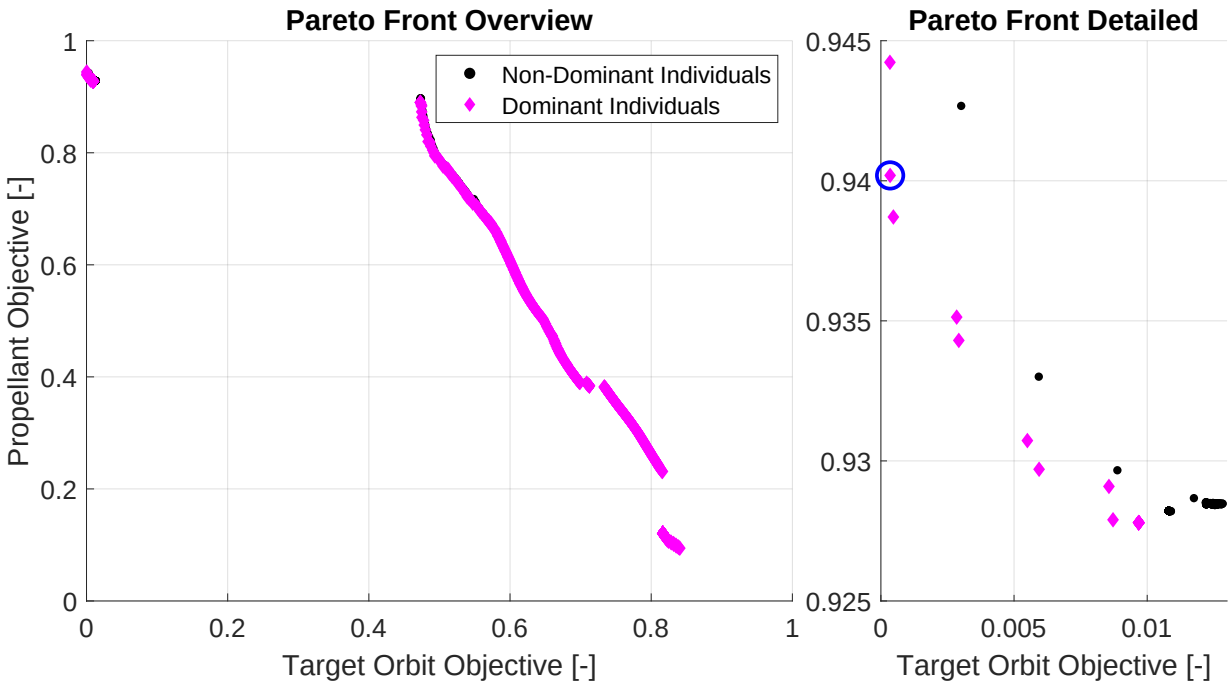

Pareto front of the optimization for the ascent trajectory with an initial time of −1800 seconds. The 500^{th} generation is considered, with all three seeds included in the Pareto front.

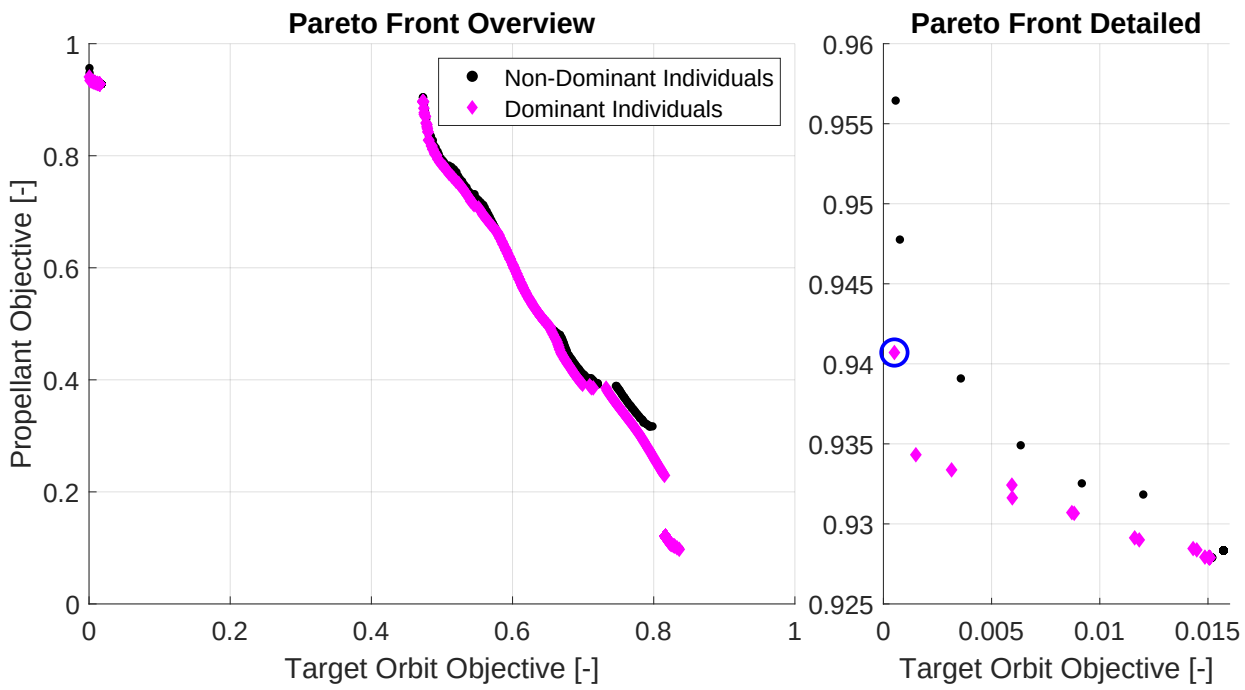

Pareto front of the optimization for the ascent trajectory with an initial time of 1200 seconds. The 500^{th} generation is considered, with all three seeds included in the Pareto front.

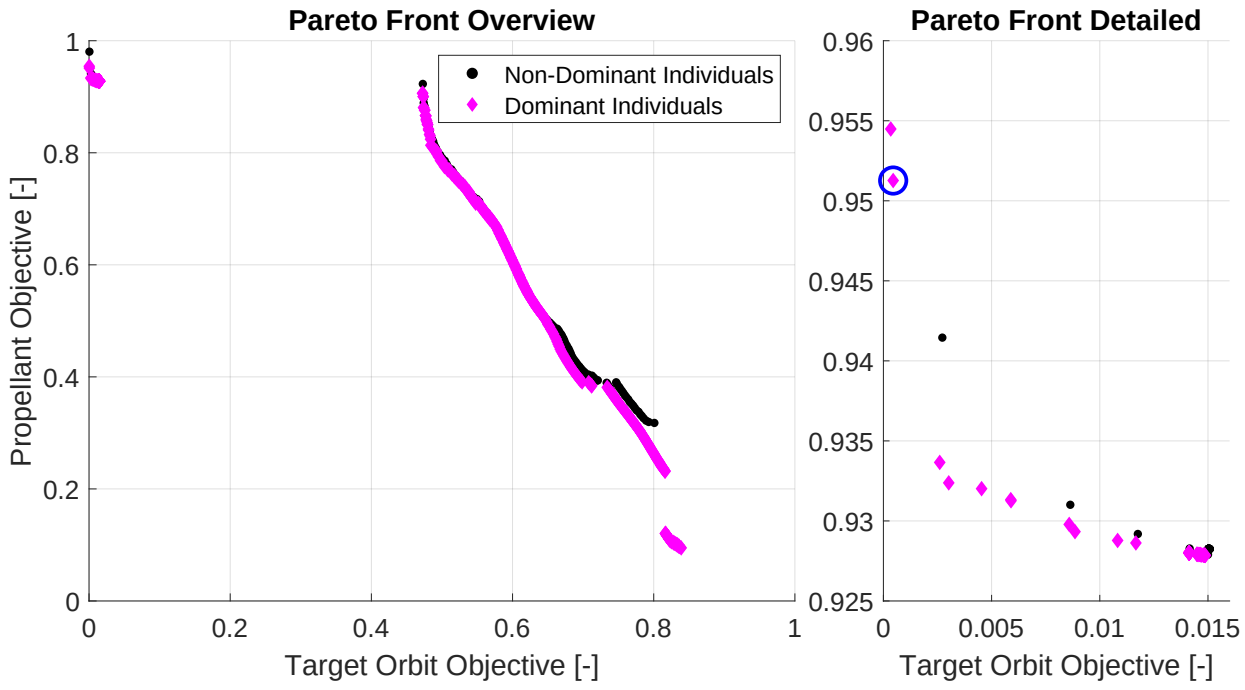

Pareto front of the optimization for the ascent trajectory with an initial time of -1200 seconds. The 500^{th} generation is considered, with all three seeds included in the Pareto front.

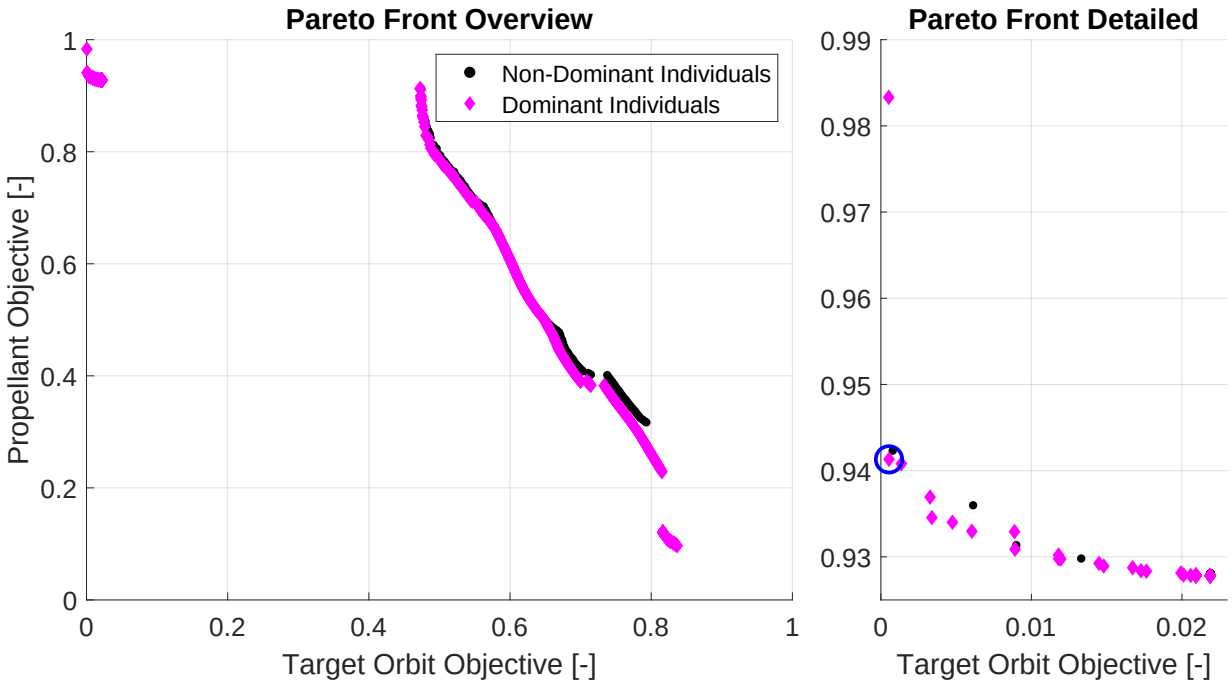

Pareto front of the optimization for the ascent trajectory with an initial time of 1800 seconds. The 500^{th} generation is considered, with all three seeds included in the Pareto front.

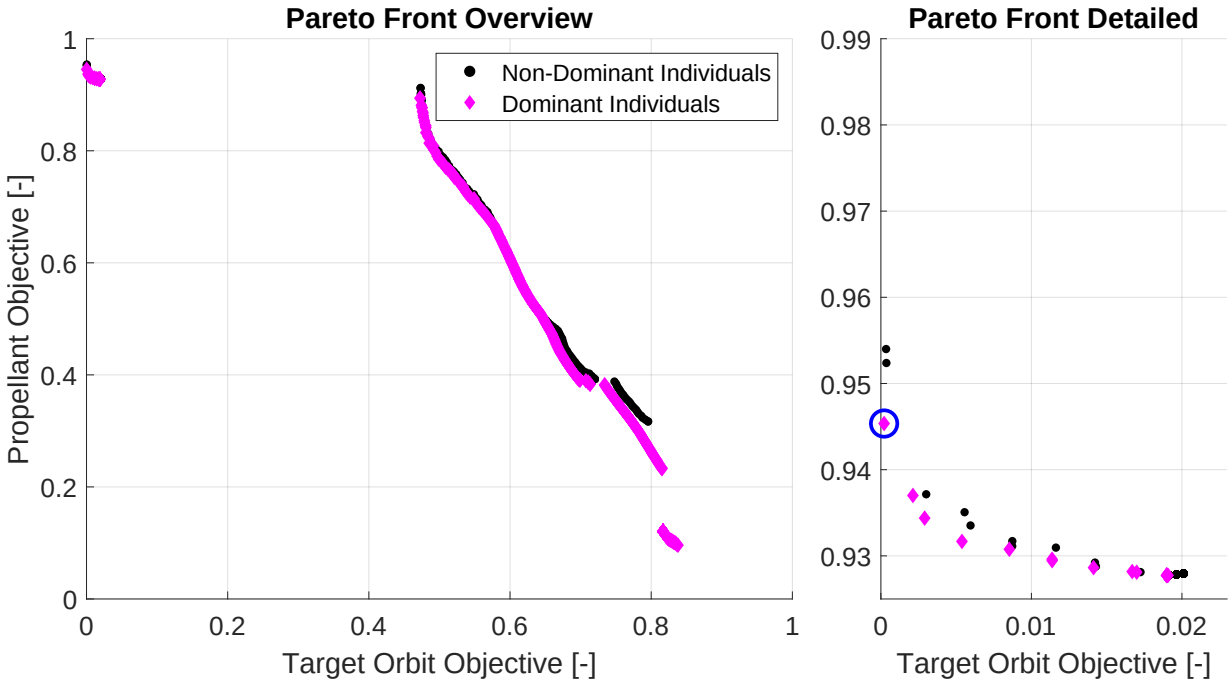

Pareto front of the optimization for the ascent trajectory with an initial time of −1800 seconds. The 500^{th} generation is considered, with all three seeds included in the Pareto front.

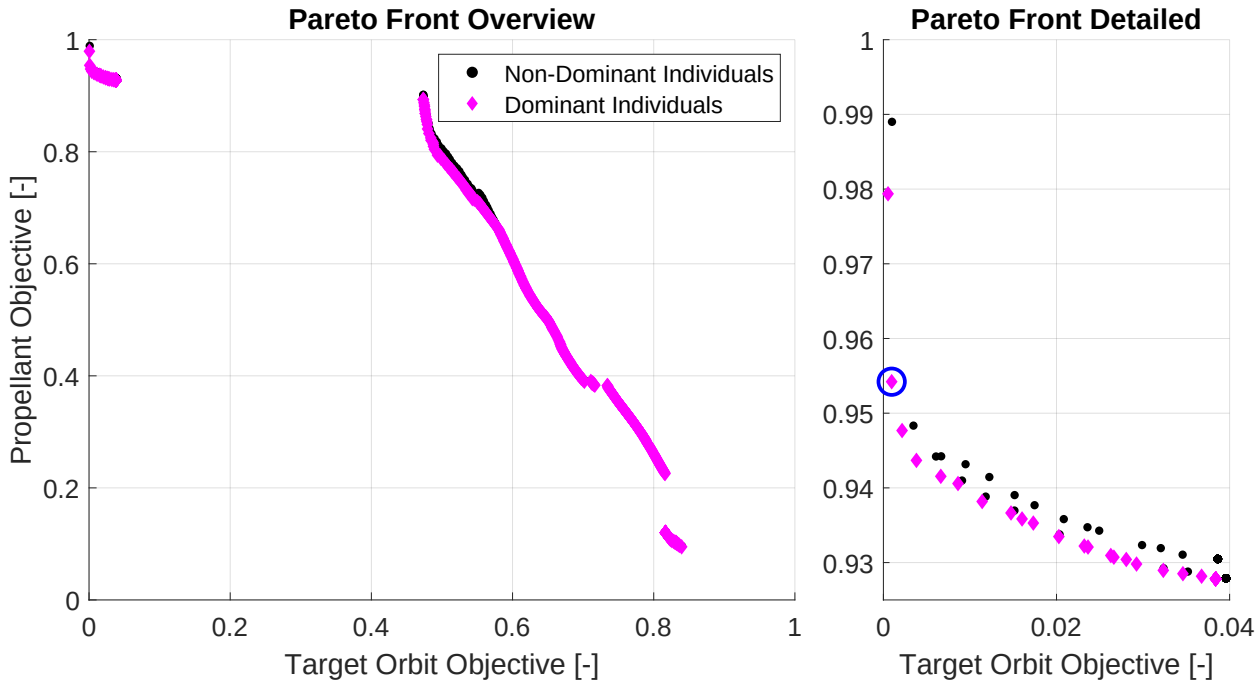

Pareto front of the optimization for the ascent trajectory with an initial time of 3600 seconds. The 500^{th} generation is considered, with all three seeds included in the Pareto front.

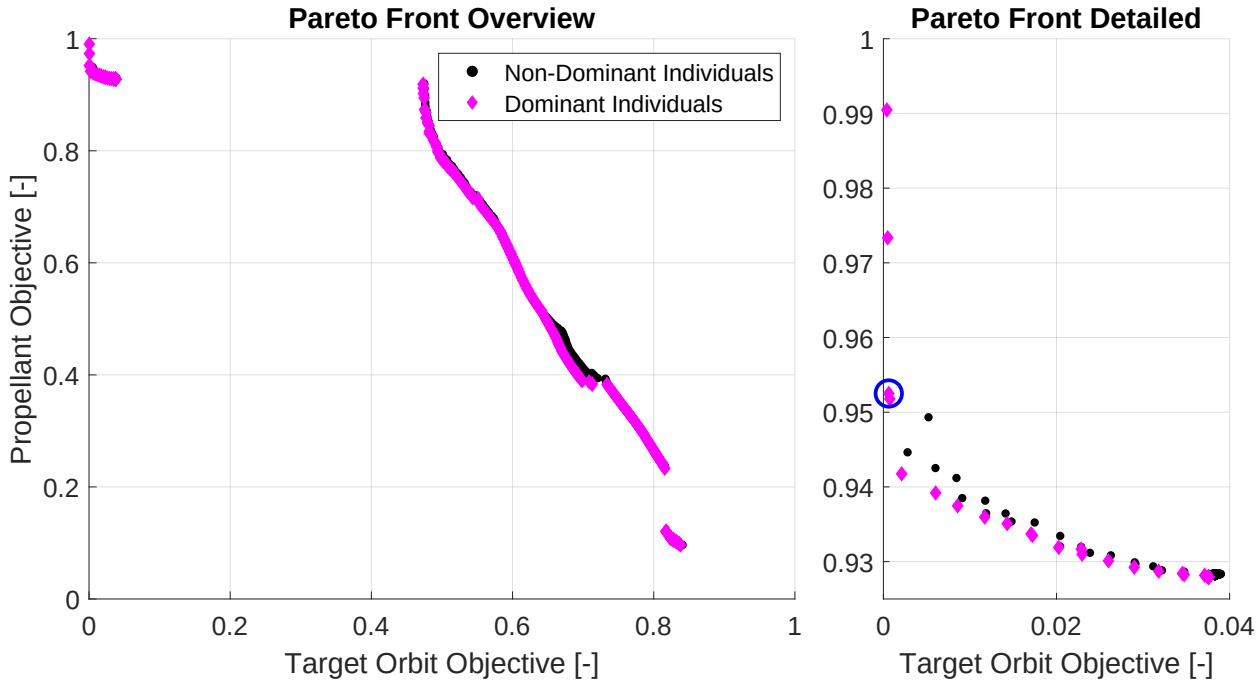

Pareto front of the optimization for the ascent trajectory with an initial time of -3600 seconds. The 500^{th} generation is considered, with all three seeds included in the Pareto front.

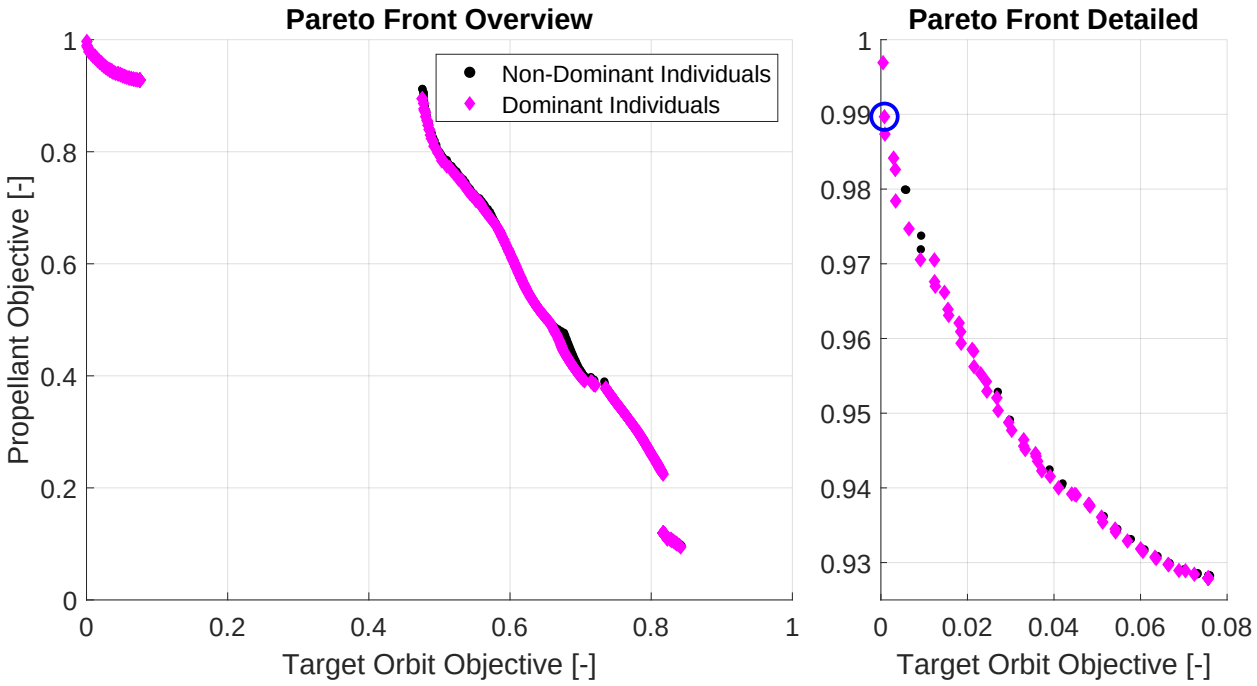

Pareto front of the optimization for the ascent trajectory with an initial time of 7200 seconds. The 500^{th} generation is considered, with all three seeds included in the Pareto front.

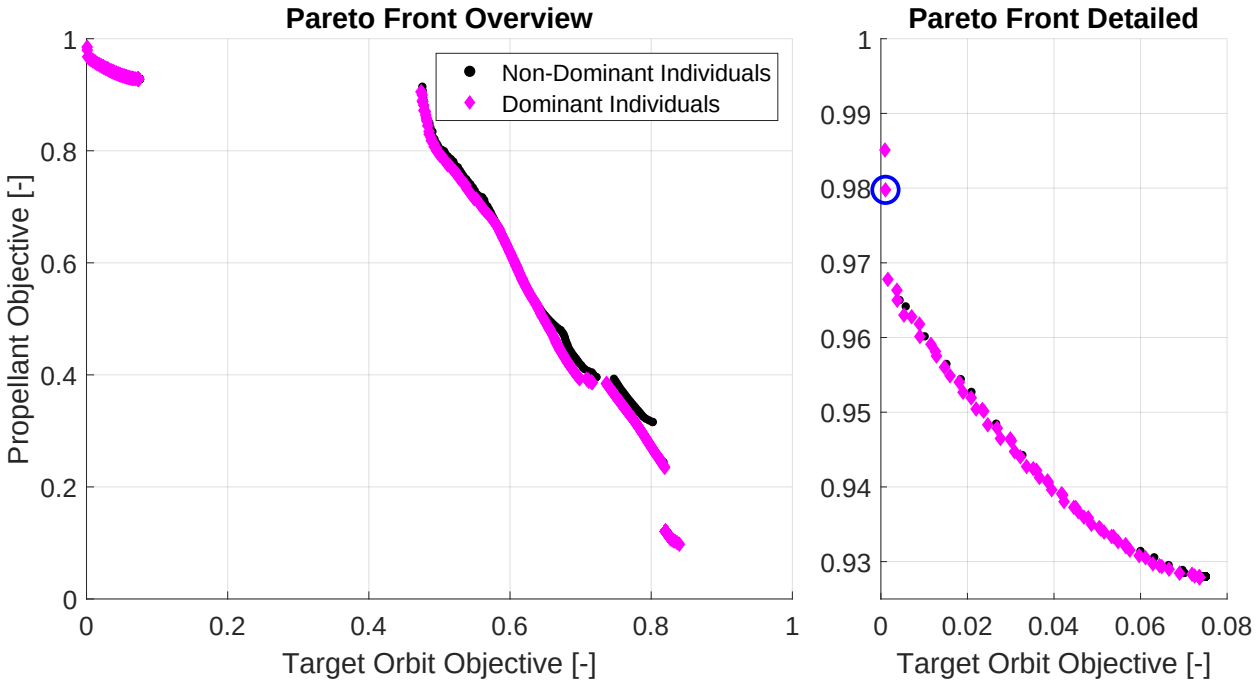

Pareto front of the optimization for the ascent trajectory with an initial time of −7200 seconds. The 500^{th} generation is considered, with all three seeds included in the Pareto front.

B

Convergence of the Global Optimization

In this appendix the convergence of the global optimization is shown for the different launch times. In these figures, both the minimum and average value is shown for the two objectives. Furthermore, only individuals that reach the target orbit are considered to find and compute the minimum and average objective value, respectively.

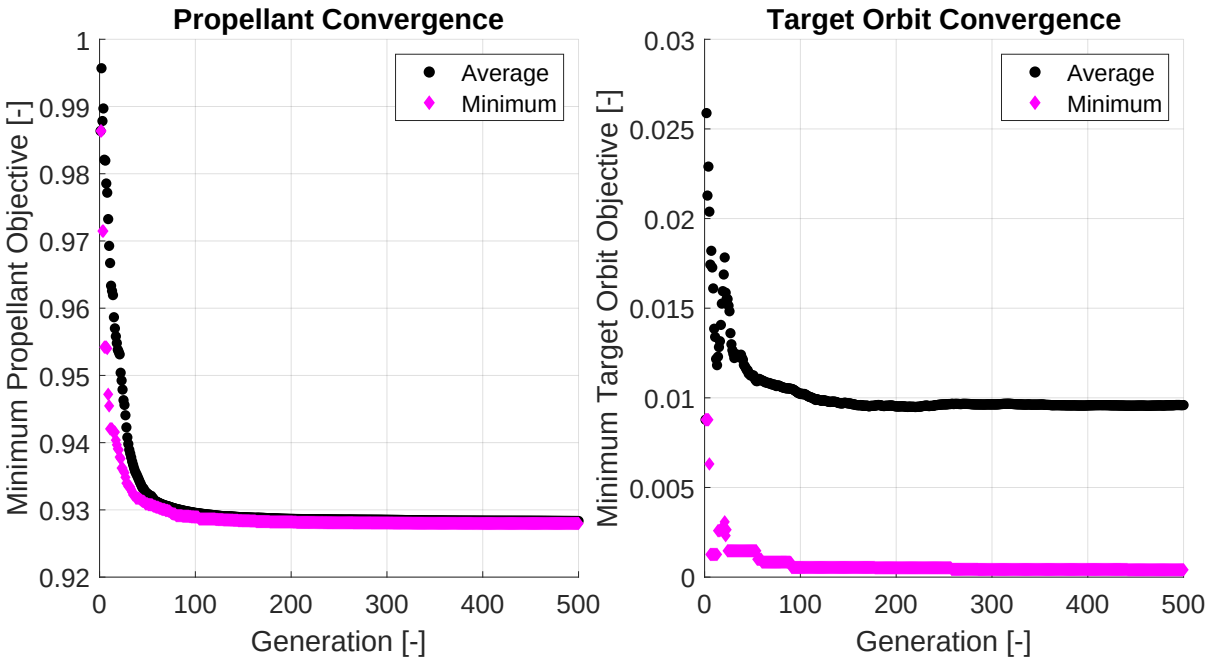

Evolution of the objective values for an initial time of $t_0 = 0$ s, where both the minimum and average of both objectives are shown per generation.

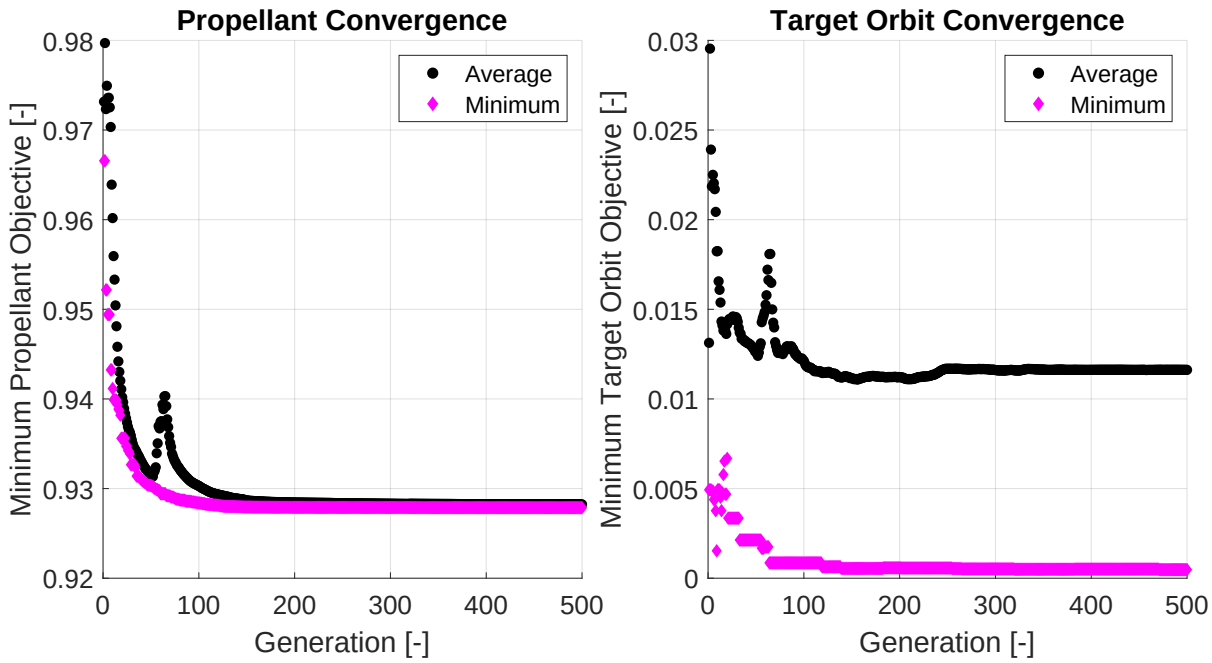

Evolution of the objective values for an initial time of $t_0 = 600$ s, where both the minimum and average of both objectives are shown per generation.

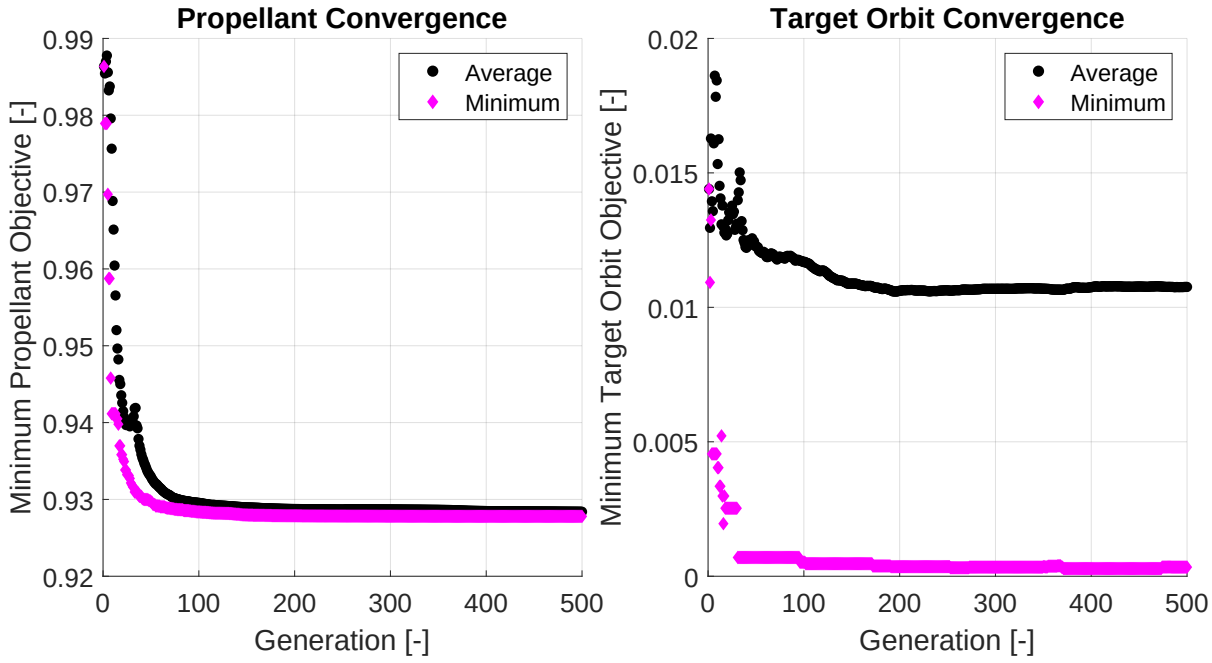

Evolution of the objective values for an initial time of $t_0 = -600$ s, where both the minimum and average of both objectives are shown per generation.

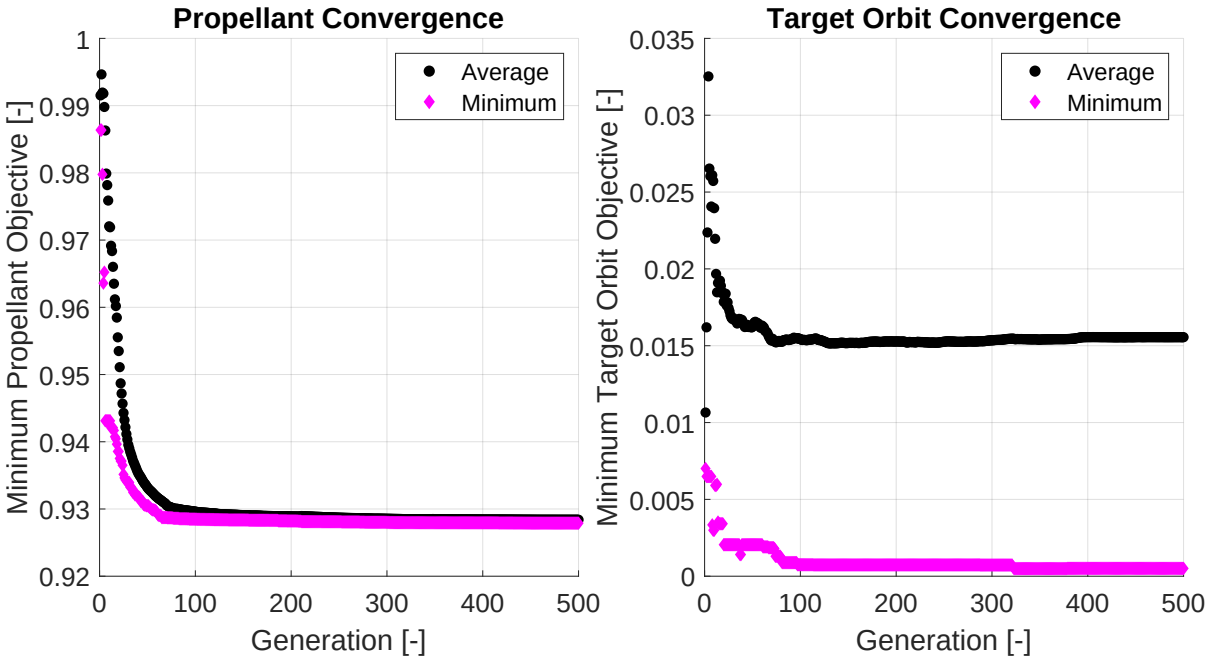

Evolution of the objective values for an initial time of $t_0 = 1200$ s, where both the minimum and average of both objectives are shown per generation.

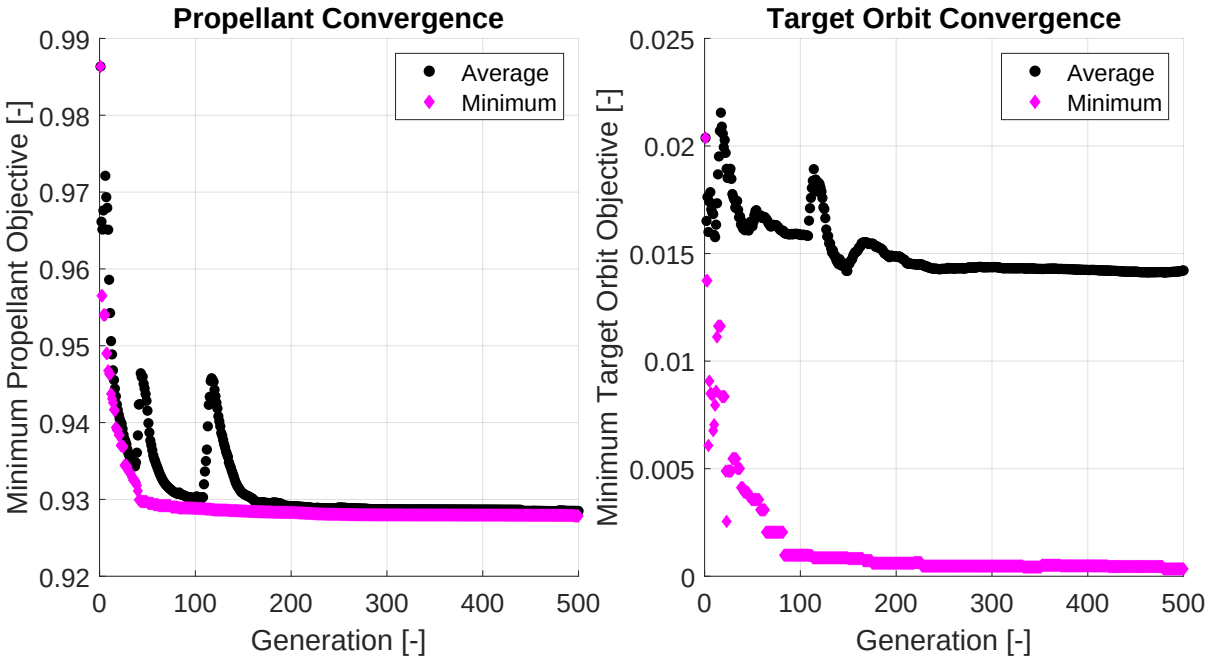

Evolution of the objective values for an initial time of $t_0 = -1200$ s, where both the minimum and average of both objectives are shown per generation.

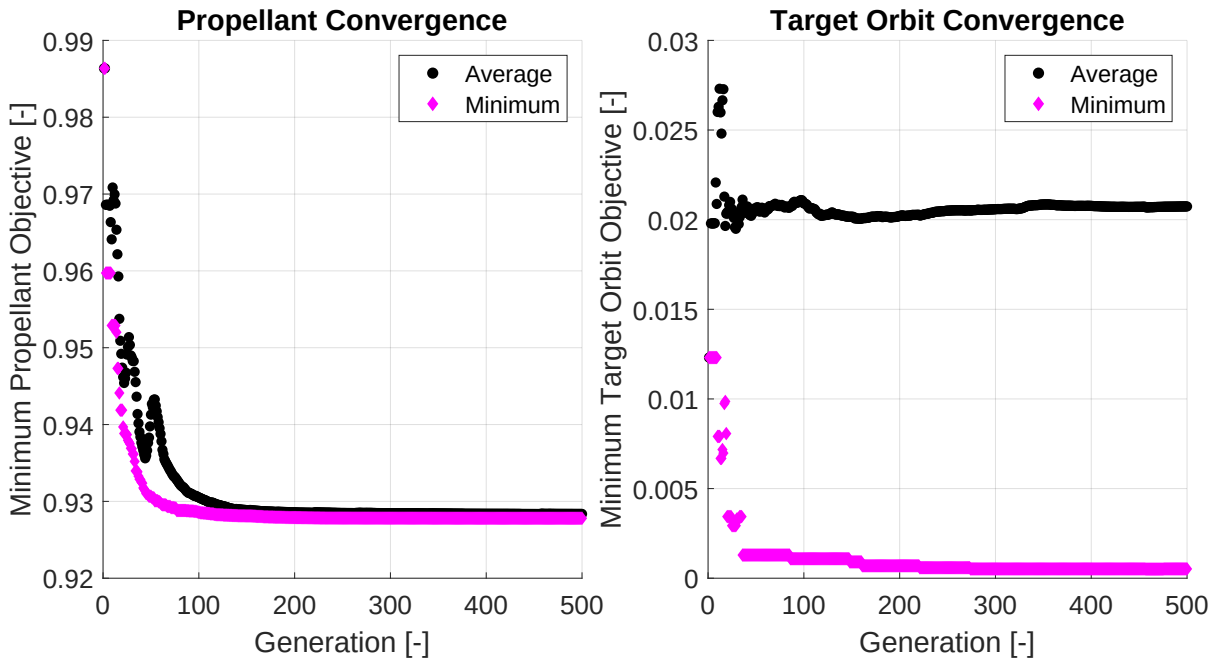

Evolution of the objective values for an initial time of $t_0 = 1800$ s, where both the minimum and average of both objectives are shown per generation.

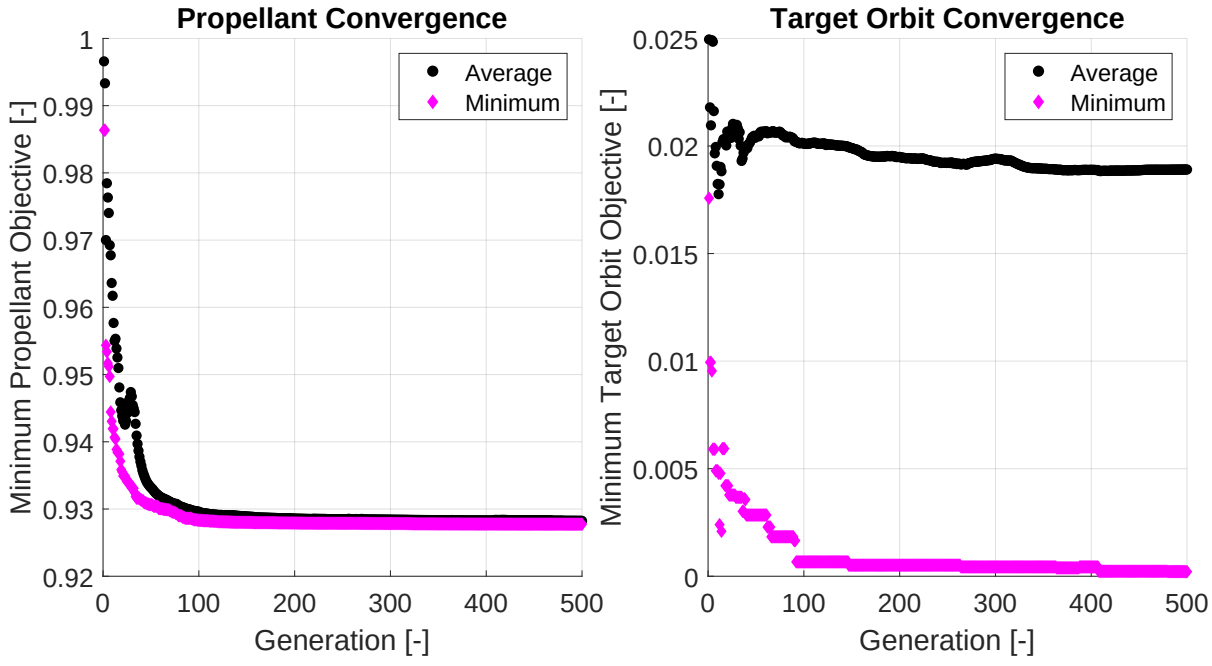

Evolution of the objective values for an initial time of $t_0 = -1800$ s, where both the minimum and average of both objectives are shown per generation.

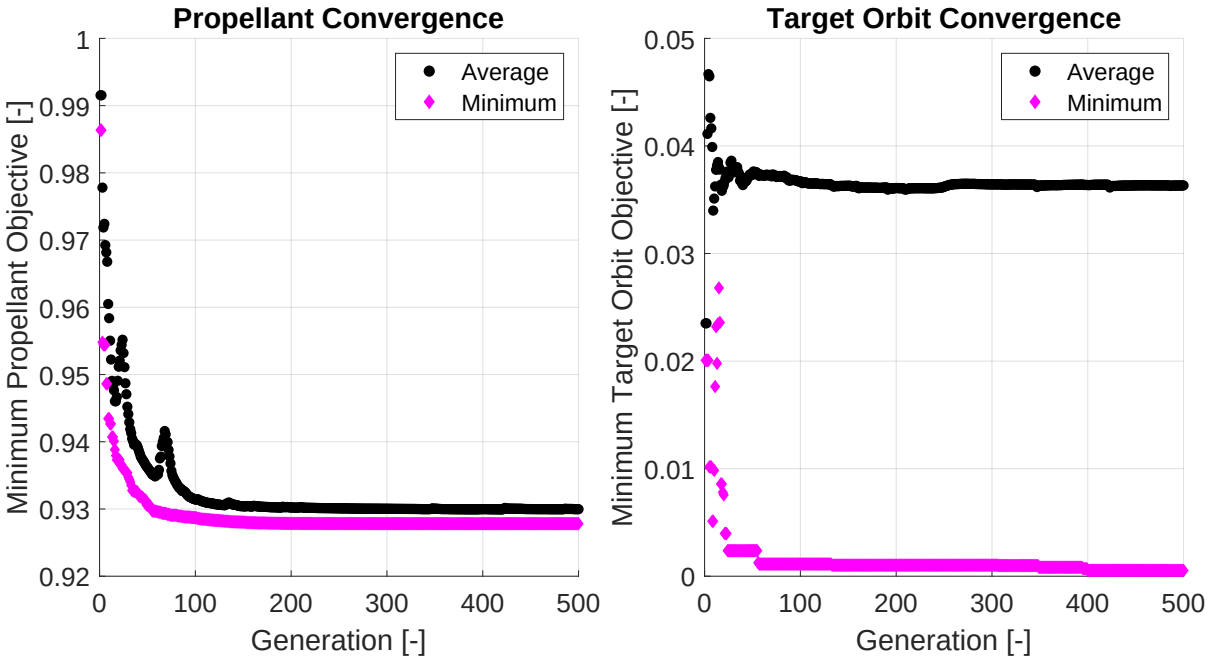

Evolution of the objective values for an initial time of $t_0 = 3600$ s, where both the minimum and average of both objectives are shown per generation.

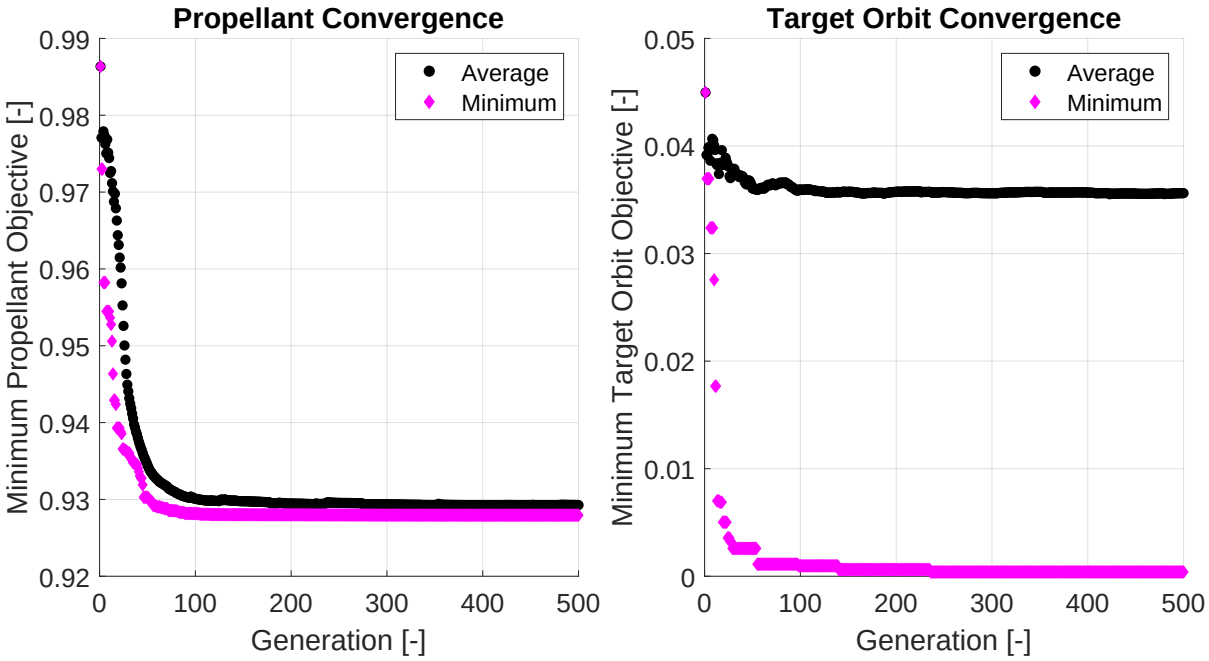

Evolution of the objective values for an initial time of $t_0 = -3600$ s, where both the minimum and average of both objectives are shown per generation.

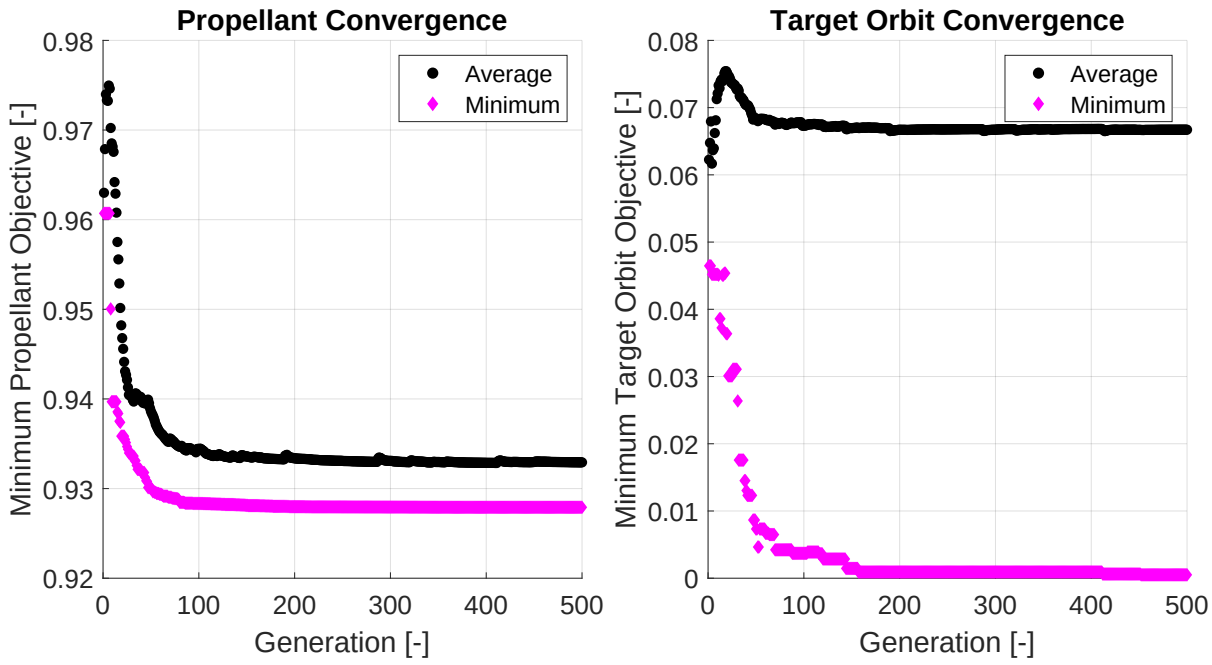

Evolution of the objective values for an initial time of $t_0 = 7200$ s, where both the minimum and average of both objectives are shown per generation.

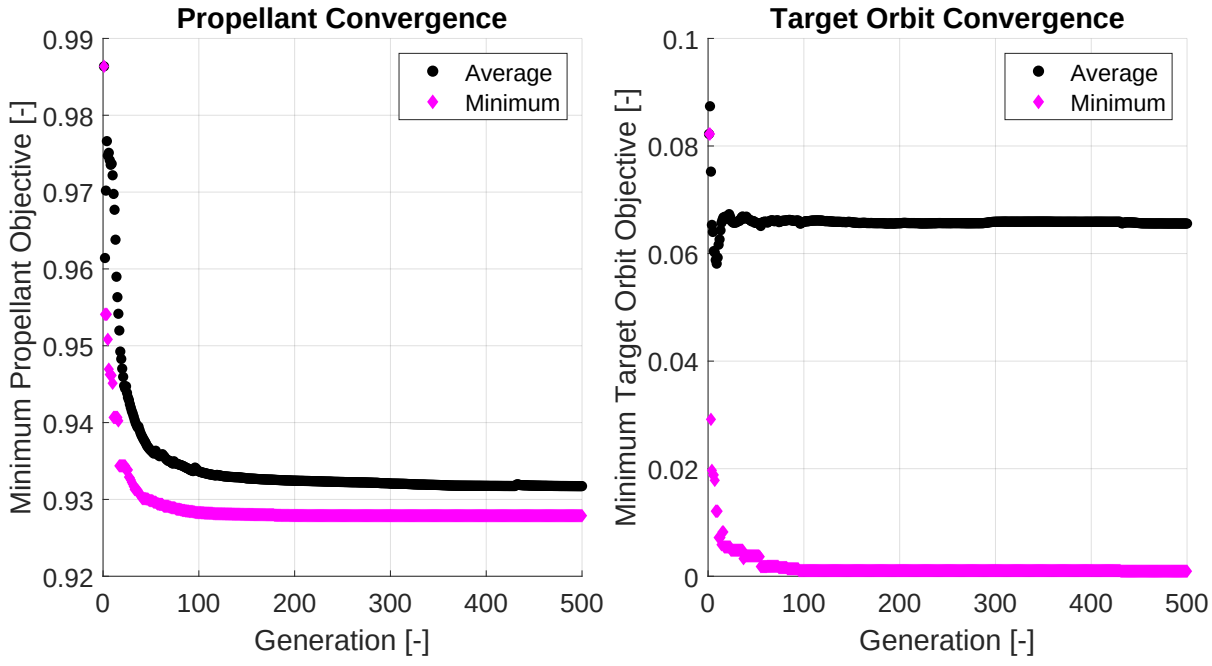

Evolution of the objective values for an initial time of $t_0 = -7200$ s, where both the minimum and average of both objectives are shown per generation.

C

Pareto Front Local Refinement

In this appendix the Sobol analysis is shown, which was used to refine the Pareto front. The figures depicted show first the Sobol individuals in green, followed by a Pareto assessment, which includes any individuals that will improve upon the front.

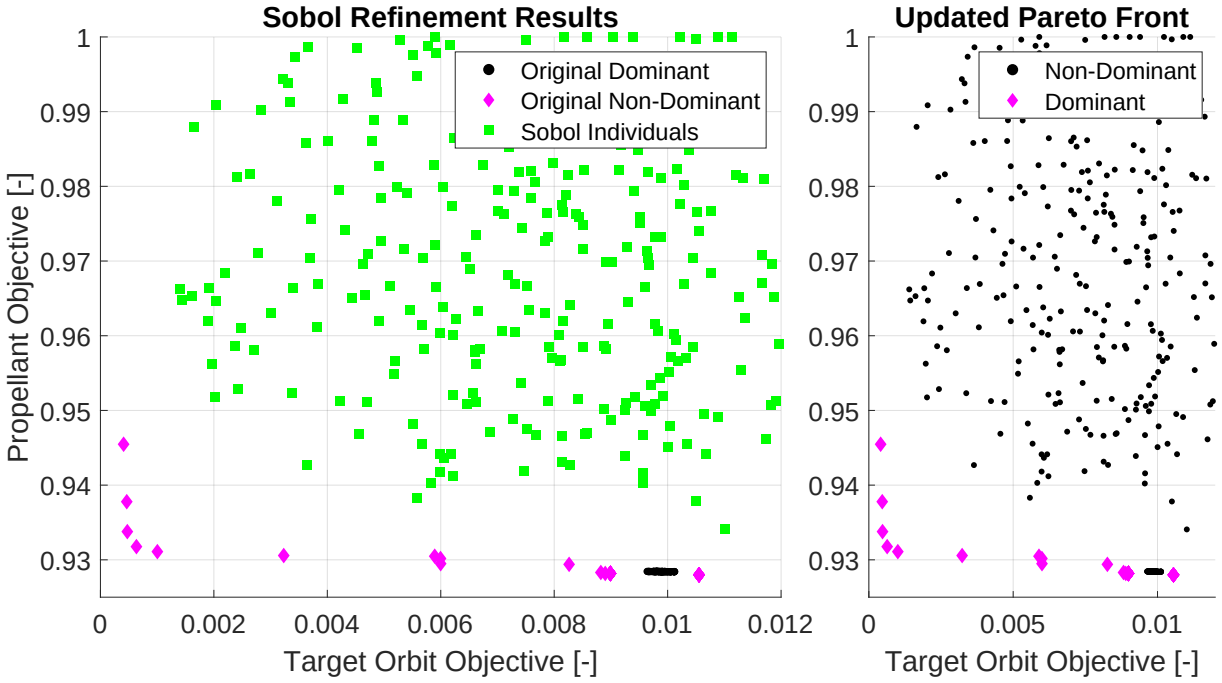

Overview of the Pareto front from the global optimization for an initial time of $t_0 = 0$ s, with the individuals of the Sobol sequence that reach the target altitude.

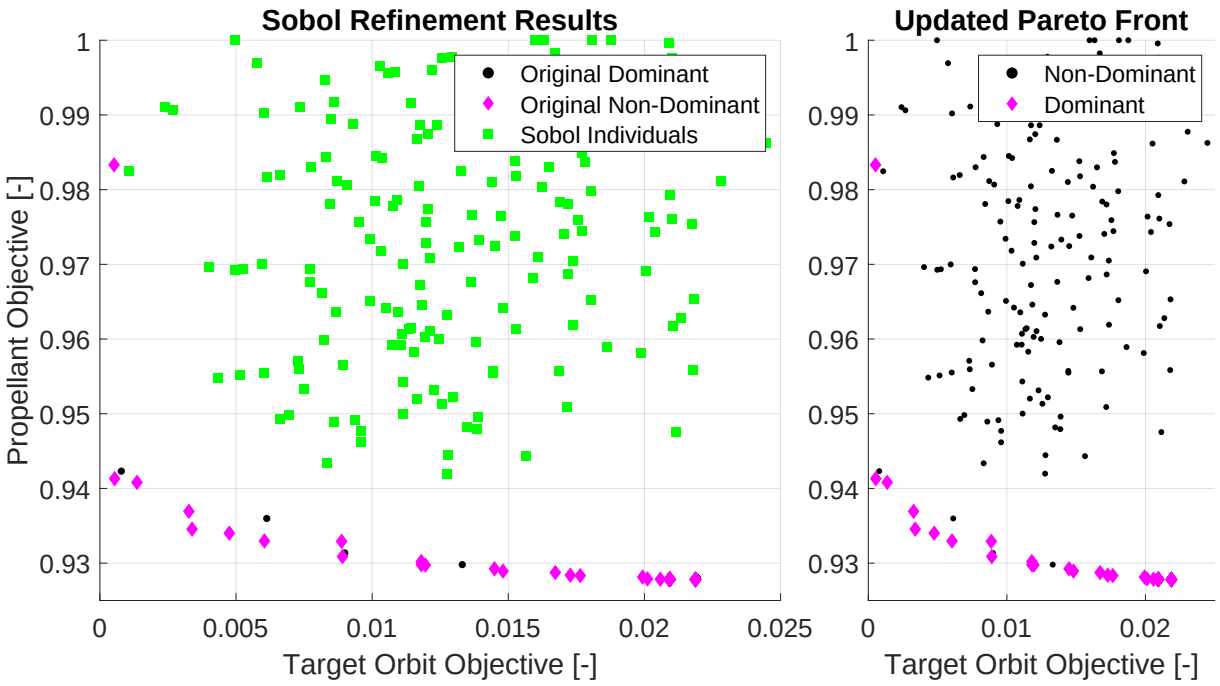

Overview of the Pareto front from the global optimization for an initial time of $t_0 = 1800$ s, with the individuals of the Sobol sequence that reach the target altitude.

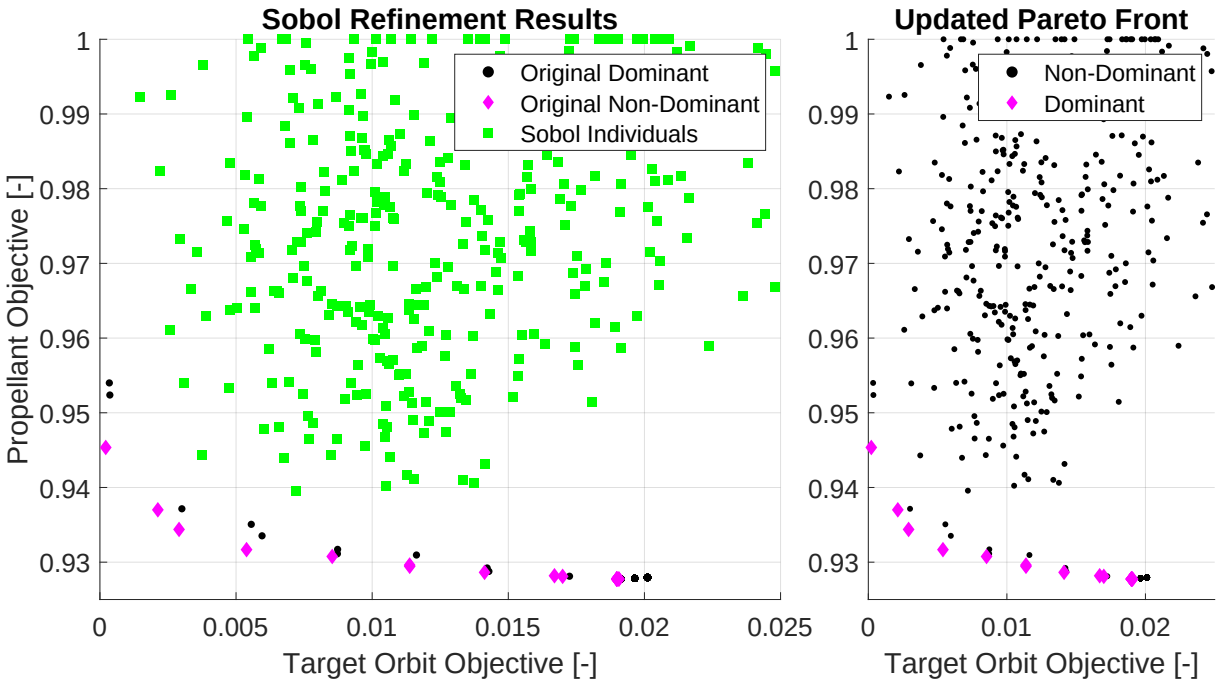

Overview of the Pareto front from the global optimization for an initial time of $t_0 = -1800$ s, with the individuals of the Sobol sequence that reach the target altitude.

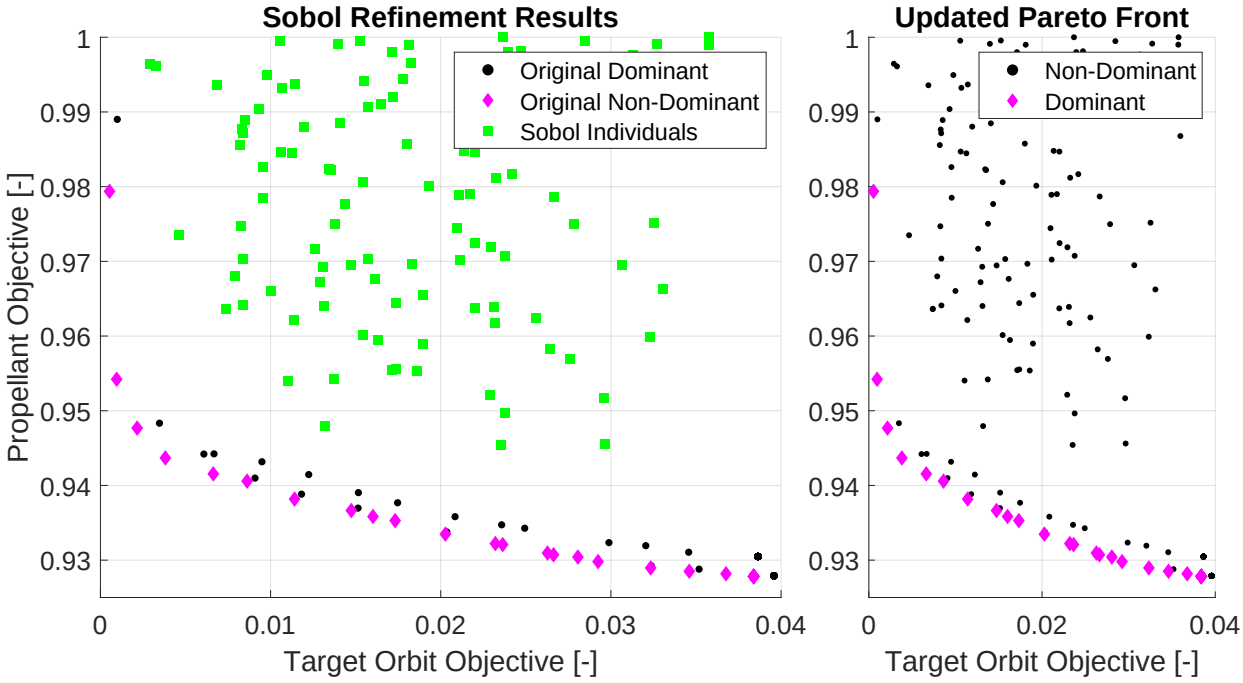

Overview of the Pareto front from the global optimization for an initial time of $t_0 = 3600$ s, with the individuals of the Sobol sequence that reach the target altitude.

Overview of the Pareto front from the global optimization for an initial time of $t_0 = -3600$ s, with the individuals of the Sobol sequence that reach the target altitude.

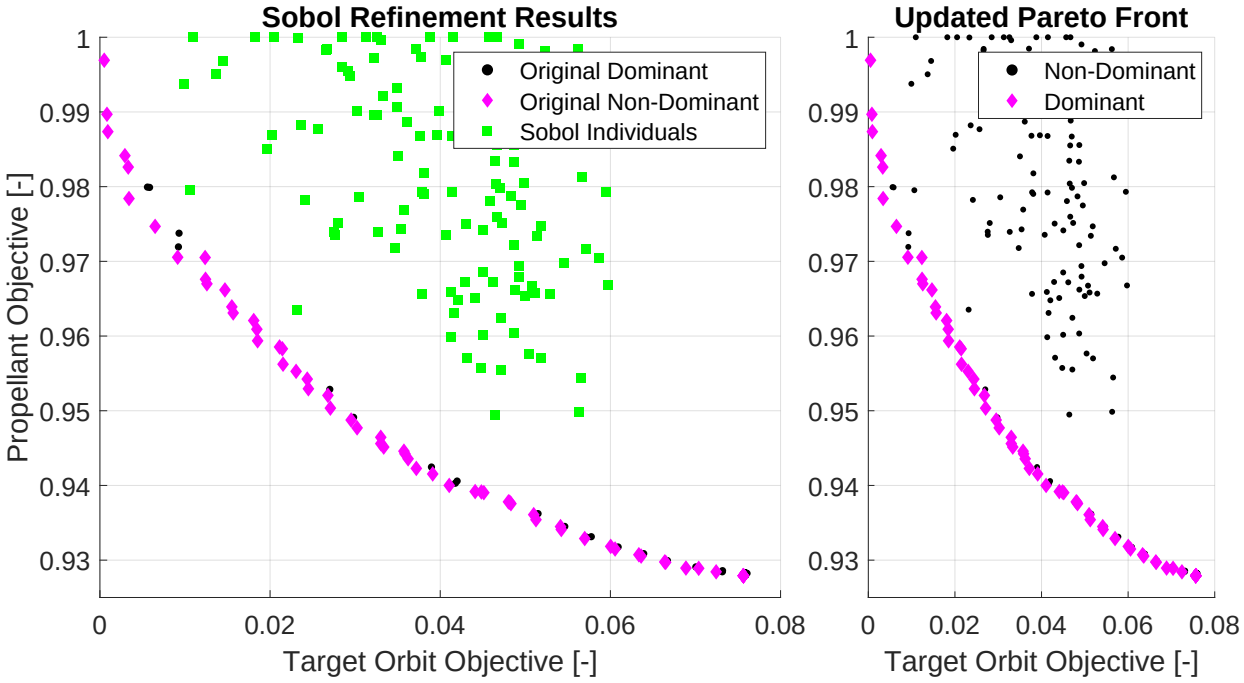

Overview of the Pareto front from the global optimization for an initial time of $t_0 = 7200$ s, with the individuals of the Sobol sequence that reach the target altitude.

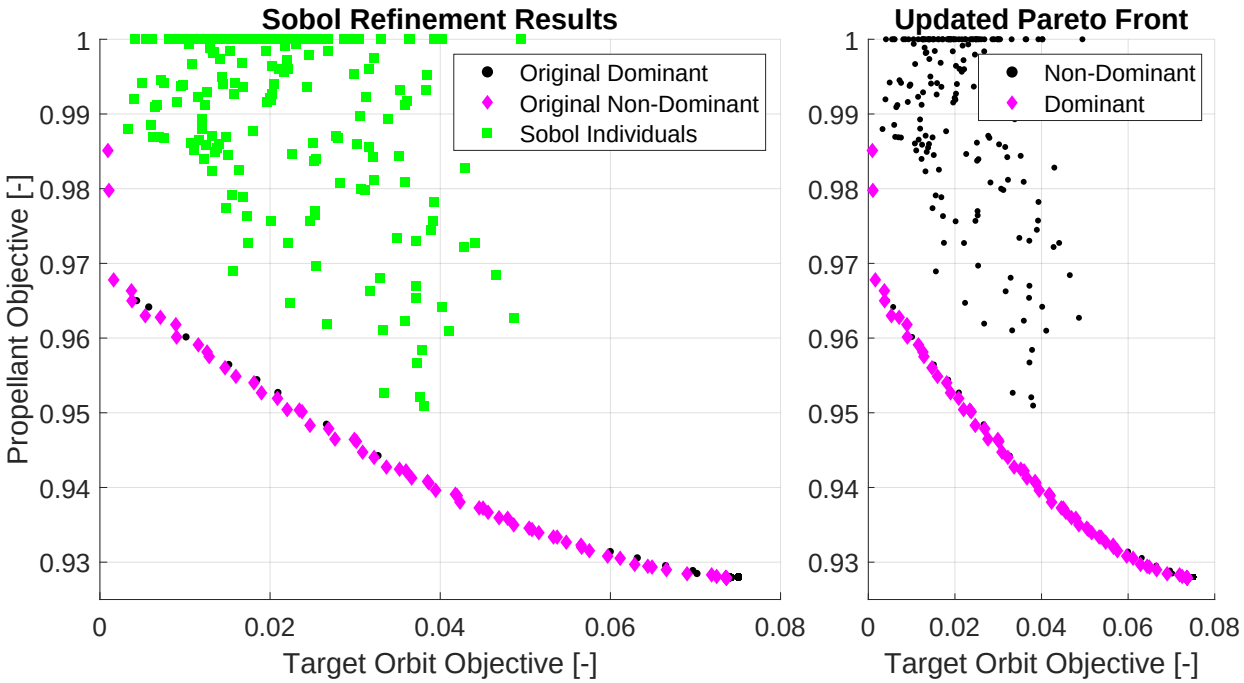

Overview of the Pareto front from the global optimization for an initial time of $t_0 = -7200$ s, with the individuals of the Sobol sequence that reach the target altitude.

D

Insight in the Lateral Optimization Parameters

In this appendix an insight is given in the behavior of the lateral optimization parameters. For each launch time, the deviation in inclination, steepness of the sigmoid function, and halfway point of the sigmoid function is shown.

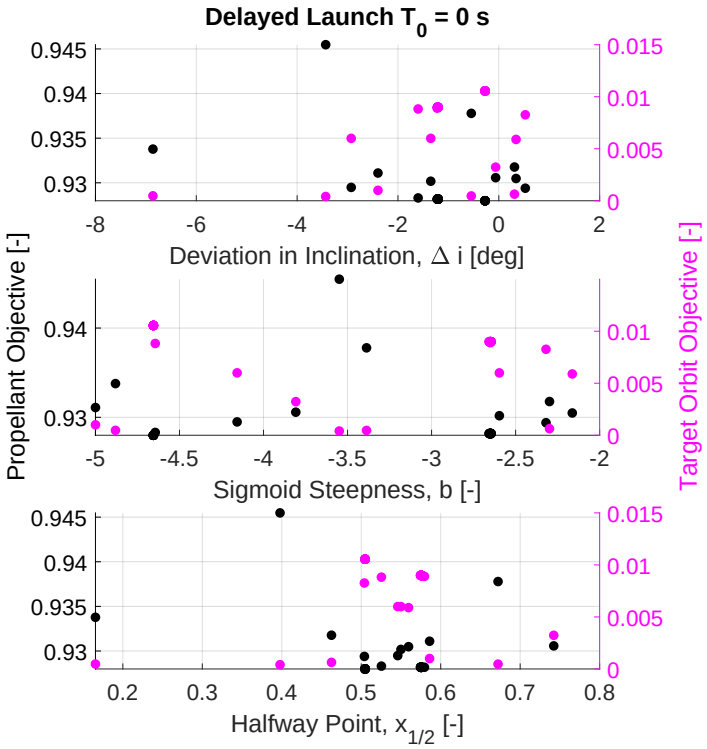

Overview of the lateral optimization parameters for an initial time of $t_0 = 0$ s.

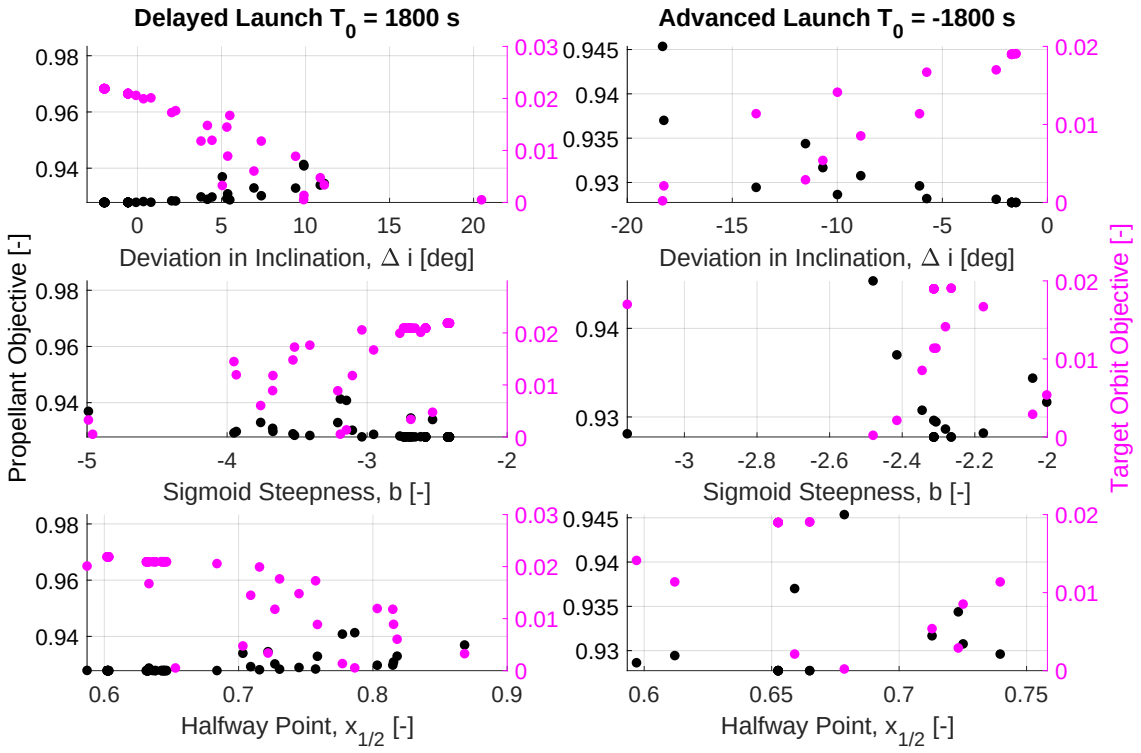

Overview of the lateral optimization parameters for an initial times of $t_0 = 1800$ s and $t_0 = -1800$ s.

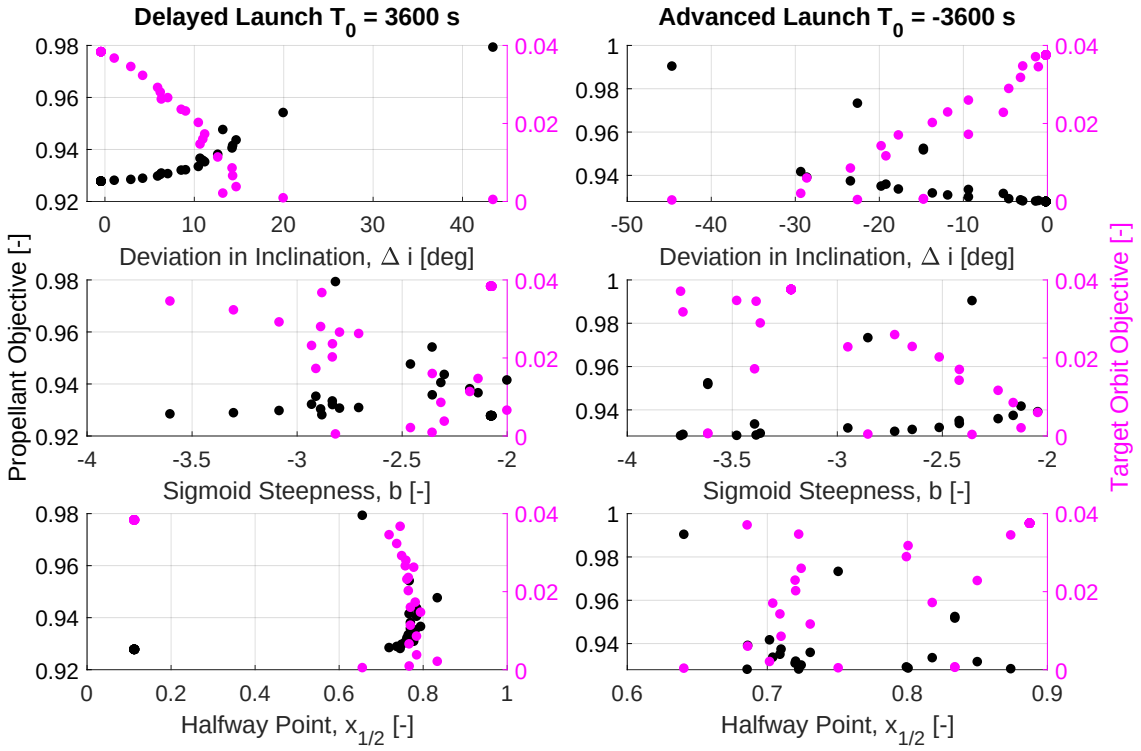

Overview of the lateral optimization parameters for an initial times of $t_0 = 3600$ s and $t_0 = -3600$ s.

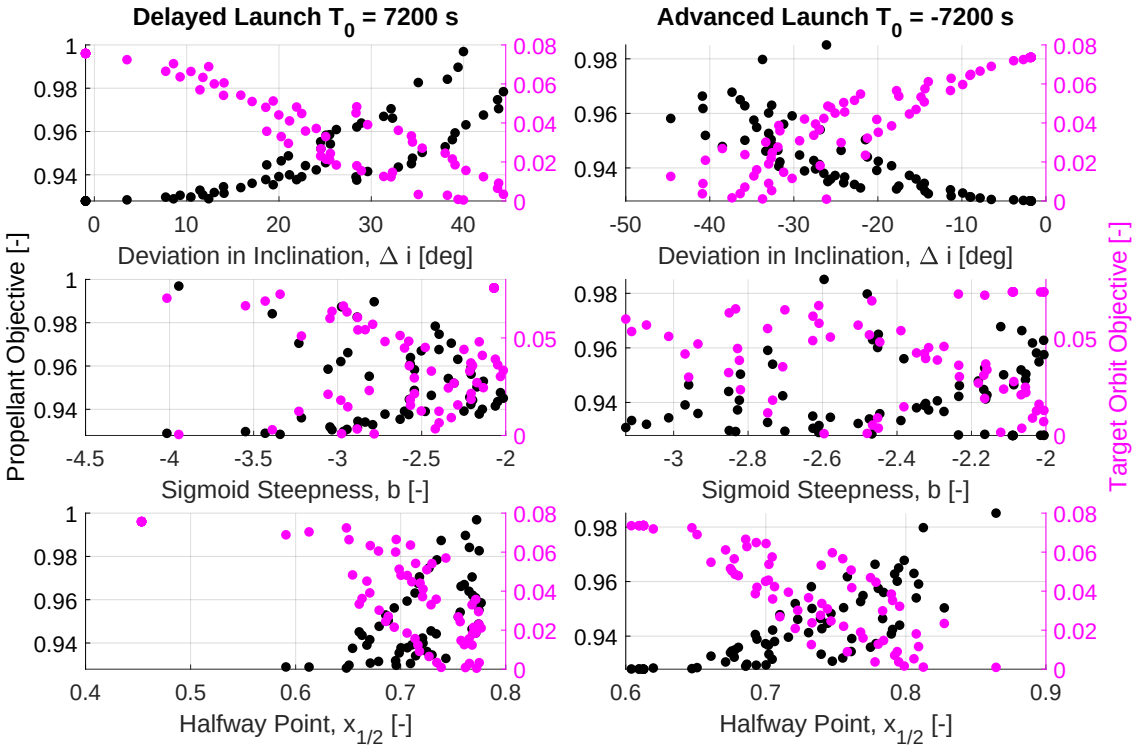

Overview of the lateral optimization parameters for an initial times of $t_0 = 7200$ s and $t_0 = -7200$ s.

References

Anderson, J. (2006). *Hypersonic and high-temperature gas dynamics*. 2nd. American Institute of Aeronautics and Astronautics. ISBN: 9781624105142.

— (2010). *Fundamentals of Aerodynamics*. McGraw-Hill Education. ISBN: 9780073398105.

Betts, J. T. (2010). *Practical Methods for Optimal Control and Estimation Using Nonlinear Programming*. Second Edition. Society for Industrial and Applied Mathematics. ISBN: 978-0-898716-88-7. URL: https://app.knovel.com/hotlink/toc/id:kpPMOCEUNA/practical-methods-optimal/practical-methods-optimal.

Biscani, F. and Izzo, D. (2020). "A parallel global multiobjective framework for optimization: pagmo". *Journal of Open Source Software* **5**.53, p. 2338. DOI: 10.21105/joss.02338.

Brown, D. A. (1986). "British Government, Industry Agree to Fund Hotol Launcher Studies". *Aviation Week & Space Technology* **124**.08, pp. 62–64.

Conway, B. A. (2010). *Spacecraft Trajectory Optimization*. Cambridge Aerospace Series. Cambridge University Press. DOI: 10.1017/CBO9780511778025.

Coppinger, R. (2005). "Composite cryogenic tank under development". *Flight International* **167**.4981, p. 29. URL: https://search.proquest.com/magazines/composite-cryogenic-tank-under-development/docview/225119557/se-2?accountid=27026.

Cornelisse, J., Schöyer, H., and Wakker, K. (1979). *Rocket Propulsion and Spaceflight Dynamics*. Aerospace Engineering Series. Pitman. ISBN: 9780273011415.

Dirkx, D. and Cowan, K. (2019). *AE4868 – Numerical Astrodynamics. Numerical Integration*.

Dirkx, D. and Mooij, E. (2017). *Conceptual Shape Optimization of Entry Vehicles*. Springer Aerospace Techn. Springer. DOI: 10.1007/978-3-319-46055-0.

Dujarric, C. (1999). "Possible future European launchers - A process of convergence". *ESA bulletin. Bulletin ASE. European Space Agency*, pp. 11–19. URL: http://www.esa.int/esapub/bulletin/bullet97/dujarric.pdf.

Freeman Jr., D. C., Stanley, D. O., Camarda, C. J., Legsch, R. A., and Cook, S. A. (1995). "Single-Stage-To-Orbit – a step closer". *Acta Atronautica* **37**.01, pp. 87–94. DOI: 10.1016/0094-5765(95)00087-G.

Hankey, W. L. (1988). *Re-entry Aerodynamics*. American Institute of Aeronautics and Astronautics.

Hartsfield, C., Branam, R. D., Hall, J., and Simmons, J. (2011). "Aerospike Rockets for Increased Space Launch Capability". *Air & Space Power Journal* **25**.2, pp. 65–73.

Hempsell, M. (2013). "Progress on SKYLON and SABRE". *Proceedings of the International Astronautical Congress, IAC* **11**, pp. 8427–8440.

Hempsell, M. and Longstaff, R. (2009). *SKYLON USERS' MANUAL*. English. Version 1 – Revision 1. Reaction Engines Limited. 52 pp.

Hiraiwa, T., Ito, K., Sato, S., Ueda, S., Tani, K., Tomioka, S., and Kanda, T. (2008). "Recent progress in scramjet/combined cycle engines at JAXA, Kakuda space center". *Acta Astronautica* **63**.5, pp. 565–574. DOI: 10.1016/j.actaastro.2008.04.011.

Huang, D. H. and Huzel, D. K. (1971). *Design of Liquid Propellant Rocket Engines*. Tech. rep. 19710019929. National Aeronautics and Space Administration. URL: https://ntrs.nasa.gov/citations/19710019929.

Idris, A. C., Saad, M. R., Zare-Behtash, H., and Kontis, K. (2014). "Luminescent Measurement Systems for the Investigation of a Scramjet Inlet-Isolator". *Sensors (Basel, Switzerland)* **14**, pp. 6606–32. DOI: 10.3390/s140406606.

Klees, R. and Dwight, R. (2014). *Applied Numerical Analysis (AE2220-I). Lecture Notes*.

Krevor, Z. C., Howard, R. D., Mosher, T., Scott, K. P., Voss, J. S., Sanchez, M. J., and Curry, J. M. (2011). "Dream Chaser Commercial Crewed Spacecraft Overview". *17th AIAA International Space Planes and Hypersonic Systems and Technologies Conference*. DOI: 10.2514/6.2011-2245.

Launius, R. D. (1994). "NASA and the Decision to Build the Space Shuttle, 1969-72". *The Historian* **57**.01, pp. 17–34. URL: https://www.jstor.org/stable/24449159.

— (2013). "The Strange Career of the American Spaceplane: The Long History of Wings and Wheels in Human Space Operations". *Centaurus* **55**.4, pp. 412–432. DOI: 10.1111/1600-0498.12037.

Lu, P. (2016). "Fault Diagnosis and Fault-Tolerant Control for Aircraft Subjected to Sensor and Actuator Faults". PhD thesis. Technical University of Delft. DOI: 10.4233/uuid:11be69d2-44ae-429c-9746-7e3ced35f464.

Lu, P. (1993). "Inverse dynamics approach to trajectory optimization for an aerospace plane". *Journal of Guidance, Control, and Dynamics* **16**.4, pp. 726–732. DOI: 10.2514/3.21073.

Maddock, C. A. and Minisci, E. (2016). "Spaceplane trajectory optimisation with evolutionary-based initialisation". *2016 IEEE Symposium Series on Computational Intelligence (SSCI)*, pp. 1–8. DOI: 10.1109/SSCI.2016.7850109.

Mateu, M. M. (2013). "Study of an air-breathing engine for hypersonic flight". PhD thesis. UPC, Escola Tècnica Superior d'Enginyeries Industrial i Aeronàutica de Terrassa. URL: http://hdl.handle.net/2099.1/20295.

Mooij, E. (1994). *The Motion of a Vehicle in a Planetary Atmosphere*. Delft University of Technology. ISBN: 9056230034.

— (1998). "Aerospace-plane Flight Dynamics – Analysis of guidance and control concepts". PhD thesis. Technical University of Delft.

— (2019a). *AE4870B – Re-entry Systems. Lecture Notes (2019–2020)*.

— (2019b). "Single-Stage-to-Orbit Space-Plane Trajectory Performance Analysis". *Modeling and Optimization in Space Engineering*, pp. 307–342. DOI: 10.1007/978-3-030-10501-3.

Mooij, E. and Dirkx, D. (2020). *AE4-866 – Propagation and Optimisation in Astrodynamics. Global Optimisation*.

Mukundan, V., Maity, A., Kumar, S. R., and Rajeev, U. P. (2019). "Ascent Trajectory Optimization of Launch Vehicles with Air-Breathing Propulsion". *IFAC-PapersOnLine* **52**.12. 21st IFAC Symposium on Automatic Control in Aerospace ACA 2019, pp. 274–279. ISSN: 2405-8963. DOI: https://doi.org/10.1016/j.ifacol.2019.11.255.

Mulder, J., Staveren, W. van, Vaart, J. van der, Weerdt, E. de, Visser, C. de, 't Veld, A. in, and Mooij, E. (2013). *AE3202 – Flight Dynamics. Lecture Notes*.

Murillo, O. and Lu, P. (2010). "Fast Ascent Trajectory Optimization for Hypersonic Air-Breathing Vehicles". *AIAA Guidance, Navigation, and Control Conference*. DOI: 10.2514/6.2010-8173.

National Research Council (1995). *Reusable Launch Vehicle: Technology Development and Test Program*. Washington, DC: The National Academies Press. ISBN: 978-0-309-05437-9. DOI: 10.17226/5115.

Newton, I., Bernard, I., and Whitman, A. (1999). *The principia: mathematical principles of natural philosophy*. University of California Press.

Noomen, R. (2019). *AE4-878 – Space Mission Design. Integrators*.

Olds, J. R. and Bradford, J. E. (2001). "SCCREAM: A Conceptual Rocket-Based Combined-Cycle Engine Performance Analysis Tool". *Journal of Propulsion and Power* **17**.2, pp. 333–339. DOI: 10.2514/2.5746.

Pescetelli, F., Minisci, E., Maddock, C., Taylor, I., and Brown, R. (2012). "Ascent Trajectory Optimisation for a Single-Stage-to-Orbit Vehicle with Hybrid Propulsion". *18th AIAA/3AF International Space Planes and Hypersonic Systems and Technologies Conference*. DOI: 10.2514/6.2012-5828.

Picone, J., Hedin, A., Drob, D., and Aikin, A. (2002). "NRLMSISE-00 empirical model of the atmosphere: Statistical comparison and scientific issues". *Journal of Geophysical Research* **107**. DOI: 10.1029/2002JA009430.

Powell, R. W., Shaughnessy, J. D., Cruz, C. I., and Naftel, J. C. (1991). "Ascent performance of an air-breathing horizontal-takeoff launch vehicle". *Journal of Guidance, Control, and Dynamics* **14**.4, pp. 834–839. DOI: 10.2514/3.20719.

Rao, A. V. (2014). "Trajectory Optimization: A Survey". *Optimization and Optimal Control in Automotive Systems*. Ed. by H. Waschl, I. Kolmanovsky, M. Steinbuch, and L. del Re. Springer, pp. 3–21.

Segal, C. (2005). *Propulsion Systems for Hypersonic Flight*. The Research and Technology Organisation of NATO. ISBN: 92-837-1138-6.

Shaughnessy, J. D. (1992). *Trim drag reduction concepts for horizontal takeoff single-stage-to-orbit vehicles*. Tech. rep. 102687. National Aeronautics and Space Administration.

Shaughnessy, J. D., Pinckney, S. Z., McMinn, J. D., Cruz, C. I., and Kelley, M. .-. (1990). *Hypersonic Vehicle Simulation Model: Winged-Cone Configuration*. Tech. rep. 23665-5225. National Aeronautics and Space Administration.

Sieberling, S., Chu, Q. P., and Mulder, J. A. (2010). "Robust Flight Control Using Incremental Nonlinear Dynamic Inversion and Angular Acceleration Prediction". *Journal of Guidance, Control, and Dynamics* **33**.6, pp. 1732–1742. DOI: 10.2514/1.49978.

Sippel, M., Klevanski, J., and Kauffmann, J. (2001). "Innovative Method for Return to the Launch Site of Reusable Winged Stages". *52nd International Astronautical Congress, Toulouse, 1.-5. Oct. 2001*. URL: https://elib.dlr.de/1538/.

Sippel, M., Trivailo, O., Bussler, L., Lipp, S., and Valluchi, C. (2016). "Evolution of the SpaceLiner towards a Reusable TSTO-Launcher". *International Astronautical Congress 2016*. IAC-16-D2.4.03. URL: https://elib.dlr.de/107554/.

Spillenaar Bilgen, J. (2017). "Global Ascent Trajectory Optimization of a Space Plane". MA thesis. Technical University of Delft.

Stone, H. W. and Piland, W. M. (1991). "The HL-20 Lifting-Body Personnel Launch System". *SAE Transactions* **100**, pp. 1955–1968. URL: http://www.jstor.org/stable/44548056.

Sutton, G. P. and Biblarz, O. (2016). *Rocket Propulsion Elements*. Ninth Edition. Hoboken, New Jersey: John Wiley & Sons. ISBN: 978-1-118-75365-1.

Taylor, N., Hempsell, C., Macfarlane, J., Osborne, R., Varvill, R., Bond, A., and Feast, S. (2010). "Experimental investigation of the evacuation effect in expansion deflection nozzles". *Acta Astronautica* **66**.3, pp. 550–562. ISSN: 0094-5765. DOI: 10.1016/j.actaastro.2009.07.016.

Tomioka, S., Takegoshi, M., Kochi, T., Kato, K., Saito, T., and Tani, K. (2021). "Sea-Level Static Tests of Rocket–Ramjet Combined Cycle Engine Model". *Journal of Propulsion and Power* **37**.3, pp. 381–390. DOI: 10.2514/1.B37683.

Varvill, R. and Bond, A. (2003). "A Comparison of Propulsion Concepts for SSTO Reusable Launchers". *Journal of the British Interplanetary Society* **56**, pp. 108–117.

Veeran, S., Pesyridis, A., and Ganippa, L. (2018). "Ramjet Compression System for a Hypersonic Air Transportation Vehicle Combined Cycle Engine". *Energies* **11**.10. ISSN: 1996-1073. DOI: 10.3390/en11102558.

Wakker, K. F. (2015). *FUNDAMENTALS OF ASTRODYNAMICS*. Delft University of Technology. ISBN: 978-94-6186-419-2.

Webber, H., Bond, A., and Hempsell, M. (2006). "Sensitivity of precooled air-breathing engine performance to heat exchanger design parameters". *AIAA 57th International Astronautical Congress, IAC 2006* **12**, pp. 8258–8268.

Wie, B. (2008). *Space Vehicle Dynamics and Control*. American Institue of Aeronauthics and Astronautics. ISBN: 78-1-56347-953-3.

Zhang, Y. and Jiang, J. (2008). "Bibliographical review on reconfigurable fault-tolerant control systems". *Annual Reviews in Control* **32**.2, pp. 229–252. DOI: https://doi.org/10.1016/j.arcontrol.2008.03.008.

Zhou, H., Wang, X., and Cui, N. (2020). "Ascent trajectory optimization for air-breathing vehicles in consideration of launch window". *Optimal Control Applications and Methods* **41**.2, pp. 349–368. DOI: 10.1002/oca.2546.